frontiers | Research Topics

Novel brain imaging methods for the aid of neurological and neuropsychiatric disorders

Edited by
Takao Yamasaki and Zhiyong Zhao

Published in
Frontiers in Neuroscience
Frontiers in Neuroimaging

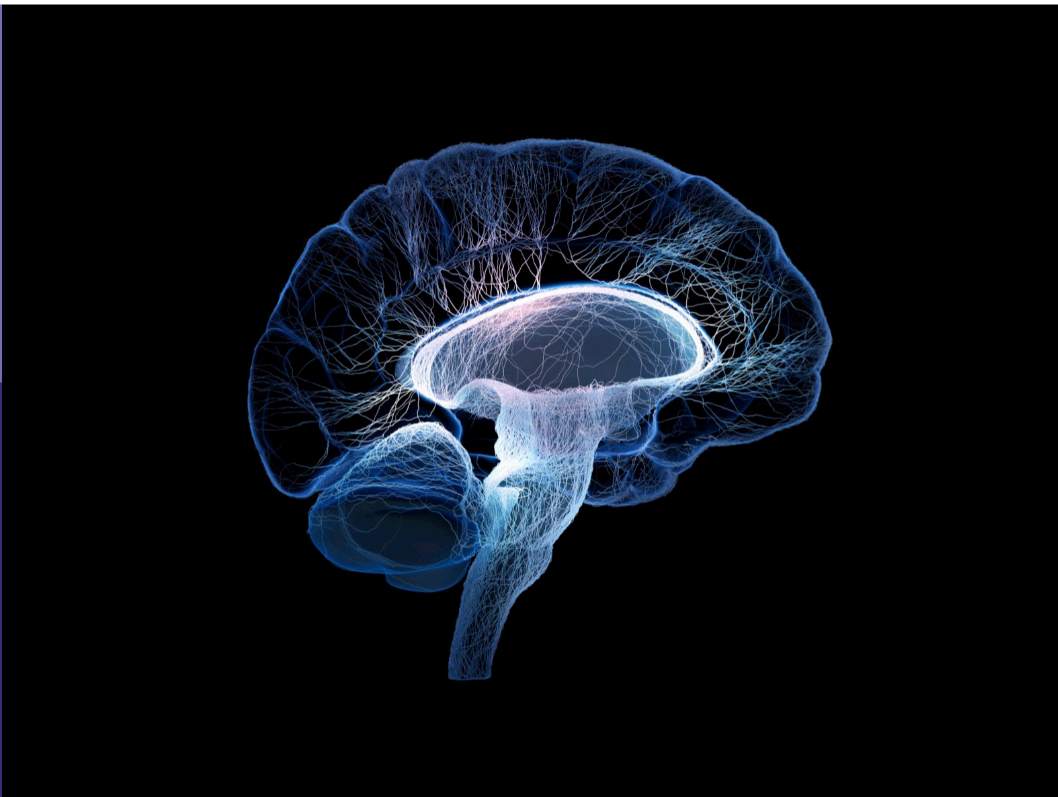

ISSN 1664-8714
ISBN 978-2-8325-5336-7
DOI 10.3389/978-2-8325-5336-7

About Frontiers

Frontiers is more than just an open access publisher of scholarly articles: it is a pioneering approach to the world of academia, radically improving the way scholarly research is managed. The grand vision of Frontiers is a world where all people have an equal opportunity to seek, share and generate knowledge. Frontiers provides immediate and permanent online open access to all its publications, but this alone is not enough to realize our grand goals.

Frontiers journal series

The Frontiers journal series is a multi-tier and interdisciplinary set of open-access, online journals, promising a paradigm shift from the current review, selection and dissemination processes in academic publishing. All Frontiers journals are driven by researchers for researchers; therefore, they constitute a service to the scholarly community. At the same time, the *Frontiers journal series* operates on a revolutionary invention, the tiered publishing system, initially addressing specific communities of scholars, and gradually climbing up to broader public understanding, thus serving the interests of the lay society, too.

Dedication to quality

Each Frontiers article is a landmark of the highest quality, thanks to genuinely collaborative interactions between authors and review editors, who include some of the world's best academicians. Research must be certified by peers before entering a stream of knowledge that may eventually reach the public - and shape society; therefore, Frontiers only applies the most rigorous and unbiased reviews. Frontiers revolutionizes research publishing by freely delivering the most outstanding research, evaluated with no bias from both the academic and social point of view. By applying the most advanced information technologies, Frontiers is catapulting scholarly publishing into a new generation.

What are Frontiers Research Topics?

Frontiers Research Topics are very popular trademarks of the *Frontiers journals series*: they are collections of at least ten articles, all centered on a particular subject. With their unique mix of varied contributions from Original Research to Review Articles, Frontiers Research Topics unify the most influential researchers, the latest key findings and historical advances in a hot research area.

Find out more on how to host your own Frontiers Research Topic or contribute to one as an author by contacting the Frontiers editorial office: frontiersin.org/about/contact

Novel brain imaging methods for the aid of neurological and neuropsychiatric disorders

Topic editors
Takao Yamasaki — Minkodo Minohara Hospital, Japan
Zhiyong Zhao — Zhejiang University, China

Citation
Yamasaki, T., Zhao, Z., eds. (2024). *Novel brain imaging methods for the aid of neurological and neuropsychiatric disorders*. Lausanne: Frontiers Media SA.
doi: 10.3389/978-2-8325-5336-7

Table of contents

frontiers | Frontiers in Neuroscience

TYPE Editorial
PUBLISHED 07 August 2024
DOI 10.3389/fnins.2024.1468794

Check for updates

OPEN ACCESS

EDITED AND REVIEWED BY
Vince D. Calhoun,
Georgia State University, United States

*CORRESPONDENCE
Takao Yamasaki
✉ yamasaki_dr@apost.plala.or.jp

RECEIVED 22 July 2024
ACCEPTED 26 July 2024
PUBLISHED 07 August 2024

CITATION
Yamasaki T and Zhao Z (2024) Editorial: Novel brain imaging methods for the aid of neurological and neuropsychiatric disorders. *Front. Neurosci.* 18:1468794.
doi: 10.3389/fnins.2024.1468794

Editorial: Novel brain imaging methods for the aid of neurological and neuropsychiatric disorders

Takao Yamasaki[1,2]* and Zhiyong Zhao[3]

[1]Department of Neurology, Minkodo Minohara Hospital, Fukuoka, Japan, [2]Kumagai Institute of Health Policy, Fukuoka, Japan, [3]Children's Hospital, Zhejiang University School of Medicine, National Clinical Research Center for Child Health, Hangzhou, China

KEYWORDS

brain imaging methods, neuroimaging, neurological and neuropsychiatric disorders, biomarkers, analytical methods, therapeutic application

Editorial on the Research Topic
Novel brain imaging methods for the aid of neurological and neuropsychiatric disorders

1 Introduction

The human brain is a highly complex and dynamic system comprising extensive structural and functional networks connecting different brain regions, operating at multiple spatial and temporal scales (Bassett and Bullmore, 2009; Bullmore and Sporns, 2009). This network system is the basis for our daily activities and cognitive functions, and its disruptions can cause various neurological and neuropsychiatric disorders, including Alzheimer's disease, Parkinson's disease, major depressive disorder (MDD), schizophrenia (SZ), and autism spectrum disorder (ASD) (Yamasaki et al., 2017; Miraglia et al., 2022; Cattarinussi et al., 2023; Tura and Goya-Maldonado, 2023).

Neuroimaging techniques, such as electroencephalography (EEG), magnetoencephalography (MEG), functional near-infrared spectroscopy (fNIRS), and magnetic resonance imaging (MRI), play a vital role in examining the healthy and pathological functions of the human brain network system. These techniques allow us to explore the brain at different temporal and spatial scales, taking advantage of the unique characteristics of each method (Yen et al., 2023; Zhu et al., 2023). Moreover, with the rapid development and widespread use of these neuroimaging techniques, the image analysis method has made considerable advances (Zhang et al., 2020) to help us in clarifying the pathological mechanism, early diagnosis, and complementary treatment of various clinical disorders.

Therefore, the purpose of this Research Topic is to collect data on the latest biomarkers, analytical methods, and therapeutic applications that will be useful for treating neurological and neuropsychiatric disorders.

2 Research on neuroimaging biomarkers

2.1 MRI

Among the various types of MRI techniques, diffusion tensor imaging (DTI) and resting-state functional MRI (rs-fMRI) have been widely used to investigate the structural and functional connectivity of the brain, respectively (Zhu et al., 2023). A significant advantage of MRI techniques is their excellent spatial resolution (Bassett and Bullmore, 2009).

This Research Topic includes one study on DTI and three studies on rs-fMRI biomarkers. In the DTI study, Zheng et al. revealed that DTI analysis along the perivascular space index, possibly indicating glymphatic activity, might be useful as a new biomarker for the early diagnosis of radiation encephalopathy. Regarding the rs-fMRI studies, Cheng et al. observed that the functional connectivity of the corticobasal ganglia network was altered in patients with idiopathic blepharospasm and correlated with disease severity, thus indicating its potential use as a quantitative marker of disease severity. Li Y. et al. showed frequency-specific alterations in causal influences among triple networks (i.e., default mode network, salience network, and central executive network) in patients with MDD, which might be useful as accurate and reliable biomarkers for MDD. Furthermore, Zhu et al. demonstrated that first-episode and recurrent MDD exerted distinct effects on the effective connectivity among large-scale brain networks, which might be potential neural mechanisms underlying the different clinical manifestations for the two MDD subtypes.

2.2 fNIRS

fNIRS is an optical neuroimaging technique used to image hemodynamic activity and connectivity in the brain and has better temporal resolution than fMRI (Pinti et al., 2020).

This Research Topic includes two studies on fNIRS biomarkers. Peng et al. showed that compared with that in the resting-state, brain network properties in the task-state were significantly different between poststroke depression (PSD) and non-PSD groups, resulting in improved classification performance. These findings demonstrated the feasibility and superiority of brain network properties in the task-state for exploring the neural mechanisms of PSD. Wu et al. found that patients with short-term insomnia disorder (SID) exhibited an aberrant functional connectivity pattern in the prefrontal cortex during the verbal fluency test task, which correlated with the severity of sleep disturbances. Hence, fNIRS can contribute to the early detection and diagnosis of patients with SID, thereby effectively reducing the risk of disease progression.

2.3 EEG and MEG

EEG and MEG signals are more directly related to neuronal activity and have more excellent temporal resolution than fMRI and fNIRS (Bassett and Bullmore, 2009; Gross, 2019).

This Research Topic includes one study each on EEG and MEG. Using a 128ch EEG system, Liu et al. recorded auditory evoked potential in patients with chronic fatigue syndrome (CFS) and demonstrated the significant correlation between the P50 sensory gate ratio and clinical symptoms such as fatigue, anxiety, and depression. The P50 sensory gate ratio may be remarkably used for clarifying the mechanism, classification, treatment, and prognosis of CFS. In the MEG study, Nakanishi et al. reported that the abnormal phase lead on 80 Hz auditory steady-state response exhibited the highest discriminative power between patients with SZ and healthy individuals. They concluded that this testing technique has significant potential as a strong candidate for identifying neurophysiological endophenotypes associated with SZ.

3 Research on neuroimaging analysis methods

ROI-based and data-driven methods are two common approaches used to analyze functional connectivity derived from rs-fMRI data. The ROI-based method requires prior knowledge of targeted regions and consists of statistical parametric mapping, coherence analysis, and cross-correlation analysis. However, the data-driven method relies on acquired data, including decomposition [clustering analysis and principal component analysis/independent component analysis (ICA)], graph theory, and machine learning (Chauhan and Choi, 2022).

This Research Topic includes two studies on state-of-the-art rs-fMRI analysis methods. Jing et al. found that both group information-guided ICA (GIG-ICA) and independent vector analysis-Gaussian-Laplacian density models (IVA-GL) demonstrated distinct capabilities in identifying brain network modules in patients with ASD and healthy subjects. GIG-ICA can detect more regions with higher amplitudes in spatial network differences, and IVA-GL can identify more networks associated with ASD. This study provides further insights into using different data-driven methods to investigate neurological disorders using rs-fMRI. In the other study, Li W.-X. et al. showed that directed functional connectivity quantified using a new complex-valued transfer entropy (CTE) method had higher classification accuracy between patients with SZ and healthy subjects than other methods. Therefore, their proposed CTE provides a new general method for fully detecting highly predictive directed connectivity from complex-valued fMRI data.

4 Research on the application of neuroimaging to rehabilitation and treatment

This Research Topic includes two studies on the application of neuroimaging to rehabilitation and treatment. Neurofeedback using neuroimaging techniques (e.g., EEG, MEG, and fMRI) has been used as a cognitive training tool to improve brain functions (Loriette et al., 2021). Takahashi et al. developed a portable, wearable NIRS-based neurofeedback system and demonstrated the usefulness of this system for older adults and its potential to reduce cognitive decline. Electrical stimulation, such as transcranial direct current stimulation (tDCS), is widely used to treat neurological and neuropsychiatric disorders (Stagg and Nitsche, 2011). Computational modeling is an important approach for understanding the mechanisms underlying tDCS and optimizing treatment plans. Katoch et al. conducted *in vivo* magnetic resonance conductivity tensor imaging (CTI) experiments on the entire brain to precisely estimate tissue responses to electrical stimulation. They suggested that this CTI-based, subject-specific model can provide detailed information on tissue responses for personalized tDCS treatment plans.

5 Conclusion

This Research Topic provides information on novel brain imaging methods that can aid in the treatment of neurological and neuropsychiatric disorders, with a particular focus on the latest biomarkers, analytical methods, and therapeutic applications. We believe that this Research Topic will provide valuable insights to guide future research efforts and clinical practice.

Author contributions

TY: Writing – original draft, Writing – review & editing. ZZ: Writing – review & editing.

Funding

The author(s) declare that no financial support was received for the research, authorship, and/or publication of this article.

Acknowledgments

We would like to thank all authors for their contribution to this Research Topic.

Conflict of interest

The authors declare that the research was conducted in the absence of any commercial or financial relationships that could be construed as a potential conflict of interest.

The author(s) declared that they were an editorial board member of Frontiers, at the time of submission. This had no impact on the peer review process and the final decision.

Publisher's note

References

Bassett, D. S., and Bullmore, E. T. (2009). Human brain networks in health and disease. *Curr. Opin. Neurol.* 22, 340–347. doi: 10.1097/WCO.0b013e32832d93dd

Bullmore, E., and Sporns, O. (2009). Complex brain networks: graph theoretical analysis of structural and functional systems. *Nat. Rev. Neurosci.* 10, 186–198. doi: 10.1038/nrn2575

Cattarinussi, G., Di Giorgio, A., Moretti, F., Bondi, E., and Sambataro, F. (2023). Dynamic functional connectivity in schizophrenia and bipolar disorder: a review of the evidence and associations with psychopathological features. *Prog. Neuropsychopharmacol. Biol. Psychiatry* 127:110827. doi: 10.1016/j.pnpbp.2023.110827

Chauhan, N., and Choi, B. J. (2022). Comparison of functional connectivity analysis methods in Alzheimer's disease. *Appl. Sci.* 12:8096. doi: 10.3390/app12168096

Gross, J. (2019). Magnetoencephalography in cognitive neuroscience: a primer. *Neuron* 104, 189–204. doi: 10.1016/j.neuron.2019.07.001

Loriette, C., Ziane, C., and Ben Hamed, S. (2021). Neurofeedback for cognitive enhancement and intervention and brain plasticity. *Rev. Neurol.* 177, 1133–1144. doi: 10.1016/j.neurol.2021.08.004

Miraglia, F., Vecchio, F., Pappalettera, C., Nucci, L., Cotelli, M., Judica, E., et al. (2022). Brain connectivity and graph theory analysis in Alzheimer's and Parkinson's disease: the contribution of electrophysiological techniques. *Brain Sci.* 12:402. doi: 10.3390/brainsci12030402

Pinti, P., Tachtsidis, I., Hamilton, A., Hirsch, J., Aichelburg, C., Gilbert, S., et al. (2020). The present and future use of functional near-infrared spectroscopy (fNIRS) for cognitive neuroscience. *Ann. N. Y. Acad. Sci.* 1464, 5–29. doi: 10.1111/nyas.13948

Stagg, C. J., and Nitsche, M. A. (2011). Physiological basis of transcranial direct current stimulation. *Neuroscientist* 17, 37–53. doi: 10.1177/1073858410386614

Tura, A., and Goya-Maldonado, R. (2023). Brain connectivity in major depressive disorder: a precision component of treatment modalities? *Transl. Psychiatry* 13:196. doi: 10.1038/s41398-023-02499-y

Yamasaki, T., Maekawa, T., Fujita, T., and Tobimatsu, S. (2017). Connectopathy in autism spectrum disorders: a review of evidence from visual evoked potentials and diffusion magnetic resonance imaging. *Front. Neurosci.* 11:627. doi: 10.3389/fnins.2017.00627

Yen, C., Lin, C. L., and Chiang, M. C. (2023). Exploring the frontiers of neuroimaging: a review of recent advances in understanding brain functioning and disorders. *Life* 13:1472. doi: 10.3390/life13071472

Zhang, J., Chen, K., Wang, D., Gao, F., Zheng, Y., and Yang, M. (2020). Editorial: advances of neuroimaging and data analysis. *Front. Neurol.* 11:257. doi: 10.3389/fneur.2020.00257

Zhu, H., Li, T., and Zhao, B. (2023). Statistical learning methods for neuroimaging data analysis with applications. *Annu. Rev. Biomed. Data Sci* 6, 73–104. doi: 10.1146/annurev-biodatasci-020722-100353

frontiers | Frontiers in Neuroscience

TYPE Original Research
PUBLISHED 30 March 2023
DOI 10.3389/fnins.2023.1159883

EDITED BY
Zhiyong Zhao,
Zhejiang University, China

REVIEWED BY
Xiang Huang,
Sichuan University, China
Nian Xiong,
Huazhong University of Science
and Technology, China

*CORRESPONDENCE
Gang Liu
✉ liug26@mail.sysu.edu.cn
Jinping Xu
✉ jp.xu@siat.ac.cn
Kangqiang Peng
✉ pengkq@sysucc.org.cn

†These authors have contributed equally to this work

SPECIALTY SECTION
This article was submitted to
Brain Imaging Methods,
a section of the journal
Frontiers in Neuroscience

RECEIVED 06 February 2023
ACCEPTED 15 March 2023
PUBLISHED 30 March 2023

CITATION
Cheng Q, Xiao H, Luo Y, Zhong L, Guo Y, Fan X, Zhang X, Liu Y, Weng A, Ou Z, Zhang W, Wu H, Hu Q, Peng K, Xu J and Liu G (2023) Cortico-basal ganglia networks dysfunction associated with disease severity in patients with idiopathic blepharospasm. *Front. Neurosci.* 17:1159883. doi: 10.3389/fnins.2023.1159883

Cortico-basal ganglia networks dysfunction associated with disease severity in patients with idiopathic blepharospasm

Qinxiu Cheng[1]†, Han Xiao[2]†, Yuhan Luo[3]†, Linchang Zhong[4], Yaomin Guo[3], Xinxin Fan[1], Xiaodong Zhang[1], Ying Liu[3], Ai Weng[3], Zilin Ou[3], Weixi Zhang[3], Huawang Wu[5], Qingmao Hu[1], Kangqiang Peng[4]*, Jinping Xu[1]* and Gang Liu[3]*

[1]Chinese Academy of Sciences, Institute of Biomedical and Health Engineering, Shenzhen Institutes of Advanced Technology, Shenzhen, China, [2]Department of Nuclear Medicine, Guangdong Second Provincial General Hospital, Guangzhou, China, [3]Department of Neurology, National Key Clinical Department and Key Discipline of Neurology, Guangdong Provincial Key Laboratory for Diagnosis and Treatment of Major Neurological Diseases, The First Affiliated Hospital, Sun Yat-sen University, Guangzhou, China, [4]Department of Medical Imaging, Sun Yat-sen University Cancer Center, State Key Laboratory of Oncology in Southern China, Collaborative Innovation Center for Cancer Medicine, Guangzhou, China, [5]Guangzhou Huiai Hospital, The Affiliated Brain Hospital of Guangzhou Medical University, Guangzhou, China

Background: Structural changes occur in brain regions involved in cortico-basal ganglia networks in idiopathic blepharospasm (iBSP); whether these changes influence the function connectivity patterns of cortico-basal ganglia networks remains largely unknown. Therefore, we aimed to investigate the global integrative state and organization of functional connections of cortico-basal ganglia networks in patients with iBSP.

Methods: Resting-state functional magnetic resonance imaging data and clinical measurements were acquired from 62 patients with iBSP, 62 patients with hemifacial spasm (HFS), and 62 healthy controls (HCs). Topological parameters and functional connections of cortico-basal ganglia networks were evaluated and compared among the three groups. Correlation analyses were performed to explore the relationship between topological parameters and clinical measurements in patients with iBSP.

Results: We found significantly increased global efficiency and decreased shortest path length and clustering coefficient of cortico-basal ganglia networks in patients with iBSP compared with HCs, however, such differences were not observed between patients with HFS and HCs. Further correlation analyses revealed that these parameters were significantly correlated with the severity of iBSP. At the regional level, the functional connectivity between the left orbitofrontal area and left primary somatosensory cortex and between the right anterior part of pallidum and right anterior part of dorsal anterior cingulate cortex was significantly decreased in patients with iBSP and HFS compared with HCs.

Conclusion: Dysfunction of the cortico-basal ganglia networks occurs in patients with iBSP. The altered network metrics of cortico-basal ganglia networks might be served as quantitative markers for evaluation of the severity of iBSP.

KEYWORDS

cortico-basal ganglia networks, graph theoretical analysis, hemifacial spasm, idiopathic blepharospasm, resting-state functional magnetic resonance imaging

Introduction

Idiopathic blepharospasm (iBSP) is a common sub-type of focal dystonia, which is characterized by bilateral intermittent or sustained spasms of the orbicularis oculi muscle, and commonly associated with psychiatric and cognitive co-morbidities that lead to heterogeneous clinical expressions (Alemán et al., 2009; Defazio et al., 2017). Although immense effort has been dedicated to identify its etiology, the full pathophysiology of iBSP is still not well understood. Hemifacial spasm (HFS) was known to be caused often by vessel compression at the root exit zone of the facial nerve (Tan et al., 2004), which is characterized by unilateral clonic or tonic contractions of facial muscles (Chaudhry et al., 2015). Since it showed similar clinical symptoms with iBSP especially for facial hyperkinetic movements, it was commonly used as a control group to further differentiate changes that occur due to dystonia-specific abnormalities or facial hyperkinetic movements (Guo et al., 2021; Xu et al., 2022).

Traditionally, iBSP has been thought to be related to abnormalities in the basal ganglia (Suzuki et al., 2007; Zoons et al., 2011; Guo et al., 2021). With the development of magnetic resonance imaging (MRI) techniques, structural changes extend to many brain regions involved in the basal ganglia-thalamo-cortical motor circuit in iBSP (Obermann et al., 2007; Suzuki et al., 2011; Horovitz et al., 2012; Worbe et al., 2012; Tomić et al., 2021). Classically, these abnormalities observed outside the basal ganglia have been commonly thought as secondary phenomena due to abnormal motor output/sensory input from excessive movements (Lehéricy et al., 2013). However, in addition to motor circuit, the cortical-basal ganglia networks also included brain regions mainly responding for cognitive and emotional processing, such as posterior cingulate, prefrontal, orbitofrontal area, anterior cingulate, insular, hippocampus, and amygdala. The structural changes in these regions were also found to be associated with iBSP (Obermann et al., 2007; Suzuki et al., 2011; Horovitz et al., 2012; Worbe et al., 2012; Tomić et al., 2021). To better understand the pathophysiology of iBSP, a network model has been put forward in a previous review and was further supported by other reviews (Neychev et al., 2011; Niethammer et al., 2011). They suggested that iBSP is a network disorder associated with structural and functional derangement in a network connecting frontal and parietal cortical regions, basal ganglia, thalamus, the cerebellum and et al., rather than resulted from particular abnormalities in certain brain regions. These suggestions were further supported by results from functional MRI (fMRI) studies in the iBSP. Specially, different fMRI methodologies, such as amplitude of low frequency fluctuations, regional homogeneity analysis, seed-based analysis, voxel-mirrored homotopic connectivity, independent component analysis, and graph theoretical analysis, have been widely applied to explore the functional mechanism underlying iBSP (Zhou et al., 2013; Wei et al., 2018; Jiang et al., 2019). They reported abnormal functional connectivity in various cortical and subcortical regions, as well as within default mode network, sensory motor network, fronto-parietal network, and salience network in patients with iBSP (Huang et al., 2017). These results further in favor for the suggestion that iBSP is a network disorder. Among these methodologies, the graph theoretical analysis is the best way to measure brain functional organization at a brain network level or even at the whole brain connectivity patterns (Smitha et al., 2017). Using this method, iBSP patients showed an abnormal functional network architecture at whole brain level characterized by abnormal expansion or shrinkage of neural communities (Battistella et al., 2017). To our best knowledge, no study has examined cortico-basal ganglia networks using resting-state fMRI (rs-fMRI) despite a large body of evidence pointing toward dysfunction in certain regions of cortico-basal ganglia networks in iBSP (Yang et al., 2013; Jochim et al., 2017; Fang et al., 2021). Therefore, how structural changes could influence the functional patterns of cortico-basal ganglia networks and further related to symptom expression, as well as whether these functional alterations were due to dystonic origin or facial hyperkinetic movements in patients with iBSP remain largely unclear.

In the present study, in accordance with the hypothesis that extensively altered functional connections exist in the large-scale cortico-basal ganglia networks in iBSP, we evaluated the global and local organization of functional connections using graph theoretical analysis of cortico-basal ganglia networks between patients with iBSP and healthy controls (HCs). A group of age-, gender-, and duration-matched patients with HFS was also recruited to determine whether these functional alterations in iBSP are derived from dystonic origin or excessive facial movements. Finally, correlation analyses were performed to explore relationships between topological parameters and clinical measurements (e.g., severity and disease duration of iBSP) in patients with iBSP.

Materials and methods

Subjects

Patients were recruited from an outpatient clinic of the First Affiliated Hospital of Sun Yat-sen University. They were diagnosed as adult-onset iBSP or HFS based on the standard criteria by

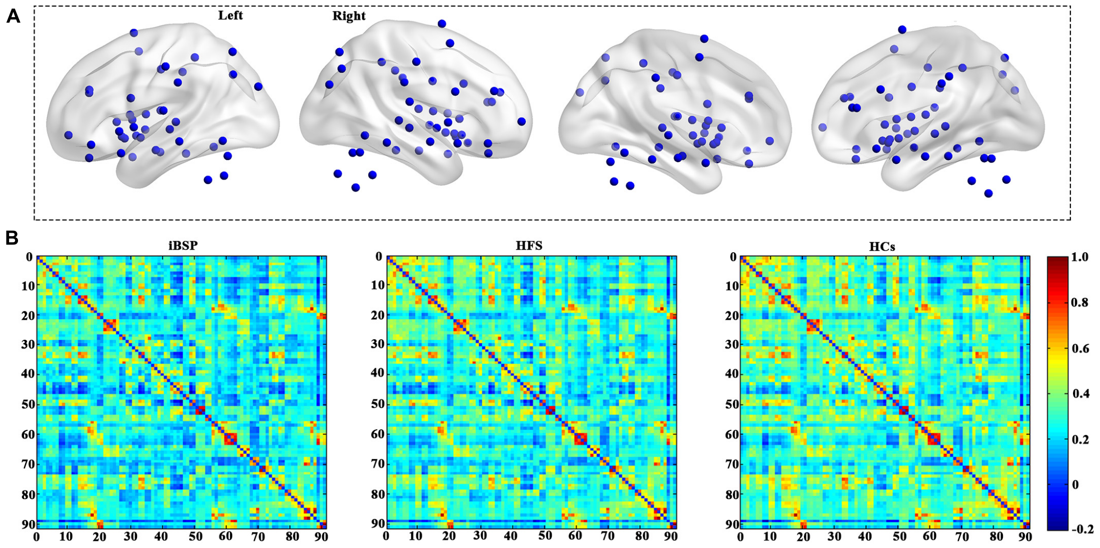

FIGURE 1
Cortico-basal ganglia networks. **(A)** Distributions of all brain regions in the cortico-basal ganglia networks. All regions are listed in Supplementary Table 1. **(B)** The average functional connectivity matrix of the cortico-basal ganglia networks for patients with idiopathic blepharospasm and hemifacial spasm and HCs. HCs, healthy controls; HFS, hemifacial spasm; iBSP, idiopathic blepharospasm.

two senior neurologists (G Liu and WX Zhang). The exclusion criteria for iBSP and HFS patients were the same with the following items: (i) aged less than 18 or more than 80; (ii) left handed; (iii) received botulinum toxin (BoNT) injections within 3 months before MRI scanning; (iv) had a family history of movement disorders; (v) reported evidence of stroke and traumatic brain injury, or any conditions which might be cause secondary blepharospasm; (vi) reported evidence of neurological diseases, such as Parkinson's disease, Alzheimer's disease, major depressive disorder, and epilepsy; (vii) had a history of exposure to previous neuroleptic medication; (viii) had any conditions that contradicted with cerebral MRI; (ix) show evidence of possible anxiety (Hamilton anxiety rating scale score of > 14); and (x) received oral medications for approximately 24 h before MRI scans. HCs were also recruited using the same exclusion criteria. This study was performed according to the Declaration of Helsinki and was approved by the Ethics Committee of the First Affiliated Hospital of Sun Yat-sen University [(2020)323]. Written informed consent was obtained from all subjects. Finally, 62 patients with iBSP, 62 with HFS (31, left side), and 62 HCs were included in the current study.

Clinical measurements

The demographics and clinical characteristics, including patients' age, gender, education, duration of disease, and duration of BoNT injections, were obtained from all patients *via* face-to-face interviews before MRI scanning. The disease severity of patients was evaluated using the 0–4 scale Jankovic Rating Scale (JRS), which includes two subscales that measure severity (0 = None; 1 = Increased blinking only with external stimulus; 2 = Mild but spontaneous eyelid fluttering, but not functionally disabling; 3 = Moderate spasm, mildly incapacitating; and 4 = Severe, incapacitating spasm including eyelid and other facial muscles) and frequency (0 = None; 1 = Slightly increased blinking frequency; 2 = Eyelid fluttering shaking lasting less than 1 s; 3 = Orbicularis oculi muscle spasm lasting more than 1 s with eyes opening more than 50% of awake time; and 4 = Functionally "blind") of involuntary orbicularis oculi muscle contraction, respectively (Jankovic et al., 2009).

Data acquisition

All rs-fMRI data were obtained using a 3T Siemens scanner (Tim Trio; Siemens, Erlangen, Germany). Participants were instructed to keep their eyes closed and their heads motionless during scanning. An echo-planar imaging sequence with the following parameters was used: repetition time = 2,000 ms, echo time = 30 ms, flip angle = 90°, acquisition matrix = 64×64; voxel size = 3.4375 $mm^3 \times 3.4375$ $mm^3 \times 3$ mm^3, 33 slices, and volumes = 240.

Data pre-processing

The rs-fMRI data were pre-processed using the Data Processing and Analysis of Brain Imaging (DPABI) toolbox[1] (Yan et al., 2016). The main steps including: (i) discarding the first 10 volumes to allow for magnetization equilibrium; (ii) realigning to the first volume to account for head motion (subjects showing a maximum displacement of more than 3 mm and an angular motion of more than 3° were removed); (iii) normalizing to 3 mm × 3 mm × 3 mm resolution in the Montreal Neurological Institute (MNI) template;

---

[1] http://rfmri.org/dpabi

TABLE 1 Subjects' demographics and clinical characteristics.

Groups	iBSP	HFS	HCs	*P*-values
Subjects	62	62	62	–
Median age, years (range)	55 (28–75)	53.5 (30–72)	57 (26–75)	0.472
Gender (male/female)	32/30	38/24	35/27	0.820
Median disease duration, years (range)	5 (0.5–25)	4 (0.08–20)	–	0.923
Median JRS total scores (range)	6 (2–8)	6 (0–8)	–	0.125
BoNT injections (yes/no)	48/14	41/21	–	0.231
Median BoNT injections duration, years (range)	3 (0.17–20)	2 (0.25–16)	–	0.554

BoNT, botulinum toxin; HCs, healthy controls; HFS, hemifacial spasm; iBSP, idiopathic blepharospasm; JRS, Jankovic Rating Scale.

(iv) spatially smoothing with a Gaussian kernel of 6 mm full-width at half maximum; (v) regression out Friston-24 head motion parameters, white matter, and cerebrospinal fluid signals (as regression out global mean signals can lead to spurious resting-state functional correlations and false inferences, they were not regression out in the current study); (vi) filtering with the temporal band-path (0.01–0.1 Hz); and (vii) scrubbing bad images (before two time points and after one time point) which exceed the pre-set criterion (frame displacement < 0.5) for excessive motion.

Network construction

To construct the cortico-basal ganglia networks for each participant, we used 91 MNI coordinates that were previously reported (**Figure 1A** and **Supplementary Table 1**; Worbe et al., 2012). The node was defined as a sphere with a radius of 6 mm centered at each coordinate and resampled to 3 mm × 3 mm × 3 mm resolution. The functional network edge was defined with resting-state functional connectivity measured using Pearson's correlation coefficient between the mean time series of each pair of the 91 regions. As a result, a symmetric 91×91 functional connectivity matrix was obtained for each participant for further analyses (**Figure 1B**). Consistent with previous studies, we only used positive connectivity in the further analysis (Xu et al., 2020; Pang et al., 2022).

Graph theory-based network analyses

To identify changes in global topological characteristics of the cortico-basal ganglia networks among three groups, global network parameters including global efficiency (E_{glob}) that can indicate the efficiency of information transference across a network, clustering coefficients (C_p) that quantify the local inter-connectivity of a network, and the shortest path length (L_p) that can quantify the integration of a network, were calculated using a graph theoretical network analysis toolbox (GRETNA v2.0).[2] E_{glob} and L_p are used to measure brain network integration, and C_p is employed to investigate brain network segregation. To avoid bias choice of a certain value, the complex network analyses were performed at a sparsity range from 0.1 to 0.5 with an interval of 0.05, and the area under curve (AUC) values under this range of sparsity were calculated for the statistical analyses (Xu et al., 2017). The group difference of network parameters was explored using analysis of covariance (ANCOVA) and *post-hoc* two-sample *t*-tests between any two groups, with age and gender as covariates. The significance level was set at $P < 0.05$.

Functional connectivity comparisons

To explore group differences in functional connections, an ANCOVA was used to identify differences among the three groups, and two-sample *t*-tests were used to identify differences between any two groups. The results were corrected by Bonferroni corrections of $P < 1.22\times10^{-5}$.

Regional indexes comparisons

Moreover, we also calculated the betweenness centrality and degree centrality as regional indexes for each region. To avoid bias choice of a certain value, the complex network analyses were performed at a sparsity range from 0.1 to 0.5 with an interval of 0.05, and the AUC values under this range of sparsity were calculated for the statistical analyses (Xu et al., 2017). The group differences of network parameters and regional indexes were explored using ANCOVA and *post-hoc* two-sample *t*-tests between any two groups, with age and gender as covariates. The significance level was set at $P < 0.05$ for network parameters, and $P < 0.05/91$ (Bonferroni corrections) for regional indexes.

Correlation with clinical measurements

To reveal whether the changed global metrics and functional connections in the cortico-basal ganglia networks showed associations with clinical measurements in patients with iBSP, partial correlation analyses between changed indices and disease duration and JRS total scores were performed, using age and gender as covariates. The significance level was set at $P < 0.05$.

Statistical analyses

We analyzed all the subjects' demographics and clinical characteristics using SPSS 23.0 (IBM, Armonk, NY, USA). Differences in the age among the iBSP, HFS, and HCs groups were identified using the non-parametric Kruskal–Wallis *H* test. Gender differences among the three groups and the number of patients receiving BoNT injections between patients with iBSP and HFS

---

[2] http://www.nitrc.org/projects/gretna/

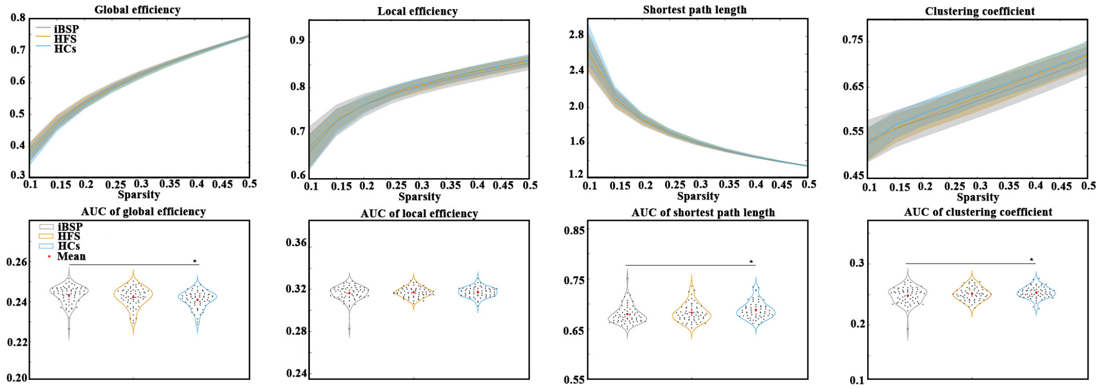

FIGURE 2
Comparisons of topological characteristics among groups. The top row shows the topological characteristics across a range of sparsity (0.1–0.5) at an interval of 0.05, and the bottom row shows the area under the curve of each topological characteristic. Group differences in network parameters were explored using analysis of covariance and *post-hoc* two-sample *t*-tests between any two groups, with age and gender as covariates. *Represents significant results with $P < 0.05$. AUC, area under the curve; HCs, healthy controls; HFS, hemifacial spasm; iBSP, idiopathic blepharospasm.

were compared using the Pearson χ^2 test. Moreover, differences in the disease duration, JRS total scores, and duration of BoNT injections between patients with iBSP and HFS were assessed using the Mann–Whitney *U* test. A two-tailed *P*-value < 0.05 indicated statistical significance.

Results

Demographic information and clinical characteristics

The clinical and demographic characteristics of the 62 patients with iBSP, 62 with HFS, and 62 HCs are presented in Table 1. Both patient groups were similar to HCs in terms of age and gender. The iBSP and HFS groups did not differ in terms of the disease duration, JRS total scores, number of patients receiving BoNT injections, and duration of BoNT injections.

Between-group differences in network topological characteristics

The E_{glob} of the cortico-basal ganglia networks was significantly increased, whereas the C_p and L_p of the cortico-basal ganglia networks were significantly decreased in patients with iBSP compared to HCs (Figure 2 and Table 2). No significant difference in global metrics was identified between the iBSP and HFS groups or between HFS groups and HCs.

Between-group functional connectivity differences

At the regional level, the functional connectivity between the left Brodmann area 11 (BA 11; orbitofrontal area) and left BA 2 (primary somatosensory cortex) and between the right anterior part of the pallidum (aPAL) and the right anterior part of BA 32 (dorsal anterior cingulate cortex) were significantly decreased in patients with iBSP and HFS compared to HCs (Figure 3 and Tables 3, 4) after Bonferroni corrections. No significant differences were found in these functional connections between iBSP and HFS groups. The functional connectivity between the right aPAL and the left anterior part of the insula (aINS) was lower in patients with iBSP, but not HFS, than HCs.

Between-group differences in regional indexes

No significant differences of regional indexes were found among three groups after Bonferroni corrections.

Correlations between network properties and clinical characteristics

The E_{glob} of the cortico-basal ganglia networks was positively correlated with JRS total scores, whereas C_p and L_p were negatively correlated with JRS total scores in patients with iBSP. Moreover, the C_p of the cortico-basal ganglia networks was positively correlated with disease duration in patients with iBSP (Figure 4 and Table 2).

Discussion

In this study, we found that patients with iBSP displayed alterations in integration and segregation in the functional cortico-basal ganglia networks and decreased functional connectivity in the orbitofrontal area, primary somatosensory cortex, anterior cingulate cortex, and pallidum compared with HCs. Current results support the hypothesis that extensively altered functional connections

TABLE 2 Differences of network parameters among three groups and their relationships with clinical measurements in patients with iBSP.

	Metric values (mean ± SD)			Group comparisons				Correlations	
	iBSP	HFS	HCs	iBSP-HFS-HCs	iBSP-HFS	iBSP-HCs	HFS-HCs	Duration (R, *P*)	JRS (R, *P*)
E_{glob}	0.243 ± 0.004	0.242 ± 0.004	0.241 ± 0.004	0.016*	0.658	0.013*	0.306	(−0.240, 0.065)	(0.278, 0.031)*
C_p	0.248 ± 0.013	0.251 ± 0.010	0.253 ± 0.009	0.042*	0.636	0.036*	0.607	(0.305, 0.018)*	(−0.265, 0.041)*
L_p	0.679 ± 0.018	0.682 ± 0.017	0.688 ± 0.017	0.021*	1.000	0.021*	0.167	(0.230, 0.077)	(−0.272, 0.035)*

*Represents significant differences with $P < 0.05$. Group differences of network parameters were explored using analysis of covariance and *post-hoc* two-sample *t*-tests between any two groups with age and gender as covariates. Correlations between metric values and clinical measurements in iBSP were performed using partial correlation analyses with age and gender as covariates. C_p, clustering coefficient; E_{glob}, global efficiency; HCs, healthy controls; HFS, hemifacial spasm; iBSP, idiopathic blepharospasm; L_p, shortest path length; SD, standard deviation. *Means significant results.

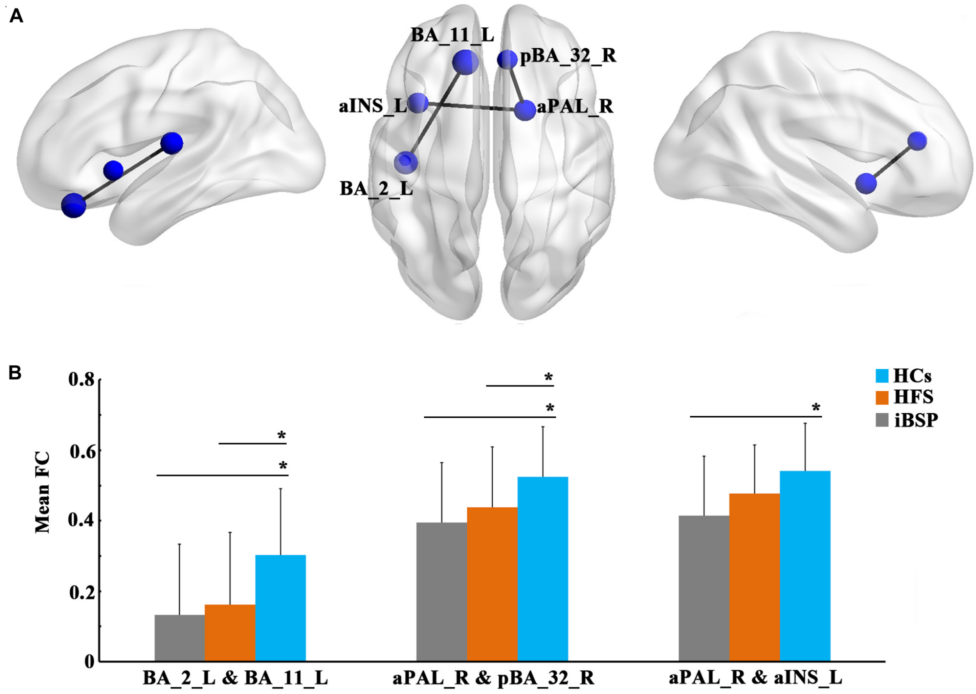

FIGURE 3
Decreased functional connections at the regional level. **(A)** Significantly decreased functional connections at the regional level in patients with idiopathic blepharospasm compared with healthy controls (HCs). The results were corrected by Bonferroni corrections of $P < 1.22\times10^{-5}$.
(B) Differences in mean functional connectivity among the three groups. Group differences in functional connectivity were explored using analysis of covariance and *post-hoc* two-sample *t*-tests between any two groups, with age and gender as covariates. *Represents significant results with $P < 0.05$. Abbreviations are listed in Table 3.

TABLE 3 The MNI coordinates of between-group functional connectivity differences of brain regions.

Abnormal brain regions	Full name	MNI coordinates (x, y, z)
BA_2_L	Left Brodmann area 2	(−43.4, −18.1, 12.1)
BA_11_L	Left Brodmann area 11	(−13.1, 35, −21.8)
aPAL_R	Right anterior part of pallidum	(17.1, 9.6, −6.6)
pBA_32_R	Right posterior part of Brodmann area 32	(8.1, 36.4, 16.1)
aINS_L	Left anterior part of insula	(−37.3, 13.5, −2.8)

MNI, Montreal Neurological Institute.

in the large-scale cortico-basal ganglia networks occur in patients with iBSP.

Considering that E_{glob} is inversely correlated with L_p between brain regions, our results (patients with iBSP displayed increased E_{glob} and decreased C_p and L_p compared with HCs) might suggest enhanced information transformation due to excessively optimized topological organization and global integration abilities in the cortico-basal ganglia networks in patients with iBSP. In addition, the existence of significant correlations between the severity of iBSP and graph theoretical metrics of the cortico-basal ganglia networks raises the possibility that abnormal topological organization in the cortico-basal ganglia networks is at least partly caused by excessive facial movements. Moreover, this possibility is further enhanced since these differences in E_{glob}, C_p, and L_p were not identified between iBSP and HFS groups. Thus, it is reasonable to speculate that facial hyperkinesia-related brain functional network changes in patients with iBSP might be attributed to the increase in facial activity and plastic changes in the brain white matter. This hypothesis is supported by a recent diffusion tensor imaging (DTI) study, which demonstrated that patients with iBSP exhibited increased network integration (significantly increased E_{glob} and

TABLE 4 Differences of resting-state functional connectivity among three groups and their relationships with clinical measurements in iBSP.

	Mean FC (mean ± SD)			Group comparisons				Correlations	
	iBSP	HFS	HCs	*F*-value	iBSP-HFS	iBSP-HCs	HFS-HCs	Duration (R, *P*)	JRS (R, *P*)
BA_2_L and BA_11_L	0.132 ± 0.200	0.161 ± 0.205	0.302 ± 0.188	< 0.001*	1	< 0.001*	< 0.001*	(−0.121, 0.362)	(0.005, 0.971)
aPAL_R and pBA_32_R	0.394 ± 0.170	0.437 ± 0.171	0.524 ± 0.142	< 0.001*	0.467	< 0.001*	0.007*	(0.036, 0.785)	(0.015, 0.911)
aPAL_R and aINS_L	0.414 ± 0.169	0.477 ± 0.137	0.540 ± 0.135	< 0.001*	0.049*	< 0.001*	0.058	(0.194, 0.141)	(−0.075, 0.571)

*Represents significant results with $P < 0.05$. Group differences of functional connectivity were explored using analysis of covariance and *post-hoc* two-sample *t*-tests between any two groups with age and gender as covariates. Correlations between functional connectivity and clinical measurements in iBSP were performed using partial correlation analyses with age and gender as covariates. aINS, anterior part of insula; aPAL, anterior part of pallidum; BA, Brodmann area; FC, functional connectivity; HCs, healthy controls; HFS, hemifacial spasm; iBSP, idiopathic blepharospasm; JRS, Jankovic Rating Scale; L, left; pBA, posterior part of Brodmann area; R, right; SD, standard deviation. *Means significant results.

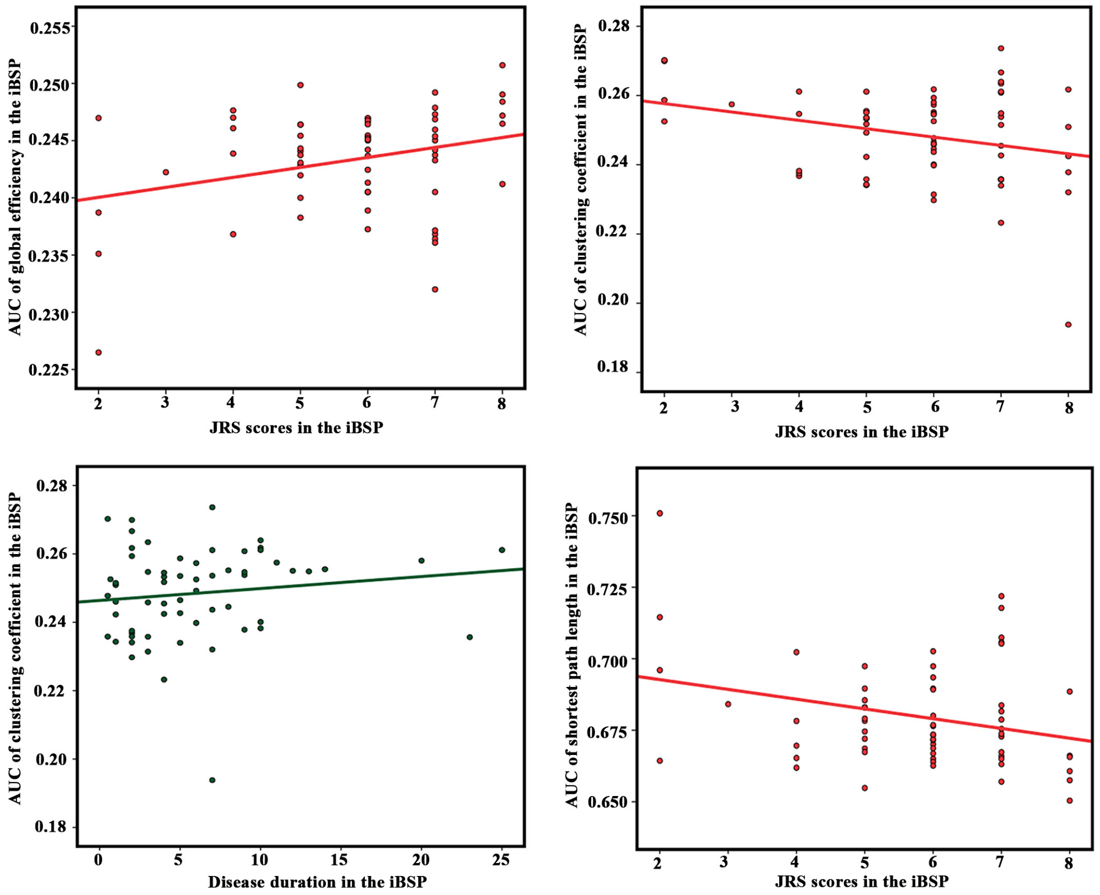

FIGURE 4

Correlation results between network parameters and clinical measurements in the idiopathic blepharospasm group. Partial correlation analyses were performed with age and gender as covariates. The significance level was set as $P < 0.05$. AUC, area under the curve; idiopathic blepharospasm (iBSP), idiopathic blepharospasm; JRS, Jankovic Rating Scale.

decreased C_p and L_p) in the whole-brain white matter networks (Guo et al., 2021), but such changes were no longer significant when patients with iBSP were compared to patients with HFS. The study also reported that patients with iBSP showed increased nodal efficiency in some regions located in the cortico-basal ganglia networks involved in sensorimotor, cognitive, and emotional processing, such as primary motor cortex, caudate nucleus, middle temporal regions, and posterior cingulate, and temporal thalamus. Moreover, these changes were not observed in patients with iBSP when compared with patients with HFS. In addition, plastic changes in multiple white matter tracts that mainly connect the basal ganglia, cortices, brainstem, and thalamus were reported in the iBSP group in another DTI study (Guo et al., 2020).

Interestingly, increased E_{glob} and decreased L_p of the cortico-basal ganglia networks were positively and negatively correlated with severity in patients with iBSP, respectively. Current evidence obtained from fMRI studies suggests that the basal ganglia circuit is involved in the triggering of spasms, whereas the cerebello-thalamo-cortical network plays a key role in symptom severity in the iBSP (Glickman et al., 2020). Moreover, the findings of DTI studies also suggest that the cerebellum or its pathways are involved in the intensity of dystonic spasms in the iBSP (Yang et al., 2014; Berman et al., 2018). In addition, Guo et al. (2021) did not find significant correlations of increased E_{glob} and decreased L_p in the whole-brain white matter networks with disease severity. They explained that the absence of infratentorial brain structures in the BNA-246 atlas they used may be responsible for it (Guo et al., 2021). The key brain regions that constitute the cerebello-thalamo-cortical network are partial components of the cortico-basal ganglia networks in our study. Whether the correlations between increased E_{glob} and decreased L_p in the functional cortico-basal ganglia networks and disease severity are mainly attributed to changes in the cerebello-thalamo-cortical network remains unclear; further studies are needed to address this question.

We also found that the functional connectivity between the left orbitofrontal area and left primary somatosensory cortex and between the aPAL and anterior part of the dorsal anterior cingulate cortex was significantly decreased in patients with iBSP and HFS compared to HCs. It has been shown that activation of the orbitofrontal area is involved in eye blinking (Tsubota et al., 1999). An fMRI study has also found that this area is associated with sensorimotor output (Yang et al., 2013). The primary somatosensory cortex, a vital component of the sensory system, has a significant role in somatosensory processing (Defazio et al., 2007). It has been proposed that focal dystonia should be considered a sensory system disorder characterized by defective somatosensory processing and impaired somatosensory capabilities (Tinazzi et al., 2000, 2009), suggesting that sensory dysfunction plays a key role in the pathophysiology of dystonia. Decreased connectivity of the primary somatosensory cortex with the orbitofrontal area in patients with iBSP and HFS might affect sensorimotor functional integration and indicate that iBSP and HFS may share overlapping pathophysiological mechanisms. The aPAL and anterior part of the dorsal anterior cingulate cortex is components of the limbic network. The aPAL is associated with behavior and cognitive performance without motor symptoms (Saad et al., 2020). The anterior cingulate cortex, particularly the dorsal portion, is involved in decision-making and working memory processes (Apps et al., 2016; Rolls, 2019). Previous studies demonstrated that patients with iBSP suffered from cognitive impairment (Alemán et al., 2009). Unfortunately, in the current study, we did not evaluate the cognitive function in patients with iBSP. Whether the abnormal functional connection between the aPAL and anterior part of the dorsal anterior cingulate cortex is related to impairments in non-motor (e.g., cognitive) aspects of iBSP requires further exploration.

This study has the following limitations. First, global signal regression in rs-fMRI remains to be debated; we did not perform this step for image pre-processing since global mean signal regression can lead to spurious resting-state functional correlations and false inferences. Second, some patients with iBSP or HFS were treated with BoNT injections; at present, the effects of BoNT on functional connections between regions in the cortico-basal ganglia networks at rest remain unclear. This limitation should be considered in further studies. Third, given the prevalence of depression, obsessive/compulsive symptoms, and cognitive dysfunction in specific cognitive domains in patients with iBSP, the associations between the dysfunction of cortico-basal ganglia networks and aforementioned non-motor symptoms in patients with iBSP are worth exploring in a future study. Finally, we did not find any difference in regional indexes between iBSP and HFS, or any correlations between these regional indexes and clinical measurements in the iBSP or HFS after Bonferroni corrections. Therefore, it is hard to determine which region was special for iBSP or HFS based on our current results.

In conclusion, we found a strong functional integration characterized by a high E_{glob} and a short L_p in the cortico-basal ganglia networks in patients with iBSP. Moreover, these network metrics were significantly correlated with disease severity of iBSP and might serve as quantitative markers for the evaluation of clinical symptom severity of iBSP.

Data availability statement

The original contributions presented in this study are included in the article/**Supplementary material**, further inquiries can be directed to the corresponding authors.

Ethics statement

The studies involving human participants were reviewed and approved by the Ethics Committee of the First Affiliated Hospital of Sun Yat-sen University. The patients/participants provided their written informed consent to participate in this study.

Author contributions

QC: data analysis and drafting the manuscript. HX and YLu: data acquisition and drafting the manuscript. LZ, YG, YLi, AW, and ZO: data acquisition. XF and XZ: data analysis. WZ, HW, and QH: revising the manuscript. KP: design and revising the manuscript. JX: design, data analysis, drafting, and revising the manuscript. GL: design, data acquisition, drafting, and revising the manuscript. All authors contributed to the article and approved the submitted version.

Funding

This work was funded by the National Natural Science Foundation of China (82271300, 82101399, 81771137, 62001462, 62006220, and 81971103), Natural Science Foundation of Guangdong Province (2023A1515012739), Science and Technology Program of Guangzhou (2023B03J0466), Sun Yat-sen University Clinical Research 5010 Program (2018001), Guangdong Provincial Key Laboratory of Diagnosis and Treatment of Major Neurological Diseases (2020B1212060017), Southern China International Cooperation Base for Early Intervention and Functional Rehabilitation of Neurological Diseases (2015B050501003 and 2020A0505020004), Shenzhen Science and Technology Research Program (JCYJ20200109114816594), Guangdong Provincial Engineering Center for Major Neurological Disease

Treatment, and Guangdong Provincial Translational Medicine Innovation Platform for Diagnosis and Treatment of Major Neurological Disease.

Acknowledgments

We would like to thank Editage (www.editage.cn) for English language editing.

Conflict of interest

The authors declare that the research was conducted in the absence of any commercial or financial relationships that could be construed as a potential conflict of interest.

Publisher's note

Supplementary material

The Supplementary Material for this article can be found online at: https://www.frontiersin.org/articles/10.3389/fnins.2023.1159883/full#supplementary-material

References

Alemán, G. G., de Erausquin, G. A., and Micheli, F. (2009). Cognitive disturbances in primary blepharospasm. *Mov. Disord.* 24, 2112–2120. doi: 10.1002/mds.22736

Apps, M. A., Rushworth, M. F., and Chang, S. W. (2016). The anterior cingulate gyrus and social cognition: tracking the motivation of others. *Neuron* 90, 692–707. doi: 10.1016/j.neuron.2016.04.018

Battistella, G., Termsarasab, P., Ramdhani, R. A., Fuertinger, S., and Simonyan, K. (2017). Isolated focal dystonia as a disorder of large-scale functional networks. *Cereb. Cortex* 27, 1203–1215. doi: 10.1093/cercor/bhv313

Berman, B. D., Honce, J. M., Shelton, E., Sillau, S. H., and Nagae, L. M. (2018). Isolated focal dystonia phenotypes are associated with distinct patterns of altered microstructure. *Neuroimage Clin.* 19, 805–812. doi: 10.1016/j.nicl.2018.06.004

Chaudhry, N., Srivastava, A., and Joshi, L. (2015). Hemifacial spasm: The past, present and future. *J. Neurol. Sci.* 356, 27–31. doi: 10.1016/j.jns.2015.06.032

Defazio, G., Berardelli, A., and Hallett, M. (2007). Do primary adult-onset focal dystonias share aetiological factors? *Brain* 130, 1183–1193. doi: 10.1093/brain/awl355

Defazio, G., Hallett, M., Jinnah, H. A., Conte, A., and Berardelli, A. (2017). Blepharospasm 40 years later. *Mov. Disord.* 32, 498–509. doi: 10.1002/mds.26934

Fang, T. C., Chen, C. M., Chang, M. H., Wu, C. H., and Guo, Y. J. (2021). Altered functional connectivity and sensory processing in blepharospasm and hemifacial spasm: coexistence and difference. *Front. Neurol.* 12:759869. doi: 10.3389/fneur.2021.759869

Glickman, A., Nguyen, P., Shelton, E., Peterson, D. A., and Berman, B. D. (2020). Basal ganglia and cerebellar circuits have distinct roles in blepharospasm. *Parkinsonism Relat. Disord.* 78, 158–164. doi: 10.1016/j.parkreldis.2020.06.034

Guo, Y., Peng, K., Liu, Y., Zhong, L., Dang, C., Yan, Z., et al. (2021). Topological alterations in white matter structural networks in blepharospasm. *Mov. Disord.* 36, 2802–2810. doi: 10.1002/mds.28736

Guo, Y., Peng, K., Ou, Z., Zhong, L., Wang, Y., Xie, C., et al. (2020). Structural brain changes in blepharospasm: A cortical thickness and diffusion tensor imaging study. *Front. Neurosci.* 14:543802. doi: 10.3389/fnins.2020.543802

Horovitz, S. G., Ford, A., Najee-Ullah, M. A., Ostuni, J. L., and Hallett, M. (2012). Anatomical correlates of blepharospasm. *Transl. Neurodegener.* 1:12. doi: 10.1186/2047-9158-1-12

Huang, X. F., Zhu, M. R., Shan, P., Pei, C. H., Liang, Z. H., Zhou, H. L., et al. (2017). Multiple neural networks malfunction in primary blepharospasm: An independent components analysis. *Front. Hum. Neurosci.* 11:235. doi: 10.3389/fnhum.2017.00235

Jankovic, J., Kenney, C., Grafe, S., Goertelmeyer, R., and Comes, G. (2009). Relationship between various clinical outcome assessments in patients with blepharospasm. *Mov. Disord.* 24, 407–413. doi: 10.1002/mds.22368

Jiang, W., Lan, Y., Cen, C., Liu, Y., Feng, C., Lei, Y., et al. (2019). Abnormal spontaneous neural activity of brain regions in patients with primary blepharospasm at rest. *J. Neurol. Sci.* 403, 44–49. doi: 10.1016/j.jns.2019.06.002

Jochim, A., Li, Y., Gora-Stahlberg, G., Mantel, T., Berndt, M., Castrop, F., et al. (2017). Altered functional connectivity in blepharospasm/orofacial dystonia. *Brain Behav.* 8:e00894. doi: 10.1002/brb3.894

Lehéricy, S., Tijssen, M. A., Vidailhet, M., Kaji, R., and Meunier, S. (2013). The anatomical basis of dystonia: Current view using neuroimaging. *Mov. Disord.* 28, 944–957. doi: 10.1002/mds.25527

Neychev, V. K., Gross, R. E., Lehéricy, S., Hess, E. J., and Jinnah, H. A. (2011). The functional neuroanatomy of dystonia. *Neurobiol. Dis.* 42, 185–201. doi: 10.1016/j.nbd.2011.01.026

Niethammer, M., Carbon, M., Argyelan, M., and Eidelberg, D. (2011). Hereditary dystonia as a neurodevelopmental circuit disorder: Evidence from neuroimaging. *Neurobiol. Dis.* 42, 202–209. doi: 10.1016/j.nbd.2010.10.010

Obermann, M., Yaldizli, O., De Greiff, A., Lachenmayer, M. L., Buhl, A. R., Tumczak, F., et al. (2007). Morphometric changes of sensorimotor structures in focal dystonia. *Mov. Disord.* 22, 1117–1123. doi: 10.1002/mds.21495

Pang, Y., Wei, Q., Zhao, S., Li, N., Li, Z., Lu, F., et al. (2022). Enhanced default mode network functional connectivity links with electroconvulsive therapy response in major depressive disorder. *J. Affect. Disord.* 306, 47–54. doi: 10.1016/j.jad.2022.03.035

Rolls, E. T. (2019). The cingulate cortex and limbic systems for emotion, action, and memory. *Brain Struct. Funct.* 224, 3001–3018. doi: 10.1007/s00429-019-01945-2

Saad, P., Shendrik, K. S., Karroum, P. J., Azizi, H., and Jolayemi, A. (2020). The anterior globus pallidus externus of basal ganglia as primarily a limbic and associative territory. *Cureus* 12:e11846. doi: 10.7759/cureus.11846

Smitha, K. A., Akhil Raja, K., Arun, K. M., Rajesh, P. G., Thomas, B., Kapilamoorthy, T. R., et al. (2017). Resting state fMRI: A review on methods in resting state connectivity analysis and resting state networks. *Neuroradiol. J.* 30, 305–317. doi: 10.1177/1971400917697342

Suzuki, Y., Kiyosawa, M., Wakakura, M., Mochizuki, M., and Ishii, K. (2011). Gray matter density increase in the primary sensorimotor cortex in long-term essential blepharospasm. *Neuroimage* 56, 1–7. doi: 10.1016/j.neuroimage.2011.01.081

Suzuki, Y., Mizoguchi, S., Kiyosawa, M., Mochizuki, M., Ishiwata, K., Wakakura, M., et al. (2007). Glucose hypermetabolism in the thalamus of patients with essential blepharospasm. *J. Neurol.* 254, 890–896. doi: 10.1007/s00415-006-0468-5

Tan, E. K., Chan, L. L., and Koh, K. K. (2004). Coexistent blepharospasm and hemifacial spasm: Overlapping pathophysiologic mechanism? *J. Neurol. Neurosurg. Psychiatry* 75, 494–496. doi: 10.1136/jnnp.2003.019331

Tinazzi, M., Fiorio, M., Fiaschi, A., Rothwell, J. C., and Bhatia, K. P. (2009). Sensory functions in dystonia: Insights from behavioral studies. *Mov. Disord.* 24, 1427–1436. doi: 10.1002/mds.22490

Tinazzi, M., Priori, A., Bertolasi, L., Frasson, E., Mauguière, F., and Fiaschi, A. (2000). Abnormal central integration of a dual somatosensory input in dystonia. Evidence for sensory overflow. *Brain* 123, 42–50. doi: 10.1093/brain/123.1.42

Tomić, A., Agosta, F., Sarasso, E., Svetel, M., Kresojević, N., Fontana, A., et al. (2021). Brain structural changes in focal dystonia-What about task specificity? A multimodal MRI study. *Mov. Disord.* 36, 196–205. doi: 10.1002/mds.28304

Tsubota, K., Kwong, K. K., Lee, T. Y., Nakamura, J., and Cheng, H. M. (1999). Functional MRI of brain activation by eye blinking. *Exp. Eye Res.* 69, 1–7. doi: 10.1006/exer.1999.0660

Wei, J., Wei, S., Yang, R., Yang, L., Yin, Q., Li, H., et al. (2018). Voxel-mirrored homotopic connectivity of resting-state functional magnetic resonance imaging in blepharospasm. *Front. Psychol.* 9:1620. doi: 10.3389/fpsyg.2018.01620

Worbe, Y., Malherbe, C., Hartmann, A., Pélégrini-Issac, M., Messé, A., Vidailhet, M., et al. (2012). Functional immaturity of cortico-basal ganglia networks in Gilles de la Tourette syndrome. *Brain* 135, 1937–1946. doi: 10.1093/brain/aws056

Xu, J., Luo, Y., Peng, K., Zhong, L., Liu, Y., Weng, A., et al. (2022). Supplementary motor area driving changes of structural brain network in blepharospasm. *Brain* awac341. doi: 10.1093/brain/awac341 [Epub ahead of print].

Xu, J., Wei, Q., Bai, T., Wang, L., Li, X., He, Z., et al. (2020). Electroconvulsive therapy modulates functional interactions between submodules of the emotion regulation network in major depressive disorder. *Transl. Psychiatry.* 10:271. doi: 10.1038/s41398-020-00961-9

Xu, J., Zhang, J., Zhang, J., Wang, Y., Zhang, Y., Wang, J., et al. (2017). Abnormalities in structural covariance of cortical gyrification in Parkinson's disease. *Front. Neuroanat.* 11:12. doi: 10.3389/fnana.2017.00012

Yan, C. G., Wang, X. D., Zuo, X. N., and Zang, Y. F. (2016). DPABI: Data processing & analysis for (resting-state) brain imaging. *Neuroinformatics* 14, 339–351. doi: 10.1007/s12021-016-9299-4

Yang, J., Luo, C., Song, W., Chen, Q., Chen, K., Chen, X., et al. (2013). Altered regional spontaneous neuronal activity in blepharospasm: a resting state fMRI study. *J. Neurol.* 260, 2754–2760. doi: 10.1007/s00415-013-7042-8

Yang, J., Luo, C., Song, W., Guo, X., Zhao, B., Chen, X., et al. (2014). Diffusion tensor imaging in blepharospasm and blepharospasm-oromandibular dystonia. *J. Neurol.* 261, 1413–1424. doi: 10.1007/s00415-014-7359-y

Zhou, B., Wang, J., Huang, Y., Yang, Y., Gong, Q., and Zhou, D. (2013). A resting state functional magnetic resonance imaging study of patients with benign essential blepharospasm. *J. Neuroophthalmol.* 33, 235–240. doi: 10.1097/WNO.0b013e31828f69e5

Zoons, E., Booij, J., Nederveen, A. J., Dijk, J. M., and Tijssen, M. A. (2011). Structural, functional and molecular imaging of the brain in primary focal dystonia-a review. *Neuroimage* 56, 1011–1020. doi: 10.1016/j.neuroimage.2011.02.045

Frontiers in Neuroscience

TYPE Original Research
PUBLISHED 23 May 2023
DOI 10.3389/fnins.2023.1197452

Estimation of brain tissue response by electrical stimulation in a subject-specific model implemented by conductivity tensor imaging

Nitish Katoch[1†], Youngsung Kim[2†], Bup Kyung Choi[1], Sang Woo Ha[3], Tae Hoon Kim[4], Eun Ju Yoon[5], Sang Gook Song[5], Jin Woong Kim[5]* and Hyung Joong Kim[1]*

[1]Department of Biomedical Engineering, Kyung Hee University, Seoul, Republic of Korea, [2]Office of Strategic R&D Planning (MOTIE), Seoul, Republic of Korea, [3]Department of Neurosurgery, Chosun University Hospital and Chosun University College of Medicine, Gwangju, Republic of Korea, [4]Medical Convergence Research Center, Wonkwang University Hospital, Iksan, Republic of Korea, [5]Department of Radiology, Chosun University Hospital and Chosun University College of Medicine, Gwangju, Republic of Korea

OPEN ACCESS

EDITED BY
Zhiyong Zhao,
Zhejiang University, China

REVIEWED BY
Arianna Menardi,
Universitàdi Padova, Italy
Sam Sedaghat,
University of California San Diego,
United States

*CORRESPONDENCE
Jin Woong Kim
✉ jw4249@gmail.com
Hyung Joong Kim
✉ bmekim@khu.ac.kr

†These authors have contributed equally to this work

RECEIVED 31 March 2023
ACCEPTED 09 May 2023
PUBLISHED 23 May 2023

CITATION
Katoch N, Kim Y, Choi BK, Ha SW, Kim TH, Yoon EJ, Song SG, Kim JW and Kim HJ (2023) Estimation of brain tissue response by electrical stimulation in a subject-specific model implemented by conductivity tensor imaging. *Front. Neurosci.* 17:1197452.
doi: 10.3389/fnins.2023.1197452

Electrical stimulation such as transcranial direct current stimulation (tDCS) is widely used to treat neuropsychiatric diseases and neurological disorders. Computational modeling is an important approach to understand the mechanisms underlying tDCS and optimize treatment planning. When applying computational modeling to treatment planning, uncertainties exist due to insufficient conductivity information inside the brain. In this feasibility study, we performed *in vivo* MR-based conductivity tensor imaging (CTI) experiments on the entire brain to precisely estimate the tissue response to the electrical stimulation. A recent CTI method was applied to obtain low-frequency conductivity tensor images. Subject-specific three-dimensional finite element models (FEMs) of the head were implemented by segmenting anatomical MR images and integrating a conductivity tensor distribution. The electric field and current density of brain tissues following electrical stimulation were calculated using a conductivity tensor-based model and compared to results using an isotropic conductivity model from literature values. The current density by the conductivity tensor was different from the isotropic conductivity model, with an average relative difference $|rD|$ of 52 to 73%, respectively, across two normal volunteers. When applied to two tDCS electrode montages of C3-FP2 and F4-F3, the current density showed a focused distribution with high signal intensity which is consistent with the current flowing from the anode to the cathode electrodes through the white matter. The gray matter tended to carry larger amounts of current densities regardless of directional information. We suggest this CTI-based subject-specific model can provide detailed information on tissue responses for personalized tDCS treatment planning.

KEYWORDS

electrical stimulation, conductivity tensor, transcranial direct current stimulation, magnetic resonance imaging, electric field, current density

1. Introduction

Electrical stimulation of brain has been used for the treatment of neuropsychiatric and neurodegenerative diseases (Stagg and Nitsche, 2011). Transcranial direct current stimulation (tDCS) is a typical neuro-stimulation technique that delivers low-intensity direct current (DC) into the brain through a pair, or through multiple surface electrodes. The injected current may cause exogenous modulation of neuronal membrane potentials, leading to an enhancement of brain functions (Nitsche and Paulus, 2000; Woods et al., 2016). The tDCS is clinically used for enhancing motor or memory functions and treatments of neuropsychiatric and neurodegenerative diseases (Fregni et al., 2006; Márquez-Ruiz et al., 2012; Reinhart et al., 2015; Lindenmayer et al., 2019). When electrical stimulation is applied to the head, the injected current through the brain generates voltage, electric field, and current density, which are affected by head geometry, electrode configuration, and the internal conductivity distribution (Bikson et al., 2012; Woods et al., 2016). To calculate these internal distributions, modeling studies have focused on designing electrode montages, modifying the sizes and shapes, and adjusting the amount of current applied (Miranda et al., 2006; Bikson et al., 2012). Moreover, subject-specific head models have been developed by segmenting structural MR images to handle the effects of the head geometry and electrode configuration (Miranda et al., 2006; Bikson et al., 2012; Datta et al., 2012). Several studies have proposed methods to incorporate *in vivo* distribution of internal conductivity and/or its tensors in individual subjects (Rampersad et al., 2014; Shahid et al., 2014; Opitz et al., 2015). However, its application was limited due to the lack of proper ways to measure subject-specific conductivity distribution at low-frequency ranges.

A comprehensive computational approach has been proposed to optimize the design of tDCS for clinical use (Bikson et al., 2012; Lee et al., 2021). Although the idea of subject-specific brain conductivity recognizes as an important factor (Puonti et al., 2020), the use of individual anisotropic conductivity has not been widely applied in modeling studies (Lee et al., 2021). Meanwhile, Tuch et al. introduced a linear model based on the physical relationship between conductivity tensor and water diffusion tensor (Tuch et al., 2001). Based on the idea of a cross-property relationship, several conductivity tensor models were developed and utilized for modeling of brain stimulation (Rampersad et al., 2014; Shahid et al., 2014). Recently, Katoch et al. reported that water diffusion tensor models may not fully address the effect of ion concentrations on conductivity distribution, therefore, novel model using conductivity tensor was suggested to precisely estimate the anisotropic distribution of brain (Katoch et al., 2021).

Diffusion-tensor magnetic resonance electrical impedance tomography (DT-MREIT) is currently used to image brain responses during electrical stimulation (Kwon et al., 2014; Jeong et al., 2016). The basis of DT-MREIT is that the water diffusion tensors have the same directional property as conductivity tensors (Tuch et al., 2001). There have been several experimental studies of DT-MREIT in phantoms, animals, and human subjects (Kwon et al., 2014; Jeong et al., 2016; Chauhan et al., 2018), but clinical uses may be limited due to the requirement for imaging currents of a few milliamperes through multiple surface electrodes during MRI scans. The conductivity tensor imaging (CTI) method, which does not require external current injection, was developed recently (Sajib et al., 2018). The CTI consists of a combination of magnetic resonance electrical properties tomography (MREPT) and multi-b-value diffusion weighted imaging (DWI). To reconstruct the conductivity tensor, MREPT is used to obtain high-frequency conductivity (at the Larmor frequency), and multi-b-value DWI is used to separate the information on both the extracellular and intracellular spaces. This method was validated in the designed phantoms and animal imaging studies using a 3 T MRI scanner and its feasibility was evaluated (Sajib et al., 2018). Specifically, Katoch et al. developed a model that mimicked a cell structure with giant vesicles and separated extracellular and intracellular spaces using a CTI method (Katoch et al., 2018). The relative errors between the conductivity tensor images and *in vitro* measurements of the giant vesicle suspensions were found to be about 1.1 to 11% (Katoch et al., 2018; Choi et al., 2020). In addition, Choi et al. reported that CTI can distinguish the contrast between ion concentrations and their mobility (Choi et al., 2020, 2023). The advantage of CTI is that it is easily implemented in a clinical MRI scanner without addition of hardware components. *In vivo* CTI imaging of the human brain was reported, and resulting conductivity values of white matter, gray matter, and cerebrospinal fluid were compared with those previously reported in the literature (Katoch et al., 2018; Jahng et al., 2021). Therefore, CTI is the latest method to image tensor information along with conductivity distributions inside the brain, without the need to inject imaging currents.

In this feasibility study, we performed *in vivo* CTI experiments of entire human brains and implemented subject-specific conductivity tensor-based head models to evaluate the brain response to electrical stimulation. We acquired MR images for both structural and CTI information from two normal volunteers using a 3 T clinical MRI. After segmenting the structural MR images of the heads, three-dimensional finite element models were constructed. A subject-specific head model was implemented by incorporating the conductivity tensor images into the geometrical finite element model. Applying electrical stimulation to electrode montages of tDCS, the electric field and current density of the brain were calculated using a conductivity tensor-based head model and its performance evaluated by comparing it to the isotropic conductivity models as a tool for personalized tDCS treatment planning.

2. Subjects and methods

All experimental procedures were approved by the institutional review board of Kyung Hee University (KHSIRB-18-073) and carried out in accordance with the relevant guidelines and regulations. Two healthy male volunteers (26 and 28 years old) participated and informed consent was obtained from the volunteers before the imaging experiments.

2.1. Imaging experiments

The imaging experiments were performed on a 3 T MRI scanner (Magnetom Skyra, Siemens Healthcare, Erlangen, Germany) equipped with a 16-channel head coil. For structural images of the head (Figure 1A), T1-weighted magnetization prepared rapid gradient echo (MPRAGE) sequence was applied with a cubic voxel of 1 mm edge length in sagittal plane. The parameters were as follows: repetition time (TR)/echo time (TE) = 1200/1.79 ms; flip angle = 10°; bandwidth = 510 Hz/Px; field of view (FOV) = 260 × 260 mm^2; slice per slab = 192; slice thickness = 1 mm (no gap). The acquisition time was

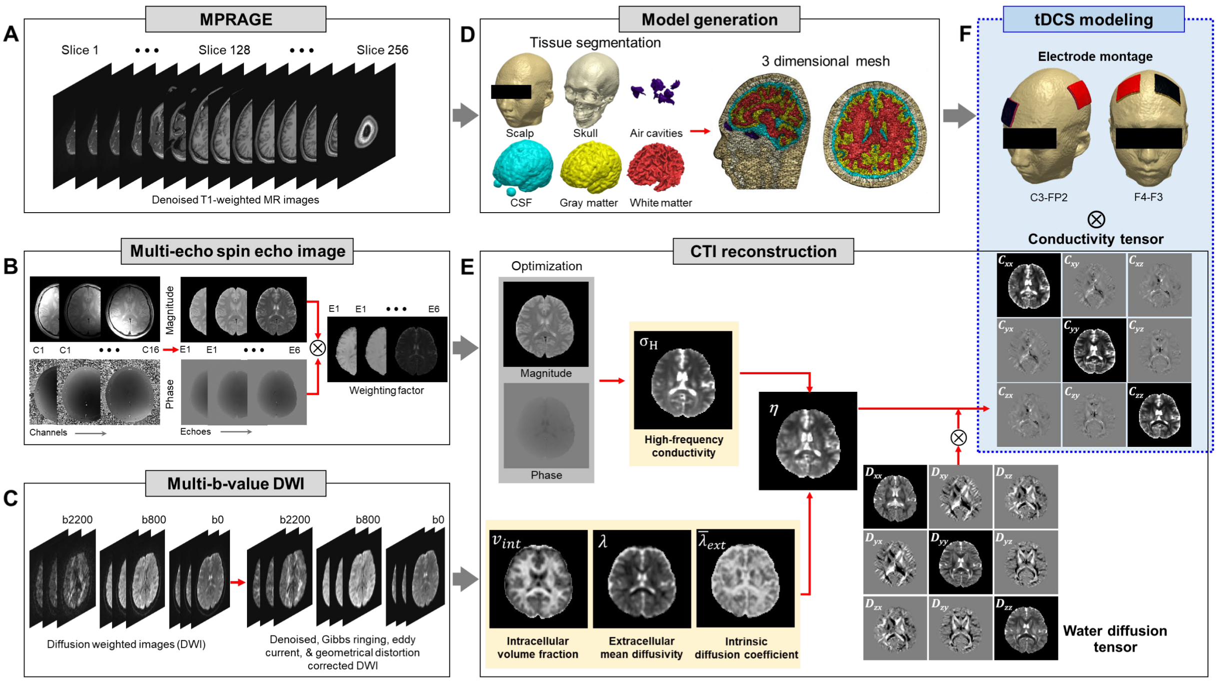

FIGURE 1
Schematic illustration of the conductivity tensor-based head model. High-resolution anatomical MR images **(A)** are used to generate the model. Multi-echo spin-echo images **(B)** and multi-*b*-value diffusion weighted images **(C)** are used to reconstruct the conductivity tensor of brain. Three-dimensional head model **(D)** and conductivity tensor information of the brain **(E)** are combined to estimate the response to tDCS electrode montages **(F)**.

5 min and 4 s. CTI requires two separate MR scans shown in Figures 1B,C. For high-frequency conductivity images by MREPT method (Figure 1B), the multi-echo spin-echo (MSE) pulse sequence with multiple refocusing pulses was adopted to acquire B1 phase maps. The parameters were as follows: TR/TE = 1500/15 ms; flip angle = 90°; bandwidth = 250 Hz/Px; number of echoes = 6; number of slices = 30; slice thickness = 4 mm; matrix size = 128 × 128 and FOV = 260 × 260 mm^2. The voxel size was 2 × 2 × 4 mm^3. The acquisition time for obtaining high-frequency conductivity images covering the whole brain area was 19 min.

To separate the influences of the extracellular and intracellular spaces, multi-band echo-planar imaging (EPI) sequence was used to acquire two-shell DWI (Figure 1C). A multi-band factor of 3 was used with the three-band RF excitation and axial spin-echo EPI (SE-EPI) readout with phase encoding (PE) in the anterior–posterior (AP) direction. The diffusion gradient was applied in 30 and 64 directions with two *b*-values of 800 and 2,200 s/mm^2. The parameters were as follows: TR/TE = 2000/80 ms; flip angle = 90°; number of slices = 30; slice thickness = 4 mm; matrix size = 128 × 128 and FOV = 260 × 260 mm^2. The acquisition time was 9 min. An additional MR scan was obtained using a non-diffusion sensitizing gradient ($b = 0$ s/mm^2) along the posterior–anterior phase encoding (PE) directions. The total acquisition time to implement the subject-specific model using CTI was 35 min.

2.2. Brain segmentation and model generation

High-resolution MPRAGE images were bias-corrected and preprocessed by applying a median filter to reduce noise (Smith et al., 2004). The automated segmentation algorithms in Statistical Parametric Mapping software (SPM 12, Wellcome Trust Centre for Neuroimaging, London, United Kingdom) were used to generate tissue probability maps. The head was segmented into six tissue types; scalp, skull, air cavity, eye, cerebrospinal fluid (CSF), gray matter (GM), and white matter (WM) (Figure 1D). After generating the initial tissue probability maps, a Matlab (Mathworks, Natick, United States) based algorithm (Huang et al., 2013) was used to correct tissue discontinuities and segmentation errors. The segmented tissue data was imported into ScanIP software (Simpleware, Synopsys, Exeter, United Kingdom) to build a three-dimensional head model (Figure 1D). The overlaps and unassigned pixels in the segmented data were removed by manual correction and all slices were confirmed to ensure proper tissue classifications. We used a recursive Gaussian filter with a kernel size of 1 × 1 × 1 to smooth the masks of tissue surfaces. Two sponge-pad electrodes with a size of 50 × 50 mm^2, were attached on the model to stimulate the brain. The thickness of the sponge-pads was 3 mm and the electrode was 2 mm thickness. The finite element meshes of the head models include 1.5 million tetrahedral and 0.3 million triangular elements with an average element quality of 0.678.

2.3. Conductivity tensor image reconstruction

Conductivity tensor images were reconstructed using an MRCI toolbox which is available at http://iirc.khu.ac.kr/toolbox.html (Sajib et al., 2017). Acquired MR data (including anatomical images, B1 phase map, and DWI) was re-oriented to standard MNI space and preprocessed using the MRtrix3[1] and FMRIB software library (FSL 6.03v, www.fmrib.ox.ac.uk/fsl) (Smith et al., 2004; Tournier et al., 2019). The B1 phase maps and DWI were registered with the anatomical T2-weighted images to minimize geometrical mismatches. The high-frequency conductivity images were reconstructed using a method proposed by Gurler and Ider (2017). The diffusion data were corrected for eddy-current effects and geometrical distortions by affine registration of the directional images of B0 using FSL software (www.fmrib.ox.ac.uk/fsl) with the FLIRT routine (Smith et al., 2004). The following CTI formula was used for all conductivity tensor image reconstructions (Katoch et al., 2018; Sajib et al., 2018):

$$\mathbf{C} = \frac{\left(1 - v_{\text{int}}\right)\sigma_{\text{H}}}{v_{\text{int}}\beta\lambda + \left(1 - v_{\text{int}}\right)\bar{\lambda}_{\text{ext}}}\mathbf{D}_{\text{e}}^{w} = \eta\mathbf{D}_{\text{e}}^{w} \qquad (1)$$

where **C** is the low-frequency conductivity tensor, σ_H is the high-frequency conductivity at the Larmor frequency, v_{int} is the intracellular volume fraction, β is the ion concentration ratio of the intracellular and extracellular spaces, λ is the intrinsic diffusion coefficient, $\bar{\lambda}_{\text{ext}}$ is the extracellular mean diffusivity, and $\mathbf{D}_e^w$ is the extracellular water diffusion tensor (Figure 1E). The details of conductivity tensor reconstruction procedures followed the works of Jahng et al. (2021). Finally, the reconstructed conductivity tensor images were incorporated into the subject-specific head models.

2.4. Modeling of electrical stimulation

Two electrode montages were modeled to visualize the brain response during tDCS using a CTI head model (Figure 1F). The first montage consisted of an anode positioned in the C3 (motor cortex) and a cathode in the FP2 (supra-orbital). The second montage consisted of an anode in the F4 (right dorsolateral prefrontal cortex, DLPFC) and a cathode in the F3 (left DLPFC). The anode and cathode are denoted as ε_A and ε_C, respectively, and currents were injected from ε_A to ε_C. The cathode ε_C was chosen as the voltage reference electrode for all numerical computations. When a DC current of I mA is injected between two electrodes ε_A and ε_C, the voltage u inside the head denoted as Ω with its boundary $\partial\Omega$ satisfies the following partial differential equation (Seo and Woo, 2012):

$$\begin{cases} \nabla \cdot \mathbf{C}\nabla u(\mathrm{r}) = 0 \ \ in \ \ \Omega \\ -\mathbf{C}\nabla u(r) \cdot \mathrm{n} = g(\mathrm{r}) \ \ on \ \ \partial\Omega \setminus \left(\varepsilon_{\text{A}} \cup \varepsilon_{\text{C}}\right) \end{cases} \qquad (2)$$

where **C** is the conductivity tensor, n is the outward unit normal vector on the boundary $\partial\Omega$, and g is the Neumann boundary condition of the injected current. The voltage u (V), electric field $-\nabla u$ (V/m), and current density $-\mathrm{C}\nabla u$ (A/m^2) were numerically calculated using COMSOL Multiphysics (COMSOL, Burlington, United States) software. The conjugate gradient method with a relative tolerance of 1×10^{-6} was used to solve linear systems of equations. The amplitude of the injected current I was 2 mA and the average current density under the electrode was 0.8 A/cm^2. The total computation time to obtain u, $-\nabla u$, and $-\mathrm{C}\nabla u$ was about 9 min.

2.5. Evaluation of CTI-based head model

The electric field and current density of the brains were calculated using a conductivity tensor-based head model and compared with those using the isotropic conductivity of brain tissues from literature values. For the conductivity tensor models, we used the reconstructed conductivity tensor images for the pixels belonging to the white matter, gray matter, and CSF regions. The isotropic low-frequency conductivity values from the literature were used for the conductivity of the other tissues such as scalp, skull, air cavity, and eye. Meanwhile, we used the isotropic literature values for all pixels for the isotropic conductivity model (Gabriel et al., 1996; Baumann et al., 1997; Datta et al., 2009; Bikson et al., 2012; Huang et al., 2013). The values (S/m) were as follows: air $= 1 \times 10^{-15}$, scalp $= 0.47$, skull $= 0.01$, eye $= 2.00$, CSF $= 1.79$, gray matter $= 0.27$, white matter $= 0.14$, electrode $= 5.99 \times 10^7$, and saline-soaked sponge $= 1.00$. For comparison of current densities between the two models, we analyzed the relative difference $|rD|$ defined as follows:

$$\text{Relative difference}\left|rD\right| = \frac{\sum_{\text{i}=1}^{\text{N}} \text{J}_{\text{CTI}} - \text{J}_{\text{ISO}}}{\sum_{\text{i}=1}^{\text{N}} \text{J}_{\text{CTI}}} \times 100\% \qquad (3)$$

where J_{CTI} and J_{ISO} are the magnitude of current density at each pixel from the conductivity tensor and isotropic conductivity models, respectively. A high error indicates that there is a significant difference between two current densities.

3. Results

3.1. CTI of human brain

Figure 2 shows the reconstructed conductivity tensor images of two normal brains using the CTI method. In Figure 2A, the high-frequency conductivity (σ_H) and intermediate images (including intracellular volume fraction, v_{int}; intrinsic and extracellular water diffusion coefficients, λ and $\bar{\lambda}_{ext}$; scale factor, η) were used to reconstruct low-frequency conductivity tensors shown in Figure 2B. To reconstruct the diffusion coefficients (v_{int}, λ and $\bar{\lambda}_{ext}$) of brain we used the software available at https://ekaden.github.io (Kaden et al., 2016). The conductivity tensor images in the white matter, gray matter, and CSF regions were clearly distinguished (orange arrows) and showed different signal intensities in the white matter depending on the fiber direction (yellow circle) (Figure 2B).

3.2. Brain tissue response by electrical stimulation

Figure 3 shows the results of brain responses to tDCS focusing on the white matter. The electric field (Figure 3A) and current density

---

[1] www.mrtrix.org

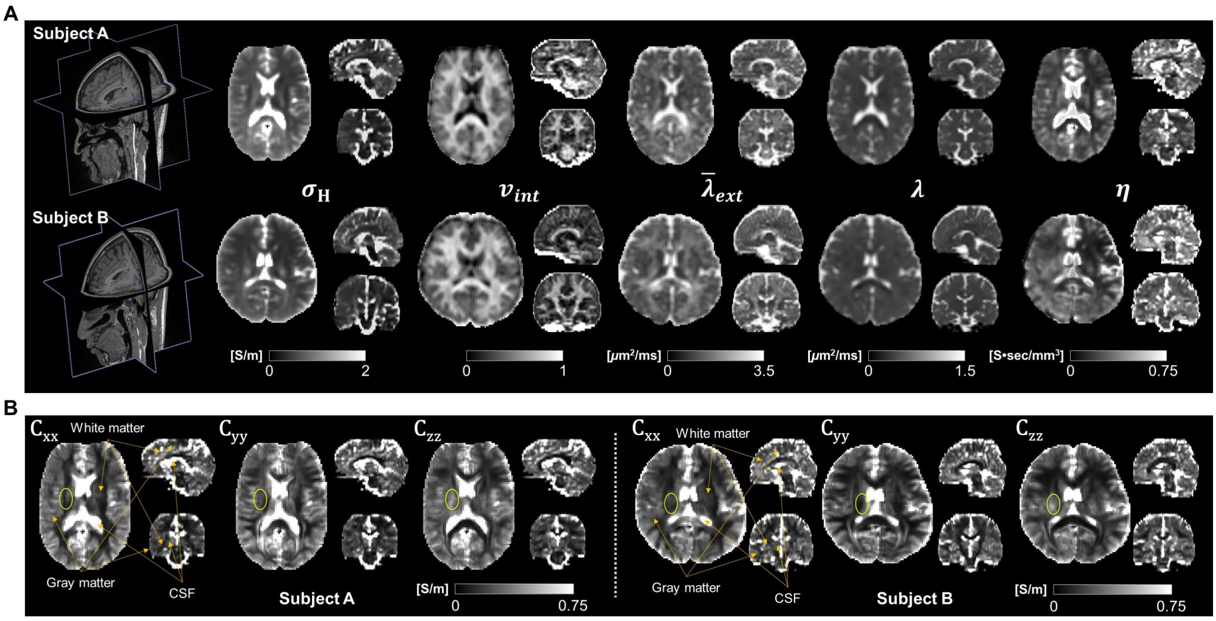

FIGURE 2
Typical conductivity tensor images acquired from two normal brains. High-frequency conductivity (σ_H), intracellular volume fraction (v_{int}), extracellular mean diffusivity ($\bar{\lambda}_{ext}$), intrinsic diffusion coefficient (λ) and scale factor (η) images **(A)** are used to calculate the conductivity tensors at three different fiber directions **(B)**.

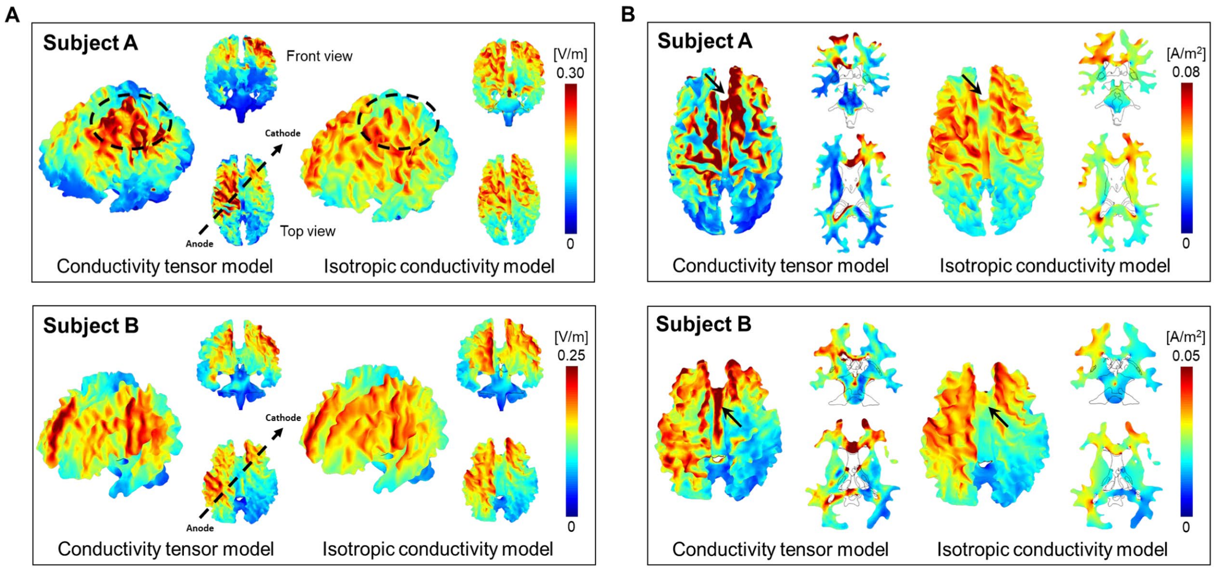

FIGURE 3
Brain response by the tDCS in the white matter of two normal brains. The three-dimensional images of electric fields **(A)** and current densities **(B)** were calculated from both the conductivity tensor model and isotropic conductivity tensor model.

(Figure 3B) distributions were obtained from both the CTI-based head model and the isotropic conductivity model with literature values. The electric field by the conductivity tensor model showed higher signal intensity in the activated area, but the activated area was wider in the isotropic conductivity model (Figure 3A). The current density in the conductivity tensor model showed a high signal intensity in the activated area, but the activated area was similar to the isotropic conductivity model (Figure 3B). The dynamic ranges of the electric field and current density were wider in subject A than in subject B. Table 1 summarizes the electric field and current density measurements in gray matter, white matter, and entire brain tissues. The conductivity tensor showed higher signal values than the isotropic conductivity model in all brain tissues. The averaged current density of the conductivity tensor in the corpus callosum (CC) were 0.073 A/m^2 and 0.061 A/m^2 in two subjects, respectively, which is twice as much as that in the isotropic conductivity model (0.034 A/m^2 and

TABLE 1 Measurements of the electric field and current density in gray matter, white matter, and entire brain tissues from isotropic and conductivity tensor models.

Model		Electric field [V/m]			Current density [A/m^2]		
		Gray matter	White matter	Entire brain	Gray matter	White matter	Entire brain
Subject A	Conductivity tensor	0.104 ± 0.060	0.117 ± 0.063	0.116 ± 0.073	0.039 ± 0.026	0.032 ± 0.027	0.042 ± 0.032
	Isotropic conductivity	0.087 ± 0.035	0.112 ± 0.029	0.098 ± 0.057	0.023 ± 0.010	0.017 ± 0.005	0.042 ± 0.053
Subject B	Conductivity tensor	0.099 ± 0.042	0.118 ± 0.045	0.097 ± 0.049	0.033 ± 0.021	0.024 ± 0.011	0.043 ± 0.032
	Isotropic conductivity	0.076 ± 0.029	0.097 ± 0.031	0.074 ± 0.039	0.021 ± 0.008	0.014 ± 0.004	0.046 ± 0.048

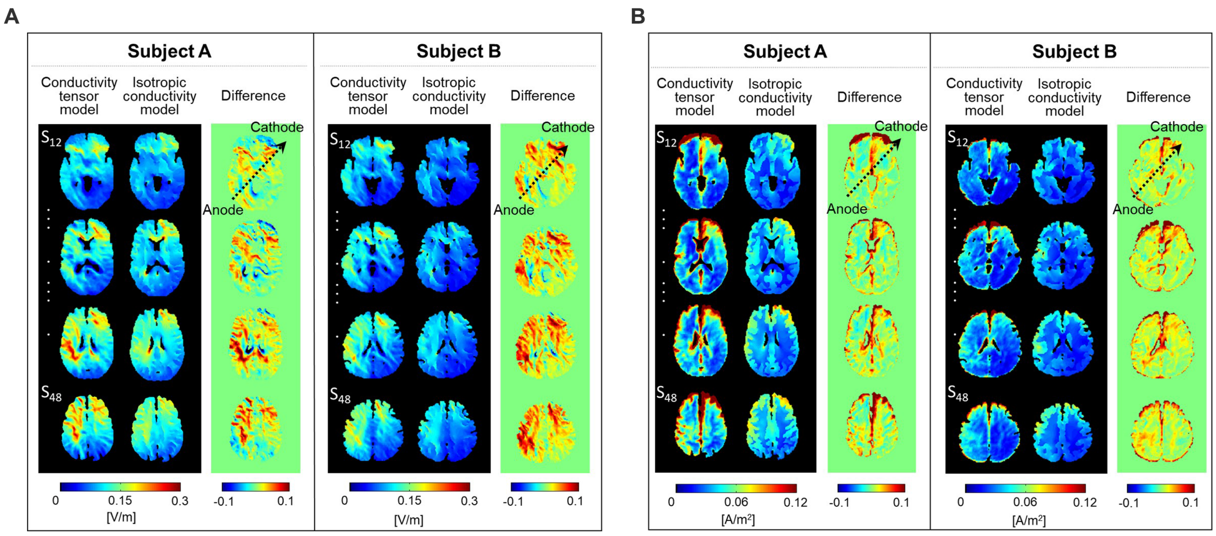

FIGURE 4
Difference images between the conductivity tensor model and isotropic conductivity model. The electric field **(A)** and current density **(B)** were calculated at a single slice whose position was chosen at 12mm from the skull.

0.022 A/m^2). This could also stem from the fact that conductivity of CC ranged 0.20 to 0.75 S/m, which is higher than that of 0.14 S/m in isotropic conductivity model.

3.3. Comparison of brain tissue response between two models

Figure 4 shows the difference images between the two models. From difference images of the electric field (Figure 4A), the conductivity tensor model showed high signal intensity around the electrode position. The current density showed high signal intensity along the direction of current flow between the two electrodes (black arrows) (Figure 4B). The signal intensity from model comparisons was different between the two subjects in both the electric field and current density.

Figure 5 shows the current density streamlines from the anode to the cathode of the two models. The streamlines in the conductivity tensor model showed a concise and concentrated distribution between the electrodes (Figure 5A), while the isotropic conductivity model showed a wider distribution (Figure 5B). The dynamic range of the current density streamline was slightly wider in subject A than in subject B for both models.

Figure 6 represents comparisons of the current densities obtained from the two models by applying a relative difference ($|rD|$). The relative difference for two electrode montages was calculated in the white matter, gray matter, and entire brains of the two subjects. The differences ranged from 55 to 73% for the subject A and from 52 to 71% for the subject B. The minimum and maximum errors ranged from 15 to 98%.

3.4. Estimation of brain tissue response by different stimulation method

Figure 7 shows the current density distribution in brains with two electrode montages (C3-FP2 and F4-F3). The current density images, which consist of one coronal and two axial slice positions, were calculated from the conductivity tensor model. From the C3-FP2 electrode montage in Figure 7A, the current density showed a high signal intensity which is consistent with the current flowing from the cortex where the anode electrode is located, through the deep brain region, and to the opposite cortex where the cathode electrode is located. In the F4-F3 electrode montage (Figure 7B), however, the current density was high in the cortex regions between the two electrodes but did not pass through the deep brain. Table 2 summarizes the measurements of current density in the entire brain. The C3-FP2 electrode montage showed higher signal values than the F4-F3 electrode montage in all slice positions.

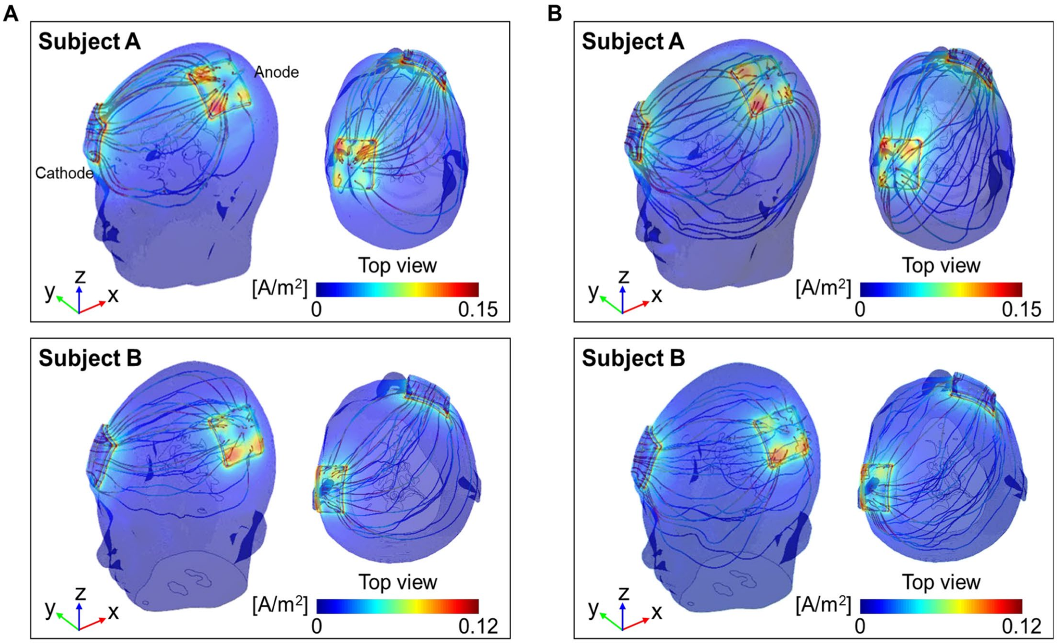

FIGURE 5
Distribution of current density streamlines inside the two brains. The colored streamline represents the magnitude of the current density obtained from the conductivity tensor **(A)** and the isotropic conductivity **(B)** models.

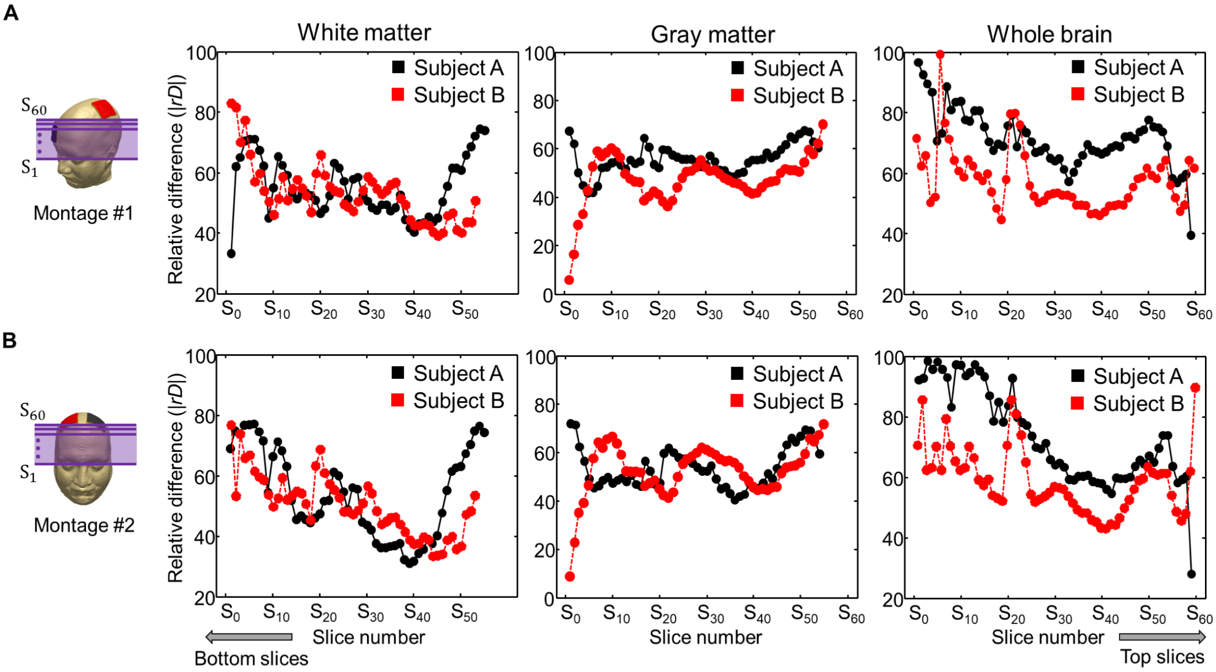

FIGURE 6
Comparison of relative difference (|*rD*|) between the current densities obtained from the two models. The current density in the brain tissues was calculated from the C3-FP2 **(A)** and F4-F3 **(B)** electrode montages.

4. Discussion

Computational modeling of electrical stimulation approaches, such as tDCS, still faces uncertainty regarding the optimal stimulation of specific anatomical structures in the brain that are affected by a given current stimulation. One reason is that there are no proper ways to measure the anisotropic conductivity distribution of each individual's brains *in vivo*. In this study, we performed *in vivo* brain imaging using a conductivity tensor imaging (CTI) method from a 3 T MRI and obtained subject-specific anisotropic conductivity tensor

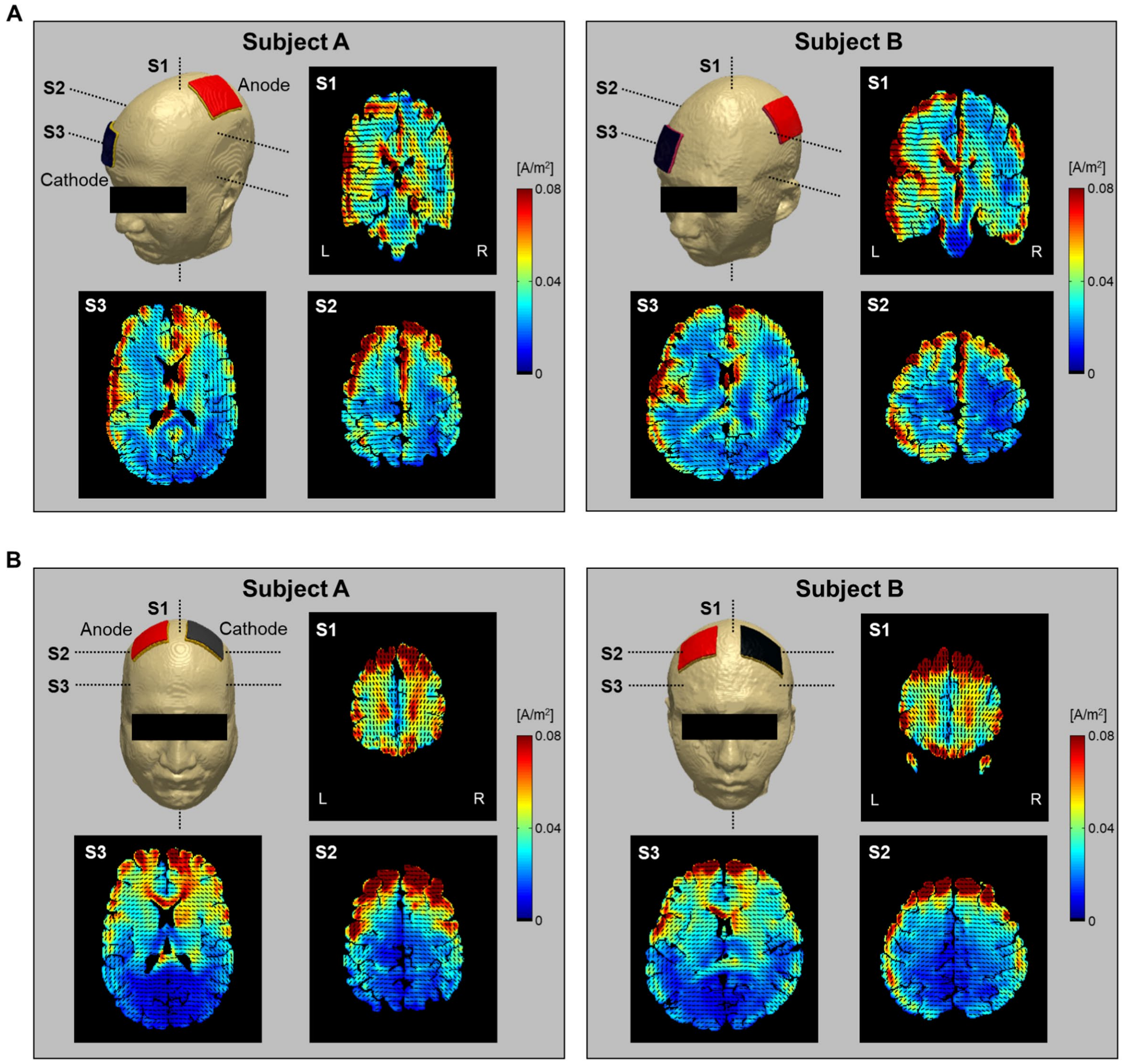

FIGURE 7
Estimation of current density distribution by electrical stimulation. The current density was calculated from the C3-FP2 **(A)** and F4-F3 **(B)** electrode montages using the conductivity tensor model. The current density distribution was imaged at single coronal slices of the heads near the anode electrode and at two axial slices of the head 75 and 25mm apart from the skull. The vector field of current pathways is represented by black dashed lines.

TABLE 2 Measurements of the current density in two electrode montages.

Electrode montage	Subject A			Subject B		
	S1	S2	S3	S1	S2	S3
C3-FP2	0.043 ± 0.026	0.045 ± 0.034	0.040 ± 0.049	0.039 ± 0.026	0.052 ± 0.037	0.044 ± 0.031
F4-F3	0.036 ± 0.022	0.028 ± 0.017	0.019 ± 0.014	0.031 ± 0.020	0.030 ± 0.017	0.022 ± 0.019

Values were obtained from the entire brain tissues at three different slice positions.

images of two normal brains. The resulting conductivity tensors in the white matter, gray matter, and CSF regions were clearly distinguished and showed similar results to those reported in a previous study (Katoch et al., 2018). In particular, the conductivity tensor of white matter tends to exhibit position dependency and inter-subject variability depending on the degree of anisotropy. Therefore, compared to the isotropic conductivity model which is based on fixed values, regional differences could be observed in estimating the electric field and current density by using the conductivity tensor model.

At low frequencies below 10 kHz, externally injected currents are mostly blocked by cell membranes, and internal current flows are constrained within extracellular pathways. The white matter exhibits strong anisotropy because the myelinated fibers running in parallel along the fiber direction behave as electrical insulators at low frequencies. From the results of electrical stimulations shown in

Figure 3A, the electric field calculated by the conductivity tensor model showed a focused distribution with higher signal intensity in the left frontoparietal lobe compared to the results from the isotropic conductivity model. In the frontal views, however, the electric field by the conductivity tensor model showed lower signal intensity in the supraorbital area. The overall signal intensity of the entire brain was high in both subjects as seen from the difference images between the two models in Figure 4A. Since the tissue response to electrical stimulation was higher in subject A than in subject B, the dynamic range of the electric field was different between two subjects.

The current density by the conductivity tensor model showed a focused distribution with high signal intensity along the current pathways. This high current density was observed in the white matter tissues such as corpus callosum, cingulum, and cortex regions around the electrodes. Especially, the high current density in the corpus callosum, which connects the left and right hemispheres, indicates that the anisotropy of the white matter is well reflected in the current density distribution produced by this model. The current density of gray matter showed a wider distribution than the white matter due to its higher isotropic conductivity. From the difference images in Figure 4B, the current density of the entire brain was high along the current pathway. This was also seen in the results of the current density streamlines in Figure 5. The current density streamlines of the isotropic conductivity model were widely distributed inside the brains whereas streamlines of the conductivity tensor model shows a more focused distribution between the two electrodes. Since the current densities are different between the two subjects, the dynamic ranges were different despite being performed under the same conditions. Therefore, our subject-specific conductivity tensor model may reflect the position dependency and inter-subject variability better than the isotropic model models.

For comparisons of the current densities between the two models, the relative difference ($|rD|$) analysis was applied to the brain tissues. Average relative difference in brain tissues were above 50% in both subjects. These large error values indicate that there is a significant difference between the two models. Similar errors were found when using white matter's directional conductivity information based upon diffusion tensor information (Shahid et al., 2013; Rampersad et al., 2014; Opitz et al., 2015). Shahid et al. reported up to 48% higher strength of current density in the white matter compared to isotropic model. In these previous studies, however, anisotropic conductivity tensors were assumed to be proportional to water diffusion tensors with one fixed global scale factor.

To evaluate the brain response to electrical stimulation, we applied our subject-specific conductivity tensor models to image the current density distributions with two different electrode montages delivering tDCS (C3-FP2 and F4-F3). In Figure 7, the current density distributions at three different slice positions showed different patterns depending on the electrode montage as well as the individual brains. Specifically, the C3-FP2 montage in Figure 7A produced a more concentrated current density according to the current flow in subject A, but the amount of current density was larger in subject B. The current density showed higher signal intensity in the interhemispheric fissure and cortical regions around the two electrodes. The current density of the CSF region, which flows outside of the brain, was higher in subject B than in subject A. The overall signal intensity inside the brains was different between the two subjects in response to the injected currents. These results could be important for estimating the polarizing effects of individual brains by the electrical current (Purpura and McMurtry, 1965; Abascal et al., 2008). For the F4-F3 montage in Figure 7B, the current density was high in the cortical regions between the two electrodes in both subjects. However, the effect of CSF was more severe in subject B than in subject A.

It is important to determine how to evaluate tissue responses to electrical stimulation. As seen tissue responses may vary depending on individual brains and the stimulation location. Though the conductivity tensor information can be obtained using other imaging methods such as DT-MREIT, CTI has an advantage for tDCS treatment planning, since it does not require externally injecting currents into the head during MRI scans and treatments. The CTI-based head model exhibits potential in that it can consider position dependency and inter-subject variability. Although this study presented the results of only two normal brains and limited electrode positions, it showed a potential as an imaging tool for the evaluation of electrical stimulation approaches such as tDCS, through the accumulation of individual data from many samples and the subsequent implementation of statistical analysis.

The proposed CTI method has several limitations and requires careful considerations in its applications. First, the reconstructed images were geometrically registered, but the resolution of conductivity tensors imaging was limited. Moreover, there might be a partial volume effect that may result in field values being less accurate within the regional boundaries of each tissue type. Future studies can utilize higher resolution images to improve the head model (Marino et al., 2021). Second, since CTI uses MREPT and DWI data, a rigorous error analysis is desirable for propagating measurement noise and artifacts. Third, cell membranes are assumed to block low-frequency currents in CTI method. The CTI method in its current form could underestimate the low-frequency conductivity value of tissue, including cells with leaky membranes. To remedy this, it would be worthwhile to investigate a more sophisticated CTI model including such cells. A potential way to validate the CTI-based model is by combining surface voltage measurements using an EIT device or current density images from MRCDI (Abascal et al., 2008; Kasinadhuni et al., 2017). Future research focuses on optimizing targeted stimuli while exploring multiple electrode locations and recommending the optimal location based on the required amount of current for effective activation. This may be essential in the field of personalized tDCS treatment planning.

5. Conclusion

Feasibility of a personalized tDCS treatment planning was evaluated using a subject-specific head model with both conductivity tensors and anatomical information. The key ingredient is the CTI method that can produce anisotropic conductivity tensor images of the human brain using a 3 T clinical MRI without injecting external currents into the head. Once the subject-specific head model is constructed, various numerical simulations and analyses can be performed for different electrode configurations and current dosages. We suggest constructing subject-specific head models using the method described in this study and quantitatively analyzing internal distributions of the electric field and current density for tDCS treatment planning.

Developing a software tool to automate the computational modeling process described in this study may facilitate the basic research and clinical applications of tDCS.

Data availability statement

The original contributions presented in the study are included in the article/supplementary material, further inquiries can be directed to the corresponding authors.

Ethics statement

The studies involving human participants were reviewed and approved by Institutional review board of Kyung Hee University (KHSIRB-18-073). The patients/participants provided their written informed consent to participate in this study.

Author contributions

NK, YK, and SH: conceptualization. NK, BC, and TK: methodology. NK: software. YK and SS: validation. BC, NK, and SH: formal analysis. EY, SS, and YK: investigation. BC, TK, and JK: data curation. EY and JK: writing—original draft preparation. HK and JK: writing—review and editing. HK: visualization and supervision. All authors contributed to the finalization and approved the content of the manuscript.

Funding

This work was funded by the National Research Foundation of Korea (NRF) grants funded by the Korea government (Nos. 2019R1A2C2088573, 2020R1I1A3065215, 2021R1A2C2004299, and 2022R1I1A1A01065565). This study was also supported by research fund from Chosun University, 2020.

Conflict of interest

The authors declare that the research was conducted in the absence of any commercial or financial relationships that could be construed as a potential conflict of interest.

Publisher's note

References

Abascal, J. F. P., Arridge, S. R., Atkinson, D., Horesh, R., Fabrizi, L., De Lucia, M., et al. (2008). Use of anisotropic modelling in electrical impedance tomography; description of method and preliminary assessment of utility in imaging brain function in the adult human head. *NeuroImage* 43, 258–268. doi: 10.1016/j.neuroimage.2008.07.023

Baumann, S. B., Wozny, D. R., Kelly, S. K., and Meno, F. M. (1997). The electrical conductivity of human cerebrospinal uid at body temperature. *I.E.E.E. Trans. Biomed. Eng.* 44, 220–223. doi: 10.1109/10.554770

Bikson, M., Rahman, A., and Datta, A. (2012). Computational models of transcranial direct current stimulation. *Clin. EEG Neurosci.* 43, 176–183. doi: 10.1177/1550059412445138

Chauhan, M., Indahlastari, A., Kasinadhuni, A. K., Schar, M., Mareci, T. H., and Sadleir, R. J. (2018). Low-frequency conductivity tensor imaging of the human head in vivo using DT-MREIT: first study. *IEEE Trans. Med. Imaging* 37, 966–976. doi: 10.1109/TMI.2017.2783348

Choi, B. K., Katoch, N., Park, J. A., Kim, J. W., Oh, T. I., Kim, H. J., et al. (2023). Measurement of extracellular volume fraction using magnetic resonance-based conductivity tensor imaging. *Front. Physiol.* 14:1132911. doi: 10.3389/fphys.2023.1132911

Choi, B. K., Katoch, N., Park, J. A., Ko, I. O., Kim, H. J., Kwon, O. I., et al. (2020). Validation of conductivity tensor imaging using giant vesicle suspensions with different ion mobilities. *Biomed. Eng. Online* 19:35. doi: 10.1186/s12938-020-00780-5

Datta, A., Bansal, V., Diaz, J., Patel, J., Reato, D., and Bikson, M. (2009). Gyri-precise head model of transcranial direct current stimulation: improved spatial focality using a ring electrode versusconventional rectangular pad. *Brain Stimul.* 2, 201–207.e1. doi: 10.1016/j.brs.2009.03.005

Datta, A., Truong, D., Minhas, P., Parra, L. C., and Bikson, M. (2012). Inter-individual variation during transcranial direct current stimulation and normalization of dose using mri-derived computational models. *Front. Psych.* 3:91. doi: 10.3389/fpsyt.2012.00091

Fregni, F., Boggio, P. S., Nitsche, M. A., Rigonatti, S. P., and Pascual-Leone, A. (2006). Cognitive effects of repeated sessions of transcranial direct current stimulation in patients with depression. *Depress. Anxiety* 23, 482–484. doi: 10.1002/da.20201

Gabriel, C., Gabriel, S., and Corthout, Y. E. (1996). The dielectric properties of biological tissues: I. literature survey. *Phys. Med. Biol.* 41, 2231–2249. doi: 10.1088/0031-9155/41/11/001

Gurler, N., and Ider, Y. Z. (2017). Gradient-based electrical conductivity imaging using MR phase. *Magn. Reson. Med.* 77, 137–150. doi: 10.1002/mrm.26097

Huang, Y., Dmochowski, J. P., Su, Y., Datta, A., Rorden, C., and Parra, L. C. (2013). Automated mri segmentation for individualized modeling of current flow in the human head. *J. Neural Eng.* 10:066004. doi: 10.1088/1741-2560/10/6/066004

Jahng, G. H., Lee, M. B., Kim, H. J., Woo, E. J., and Kwon, O. I. (2021). Low-frequency dominant electrical conductivity imaging of in vivo human brain using high-frequency conductivity at Larmor-frequency and spherical mean diffusivity without external injection current. *NeuroImage* 225:117466. doi: 10.1016/j.neuroimage.2020.117466

Jeong, W. C., Sajib, S. Z. K., Katoch, N., Kim, H. J., Kwon, O. I., and Woo, E. J. (2016). Anisotropic conductivity tensor imaging of in vivo canine brain using DT-MREIT. *IEEE Trans. Med. Imaging* 36, 124–131. doi: 10.1109/TMI.2016.2598546

Kaden, E., Kelm, N. D., Carson, R. P., Does, M. D., and Alexander, D. C. (2016). Multi-compartment microscopic diffusion imaging. *NeuroImage* 139, 346–359. doi: 10.1016/j.neuroimage.2016.06.002

Kasinadhuni, A., Indahlastari, A., Chauhan, M., Schär, M., Mareci, T., and Sadleir, R. (2017). Imaging of current flow in the human head during transcranial electrical therapy. *Brain Stimul.* 10, 764–772. doi: 10.1016/j.brs.2017.04.125

Katoch, N., Choi, B. K., Park, J. A., Ko, I. O., and Kim, H. J. (2021). Comparison of five conductivity tensor models and image reconstruction methods using MRI. *Molecules* 26:5499. doi: 10.3390/molecules26185499

Katoch, N., Choi, B. K., Sajib, S. Z. K., Lee, E. A., Kim, H. J., Kwon, O. I., et al. (2018). Conductivity tensor imaging of *in vivo* human brain and experimental validation using giant vesicle suspension. *IEEE Trans. Med. Imaging* 38, 1569–1577. doi: 10.1109/TMI.2018.2884440

Kwon, O. I., Jeong, W. C., Sajib, S. Z. K., Kim, H. J., and Woo, E. J. (2014). Anisotropic conductivity tensor imaging in MREIT using directional diffusion rate of water molecules. *Phys. Med. Biol.* 59, 2955–2974. doi: 10.1088/0031-9155/59/12/2955

Lee, J., Bestmann, S., and Evans, C. (2021). A future of current flow modelling for transcranial electrical stimulation? *Curr. Behav. Neurosci. Rep.* 8, 150–159. doi: 10.1007/s40473-021-00238-5

Lindenmayer, J., Kulsa, M. K. C., Sultana, T., Kaur, A., Yang, R., Ljuri, I., et al. (2019). Transcranial direct-current stimulation in ultra-treatment-resistant schizophrenia. *Brain Stimul.* 12, 54–61. doi: 10.1016/j.brs.2018.10.002

Marino, M., Cordero-Grande, L., Mantini, D., and Ferrazzi, G. (2021). Conductivity tensor imaging of the human brain using water mapping techniques. *Front. Neurosci.* 15:694645. doi: 10.3389/fnins.2021.694645

Márquez-Ruiz, J., Leal-Campanario, R., Sánchez-Campusano, R., Molaee-Ardekani, B., Wendling, F., Miranda, P. C., et al. (2012). Transcranial direct-current stimulation modulates synaptic mechanisms involved in associative learning in behaving rabbits. *Proc. Natl. Acad. Sci. U. S. A.* 109, 6710–6715. doi: 10.1073/pnas.1121147109

Miranda, P. C., Lomarev, M., and Hallett, M. (2006). Modeling thecurrent distribution during transcranial direct current stimulation. *Clin. Neurophysiol.* 117, 1623–1629. doi: 10.1016/j.clinph.2006.04.009

Nitsche, M. A., and Paulus, W. (2000). Excitability changes induced in the human motor cortex by weak transcranial direct current stimulation. *J. Physiol.* 527, 633–639. doi: 10.1111/j.1469-7793.2000.t01-1-00633.x

Opitz, A., Paulus, W., Will, S., Antunes, A., and Thielscher, A. (2015). Determinants of the electric field during transcranial direct current stimulation. *NeuroImage* 109, 140–150. doi: 10.1016/j.neuroimage.2015.01.033

Puonti, O., Van Leemput, K., Saturnino, G. B., Siebner, H. R., Madsen, K. H., and Thielscher, A. (2020). Accurate and robust whole-head segmentation from magnetic resonance images for individualized head modeling. *NeuroImage* 219:117044. doi: 10.1016/j.neuroimage.2020.117044

Purpura, D. P., and McMurtry, J. G. (1965). Intracellular activities and evoked potential changes during polarization of motor cortex. *J. Neurophysiol.* 28, 166–185. doi: 10.1152/jn.1965.28.1.166

Rampersad, S. M., Janssen, A. M., Lucka, F., Aydin, Ü., Lanfer, B., Lew, S., et al. (2014). Simulating transcranial direct current stimulation with a detailed anisotropic human head model. *IEEE Trans. Neural Syst. Rehabil. Eng.* 22, 441–452. doi: 10.1109/TNSRE.2014.2308997

Reinhart, R. M., Zhu, J., Park, S., and Woodman, G. F. (2015). Synchronizing theta oscillations with direct-current stimulation strengthens adaptive control in the human brain. *Proc. Natl. Acad. Sci. U. S. A.* 112, 9448–9453. doi: 10.1073/pnas.1504196112

Sajib, S. Z. K., Katoch, N., Kim, H. J., Kwon, O. I., and Woo, E. J. (2017). Software toolbox for low-frequency conductivity and current density imaging using MRI. *I.E.E.E. Trans. Biomed. Eng.* 64, 2505–2514. doi: 10.1109/TBME.2017.2732502

Sajib, S. Z. K., Kwon, O. I., Kim, H. J., and Woo, E. J. (2018). Electrodeless conductivity tensor imaging (CTI) using MRI: basic theory and animal experiments. *Biomed. Eng. Lett.* 8, 273–282. doi: 10.1007/s13534-018-0066-3

Seo, J. K., and Woo, E. J. (2012). *Nonlinear inverse problems in imaging*. Hoboken: John Wiley & Sons.

Shahid, S. S., Bikson, M., Salman, H., Wen, P., and Ahfock, T. (2014). The value and cost of complexity in predictive modelling: role of tissue anisotropic conductivity and fibre tracts in neuromodulation. *J. Neural Eng.* 11:036002. doi: 10.1088/1741-2560/11/3/036002

Shahid, S., Wen, P., and Ahfock, T. (2013). Numerical investigation of white matter anisotropic conductivity in defining current distribution under tDCS. *Comput. Methods Prog. Biomed.* 109, 48–64. doi: 10.1016/j.cmpb.2012.09.001

Smith, S. M., Jenkinson, M., Woolrich, M. W., Beckmann, C. F., Behrens, T. E., Johansen-Berg, H., et al. (2004). Advances in functional and structural MR image analysis and implementation as FSL. *NeuroImage* 23, S208–S219. doi: 10.1016/j.neuroimage.2004.07.051

Stagg, C. J., and Nitsche, M. A. (2011). Physiological basis of transcranial direct current stimulation. *Neuroscientist* 17, 37–53. doi: 10.1177/1073858410386614

Tournier, J. D., Smith, R., Raffelt, D., Tabbara, R., Dhollander, T., Pietsch, M., et al. (2019). MRtrix3: a fast, flexible and open software framework for medical image processing and visualisation. *NeuroImage* 202:116137. doi: 10.1016/j.neuroimage.2019.116137

Tuch, D. S., Wedeen, V. J., Dale, A. M., George, J. S., and Belliveau, J. W. (2001). Conductivity tensor mapping of the human brain using diffusion tensor MRI. *Proc. Natl. Acad. Sci.* 98, 11697–11701. doi: 10.1073/pnas.171473898

Woods, A. J., Antal, A., Bikson, M., Boggio, P. S., Brunoni, A. R., Celnik, P., et al. (2016). A technical guide to tDCS, and related non-invasive brain stimulation tools. *Clin. Neurophysiol.* 127, 1031–1048. doi: 10.1016/j.clinph.2015.11.012

frontiers | Frontiers in Neuroscience

TYPE Original Research
PUBLISHED 30 June 2023
DOI 10.3389/fnins.2023.1200029

Check for updates

OPEN ACCESS

EDITED BY
Takao Yamasaki,
Minkodo Minohara Hospital, Japan

REVIEWED BY
Zhengyuan Yang,
University of Macau, China
Lanxin Ji,
New York University, United States

*CORRESPONDENCE
Gang Li
✉ ligang@zjnu.cn
Zhe Zhang
✉ zhangz@hznu.edu.cn

†These authors have contributed equally to this work

RECEIVED 04 April 2023
ACCEPTED 13 June 2023
PUBLISHED 30 June 2023

CITATION
Li Y, Qian L, Li G and Zhang Z (2023) Frequency specificity of aberrant triple networks in major depressive disorder: a resting-state effective connectivity study.
Front. Neurosci. 17:1200029.
doi: 10.3389/fnins.2023.1200029

Frequency specificity of aberrant triple networks in major depressive disorder: a resting-state effective connectivity study

Ying Li[1]†, Linze Qian[2]†, Gang Li[3,4]* and Zhe Zhang[5,6]*

[1]Department of Electronics and Information Engineering, Lanzhou Institute of Technology, Lanzhou, China, [2]College of Biomedical Engineering and Instrument Science, Zhejiang University, Hangzhou, China, [3]Key Laboratory of Urban Rail Transit Intelligent Operation and Maintenance Technology & Equipment of Zhejiang Provincial, Zhejiang Normal University, Jinhua, China, [4]College of Mathematical Medicine, Zhejiang Normal University, Jinhua, China, [5]School of Physics, Hangzhou Normal University, Hangzhou, China, [6]Institute of Brain Science, Hangzhou Normal University School of Basic Medical Sciences, Hangzhou, China

Major depressive disorder (MDD) has been associated with aberrant effective connectivity (EC) among the default mode network (DMN), salience network (SN), and central executive network (CEN)—collectively referred to as triple networks. However, prior research has predominantly concentrated on broad frequency bands (0.01–0.08 Hz or 0.01–0.15 Hz), ignoring the influence of distinct rhythms on triple network causal dynamics. In the present study, we aim to investigate EC alterations within the triple networks across various frequency bands in patients with MDD. Utilizing a data-driven frequency decomposition approach and a multivariate Granger causality analysis, we characterized frequency-specific EC patterns of triple networks in 49 MDD patients and 54 healthy controls. A support vector machine classifier was subsequently employed to assess the discriminative capacity of the frequency-specific EC features. Our findings revealed that, compared to controls, patients exhibited not only enhanced mean EC within the CEN in the conventional frequency band (0.01–0.08 Hz), but also decreased mean EC from the SN to the DMN in a higher frequency band (0.12–0.18 Hz), and increased mean EC from the CEN to the SN in a sub-frequency band (0.04–0.08 Hz); the latter was significantly correlated with disease severity. Moreover, optimal classification performance for distinguishing patients from controls was attained by combining EC features across all three frequency bands, with the area under the curve (AUC) value of 0.8831 and the corresponding accuracy, sensitivity, and specificity of 89.97%, 92.63%, and 87.32%, respectively. These insights into EC changes within the triple networks across multiple frequency bands offer valuable perspectives on the neurobiological basis of MDD and could aid in developing frequency-specific EC features as potential biomarkers for disease diagnosis.

KEYWORDS

major depressive disorder, triple networks, frequency specificity, effective connectivity, classification

1. Introduction

Major depressive disorder (MDD) constitutes a debilitating psychiatric affliction, impacting approximately 7% of the global population (Mathers and Loncar, 2006). The condition is typified by persistent emotions of sadness, guilt, and worthlessness, as well as heightened suicide risk (Gotlib and Joormann, 2010). Despite the unidentified neurological substrates underpinning MDD, contemporary neuroimaging investigations have revealed functional connectivity (FC) anomalies across extensive brain networks (Otte et al., 2016; Li et al., 2018; Yan et al., 2019; Peng et al., 2020; Yang et al., 2021). These findings have reconceptualized MDD as a disorder of brain network dysfunction, offering novel perspectives for understanding its pathophysiology.

The triple-network model serves as a notable approach for investigating brain dysconnectivity in psychiatric disorders, delineating a core connectivity pattern that underlies cognitive, perceptual, affective, and social functions, encompassing the default mode network (DMN), salience network (SN), and central executive network (CEN) (Menon, 2011). In MDD patients, FC disruptions within these triple networks have been recurrently observed (Balaev et al., 2018; Cheng et al., 2018; Yan et al., 2019). Notably, the bulk of prior studies gauged FC by calculating Pearson's correlation between time series of two given brain regions, hindering exploration of the influence of one brain region over another. In contrast, more recent studies have begun to probe the effective connectivity (EC) within MDD's triple networks, examining the causal or directed influence of one brain region upon another. For example, research employing spectral dynamic causal modeling uncovered weakened connection strength from the SN to the CEN region in MDD patients (Kandilarova et al., 2018). Another study involving 336 MDD patients revealed both increased and reduced ECs from the SN regions (e.g., temporal pole) to other brain regions (Rolls et al., 2018). These findings collectively suggest that abnormal directed influences between triple network regions may be pivotal in MDD etiology. However, these studies primarily focused on MDD-induced EC changes within a broad frequency band (0.01–0.08 Hz or 0.01–0.15 Hz), potentially obscuring information regarding physiological fluctuations at specific frequencies.

The human brain, a biologically intricate system, features myriad oscillatory waves working in concert (Buzsáki and Draguhn, 2004; Samaha et al., 2020). Blood oxygen level-dependent (BOLD) signals at distinct frequency bands can partially reflect these neural processes and corresponding physiological functions (Zuo et al., 2010; Cole and Voytek, 2017; Hu et al., 2021). Previous MDD research has often identified frequency-specific alterations in spontaneous brain activity and connectivity. For instance, a study examined resting-state signal amplitude variability across two discrete frequency bands (slow-5: 0.01–0.027 Hz and slow-4: 0.027–0.073 Hz), revealing that the balance between the DMN and sensorimotor network favored the DMN in slow-5 and correlated with clinical depression symptom scores (Martino et al., 2016). Similarly, a study analyzing FC patterns in bipolar disorder depression across slow-5 and slow-4 found increased long-range FC density in the left lingual gyrus in slow-5 and decreased density in slow-4 (Yang et al., 2021). These results suggest that analyzing functional abnormalities of MDD at multiple frequencies is more rational than examining the routine band. To date, no prior study has explored EC at various low-frequency bands in MDD patients, and the impact of different rhythms on triple network causal processes in the disorder remains uncertain.

This study endeavors to assess EC changes of the triple networks at disparate frequency bands in MDD patients. By employing a data-driven method called complete ensemble empirical mode decomposition with adaptive noise (CEEMDAN) (Colominas et al., 2014), we initially decomposed BOLD oscillations into five distinct frequency bands. Subsequently, we quantified frequency-specific EC patterns among triple network components by integrating group independent component analysis (GICA) with multivariate Granger causality analysis (mGCA). We also conducted a correlation analysis to evaluate the association between EC changes and clinical measures in patients. Moreover, we utilized a support vector machine (SVM) to ascertain whether frequency-specific EC features of the triple networks could facilitate the differentiation of MDD patients from healthy controls (HCs). Based on prior evidence indicating disrupted triple networks in MDD, we hypothesized that (a) the EC in the triple networks would exhibit alterations in patients across various frequency bands; and (b) frequency-specific EC could serve as a biomarker for distinguishing patients from controls.

2. Materials and methods

2.1. Participants

This study enrolled 58 patients with MDD and 57 age-, gender-, and education-matched HCs. MDD patients were recruited from Gansu Provincial Hospital, while the HCs were obtained through newspaper advertisements. MDD diagnosis followed the Diagnostic and Statistical Manual of Mental Disorders, Fifth Edition (DSM-V). Exclusion criteria for MDD patients encompassed acute physical illness history, substance abuse/dependence, head trauma resulting in unconsciousness, claustrophobia, bipolar depression, and other neurological disorders. Hamilton Depression Scale (HAMD) and Hamilton Anxiety Scale (HAMA) evaluated depression and anxiety severity in MDD individuals. HCs were interviewed using the DSM-IV non-patient edition. All participants provided written informed consent before study procedures. The study adhered to the Helsinki Declaration and received approval from the Ethics Committee of Gansu Provincial Hospital. After head motion exclusion, the remaining 49 MDD patients and 54 HCs were included in the subsequent analyses. Demographic and clinical characteristics of participants are displayed in Table 1.

2.2. Data acquisition and preprocessing

Resting-state fMRI data for all participants were collected on a 3.0 T scanner (Siemens, Erlangen, Germany) using a single-shot, gradient-recalled echo planar imaging sequence. Scanning parameters were as follows: repetition time (TR) = 2000 ms, echo time (TE) = 30 ms, flip angle (FA) = 90°, slice thickness = 3.5 mm, in-plane matrix = 64 × 64, field of view (FOV) = 220 mm × 220 mm, and 33 slices covering the entire brain. Participants were instructed to remain silent and awake with eyes closed, minimize movement, and let their thoughts wander during the scan. Data preprocessing employed

TABLE 1 Demographics and clinical characteristics of the participants.

Characteristics	MDD (n =49)	HC (n =54)	p value
Age (years)	34.09 ± 12.06	34.56 ± 12.16	0.83[a]
Handedness (right/left)	49/0	54/0	0.99[b]
Gender (males/females)	27/22	29/25	0.87[b]
Antidepressants (yes/no)	7/42	–	–
HAMD	17.40 ± 5.89	–	–
HAMA	17.05 ± 7.36	–	–
Duration of illness (years)	6.83 ± 7.88	–	–
Mean FD	0.14 ± 0.09	0.14 ± 0.07	0.86[a]

Values represented mean ± SD. SD, standard deviation; HAMD, Hamilton depression scale; HAMA, Hamilton anxiety scale; FD, frame-wise displacement; MDD, major depressive disorder; HC, healthy control.

[a] p value was obtained by two-sample t tests.

[b] p value was obtained by Chi square test.

DPARSF software[1] based on the SPM12 toolbox,[2] including discarding the initial 10 functional images, realignment, time-slicing, head motion correction, spatial normalization to the Montreal Neurological Institute (MNI) template, linear detrending, and nuisance covariate regression. Participants with head movement exceeding 1.5 mm translation or 1.5° rotation or with mean frame-wise displacement (FD) values over 0.5 mm were excluded from the analysis.

2.3. Definition of frequency of interest

A data driven CEEMDAN method was adopted to decompose BOLD signals into distinct frequency bands without rigidly predefined band-pass filters. Briefly, a time series $x(t)$ can be represented as $x(t)=\sum_{i=1}^{K} IMF_i(t)+r(t)$, where $IMF_i(t), i=1,2,\cdots,K$ is a set of intrinsic mode functions, $r(t)$ is the monotonic residue signal, and t, i, and K are the length of scanning time, the order of IMF, and the number of IMF, respectively. CEEMDAN employs an iterative technique, the sifting algorithm, based on Empirical Mode Decomposition (EMD) to extract IMFs. This algorithm comprises the following steps: (1) Initially, EMD is used to derive the first residual component; (2) The first IMF is subsequently calculated by subtracting this first residual component from the original signal; (3) The second residual component is then estimated, and this defines the second IMF; (4) These steps are iteratively repeated until the final IMF is successfully extracted. Note that each IMF component occupies a distinct frequency band. In particular, the first and last IMF occupies the highest and lowest frequency bands, while the remaining IMF occupy the frequency bands in between. After decomposition, the Hilbert weighted frequency (HWF) was utilized to represent the mean oscillation frequency of an intrinsic mode function (IMF) using amplitude and phase from the instantaneous spectrum. HWF distribution histograms for each participant were calculated by determining the HWF of each IMF. A frequency of interest (FOI) was derived from each component of the HWF distribution within 95% confidence intervals to isolate frequency bands and minimize the influence of extreme values. Detailed procedures for defining FOIs can be found in a previous study (Zhang et al., 2018). Five frequency intervals (0.12–0.18 Hz, 0.04–0.08 Hz, 0.02–0.04 Hz, 0.01–0.02 Hz, and 0–0.01 Hz) were chosen as FOIs to represent EC alterations in MDD patients (Figure 1). To simplify, these intervals were designated as FOI-1 to FOI-5, with FOI-1 representing the highest frequency interval and FOI-5 the lowest. Additionally, for comparative purposes, the conventional frequency band ranging from 0.01 to 0.08 Hz was selected as the normal frequency of interest (FOI-N).

2.4. Triple network identification

A spatial GICA was applied to decompose resting-state fMRI data, using the GIFT toolbox. Global signal regression was first implemented within the GICA framework, where the global mean signal per time point was removed as a standard processing step preceding PCA. PCA was employed to condense subject-specific data into 120 principal components. Subsequently, we concatenated subject-reduced data across time for all participants, reducing them into 100 ICs using the infomax algorithm (Bell and Sejnowski, 1995). To ensure decomposition reliability and stability, the infomax ICA algorithm was run 20 times using ICASSO. We employed a group information-guided ICA approach to reconstruct subject-specific spatial maps and corresponding time courses after estimating group spatial maps. ICNs among the 100 ICs were identified through a combination of spatial template-matching and visual inspection, using templates derived from ICA analyses as previously described (Allen et al., 2014; Tu et al., 2019). Components were evaluated based on the following criteria: (1) peak activation coordinates primarily located in gray matter; (2) minimal spatial overlap with known vascular, ventricular, motion, and susceptibility artifacts; (3) time courses predominantly characterized by low-frequency fluctuations (Kim et al., 2017; Fiorenzato et al., 2019). We further post-processed the time courses of ICNs to remove residual noise sources by detrending linear, quadratic, and cubic trends, regressing the six realignment parameters and their temporal derivatives, despiking detected outliers, and applying low pass filtering with a cutoff frequency of 0.15 Hz.

2.5. Granger causality analysis

We employed GCA to investigate EC between ICs in resting-state fMRI data, a widely-used method for predicting one system's causal influence over another (David et al., 2008; Deshpande and Hu, 2012). GCA, unlike other EC measures, quantified causal influence among multiple brain regions in a data-driven manner, without necessitating a predefined model (Deshpande and Hu, 2012). GCA's concept can be described as follows: for two signals $s_1(t)$ and $s_2(t)$, if knowing the past information of $s_1(t)$ aids in predicting $s_2(t)$'s future, $s_1(t)$ has a causal influence on $s_2(t)$. In this study, we evaluated the causal influences among the time courses of DM components using the mGCA method (Liao et al., 2011). For each participant, the time courses set was defined as $S(t) = (s_1(t), s_2(t), \ldots, s_n(t))$, where n denotes

---

[1] http://www.restfmri.net

[2] https://www.fil.ion.ucl.ac.uk

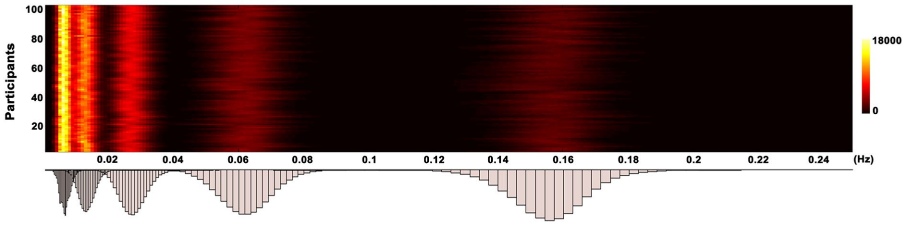

FIGURE 1
Histogram of frequency distribution. The histograms of HWF distributions show the first five intrinsic mode functions of each voxel in the whole-brain gray matter across all participants by using the CEEMDAN approach. The color bar represents the number of voxels with HWF equal to the frequency on the horizontal axis in the whole-brain gray matter. HWF, Hilbert weighted frequency; CEEMDAN, complete ensemble empirical mode decomposition with adaptive noise.

the number of DM components. The influence from all other seed components to target component k was evaluated by the multivariate auto-regressive model as follow:

$$s_k(t) = \sum_{m=1}^{p} C_k(m) S(t-m) + R_k(t)$$

where p, C_k, S and R denote the auto-regressive model order, model coefficient matrix, time courses matrix of different components and residual error matrix, respectively. The model order p was determined using Akaike's information criterion and the model coefficient matrix C_k was calculated using a standard least squares optimization, respectively. We further calculated random-effect Granger causality maps for each participant to evaluate the statistical significance of Granger causality results, corrected with a false discovery rate ($p < 0.05$).

2.6. Classification analyses

We examined whether frequency-specific EC could differentiate MDD patients from controls by employing the SVM classifier. SVM is a widely-used, high-performing supervised learning model that projects low-dimensional, non-separable data into high-dimensional, separable data (Cortes and Vapnik, 1995). A 10-fold cross-validation methodology was adopted, which incorporated nested feature selection and classifier training using a Lib-SVM framework based on a linear kernel function with parameter optimization (Pereira et al., 2009). A two-step feature selection strategy was implemented to identify the optimal feature subset and minimize the risk of overfitting. This approach comprised two components: the Minimum Redundancy and Maximum Relevance (MRMR) method and the Support Vector Machine Recursive Feature Elimination (SVM-RFE) technique. Specifically, the MRMR was employed to exclude features with weak discriminative capabilities, and the SVM-RFE was further utilized for more refined feature selection. The dataset was randomly partitioned into 10 approximately equal subsets. For each iteration, a single subset served as the test dataset, while a model induced from the remaining nine subsets was tested using a classification algorithm. Each subset was used precisely once as the testing data, this process was iterated 10 times. The feature selection was incorporated within the 10-fold cross-validation and was solely performed on the training set. Meanwhile, the chosen features were applied to the testing set. The entire procedure was conducted 10 times, and the mean value derived from the 100 results was taken as the final measure of accuracy. Additionally, we employed receiver operating characteristic (ROC) curves and the area under the curves (AUC) to evaluate EC's potential as a marker for discriminating MDD patients from controls. The LIBSVM 3.22 Matlab toolbox facilitated all classification analyses.

2.7. Statistical analysis

A permutation testing (10,000) was employed to evaluate group differences in EC metrics between patients and controls. The significance level was established at a threshold of $p < 0.05$, with false discovery rate (FDR) correction. Spearman's correlation analysis was performed to assess the relationship between EC metrics and clinical symptoms, controlling for age, gender, and mean FD. Correlations with $p < 0.05$ were considered significant, FDR-corrected.

3. Results

3.1. Independent components of the triple networks

As illustrated in Figure 2, we identified 21 ICs via group ICA and subsequently classified them into three subsets: DMN (IC 21, 33, 52, 54, 59, 78, 86, 92, and 100), SN (IC 32, 65, 69, and 71), and CEN (IC 53, 61, 73, 75, 77, 87, 88, and 96). Figure 2B present the group-averaged causal influences between each IC pair of the triple networks in the conventional low-frequency band (0.01–0.08 Hz) and the corresponding EC matrix. Detailed activation information for these ICs can be found in Supplementary Table S1.

3.2. Frequency-specific EC alterations in MDD

We examined the EC patterns and observed significant differences between the two groups. As depicted in Figure 3, patients exhibited widespread alterations in the EC patterns of the triple networks across FOI-N, FOI-1, and FOI-2 compared to the controls ($p < 0.05$, FDR-corrected). Notably, IC69 (insula), IC21 (medial frontal gyrus),

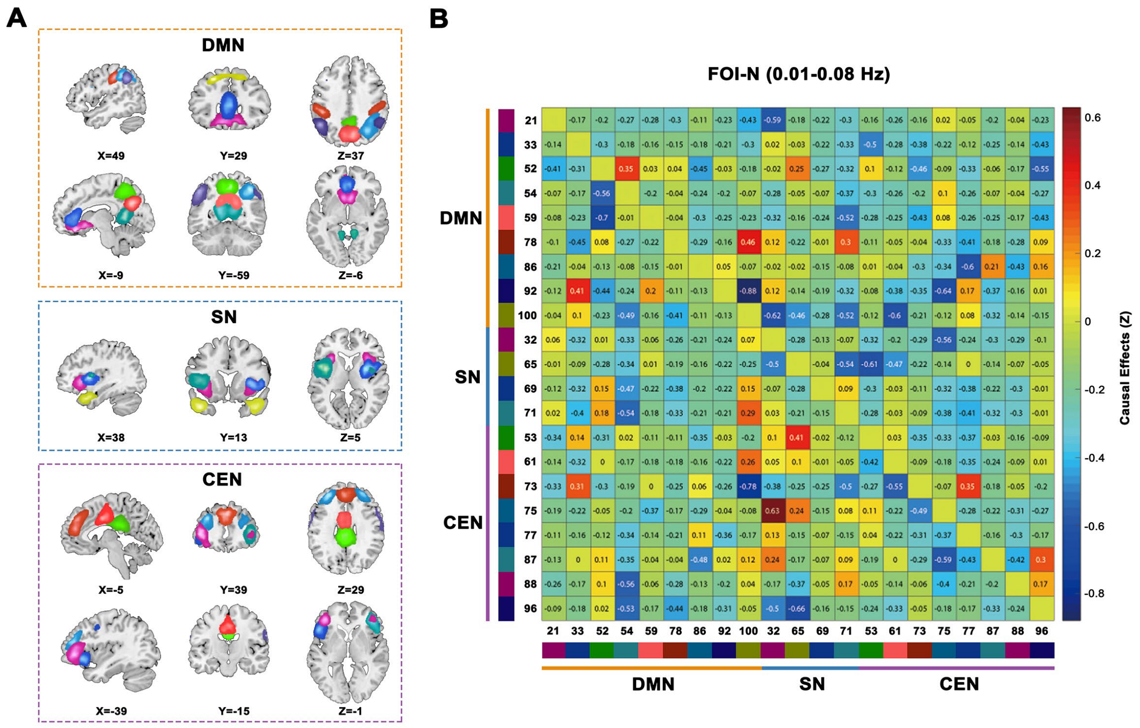

	21	33	52	54	59	78	86	92	100	32	65	69	71	53	61	73	75	77	87	88	96
21		-0.17	-0.2	-0.27	-0.28	-0.3	-0.11	-0.23	-0.43	-0.59	-0.18	-0.22	-0.3	-0.16	-0.26	-0.16	0.02	-0.05	-0.2	-0.04	-0.23
33	-0.14		-0.3	-0.18	-0.16	-0.15	-0.18	-0.21	-0.3	0.02	-0.03	-0.22	-0.33	-0.5	-0.28	-0.38	-0.22	-0.12	-0.25	-0.14	-0.43
52	-0.41	-0.31		0.35	0.03	0.04	-0.45	-0.03	-0.18	-0.02	0.25	-0.27	-0.32	0.1	-0.12	-0.46	-0.09	-0.33	-0.06	-0.17	-0.55
54	-0.07	-0.17	-0.56		-0.2	-0.04	-0.24	-0.2	-0.07	-0.28	-0.05	-0.07	-0.37	-0.3	-0.26	-0.2	0.1	-0.26	-0.07	-0.04	-0.27
59	-0.08	-0.23	-0.7	-0.01		-0.04	-0.3	-0.25	-0.23	-0.32	-0.16	-0.24	-0.52	-0.28	-0.25	-0.43	0.08	-0.26	-0.25	-0.17	-0.43
78	-0.1	-0.45	0.08	-0.27	-0.22		-0.29	-0.16	0.46	0.12	-0.22	-0.01	0.3	-0.11	-0.05	-0.04	-0.33	-0.41	-0.18	-0.28	0.09
86	-0.21	-0.04	-0.13	-0.08	-0.15	-0.01		0.05	-0.07	-0.02	-0.02	-0.15	-0.08	0.01	-0.04	-0.3	-0.34	-0.6	0.21	-0.43	0.16
92	-0.12	0.41	-0.44	-0.24	0.2	-0.11	-0.13		-0.88	0.12	-0.14	-0.19	-0.32	-0.08	-0.38	-0.35	-0.64	0.17	-0.37	-0.16	0.01
100	-0.04	0.1	-0.23	-0.49	-0.16	-0.41	-0.11	-0.13		-0.62	-0.46	-0.28	-0.52	-0.12	-0.6	-0.21	-0.12	0.08	-0.32	-0.14	-0.15
32	0.06	-0.32	0.01	-0.33	-0.06	-0.26	-0.21	-0.24	0.07		-0.28	-0.13	-0.07	-0.32	-0.2	-0.29	-0.56	-0.24	-0.3	-0.29	-0.1
65	-0.01	-0.09	-0.28	-0.34	0.01	-0.19	-0.16	-0.22	-0.25	-0.5		-0.04	-0.54	-0.61	-0.47	-0.22	-0.14	0	-0.14	-0.07	-0.05
69	-0.12	-0.32	0.15	-0.47	-0.22	-0.38	-0.2	-0.22	0.15	-0.07	-0.28		0.09	-0.3	-0.03	-0.11	-0.32	-0.38	-0.22	-0.3	-0.01
71	0.02	-0.4	0.18	-0.54	-0.18	-0.33	-0.21	-0.21	0.29	0.03	-0.21	-0.15		-0.28	-0.03	-0.09	-0.38	-0.41	-0.32	-0.3	-0.01
53	-0.34	0.14	-0.31	0.02	-0.11	-0.11	-0.35	-0.03	-0.2	0.1	0.41	-0.02	-0.12		0.03	-0.35	-0.33	-0.37	-0.03	-0.16	-0.09
61	-0.14	-0.32	0	-0.17	-0.18	-0.18	-0.16	-0.22	0.26	0.05	0.1	-0.01	-0.05	-0.42		-0.09	-0.18	-0.35	-0.24	-0.09	0.01
73	-0.33	0.31	-0.3	-0.19	0	-0.25	0.06	-0.26	-0.78	-0.38	-0.25	-0.25	-0.5	-0.27	-0.55		-0.07	0.35	-0.18	-0.05	-0.2
75	-0.19	-0.22	-0.05	-0.2	-0.37	-0.17	-0.29	-0.04	-0.08	0.63	0.24	-0.15	0.08	0.11	-0.22	-0.49		-0.28	-0.22	-0.31	-0.27
77	-0.11	-0.16	-0.12	-0.34	-0.14	-0.21	0.11	-0.36	-0.17	0.13	-0.15	-0.07	-0.15	0.04	-0.22	-0.31	-0.37		-0.16	-0.3	-0.17
87	-0.13	0	0.11	-0.35	-0.04	-0.04	-0.48	0.02	0.12	0.24	-0.17	-0.07	0.09	-0.19	0	-0.29	-0.59	-0.43		-0.42	0.3
88	-0.26	-0.17	0.1	-0.56	-0.06	-0.28	-0.13	-0.2	0.04	-0.17	-0.37	-0.05	0.17	-0.05	-0.14	-0.06	-0.4	-0.21	-0.2		0.17
96	-0.09	-0.18	0.02	-0.53	-0.17	-0.44	-0.18	-0.31	-0.05	-0.5	-0.66	-0.16	-0.15	-0.24	-0.33	-0.05	-0.18	-0.17	-0.33	-0.24	

FIGURE 2
Triple-networks identified by a group ICA. **(A)** Three resting-state networks (DMN, SN, and CEN) were identified by grouping subsets of the 21 ICs. **(B)** Whole sample averaged causal influences between ICs was computed in conventional frequency band (0.01–0.08Hz). Index numbers of ICs are written on the left and bottom side of the matrix, along with a color-coded legend, which matches to the overlaid colors of the spatial maps in **(A)**. ICA, independent component analysis; DMN, default mode network; SN, salience network; CEN, cognitive executive network; ICs, independent components.

and IC88 (inferior frontal gyrus) demonstrated the most EC differences compared to other RNSs in FOI-N, FOI-1, and FOI-2, respectively. The corresponding statistical results within each FOI are provided in Figures 3B,D,F. No significant differences between groups were observed in other frequency bands.

We then explored the causal influences within and between subsets of the triple networks across frequency bands. We discovered that the mean EC within the CEN was significantly increased in patients compared to controls in FOI-N ($p = 0.016$, FDR-corrected; Figure 4A). Meanwhile, the mean EC from SN to DMN and from CEN to SN were significantly decreased in patients compared to controls in FOI-1 ($p = 0.011$, FDR-corrected) and FOI-2 ($p = 0.014$, FDR-corrected), respectively (Figure 4B). These analyses suggest that the causal influences of the triple networks are altered in patients with MDD in a frequency-specific manner.

We further investigated whether EC metrics with significant group differences correlated with patients' clinical symptoms and found that the mean EC from CEN to SN in FOI-2 was negatively correlated with HAMD scores in patients ($r = -0.33$, $p = 0.02$, FDR-corrected; Figure 4C). This indicates that lower causal influences from CEN to SN in FOI-2 are associated with greater disease severity.

3.3. Classification performance

We used frequency-specific ECs (all ECs in each FOI) as input features to discriminate patients from controls. As shown in Table 2, our model accurately identified individuals with MDD in each frequency band (accuracy of 84.79%, 75.25%, and 82.20% for FOI-N, FOI-,1 and FOI-2, respectively). Importantly, when combining the EC features across all three frequency bands, we achieved the highest classification accuracy of 89.97%, sensitivity of 92.63%, specificity of 87.32%, and AUC of 0.8831. Figure 5A displays the corresponding average ROC curves for each frequency condition. We further analyzed which EC features possessed high discriminative power. The frequency of each feature selected in all 10-fold cross-validations was calculated to reflect the feature's contribution to the classification. The top 10 most recognizable EC features in each frequency band are presented in Figure 5B.

4. Discussion

In this study, we explored the anomalies in EC of triple networks across different frequency bands in MDD by combining the CEEMDAN and mGCA methodologies. Our analysis not only revealed an enhanced mean EC within the CEN in the conventional frequency band, but also a decrease in the mean EC from the SN to the DMN in FOI-1, as well as an increase in the mean EC from the CEN to the SN in FOI-2 in MDD patients. Moreover, a significant association between the mean EC from the CEN to the SN and the HAMD scores was identified in FOI-2 for individuals with MDD. By incorporating EC features across all the three frequency bands, optimal classification performance was achieved. These results reveal frequency-specific alterations in causal influences among triple networks for patients with MDD and highlight the importance of

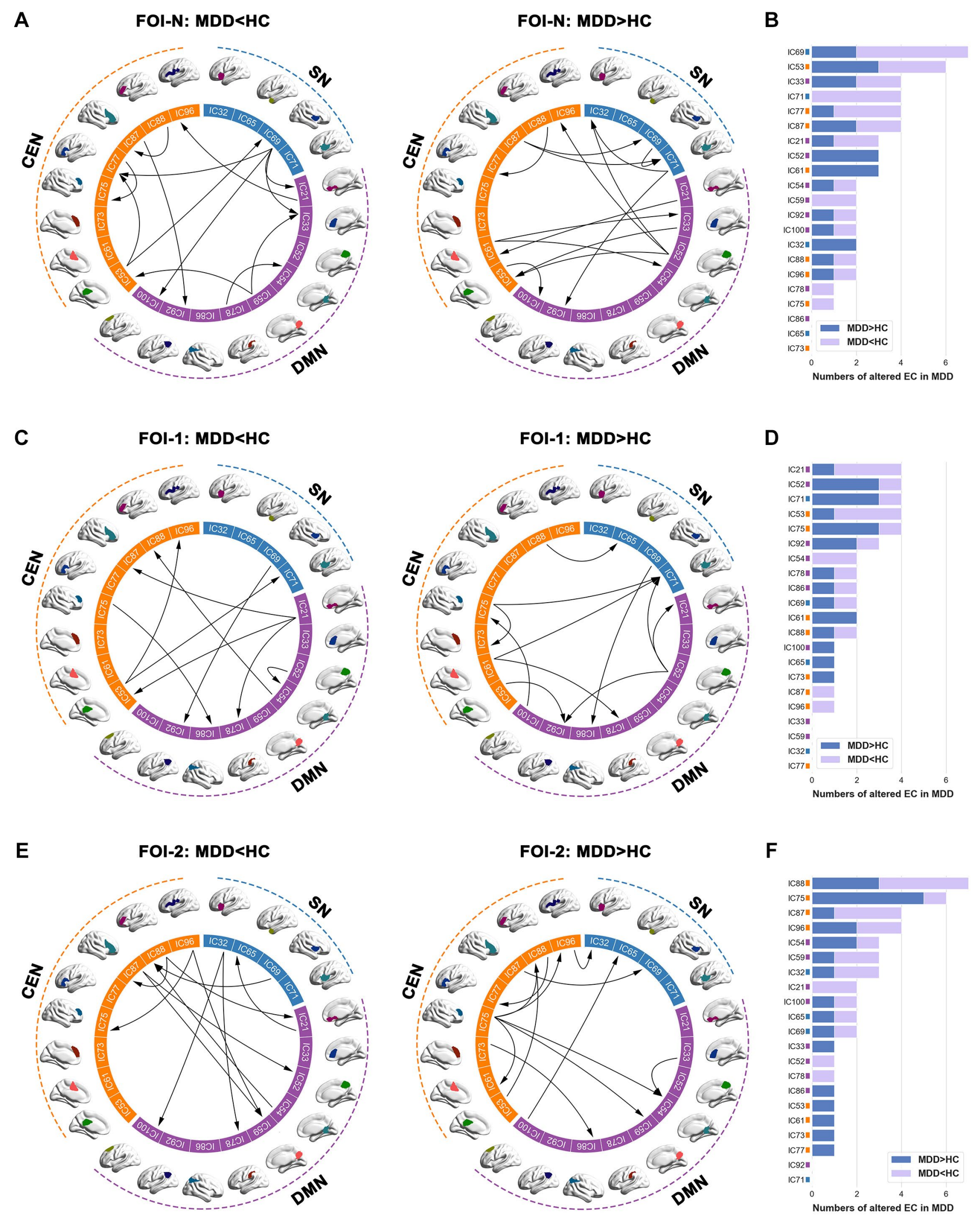

FIGURE 3

Group differences of EC across different frequency bands. **(A,C,E)** Significant between-group differences of EC in FOI-N, FOI-1 and FOI-2, and **(B,D,F)** the corresponding difference numbers of individual IC from and to the rest of ICs in each frequency band. The arrows indicate the directions of causal influences. Two sample *t*-test, significant level was set at $p<0.05$, FDR-corrected. EC, effective connectivity; FOI, frequency of interest; IC, independent component.

considering multiple frequency bands when developing more precise and dependable biomarkers for disease diagnosis.

Our findings demonstrated that the EC within the triple networks is altered in a frequency-specific manner in patients with MDD. This observation aligns with previous research that has emphasized the importance of examining connectivity patterns across multiple frequency bands in order to fully understand the neurobiological underpinnings of MDD (Wang et al., 2016; Yang et al., 2021). Specifically, we observed a significant increase in the mean EC within the CEN in MDD patients compared to unaffected controls in FOI-N ranging from 0.01 to 0.08 Hz. This finding is consistent with prior studies that have reported altered FC within the CEN in MDD patients (Mulders et al., 2015; Shen et al., 2015; Zhang et al., 2016). The increased EC within the CEN may reflect a compensatory mechanism in response to the disrupted network communications, as the CEN is responsible for higher-order cognitive processes, such as working memory and executive control (Menon, 2011). Alternatively, this alteration might be indicative of a maladaptive change contributing to the cognitive deficits frequently observed in MDD (Mulders et al., 2015; Otte et al., 2016; Kandilarova et al., 2018). Moreover, we found significant decreases in the mean EC from the SN to the DMN in patients compared to controls in FOI-1 (0.12–0.18 Hz). This result aligns with prior findings of disrupted connectivity between the SN and DMN in MDD (Balaev et al., 2018; Fettes et al., 2018; Gong et al., 2019). The SN plays a crucial role in detecting and processing emotionally salient stimuli (Etkin et al., 2011; Seo et al., 2018), while

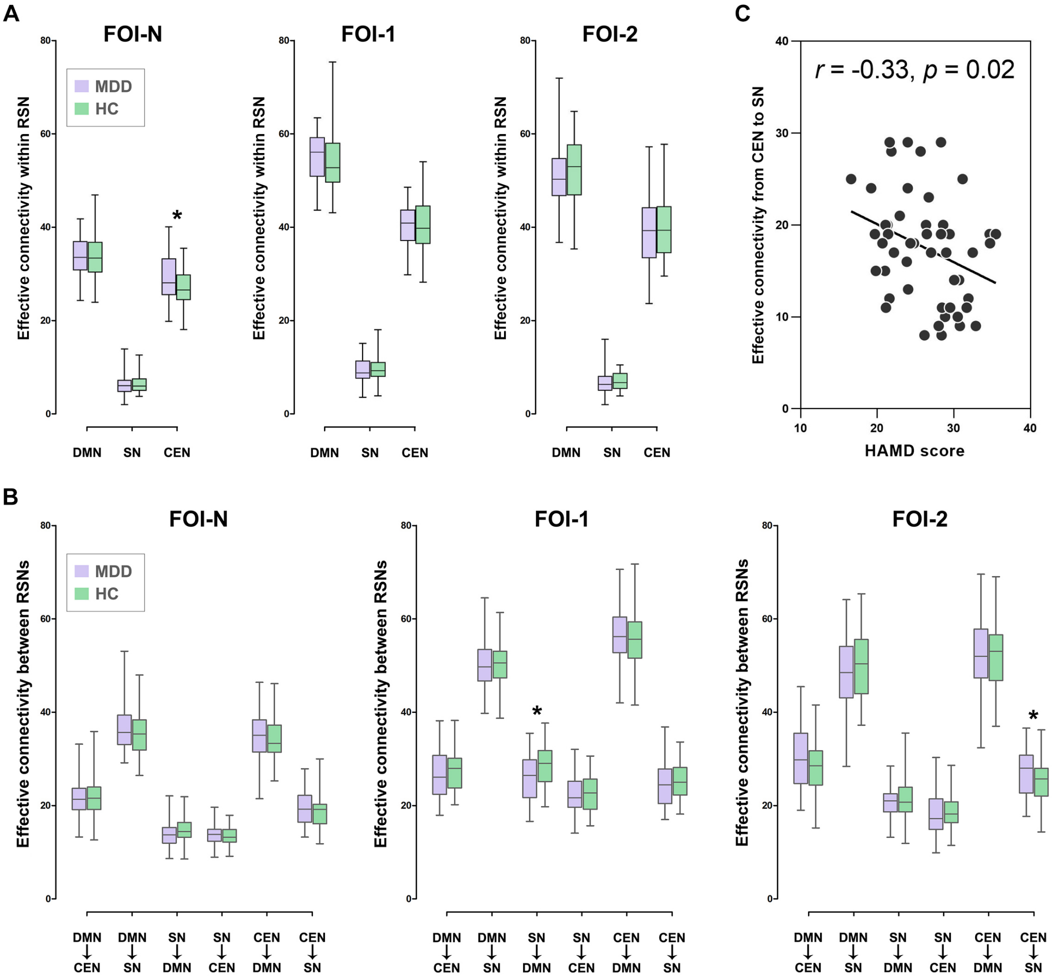

FIGURE 4
Group differences of EC in RSNs over frequency bands. **(A)** Group differences of EC within RSN in FOI-N, FOI-1 and FOI-2. **(B)** Group differences of EC between RSNs in FOI-N, FOI-1 and FOI-2. **(C)** Correlation between the HAMD score of patients and EC with significant group differences. Note that the values presented are the average ECs of all ROIs in each RSN. *$p<0.05$, FDR-corrected. HAMD, Hamilton depression scale.

TABLE 2 Discriminating the patients with MDD from the HCs by ROC analyses.

FOI	AUC	Accuracy (%)	Sensitivity (%)	Specificity (%)
FOI-N	0.8373	84.79	87.54	81.90
FOI-1	0.7651	75.25	73.61	76.67
FOI-2	0.8163	82.20	86.87	77.34
FOI-N + FOI-1 + FOI-2	0.8831	89.97	92.63	87.32

the DMN is implicated in self-referential thinking and rumination (Scheibner et al., 2017). A reduced causal influence from the SN to the DMN might indicate an impaired ability to regulate internal emotional states and a propensity for excessive rumination in MDD patients (Gandelman et al., 2019). In addition, our study demonstrated significant decreases in the mean EC from the CEN to the SN in MDD patients compared to controls in FOI-2 (0.04–0.08 Hz). This finding expands upon previous research that has reported disrupted connectivity between the CEN and SN in MDD (Kaiser et al., 2015). A decreased causal influence from the CEN to the SN might suggest an impaired top-down regulation of emotional processing in MDD patients, potentially contributing to the affective symptom characteristic of the disorder (Kennis et al., 2020). Importantly, our study expands upon existing research by exploring the multi-frequency domain, revealing that EC alterations within the triple networks in MDD may be governed by specific frequency bands. Frequency-specific alterations can reflect distinct biological processes or brain features. BOLD signals at different frequencies may signify differing neuronal activities or interactions. Thus, our finding suggests that varying sensitivities to different frequency bands may exist in the causal interactions among core network structure.

Our findings also revealed that the altered mean EC from CEN to SN in FOI-2 exhibited a significant correlation with HAMD scores in MDD patients, indicating that lower directed interactions correspond to increased disease severity. This observation aligns with prior research demonstrating associations between brain dysconnectivity and depressive symptoms (Kang et al., 2018; Yang et al., 2018; Gandelman et al., 2019). A recent investigation reported correlations between abnormal amygdala connectivity and symptom severity in MDD (Ye et al., 2023), lending further credence to the clinical

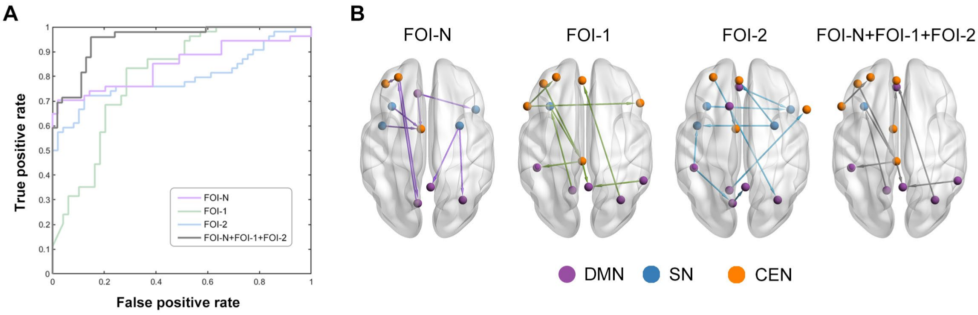

FIGURE 5
Classification performance by using EC features. **(A)** The average receiver operating characteristic curves of classification results over different frequency bands. Purple, green, blue, and grey line represent the EC in FOI-N, FOI-1, FOI-2 and FOI-N+FOI-1+FOI-2, respectively. **(B)** EC with highly discriminative power. The nodes which belong to each RSN in **(B)** are identified by different colors.

relevance of our results. Our previous work also indicated that diminished static and dynamic FCs were associated with greater MDD severity (Yao et al., 2019a,b). Importantly, the negative correlations observed exclusively in FOI-2 may represent frequency-specific symptoms of MDD, corroborating earlier findings that Slow-4 (0.027–0.073 Hz) (Yang et al., 2021), overlapping with FOI-2, may hold a crucial role in MDD diagnosis and progression monitoring. These results also suggest that FOI-2 might serve as a specific frequency band reflecting clinical symptoms in MDD patients. Furthermore, our investigation demonstrated that the highest classification accuracy was attained when combining EC features across all three frequency bands (FOI-N, FOI-1, and FOI-2), consistent with other studies reporting enhanced classification accuracy upon considering multiple frequency bands in neuropsychiatric disorders (Chen et al., 2016; Hu et al., 2021). Collectively, these findings underscore the importance of incorporating multiple frequency bands when examining the pathophysiology of MDD and indicate that a comprehensive, multi-frequency approach may yield more precise and reliable biomarkers for the diagnosis and differentiation of patients from controls.

The implications of our findings may extend to two aspects of future MDD therapy. First, this study illuminates the neural pathophysiology underpinning MDD and offers a fresh perspective on frequency-specific dysconnectivity patterns, potentially revealing treatment markers associated with disease severity. The frequency-specific EC alterations identified provide intricate insights into how these functional connections fluctuate across different frequencies. These findings could potentially be harnessed for precise therapeutic interventions, such as neurofeedback or transcranial magnetic stimulation, which can be used to modulate aberrant connectivity patterns in MDD patients (Drysdale et al., 2017). Second, our investigation supplies critical information in the pursuit of clinically valuable diagnostic markers for MDD. Numerous researchers have recently explored the potential of brain connectivity to differentiate MDD patients from unaffected controls (Zhong et al., 2017; Geng et al., 2018; Zhang et al., 2020). Consequently, the identified frequency-specific EC features capable of distinguishing patients from controls with notable accuracy could contribute to the development of more dependable and objective diagnostic instruments, assisting clinicians in the early detection of MDD (Guo et al., 2020). Nevertheless, given the limited sample sizes in this study, the high classification performance warrants validation in future research with larger samples.

There are some limitations that should be noted. First, the resting-state fMRI data acquisition employed a relatively lower repetition time (2 s), constraining the detection of dynamic fluctuations in higher frequency bands (>0.25 Hz). Future research would benefit from utilizing a higher sampling frequency. Second, while Granger causality analysis (GCA) is regarded as an effective method for evaluating EC in resting-state fMRI data, it has been postulated that directional changes might result from hemodynamic coupling differences among distinct brain regions (Pervaiz et al., 2020). Recently, alternative models, specifically the dynamic causal model (DCM)—a hemodynamic model (Friston et al., 2014), have been proposed to detect directed connectivity among hidden neuronal states (Park et al., 2018; Zarghami and Friston, 2020). Consequently, future studies employing DCM to explore frequency-specific reorganizations of EC in MDD patients would be of considerable interest. Third, the patient cohort in this study had prolonged exposure to various antidepressant medications. Prior research has assessed the impact of antidepressants on brain connectivity (Korgaonkar et al., 2019), and it cannot be ruled out that medication effects may have influenced our findings. Nonetheless, previous FC investigations involving high-risk MDD individuals have indicated that altered connectivity between triple networks occurs in the absence of antidepressant treatment (Pawlak et al., 2022). A future study with a never-medicated sample is required to corroborate our findings.

In conclusion, our study revealed frequency-specific alterations in the causal influences among the DMN, SN, and CEN in MDD, with potential ramifications for diagnosis and treatment. These findings enhance our comprehension of the neurobiological underpinnings of MDD and stress the significance of investigating EC patterns within the triple networks across multiple frequency bands. Future research endeavors should build upon these insights to further elucidate the role of frequency-specific EC patterns in MDD pathophysiology, examine their potential as therapeutic targets, and assess their applicability as objective biomarkers for MDD diagnosis.

Data availability statement

The raw data supporting the conclusions of this article will be made available by the authors, without undue reservation.

Ethics statement

The studies involving human participants were reviewed and approved by Gansu Provincial Hospital. The patients/participants provided their written informed consent to participate in this study.

Author contributions

YL designed the study and performed statistical analyses, drafted the manuscript, and approved the final manuscript as submitted. LQ and GL coordinated and carried out the data collection, revised the manuscript, and approved the final manuscript as submitted. ZZ conceptualized the study, critically reviewed the manuscript, and approved the final manuscript as submitted. All authors contributed to the article and approved the submitted version.

Funding

This work was supported by the National Natural Science Foundation of China (No. 82001918) and by the China Postdoctoral Science Foundation (No. 2020 M681865).

Conflict of interest

The authors declare that the research was conducted in the absence of any commercial or financial relationships that could be construed as a potential conflict of interest.

The reviewer ZY declared a past co-authorship with the author GL to the handling editor.

Publisher's note

Supplementary material

The Supplementary material for this article can be found online at: https://www.frontiersin.org/articles/10.3389/fnins.2023.1200029/full#supplementary-material

References

Allen, E. A., Damaraju, E., Plis, S. M., Erhardt, E. B., Eichele, T., and Calhoun, V. D. (2014). Tracking whole-brain connectivity dynamics in the resting state. *Cereb. Cortex* 24, 663–676. doi: 10.1093/cercor/bhs352

Balaev, V., Orlov, I., Petrushevsky, A., and Martynova, O. (2018). Functional connectivity between salience, default mode and frontoparietal networks in post-stroke depression. *J. Affect. Disord.* 227, 554–562. doi: 10.1016/j.jad.2017.11.044

Bell, A. J., and Sejnowski, T. J. (1995). An information-maximization approach to blind separation and blind deconvolution. *Neural Comput.* 7, 1129–1159. doi: 10.1162/neco.1995.7.6.1129

Buzsáki, G., and Draguhn, A. (2004). Neuronal oscillations in cortical networks. *Science* 304, 1926–1929. doi: 10.1126/science.1099745

Chen, H., Duan, X., Liu, F., Lu, F., Ma, X., Zhang, Y., et al. (2016). Multivariate classification of autism spectrum disorder using frequency-specific resting-state functional connectivity—a multi-center study. *Prog. Neuro-Psychopharmacol. Biol. Psychiatry* 64, 1–9. doi: 10.1016/j.pnpbp.2015.06.014

Cheng, W., Rolls, E. T., Qiu, J., Yang, D., Ruan, H., Wei, D., et al. (2018). Functional connectivity of the precuneus in unmedicated patients with depression. *Biol. Psychiatry Cogn. Neurosci. Neuroimaging* 3, 1040–1049. doi: 10.1016/j.bpsc.2018.07.008

Cole, S. R., and Voytek, B. (2017). Brain oscillations and the importance of waveform shape. *Trends Cogn. Sci.* 21, 137–149. doi: 10.1016/j.tics.2016.12.008

Colominas, M. A., Schlotthauer, G., and Torres, M. E. (2014). Improved complete ensemble EMD: a suitable tool for biomedical signal processing. *Biomed. Signal Process. Control* 14, 19–29. doi: 10.1016/j.bspc.2014.06.009

Cortes, C., and Vapnik, V. (1995). Support-vector networks. *Mach. Learn.* 20, 273–297. doi: 10.1007/BF00994018

David, O., Guillemain, I., Saillet, S., Reyt, S., Deransart, C., Segebarth, C., et al. (2008). Identifying neural drivers with functional MRI: an electrophysiological validation. *PLoS Biol.* 6, 2683–2697. doi: 10.1371/journal.pbio.0060315

Deshpande, G., and Hu, X. (2012). Investigating effective brain connectivity from fMRI data: past findings and current issues with reference to granger causality analysis. *Brain Connect.* 2, 235–245. doi: 10.1089/brain.2012.0091

Drysdale, A. T., Grosenick, L., Downar, J., Dunlop, K., Mansouri, F., Meng, Y., et al. (2017). Resting-state connectivity biomarkers define neurophysiological subtypes of depression. *Nat. Med.* 23, 28–38. doi: 10.1038/nm.4246

Etkin, A., Egner, T., and Kalisch, R. (2011). Emotional processing in anterior cingulate and medial prefrontal cortex. *Trends Cogn. Sci.* 15, 85–93. doi: 10.1016/j.tics.2010.11.004

Fettes, P. W., Moayedi, M., Dunlop, K., Mansouri, F., Vila-Rodriguez, F., Giacobbe, P., et al. (2018). Abnormal functional connectivity of Frontopolar subregions in treatment-nonresponsive major depressive disorder. *Biol. Psychiatry Cogn. Neurosci. Neuroimaging* 3, 337–347. doi: 10.1016/j.bpsc.2017.12.003

Fiorenzato, E., Strafella, A. P., Kim, J., Schifano, R., Weis, L., Antonini, A., et al. (2019). Dynamic functional connectivity changes associated with dementia in Parkinson's disease. *Brain* 142, 2860–2872. doi: 10.1093/brain/awz192

Friston, K. J., Kahan, J., Biswal, B., and Razi, A. (2014). A DCM for resting state fMRI. *NeuroImage* 94, 396–407. doi: 10.1016/j.neuroimage.2013.12.009

Gandelman, J. A., Albert, K., Boyd, B. D., Park, J. W., Riddle, M., Woodward, N. D., et al. (2019). Intrinsic functional network connectivity is associated with clinical symptoms and cognition in late-life depression. *Biol. Psychiatry Cogn. Neurosci. Neuroimaging* 4, 160–170. doi: 10.1016/j.bpsc.2018.09.003

Geng, X., Xu, J., Liu, B., and Shi, Y. (2018). Multivariate classification of major depressive disorder using the effective connectivity and functional connectivity. *Front. Neurosci.* 12:38. doi: 10.3389/fnins.2018.00038

Gong, J., Chen, G., Jia, Y., Zhong, S., Zhao, L., Luo, X., et al. (2019). Disrupted functional connectivity within the default mode network and salience network in unmedicated bipolar II disorder. *Prog. Neuro-Psychopharmacol. Biol. Psychiatry* 88, 11–18. doi: 10.1016/j.pnpbp.2018.06.012

Gotlib, I. H., and Joormann, J. (2010). Cognition and depression: current status and future directions. *Annu. Rev. Clin. Psychol.* 6, 285–312. doi: 10.1146/annurev.clinpsy.121208.131305

Guo, M., Wang, T., Zhang, Z., Chen, N., Li, Y., Wang, Y., et al. (2020). Diagnosis of major depressive disorder using whole-brain effective connectivity networks derived from resting-state functional MRI. *J. Neural Eng.* 17:056038. doi: 10.1088/1741-2552/abbc28

Hu, R., Peng, Z., Zhu, X., Gan, J., Zhu, Y., Ma, J., et al. (2021). Multi-band brain network analysis for functional neuroimaging biomarker identification. *IEEE Trans. Med. Imaging* 40, 3843–3855. doi: 10.1109/TMI.2021.3099641

Kaiser, R. H., Andrews-Hanna, J. R., Wager, T. D., and Pizzagalli, D. A. (2015). Large-scale network dysfunction in major depressive disorder: a meta-analysis of resting-state functional connectivity. *JAMA Psychiat.* 72, 603–611. doi: 10.1001/jamapsychiatry.2015.0071

Kandilarova, S., Stoyanov, D., Kostianev, S., and Specht, K. (2018). Altered resting state effective connectivity of anterior insula in depression. *Front. Psych.* 9:83. doi: 10.3389/fpsyt.2018.00083

Kang, L., Zhang, A., Sun, N., Liu, P., Yang, C., Li, G., et al. (2018). Functional connectivity between the thalamus and the primary somatosensory cortex in major depressive disorder: a resting-state fMRI study. *BMC Psychiatry* 18:339. doi: 10.1186/s12888-018-1913-6

Kennis, M., Gerritsen, L., van Dalen, M., Williams, A., Cuijpers, P., and Bockting, C. (2020). Prospective biomarkers of major depressive disorder: a systematic review and meta-analysis. *Mol. Psychiatry* 25, 321–338. doi: 10.1038/s41380-019-0585-z

Kim, J., Criaud, M., Cho, S. S., Mihaescu, A., Coakeley, S., Ghadery, C., et al. (2017). Abnormal intrinsic brain functional network dynamics in Parkinson's disease. *Brain* 140, 2955–2967. doi: 10.1093/brain/awx233

Korgaonkar, M. S., Goldstein-Piekarski, A. N., Fornito, A., and Williams, L. M. (2019). Intrinsic connectomes are a predictive biomarker of remission in major depressive disorder. *Mol. Psychiatry* 25, 1537–1549. doi: 10.1038/s41380-019-0574-2

Li, G., Rossbach, K., Zhang, A., Liu, P., and Zhang, K. (2018). Resting-state functional changes in the precuneus within first-episode drug-naive patients with MDD. *Neuropsychiatr. Dis. Treat.* 14, 1991–1998. doi: 10.2147/NDT.S168060

Liao, W., Ding, J., Marinazzo, D., Xu, Q., Wang, Z., Yuan, C., et al. (2011). Small-world directed networks in the human brain: multivariate granger causality analysis of resting-state fMRI. *NeuroImage* 54, 2683–2694. doi: 10.1016/j.neuroimage.2010.11.007

Martino, M., Magioncalda, P., Huang, Z., Conio, B., Piaggio, N., Duncan, N. W., et al. (2016). Contrasting variability patterns in the default mode and sensorimotor networks balance in bipolar depression and mania. *Proc. Natl. Acad. Sci. U. S. A.* 113, 4824–4829. doi: 10.1073/pnas.1517558113

Mathers, C. D., and Loncar, D. (2006). Projections of global mortality and burden of disease from 2002 to 2030. *PLoS Med.* 3:e442. doi: 10.1371/journal.pmed.0030442

Menon, V. (2011). Large-scale brain networks and psychopathology: a unifying triple network model. *Trends Cogn. Sci.* 15, 483–506. doi: 10.1016/j.tics.2011.08.003

Mulders, P. C., van Eijndhoven, P. F., Schene, A. H., Beckmann, C. F., and Tendolkar, I. (2015). Resting-state functional connectivity in major depressive disorder: a review. *Neurosci. Biobehav. Rev.* 56, 330–344. doi: 10.1016/j.neubiorev.2015.07.014

Otte, C., Gold, S. M., Penninx, B. W., Pariante, C. M., Etkin, A., Fava, M., et al. (2016). Major depressive disorder. *Nat. Rev. Dis. Primers*. 2, 1–20. doi: 10.1038/nrdp.2016.65

Park, H. J., Friston, K. J., Pae, C., Park, B., and Razi, A. (2018). Dynamic effective connectivity in resting state fMRI. *NeuroImage* 180, 594–608. doi: 10.1016/j.neuroimage.2017.11.033

Pawlak, M., Bray, S., and Kopala-Sibley, D. C. (2022). Resting state functional connectivity as a marker of internalizing disorder onset in high-risk youth. *Sci. Rep.* 12:21337. doi: 10.1038/s41598-022-25805-y

Peng, X., Lau, W. K. W., Wang, C., Ning, L., and Zhang, R. (2020). Impaired left amygdala resting state functional connectivity in subthreshold depression individuals. *Sci. Rep.* 10:17207. doi: 10.1038/s41598-020-74166-x

Pereira, F., Mitchell, T., and Botvinick, M. (2009). Machine learning classifiers and fMRI: a tutorial overview. *NeuroImage* 45, S199–S209. doi: 10.1016/j.neuroimage.2008.11.007

Pervaiz, U., Vidaurre, D., Woolrich, M. W., and Smith, S. M. (2020). Optimising network modelling methods for fMRI. *NeuroImage* 211:116604. doi: 10.1016/j.neuroimage.2020.116604

Rolls, E. T., Cheng, W., Gilson, M., Qiu, J., Hu, Z., Ruan, H., et al. (2018). Effective connectivity in depression. *Biol. Psychiatry Cogn. Neurosci. Neuroimaging* 3, 187–197. doi: 10.1016/j.bpsc.2017.10.004

Samaha, J., Iemi, L., Haegens, S., and Busch, N. A. (2020). Spontaneous brain oscillations and perceptual decision-making. *Trends Cogn. Sci.* 24, 639–653. doi: 10.1016/j.tics.2020.05.004

Scheibner, H. J., Bogler, C., Gleich, T., Haynes, J. D., and Bermpohl, F. (2017). Internal and external attention and the default mode network. *NeuroImage* 148, 381–389. doi: 10.1016/j.neuroimage.2017.01.044

Seo, R., Stocco, A., and Prat, C. S. (2018). The bilingual language network: differential involvement of anterior cingulate, basal ganglia and prefrontal cortex in preparation, monitoring, and execution. *NeuroImage* 174, 44–56. doi: 10.1016/j.neuroimage.2018.02.010

Shen, T., Li, C., Wang, B., Yang, W. M., Zhang, C., Wu, Z., et al. (2015). Increased cognition connectivity network in major depression disorder: a FMRI study. *Psychiatry Investig.* 12, 227–234. doi: 10.4306/pi.2015.12.2.227

Tu, Y., Fu, Z., Zeng, F., Maleki, N., Lan, L., Li, Z., et al. (2019). Abnormal thalamocortical network dynamics in migraine. *Neurology* 92, e2706–e2716. doi: 10.1212/WNL.0000000000007607

Wang, L., Kong, Q., Li, K., Su, Y., Zeng, Y., Zhang, Q., et al. (2016). Frequency-dependent changes in amplitude of low-frequency oscillations in depression: a resting-state fMRI study. *Neurosci. Lett.* 614, 105–111. doi: 10.1016/j.neulet.2016.01.012

Yan, C. G., Chen, X., Li, L., Castellanos, F. X., Bai, T. J., Bo, Q. J., et al. (2019). Reduced default mode network functional connectivity in patients with recurrent major depressive disorder. *Proc. Natl. Acad. Sci. U. S. A.* 116, 9078–9083. doi: 10.1073/pnas.1900390116

Yang, H., Chen, X., Chen, Z. B., Li, L., Li, X. Y., Castellanos, F. X., et al. (2021). Disrupted intrinsic functional brain topology in patients with major depressive disorder. *Mol. Psychiatry* 26, 7363–7371. doi: 10.1038/s41380-021-01247-2

Yang, Y., Cui, Q., Pang, Y., Chen, Y., Tang, Q., Guo, X., et al. (2021). Frequency-specific alteration of functional connectivity density in bipolar disorder depression. *Prog. Neuro-Psychopharmacol. Biol. Psychiatry* 104:110026. doi: 10.1016/j.pnpbp.2020.110026

Yang, Z., Gu, S., Honnorat, N., Linn, K. A., Shinohara, R. T., Aselcioglu, I., et al. (2018). Network changes associated with transdiagnostic depressive symptom improvement following cognitive behavioral therapy in MDD and PTSD. *Mol. Psychiatry* 23, 2314–2323. doi: 10.1038/s41380-018-0201-7

Yao, Z., Shi, J., Zhang, Z., Zheng, W., Hu, T., Li, Y., et al. (2019a). Altered dynamic functional connectivity in weakly-connected state in major depressive disorder. *Clin. Neurophysiol.* 130, 2096–2104. doi: 10.1016/j.clinph.2019.08.009

Yao, Z., Zou, Y., Zheng, W., Zhang, Z., Li, Y., Yu, Y., et al. (2019b). Structural alterations of the brain preceded functional alterations in major depressive disorder patients: evidence from multimodal connectivity. *J. Affect. Disord.* 253, 107–117. doi: 10.1016/j.jad.2019.04.064

Ye, Y., Wang, C., Lan, X., Li, W., Fu, L., Zhang, F., et al. (2023). Abnormal amygdala functional connectivity in MDD patients with insomnia complaints. *Psychiatry Res. Neuroimaging* 328:111578. doi: 10.1016/j.pscychresns.2022.111578

Zarghami, T. S., and Friston, K. J. (2020). Dynamic effective connectivity. *NeuroImage* 207:116453. doi: 10.1016/j.neuroimage.2019.116453

Zhang, B., Li, M., Qin, W., Demenescu, L. R., Metzger, C. D., Bogerts, B., et al. (2016). Altered functional connectivity density in major depressive disorder at rest. *Eur. Arch. Psychiatry Clin. Neurosci.* 266, 239–248. doi: 10.1007/s00406-015-0614-0

Zhang, Z., Liu, G., Yao, Z., Zheng, W., Xie, Y., Hu, T., et al. (2018). Changes in dynamics within and between resting-state subnetworks in juvenile myoclonic epilepsy occur at multiple frequency bands. *Front. Neurol.* 9:448. doi: 10.3389/fneur.2018.00448

Zhang, Y., Wu, W., Toll, R. T., Naparstek, S., Maron-Katz, A., Watts, M., et al. (2020). Identification of psychiatric disorder subtypes from functional connectivity patterns in resting-state electroencephalography. Nat. *Biomed. Eng.* 5, 309–323. doi: 10.1038/s41551-020-00614-8

Zhong, X., Shi, H., Ming, Q., Dong, D., Zhang, X., Zeng, L. L., et al. (2017). Whole-brain resting-state functional connectivity identified major depressive disorder: a multivariate pattern analysis in two independent samples. *J. Affect. Disord.* 218, 346–352. doi: 10.1016/j.jad.2017.04.040

Zuo, X. N., Di Martino, A., Kelly, C., Shehzad, Z. E., Gee, D. G., Klein, D. F., et al. (2010). The oscillating brain: complex and reliable. *NeuroImage* 49, 1432–1445. doi: 10.1016/j.neuroimage.2009.09.037

frontiers | Frontiers in Neuroscience

TYPE Original Research
PUBLISHED 16 August 2023
DOI 10.3389/fnins.2023.1242543

*CORRESPONDENCE
Jue Wang
✉ juewang_xjtu@126.com
Jin Qiao
✉ qiaojn123@163.com

†These authors have contributed equally to this work

RECEIVED 19 June 2023
ACCEPTED 04 August 2023
PUBLISHED 16 August 2023

CITATION
Peng Y, Zheng Y, Yuan Z, Guo J, Fan C, Li C, Deng J, Song S, Qiao J and Wang J (2023) The characteristics of brain network in patient with post-stroke depression under cognitive task condition.
Front. Neurosci. 17:1242543.
doi: 10.3389/fnins.2023.1242543

The characteristics of brain network in patient with post-stroke depression under cognitive task condition

Yu Peng[1,2†], Yang Zheng[3†], Ziwen Yuan[1,2], Jing Guo[2], Chunyang Fan[2], Chenxi Li[4], Jingyuan Deng[2], Siming Song[2], Jin Qiao[2]* and Jue Wang[1]*

[1]The Key Laboratory of Biomedical Information Engineering of Ministry of Education, School of Life Sciences and Technology, Institute of Biomedical Engineering, Xi'an Jiaotong University, Xi'an, China, [2]Department of Rehabilitation, First Affiliated Hospital of Xi'an Jiaotong University, Xi'an, China, [3]The State Key Laboratory for Manufacturing Systems Engineering, School of Mechanical Engineering, Institute of Engineering and Medicine Interdisciplinary Studies, Xi'an Jiaotong University, Xi'an, China, [4]Department of Military Medical Psychology, Air Force Medical University, Xi'an, China

Objectives: Post-stroke depression (PSD) may be associated with the altered brain network property. This study aimed at exploring the brain network characteristics of PSD under the classic cognitive task, i.e., the oddball task, in order to promote our understanding of the pathogenesis and the diagnosis of PSD.

Methods: Nineteen stroke survivors with PSD and 18 stroke survivors with no PSD (non-PSD) were recruited. The functional near-infrared spectroscopy (fNIRS) covering the dorsolateral prefrontal cortex was recorded during the oddball task state and the resting state. The brain network characteristics were extracted using the graph theory and compared between the PSD and the non-PSD subjects. In addition, the classification performance between the PSD and non-PSD subjects was evaluated using features in the resting and the task state, respectively.

Results: Compared with the resting state, more brain network characteristics in the task state showed significant differences between the PSD and non-PSD groups, resulting in better classification performance. In the task state, the assortativity, clustering coefficient, characteristic path length, and local efficiency of the PSD subjects was larger compared with the non-PSD subjects while the global efficiency of the PSD subjects was smaller than that of the non-PSD subjects.

Conclusion: The altered brain network properties associated with PSD in the cognitive task state were more distinct compared with the resting state, and the ability of the brain network to resist attack and transmit information was reduced in PSD patients in the task state.

Significance: This study demonstrated the feasibility and superiority of investigating brain network properties in the task state for the exploration of the pathogenesis and new diagnosis methods for PSD.

KEYWORDS

post-stroke depression, cognitive task, brain network, fNIRS, graph theory

1. Introduction

Post-stroke depression (PSD) is the most common neuropsychiatric complication after stroke (Taylor-Rowan et al., 2019). About one-third of stroke survivors suffer from PSD (Guo et al., 2022), which has a significant impact on their rehabilitation outcomes and quality of life (Paolucci, 2017). It has been demonstrated that early diagnosis, prevention and treatment of PSD are very important for stroke survivors (Koyanagi et al., 2021). However, the pathogenesis of PSD is still being investigated (Guo et al., 2022). Currently, the diagnosis of PSD in clinics mainly relies on the subjective scale-based evaluation of patients' emotion state and an objective indicator is urgently needed.

The combination of the modern brain imaging technology and the complex network theory, i.e., the graph theory provides a powerful tool to analyze the human brain networks (Power et al., 2010; Wang and Wang, 2014). The study of brain functional networks provides a new perspective for understanding the pathological mechanism and then the assistance for the early diagnosis of neuropsychiatric diseases (Wang et al., 2021). Previous studies have suggested that PSD might be caused by the damage to some specific brain network (Boes et al., 2015). Zhang et al. (2019) scanned the amygdala in the affective network using the functional magnetic resonance imaging (fMRI) to study the characteristics of the brain functional network in the PSD patients with left temporal lobe infarction in the resting state. They found that PSD was closely related to the reorganization of the damaged brain networks mainly involving the amygdala and the prefrontal cortex. Similarly, Shi et al. (2017) collected the fMRI data from the cingulate cortex in the resting state and compared the topological properties of the default mode network (DMN) between the stroke survivors with and without PSD. The results showed that the functional connectivity of the anterior cingulate cortex with the prefrontal cortex, cingulate cortex, and motor cortex in PSD patients was significantly reduced. However, the functional connectivity of the anterior cingulate cortex with the hippocampus, parahippocampal gyrus, insula and amygdala was enhanced. These indicated that the pathogenesis of PSD was possibly related to the altered connectivity in the DMN. Balaev et al. (2018) further demonstrated that both the DMN and the salience network were changed in the PSD patients. In another resting-state fMRI study, Egorova et al. (2018) found that the functional connectivity between the left dorsolateral prefrontal cortex and the right superior limbic gyrus in the PSD patients was significantly reduced, and the decline of the connectivity in the frontoparietal cognition control network was positively correlated with the severity of depression. In general, these studies found abnormal brain network connectivity at the prefrontal cortex, amygdala or hippocampus regions in the PSD patients. However, the brain network properties in the resting state were investigated the most, and furthermore their results were inconclusive for the cause of PSD from the view of altered brain functional networks.

Studies have shown that the pattern of brain functional connectivity in the task state was different from that in the resting state at both the neuron and system levels (Zhang et al., 2010; Cole et al., 2014; Gerchen et al., 2014; Foster et al., 2015). With most resting-state networks still being identifiable in the task state (Cole et al., 2014; Krienen et al., 2014), the differences of the brain network connectivity between the resting and task conditions observed using the noninvasive functional neuroimaging techniques at the system level might be subtle. However, these differences are widely distributed across the brain. For example, based on the Human Connectome Project (HCP) task set, up to 38% of the connectivity were significantly different between the task and resting states (Barch et al., 2013; Cole et al., 2014). Kaufmann et al. (2017) recently reported that 76.2% of the connectivity were different across 6 tasks. Although the brain network topology may remain unchanged overall, the network functional connectivity indeed reconfigured in some ways when switching from the resting to the task state (Cole et al., 2014; Krienen et al., 2014). For example, the brain became less segregated and the functional connectivity was more stable in the task state (Di et al., 2013). In addition, both the hub location and the communication frequency can be modulated by the participation of tasks. Therefore, compared with the resting state, it might provide us another alternative to explore the pathogenesis of PSD by investigating the brain network in the task state, due to its widely varied and more stable brain network connectivity.

Facial emotion recognition is one of the most commonly used tasks in the research of depression (Fusar-Poli et al., 2009), mainly involving two types of experiment paradigms. One is the explicit task that requires the subjects to judge the emotion categories, which is mostly used to study the emotional dysfunction in subjects with depression. The other one is the implicit task that requires the subjects to judge the gender with the presentation of different emotional expressions. This paradigm is typically used to estimate the ability of the brain to process emotional faces unconsciously. Via the facial emotion recognition tasks, researchers have obtained a certain understanding of the neural mechanism for the negative cognitive processing in patients with depression. However, there are some limitations in the facial emotion recognition tasks. Firstly, the expression pictures come from different countries, thus making it difficult to avoid the interference of race, age etc. Secondly, people from different countries with different cultures may have different degrees of recognition of the same expressions. Lastly, the gender might also affect the recognition of facial expressions because women generally have richer emotions and are more sensitive to expressions (Gard and Kring, 2007; Jenkins et al., 2018). Compared with the facial emotion recognition task, the classic 'oddball' task paradigm that is widely used in the event-related potential studies has no such limitations. For example, the P300 wave elicited in the oddball task is considered to be an endogenous evoked potential related to the cognitive function of brain (Polich, 2007). As a potential reliable biomarker for the advanced cognitive functions such as the attention and working memory (van Dinteren et al., 2014), the P300 wave has been widely used for the assessment of cognitive disorders. It is commonly believed that there is a close relationship between the cognition and emotion. For example, early PSD aggravates the cognitive impairments in elderly male stroke patients (Shin et al., 2022). In addition, the impairment of working memory was believed to be an important indicator of the cognitive impairment in depression. Meanwhile, researchers have found that the P300 wave was a reliable psychological measurement in both depression and healthy individuals (Klawohn et al., 2020). Based on these research findings, it was hypothesized in this study that the oddball task, as a classic experiment paradigm for cognitive function assessing, may possibly get the damaged brain network associated with PSD involved and thereby, help obtain the brain network characteristics that can reflect the neural mechanism of PSD. Meanwhile, as far as we know, no previous studies have used the oddball task paradigm to investigate the brain network property of PSD.

Most previous studies on the brain network of PSD utilized the fMRI data to measure the metabolic activities in brain. As another non-invasive brain functional imaging technique, the functional near-infrared spectroscopy (fNIRS) has the advantages of low cost, portability, and convenience for a variety of tasks (Ferrari and Quaresima, 2012; Hong and Khan, 2017) and more importantly, it has a higher temporal resolution than fMRI. Therefore, it has been applied in different clinical settings, especially in the field of neuroscience. Previous studies have shown that the oxyhemoglobin concentration (HbO) measured by fNIRS may be a useful tool for diagnosing PSD (Koyanagi et al., 2021). However, to the best of our knowledge, there is still a lack of studies that use the fNIRS signals to analyze the brain network of PSD patients.

In this study, in order to investigate the altered brain network characteristics of PSD in the task state and as a result, obtain the possible biomarkers for PSD diagnosis, the oddball task paradigm was performed by stroke survivors with and without PSD (non-PSD). The fNIRS data were collected under both the task and resting conditions, and the brain functional connectivity and network properties based on the graph theory were analyzed and compared between the PSD and non-PSD patients. Based on the previous studies, it was hypothesized that some of the altered brain network properties that accounts for PSD might be manifested in the task state other than the resting state, resulting in more distinct brain network connectivity patterns and characteristics in the cognitive task state compared with the resting state. Our results possibly provide a new perspective to explore the pathogeneses and new diagnosis methods for PSD.

2. Materials and methods

2.1. Subjects

All recruited subjects were post-stroke patients undergoing the rehabilitation therapy at the Rehabilitation Department of the First Affiliated Hospital of Xi'an Jiaotong University from June 2022 to November 2022. The inclusion criteria were as follows: (1) 30–85 years old; (2) stroke confirmed by computed tomography or magnetic resonance imaging; (3) first-ever stroke with the onset within 1–12 months from then; (4) consciousness with the ability to finish the experiment task. The exclusion criteria were: (1) history of mental illness, such as schizophrenia, mood disorders; (2) substance abuse; (3) severe neurological impairment, such as hearing impairment and physical weakness; (4) metal implants in the brain, such as deep brain stimulators; (5) cranioplasty. This study was approved by the Ethics Committee of the First Affiliated Hospital of Xi'an Jiaotong University on March 27, 2021 (approval number: XJTU1AF2023LSK-2021-175), and all patients or their authorized representatives signed the informed consent.

All subjects were assessed using the Hamilton Depression Scale with 24 items (HAMD) that has been widely used in the diagnosis and severity assessment of depression, and higher scores indicate more severe depression. The assessment was performed by 2 trained psychiatrists in the hospital. All recruited subjects were divided into 2 groups based on their HAMD scores. The subjects with the score higher than or equal to 8 constituted the PSD group. The other subjects with scores less than 8 constituted the non-PSD group. In addition, the Montreal Cognitive Assessment Test (MoCA) and the Mini-mental State Examination (MMSE) were performed to assess the cognitive state of subjects.

2.2. Experiment procedure

2.2.1. Oddball task paradigm

The classic oddball paradigm was used in this study. The subjects were presented with two kinds of auditory stimuli both at the intensity of 85 dB. The default or the non-deviant stimulus was a low-frequency tone at 1,000 Hz while the target or the deviant stimulus was a high-frequency tone at 2,000 Hz (Figure 1A). Each stimulus lasted for 0.05 s and there was a random respond interval lasting 1 ~ 3 s between two adjacent stimuli. The total stimulation or task period lasted 360 s with 25% as the deviant stimuli and 75% as the non-deviant stimuli. The subjects were requested to press the button using their thumbs of the unparalyzed side immediately after the deviant sound was heard. Before the task period, there was a 20-s resting period served as the baseline. The subjects were sat comfortably with their eyes closed and their bodies relaxed during the whole experiment, and asked to concentrated their attention on the auditory stimuli during the stimulation period.

2.2.2. Data recording

The NirScan-6000A system (Huichuang Medical Equipment Co., Ltd., Danyang, China) was used to record the fNIRS signals in this study. The wavelength of the near-infrared light used in this system was 730, 808 and 850 nm, respectively. Thirteen optodes were used including 7 light sources and 6 light detectors with an inter-optode distance of 3 cm. This optode configuration resulted in 14 channels of fNIRS signals in total covering the left and the right dorsolateral prefrontal (DLPF) cortex, respectively (Figure 1B). The sampling rate was 11 Hz and data recording was performed in a quiet and dark room.

2.3. Data processing

2.3.1. Preprocessing

The original light intensity signal was converted into the optical density (OD) signal for individual channels. Then, an automatic motion artifact removal procedure was performed using a sliding window method for individual channels. Specifically, within each 0.5-s window, if the difference between the maximum and the minimum of the OD signal was more than 6 times the standard deviation of the whole trial, the window was considered to contain motion artifacts and the corresponding OD signal was discarded and then reconstructed using the spline interpolation method. The OD signal was then filtered using a band-pass filter between 0.01 and 0.2 Hz to remove the components from the heart rate, the blood pressure and the respiratory activity. Lastly, the processed OD signal was converted into the HbO signal (Figure 1C) based on the modified Beer–Lambert law. The preprocessing was performed using the analysis program NirSpark (Danyang Huichuang Medical Equipment Co., Ltd., China).

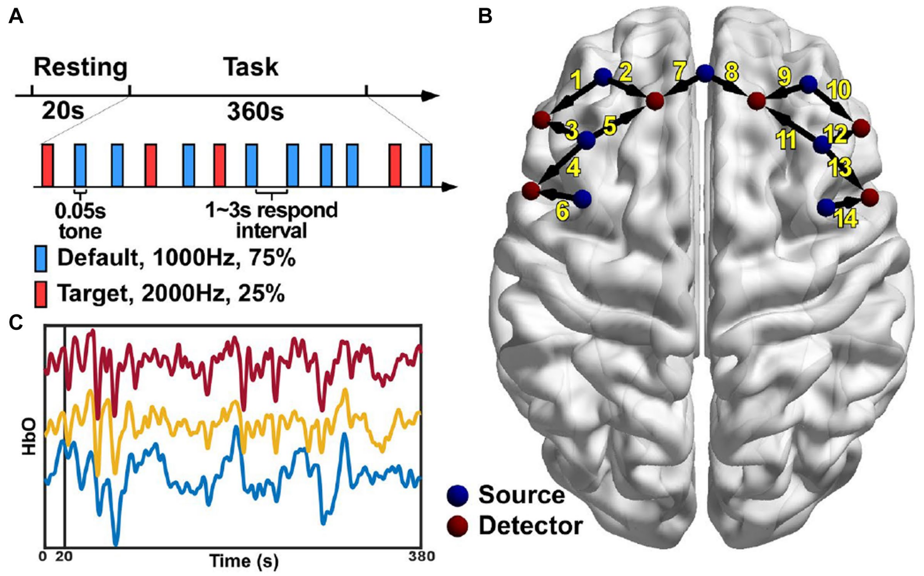

FIGURE 1
Experiment paradigm **(A)**, the locations of the 13 optodes including 7 sources and 6 detectors **(B)** and the HbO signals of three channels from a representative subject **(C)**.

2.3.2. Brain network characteristics

Pearson correlation coefficients between the HbO signals of all possible pairs of channels were calculated using the data from the task and the resting period respectively, yielding two 14 × 14 connectivity matrices for each subject. The Fisher-z transformation was then performed on the connectivity matrices. In this study, the GRETNA software (Wang et al., 2015) was used to estimate the brain network metrics according to the graph theory. Specifically, only positive connectivity was considered in this study by setting the negative matrix entries to zeros, and the connectivity matrices were then binarized using the sparsity threshold from 0.15 to 0.5 at intervals of 0.05. The threshold value was defined as the ratio of the number of retained edges divided by the maximum possible number of edges in the network. The global metrics including the small-world parameters [clustering coefficients (Cp), Gamma, Lambda, characteristic path length (Lp), Sigma], the local efficiency (Eloc), the global efficiency (Eg), the assortativity (r), and the hierarchy (b) were calculated. And the estimated nodal metrics included the nodal clustering coefficient (NCp), the nodal efficiency (Ne), the nodal local efficiency (NLe), the degree centrality (Dc), and the betweenness centrality (Bc). Since different metric values can be obtained under individual thresholds, the area under the curve (AUC) for each network metric was calculated for further analysis.

2.3.3. Classification between PSD and non-PSD patients

The diagnosis of a disease can be eventually translated into a classification problem. In this study, in order to verify whether the PSD and non-PSD patients can be distinguished using the extracted brain network characteristics, they were grouped together as the features and the cost-sensitive support vector machine (Luts et al., 2010) was used as the classifier that has been used in our previous studies (Zheng et al., 2016; Zheng and Xu, 2019). The classification accuracy defined as the ratio between the number of correctly identified patients and the total number of patients was used as the performance measurement. In order to avoid the in-sample optimization problem, the 8-fold cross-validation procedure was performed to evaluate the classification accuracy under the task and the resting condition, respectively.

2.3.4. Statistical analysis

The statistical analysis was performed using the SPSS (IBM SPSS Statistics for Windows, version 22.0, IBM Corp.). All comparison were performed between the PSD and non-PSD groups. Specifically, the demographic information was compared using the two-tail two-samples t-test for the measurement data and the Fisher's exact test for the categorical data. The connectivity strength and the brain network characteristics were compared using the one-tail two-samples t-test. The normality was verify using the Shapiro–Wilk test. If the normality was not satisfied, the Kruskal-Wallis rank sum test was then used. The significant level was set at $p < 0.05$.

3. Results

3.1. Demographic information

The basic demographic and clinical information of the recruited subjects is listed in Table 1. The statistical analysis results showed that there was no significant difference in the age, gender and the education level between the PSD and the non-PSD group. As for the stoke type, lesion location, the time after stroke onset and the available hand to press the button, there was no significant difference between the two groups either. The HAMD score of the PSD group was significantly higher than that of the non-PSD group, while the MMSE and MoCA scores that mainly reflected the cognitive state showed no significant differences.

TABLE 1 Demographic and clinical information of subjects.

	PSD	Non-PSD	*p*-value
Subject no.	19	18	–
Age (years)	65.8 ± 8.7	59.1 ± 13.6	0.077[a]
Gender (M/F)	13/6	15/3	0.447[b]
Education (≤6 years)[d]	2	0	0.486[b]
Time after onset (days)	81 (32.25–97.5)	67.5 (32–142)	0.682[c]
Manipulating hand (R/L)	12/7	8/10	0.330[b]
Stroke type (I/H)	15/4	11/7	0.295[b]
Lesion location (SC/C)	18/1	14/4	0.180[b]
MMSE score	23.1 ± 4.1	23.6 ± 4.8	0.707[a]
MoCA score	16.4 ± 5.5	18.6 ± 5.7	0.243[a]
HAMD score	15.0 (12.0–17.5)	2.5 (1.0–4.8)	0.001[c]

Values are presented as number of patients, mean ± SD, or median (Q1–Q3).
I, ischemic; H, hemorrhagic; SC, subcortex; C, cortex.
[a]T-test. [b]Fisher's exact test. [c]Kruskal-Wallis rank sum test. [d]The number of subjects with less than 6 years of education.

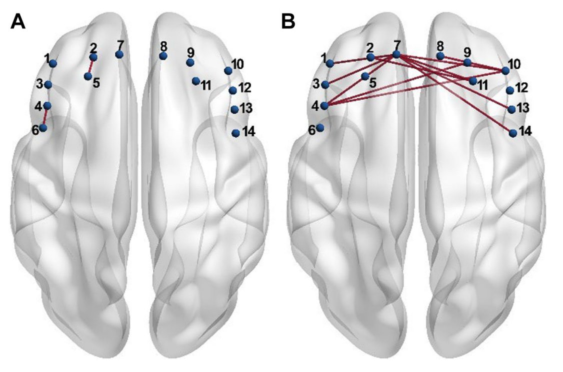

FIGURE 2
The connectivity showing significant differences between the PSD and the non-PSD groups in the resting **(A)** and the task **(B)** state, respectively.

3.2. Functional connectivity strength

Each entry in the connectivity matrix quantifies the interaction strength of the HbO signals between two brain regions covered by the two corresponding channels separately. In order to investigate whether the connectivity strength was altered by the PSD, the connectivity matrix was compared entry-by-entry between the two groups under the resting and task conditions, respectively. The statistical analysis results showed that the connectivity between channel 4 and 6, and between channel 2 and 5 for the PSD group was significantly higher than the corresponding connectivity strength for the non-PSD group in the resting state ($p < 0.05$) (Figure 2A). Compared with the resting state, more connectivity showed significant differences between the two groups in the task state (Figure 2B). In contrast to the resting state, the connectivity strength reduced significantly for the PSD group compared with the non-PSD group ($p < 0.05$). For example, the most evident difference was that the connectivity between the middle front area (channel 7) and the lateral areas (channel 1, 3, 4, 10, 11, 13, and 14) was reduced for the PSD subjects compared with the non-PSD subjects in the task state.

3.3. Brain network characteristics

3.3.1. Global metrics

The estimated global metrics including the hierarchy (b), assortativity (r), local efficiency (Eloc), and global efficiency (Eg) in the task state are compared in Figures 3A,C,E,G, respectively, between the PSD and the non-PSD group. The AUC of the four metrics across different thresholds were then estimated for individual subjects and compared between the two groups (Figures 3B,D,F,H). The results showed that the hierarchy ($p < 0.05$) and the global efficiency ($p < 0.01$) of the PSD group was significantly lower than that of the non-PSD group. On the contrary, the assortativity and the local efficiency of the PSD group were significantly higher than that of the non-PSD group ($p < 0.05$). These four metrics in the resting state were also compared between the PSD and the non-PSD group. However, none of them showed significant differences ($p > 0.05$).

Figure 4 compares the small-world properties between the PSD group and the non-PSD group in the task state. The average of the clustering coefficients (Cp), characteristic path length (Lp), Gamma, and Lambda across subjects from the PSD group was higher than that from the non-PSD group (Figures 4A,C,E,G) for all thresholds while the metric Sigma was comparable between the two groups (Figure 4I). The further statistical analysis using the two-samples *t*-test of the AUC of individual metrics showed that the metric Cp, Lp and Lambda of the PSD group was significantly higher than that of the non-PSD group ($p < 0.05$) while there was no significant differences of the metric Gamma and Sigma ($p > 0.05$). These small-world parameters in the resting state were also compared between the two groups. However, none of these small-world parameters showed significant differences between the two groups ($p > 0.05$).

3.3.2. Nodal metrics

The AUC of individual nodal metrics were fist calculated across thresholds for individual channels and individual subjects and then compared between the PSD and the non-PSD group channel-by-channel using the two-samples t-test. In the task state, the betweenness centrality (Bc) in channel 4 and 8 for the PSD group was significantly smaller compared with the non-PSD group ($p < 0.05$) (Figure 5A). The nodal efficiency (Ne) in channel 7, 8, 9, and 11 for the PSD group was also significantly reduced compared with the non-PSD group (channel 8 and 9, $p < 0.05$; channel 7 and 11, $p < 0.01$) (Figure 5C). In contrast to the above two metrics, the nodal clustering coefficient (NCp) of channel 4 and 11 (Figure 5B), and the nodal local efficiency (NLe) of channel 4 (Figure 5D) for the PSD group was significantly higher than that for the non-PSD group ($p < 0.05$).

Compared with the task state, the variation of the nodal metrics between the two groups in the restring state shows different patterns. Firstly, the betweenness centrality (Bc) showed no significant difference in either of the 14 channels. Instead, the degree centrality (Dc) of channel 10 for the PSD group was significantly lower compared with the non-PSD group ($p < 0.05$) (Figure 5E). Secondly, even though there were also significant differences of the nodal clustering coefficient (NCp), the nodal efficiency (Ne) and the nodal local efficiency (NLe) between the two groups, the channels that

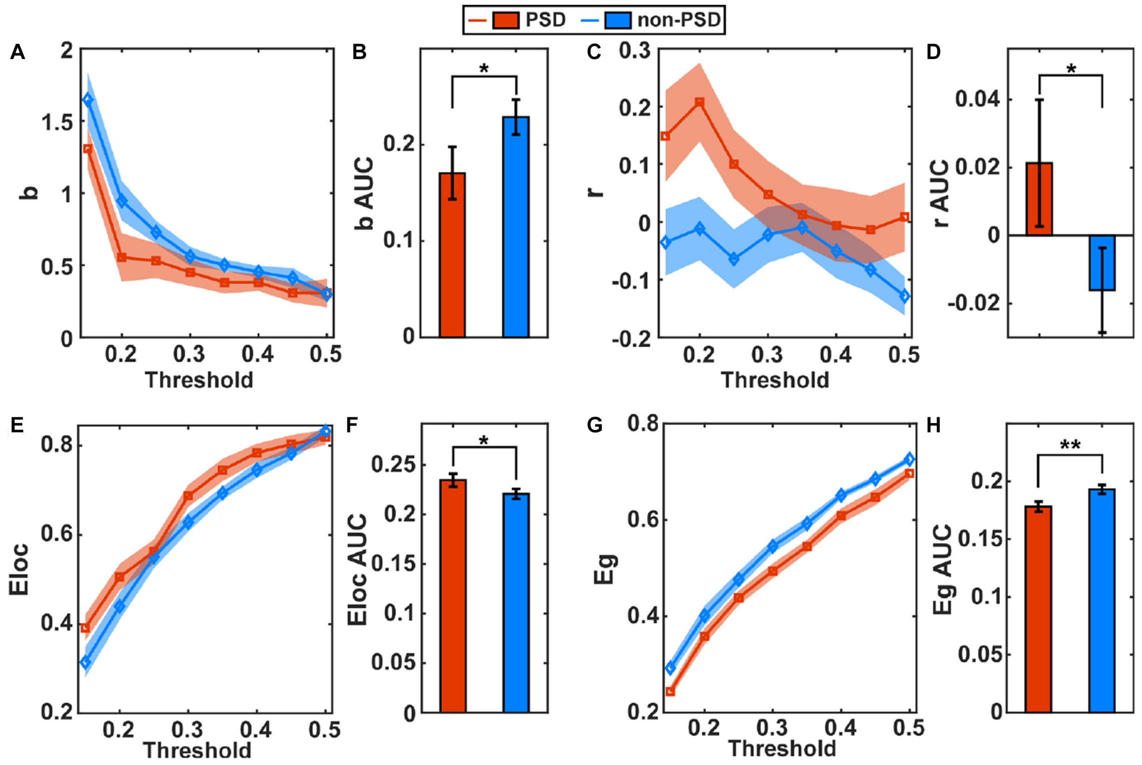

FIGURE 3
The average of the global metric hierarchy **(A)**, assortativity **(C)**, local efficiency **(E)** and global efficiency **(G)** for individual thresholds under the task condition across subjects. The shadow area represents the standard error. The comparison of the AUC of the metric hierarchy **(B)**, assortativity **(D)**, local efficiency **(F)**, and global efficiency **(H)** between the PSD and the non-PSD group. The error bars represent the standard error. $*p < 0.05$, $**p < 0.01$.

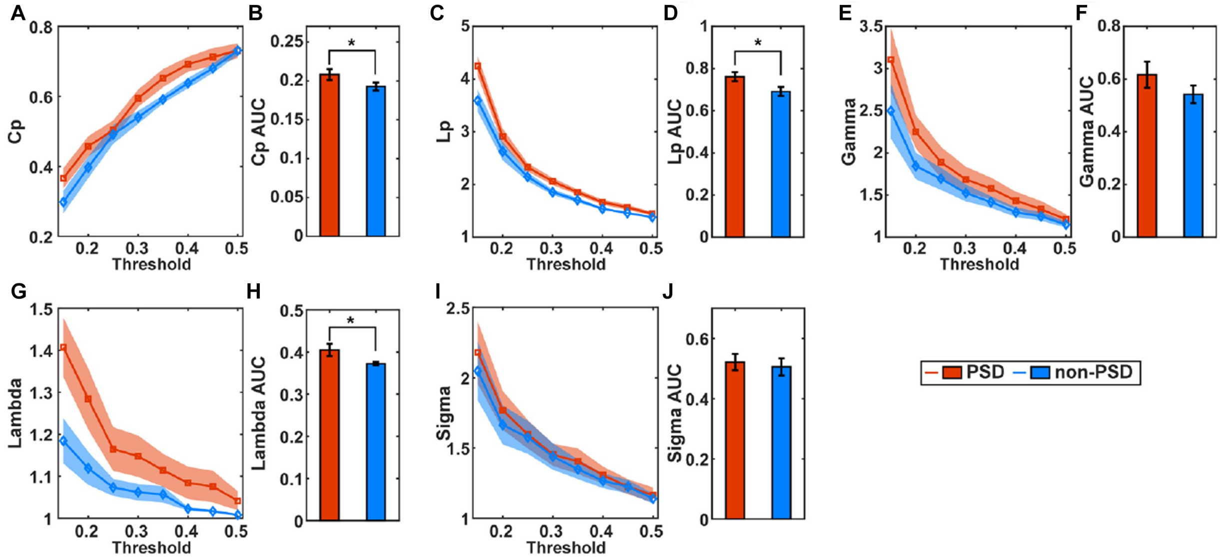

FIGURE 4
The average of the small-world parameters including the clustering coefficients (Cp), **(A)**, characteristic path length **(C)**, Gamma **(E)**, Lambda **(G),** and Sigma **(I)** for individual thresholds in the task state across subjects. The shadow area represents the standard error. The comparison of the AUC of the small-world parameters Cp **(B)**, Lp **(D)**, Gamma **(F)**, Lambda **(H),** and Sigma **(J)** between the PSD and the non-PSD group. The error bars represent the standard error. $*p < 0.05$.

showed significant differences were different from the task state. Specifically, the nodal clustering coefficient (Figure 5F) and the nodal local efficiency (Figure 5H) of channel 1, 5, and 6 for the PSD group were significantly higher compared with the non-PSD group

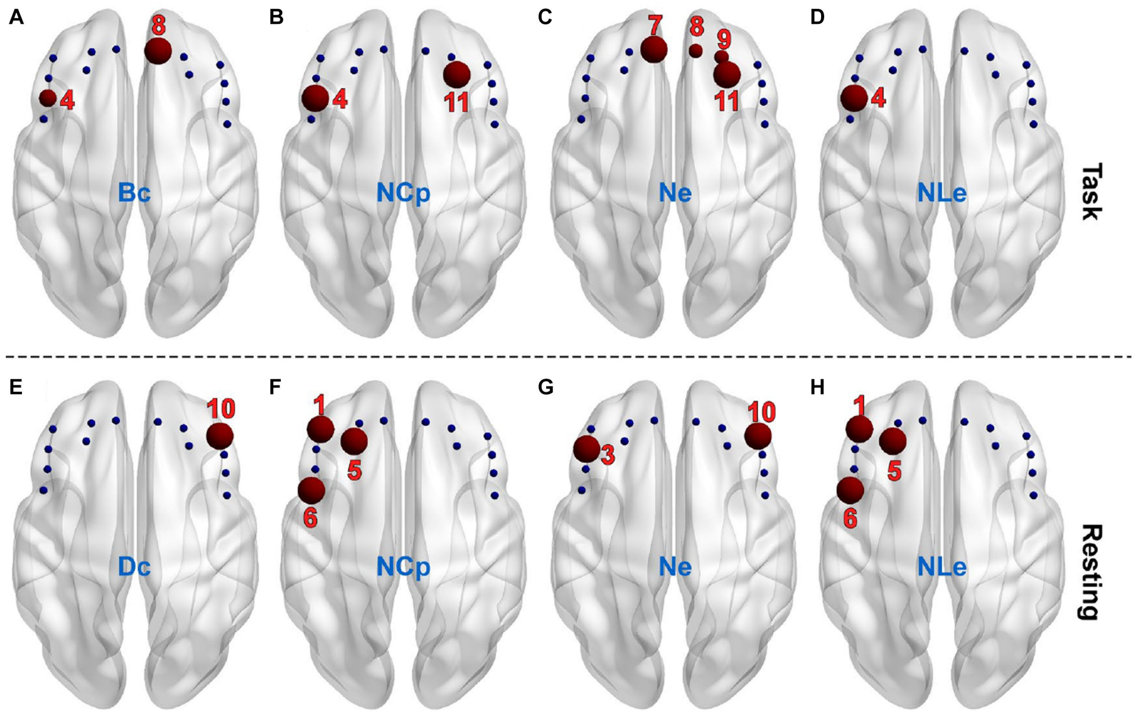

FIGURE 5
The channels (red balls) showing significant differences between the PSD and the non-PSD groups for the metric betweenness centrality **(A)**, nodal clustering coefficient **(B)**, nodal efficiency **(C)** and nodal local efficiency **(D)**, respectively in the task state. The channels showing significant differences between the PSD and the non-PSD groups for the metric degree centrality **(E)**, nodal clustering coefficient **(F)**, nodal efficiency **(G)** and nodal local efficiency **(H)**, respectively in the resting state.

($p < 0.05$), and the nodal efficiency (Figure 5G) of channel 3 and 10 for the PSD group was significantly reduced compared with the non-PSD group ($p < 0.05$).

3.3.3. Correlation with HAMD scores

In order to investigate whether the brain network characteristics can reflect the severity of depression that was quantified using the HAMD scale score, their correlation was analyzed in the task and the resting state, respectively. Specifically, the metric values and the HAMD score values from both the PSD and the non-PSD groups were combined into a single set. Then, the Spearman correlation was analyzed between the HAMD scores and the metric values. Figures 6, 7 illustrate the metrics that had a significant ($p < 0.05$) correlation with the HAMD scores in the task and the resting state, respectively. In both states, the nodal local efficiency (NLe), nodal clustering coefficient (NCp) and local efficiency (Eloc) had a positive correlation with the HAMD score. On the contrary, the metric degree centrality (Dc) and nodal efficiency (Ne) had a negative correlation with the HAMD score.

3.4. Classification

In order to verify whether the brain network characteristics can serve as the biomarkers to help the diagnosis of PSD, all the 79 (9 global metrics and 5 nodal metrics for each of 14 channels) metrics were used as the features to classify between the PSD and the non-PSD patients. Then, a feature dimension reduction procedure was performed based on the principal component analysis. The eightfold cross-validation was performed and the average classification accuracy was obtained across all folds. The cross-validation procedure was repeated 10 times and the resultant accuracy using the features in the resting and the task states are compared in Figure 8. On average, the features in the task state obtained an accuracy of 69.02% ± 3.35% while the features in the resting state only obtained an accuracy of 43.94% ± 4.47%.

4. Discussion

In this study, in order to investigate the influence of PSD on the topology of the brain functional connectivity in stroke survivors, the fNIRS signals from the left and right DLPF cortex were collected for both the PSD and non-PSD subjects during the classic oddball cognitive task and analyzed using the graph theory. To the best of our knowledge, this is the first near-infrared brain function imaging study that targeted the brain network properties under the cognitive task instead of the resting state as previous studies for the PSD patients. Our results showed that compared with the resting state, the brain network properties were more distinct between the PSD and non-PSD patients in the task state, manifested as a larger number of connectivity and network metrics showing significant differences and a resultant better classification performance between the PSD and non-PSD patients. Specifically, in the cognitive task state, the major differences of the network topography for the PSD subjects compared with the non-PSD subjects included the decreased connectivity strength, the

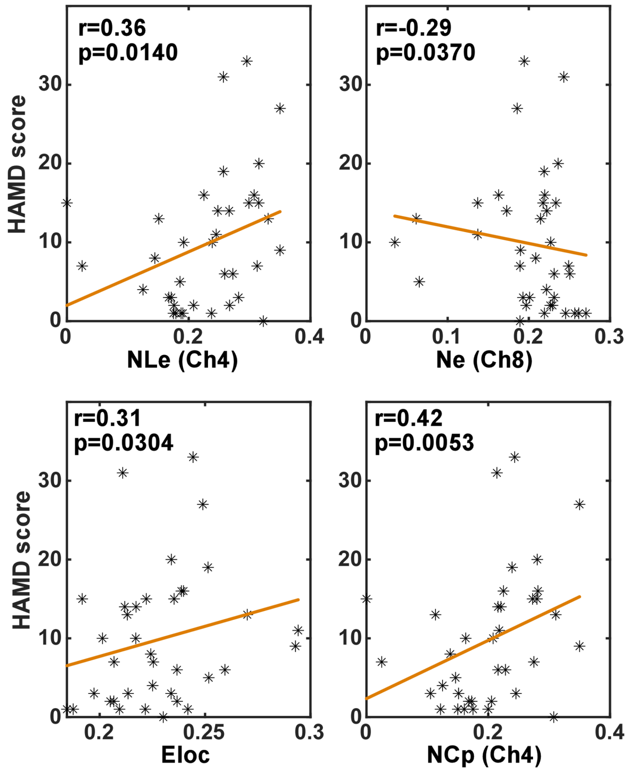

FIGURE 6
The results of the correlation analysis between the brain network characteristics and the HADM scores in the task state.

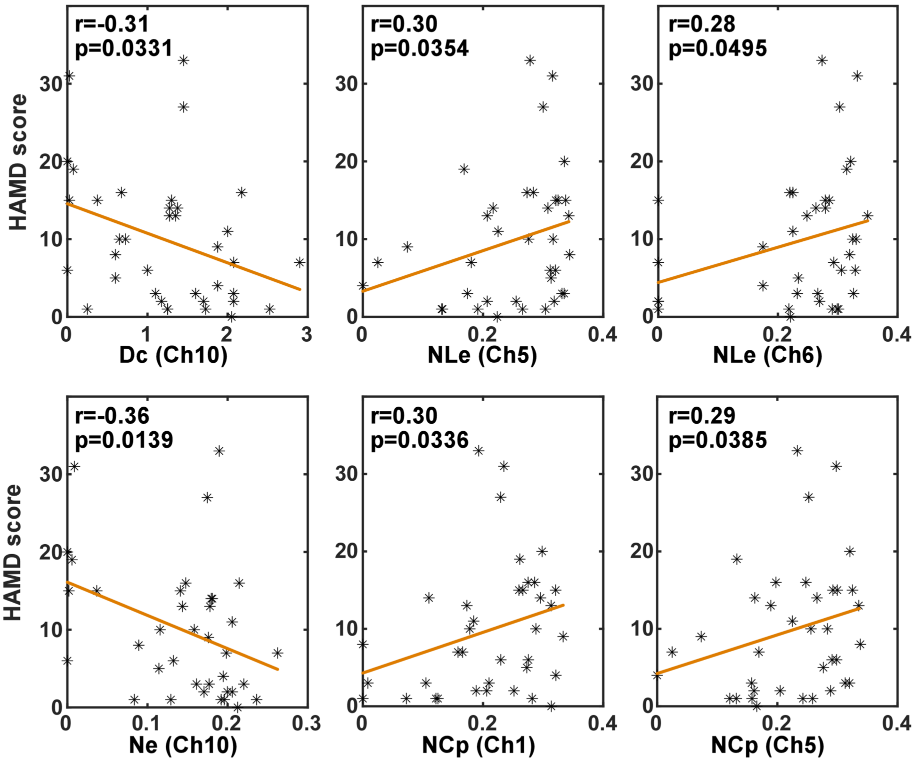

FIGURE 7
The results of the correlation analysis between the brain network characteristics and the HADM scores in the resting state.

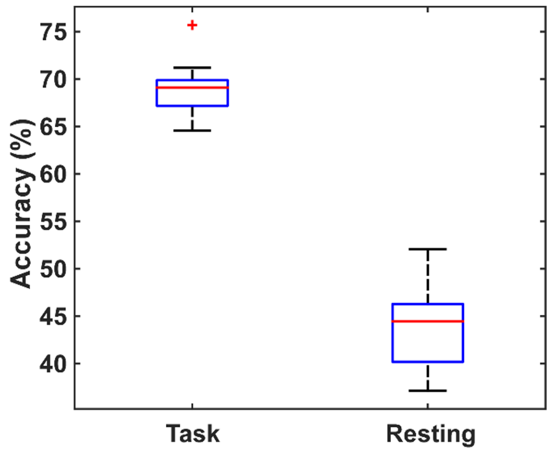

FIGURE 8
The comparison of the classification performance using the features extracted from the task state and the resting state.

reduced hierarchy (b), efficiency (Eg, Ne) and betweenness centrality (Bc), and the increased assortativity (r), local efficiency (Eloc, NLe), clustering coefficient (Cp, NCp), characteristic path length (Lp) and Lambda in the small-world property, which indicated the reduced ability of the brain network to resist attacks and transmit information, and the enhanced network flexibility. Further correlation analysis showed that some of the brain network characteristics extracted from the task state were significantly correlated with the HAMD scores. More importantly, a better classification performance can be obtained using the network characteristics in the task state (69.02 ± 3.35%) as features compared with the resting state (43.94 ± 4.47%), indicating the superiority of the brain network topography in the task state to distinguish between PSD and non-PSD patients. These findings demonstrated that the brain network properties based on the graph theory under the cognitive task might provide new insights into our understanding of PSD and new methods for the diagnosis of PSD.

Ho et al. (2015) investigated the DMN of patients with severe depression in the resting state and found that the functional connectivity between the medial prefrontal cortex and both the precuneus and the cingulate gyrus were enhanced. Moreover, for the patients with PSD in the chronic phase, researchers found that the functional connectivity in the prefrontal cortex (PFC) including the left ventromedial PFC (Zhu et al., 2012; Li et al., 2013), bilateral dorsomedial PFC (Zhu et al., 2012; Li et al., 2013) and dorsolateral PFC (Li et al., 2017) increased in the resting state. Our results showed that the brain functional connectivity in the left DLPF cortex was enhanced in the PSD patients compared with the non-PSD patients in the resting state, which is consistent with previous studies. Moreover, we found that the differences in connectivity were more pronounced in the task state than in the resting state, which is consistent with the findings of Gonzalez-Castillo and Bandettini (2018) that the differences of the functional connectivity between the resting and task states are broadly distributed in the whole brain. However, unlike the increased connectivity strength in the resting state, the connectivity strength decreased in the DLPF cortex for the PSD patients in the task state. These results indicated that the PSD patients possibly had weakened capabilities for information transmission between brain regions when performing cognitive tasks, which may be related to the decline of their cognitive function.

At present, there is no unified conclusions on the brain network characteristics of depression. Zhang et al. (2018) investigated the brain network properties using the resting-state electroencephalogram (EEG) and found that compared with the healthy controls, patients with depression had a lower clustering coefficient and characteristic path length, and a higher global efficiency. In contrast, Meng et al. (2014) using the resting-state fMRI, found that compared with the healthy individuals, the global efficiency at the whole brain level of the depression patients was reduced, while the characteristic path length was increased. The inconsistence might be caused by the fact that the EEG and fMRI signals reflect the different aspects of the brain activities due to their distinct time resolutions. In this study, we found that the clustering coefficient (Cp, NCp), the characteristic path length (Lp), and the Lambda of the PSD patients were significantly higher compared with the non-PSD patients. Meng et al. (2014) found the same changing pattern of these characteristics as ours. However, the difference in Meng's study was not significant. The possible reason was that the brain network characteristics were obtained in the task state instead of the resting state, which made the differences more obvious. It may also be cause by the fact that our research subjects were patients with PSD rather than pure depression patients. In addition, we found that the PSD patients had a higher assortative coefficient (r) and local efficiency (Eloc, NLe). Since the Sigma values were all larger than one for both the PSD and non-PSD patients in the task state (Figure 4I), it can be concluded that the brain network of both groups had small-world properties. This is consistent with the previous study that the brain network of both the depression and the healthy controls have the small-world properties (Meng et al., 2014). However, based on the variation trend of the network characteristics in the PSD patients compared with the non-PSD patients, the ability of the brain network in the PSD patients to resist attacks and integrate and transmit information was reduced. The assortativity coefficient ranging from −1 to 1 can be used to measure the network resilience (Newman, 2002). The networks with a positive assortativity coefficient are therefore likely to have a comparatively resilient core of mutually interconnected high-degree hubs (Rubinov and Sporns, 2010). If network nodes are removed from such a network or "attacked," the entire network is more likely to be destroyed. That is, the nodes in the network with a high assortativity are more closely connected, and are more vulnerable to attacks. In this study, the PSD group has a larger assortativity coefficient, which might be one of the bases for the neuropathological damage in PSD patients. The resultant inefficient transmission of information might be another neural pathogeneses of depression. The higher clustering coefficient and local efficiency reflected the enhanced local interconnectivity of the network in the PSD patients, which provided flexibility for network disruption. This topological feature may be related to the compensation mechanism of the brain in the PSD patients. Besides, the betweenness centrality and degree centrality of the PSD patients were lower than those of the non-PSD group, indicating that the centralization degree of the PSD patients was low. For the other three nodal network characteristics (NCp, NLe and Ne), the variation trend of the PSD patients compared with the non-PSD patients was the same between the resting and the task state. However, the channels with significant differences were different.

The correlation between the brain network characteristics and the HAMD scale scores was consistent in the resting and task states. That is the local efficiency (Eloc, NLe) and the clustering coefficient (NCp) was positively correlated with the HAMD score, and the global efficiency (Ne) and the degree centrality (Dc) had a negative correlation with the HAMD scores. These significant correlations indicated that the brain network characteristics can reflect the severity of PSD to some degree.

Basically speaking, the diagnosis of a disease is to identify or classify between positive and negative individuals using some biomarkers. Although potential biomarkers of a disease are often statistically significant at the population level, the discriminatory power at the individual level is often not assessed (Arbabshirani et al., 2017). In general, it is much easier to show group differences than the predictions of individual subjects, and highly significant group differences do not always equal to a satisfactory classification performance. Therefore, in the study, we used the machine learning methods to classify between the PSD and non-PSD patients, and compared the diagnostic accuracy using the extracted brain network characteristics in the resting and task states. Our results showed that the classification accuracy reached 69.02% ± 3.35% when using the network characteristics in the task state. This performance was comparable to the average accuracy of the resting-state functional connectivity research to predict other neuropsychiatric diseases (Arbabshirani et al., 2017). As a contrast, even though the same number of brain network characteristics in the resting state was used, the classification accuracy was only 43.94% ± 4.47%. The results further demonstrated that the brain network properties in the task state can be used as the potential biomarker for the diagnosis of PSD. Even though the functional brain network analysis is not currently used for diagnosis of disease, it enables us to understand the functional connectivity of human brain from the perspective of network, and the complex network theory reveals many important topological properties of human brain structures. Brain diseases can lead to the changes in the topology of brain functional networks. With the development of research methods and theories, some scholars believe that functional brain network analysis can help assist the early diagnosis of mental diseases (Wang et al., 2021). For example, Drysdale et al. analyzed the changes of brain functional network connectivity patterns in patients with depression and divided depression into four subtypes (Drysdale et al., 2017). More recently, a review stated that functional brain network imaging has been able to facilitate early diagnosis and assist in monitoring disease progression and treatment outcomes for individual patients (Matej Perovnik et al., 2023). Therefore, it is reasonable to predict that the brain functional network analysis can potentially help with the early diagnosis of brain diseases in the near future.

In this study, there were no significant differences in the age, gender, time after onset, education level, stroke type, lesion location, MMSE, and MoCA scores between the two groups, which demonstrated the homogeneity between the two groups and therefore improved the reliability of our conclusions. Although the two groups of stroke patients showed the similar degrees of brain injury, the non-PSD patients did not show the depression symptoms. This suggests that the brain injury degree may not be the determinant in the pathogenesis of PSD. Instead, other factors might be of more significance, which is consistent with recent studies (Gong and He, 2015). A recent systematic review and meta-analysis (Lu Liu et al., 2023) showed that the pooled prevalence of PSD is 27% (95% CI 25–30) at any time point after stroke, and stroke survivors with early-onset depression (within 3 months after stroke) are at high risks for remaining depressed and make up two-thirds of the incident cases during 1 year after stroke. Therefore, the inclusion criteria in this study were set to 1–12 months after stroke onset. However, the poststroke time of the recruited subjects in the end was 32.25–97.5 (Q1–Q3) days (Table 1) for the PSD subjects. This was consistent with the study showing that the pooled cumulative incidence within 1 year was 38% (95% CI 33–43), and the majority [71% (95% CI 65–76)] of cases of depression had onset during the first 3 months after stroke (Lu Liu et al., 2023). Although different clinical studies have shown the complexity of PSD prevalence and distinct trajectories of PSD for individuals, there are no studies ever tracking the brain network properties longitudinally for individual PSD patients. This might help improve our understanding of the underlying pathogenesis of PSD and would be conducted in our further study.

There were several limitations in this study. Firstly, the fNIRS signals were only collected from the dorsolateral prefrontal cortex. Although the dorsolateral prefrontal cortex is the most investigated brain area for PSD, the ventromedial prefrontal cortex, anterior cingulate gyrus, posterior cingulate gyrus/precuneus, amygdala, caudate nucleus, hippocampus, and other regions are also associated with depression. Secondly, the classification of patients in terms of lesion location is relatively rough with only two groups, i.e., lesion in cortex or subcortex. Futures studies will recruit more stroke survivors with different lesion locations and investigate the brain network properties at the whole brain level in the task state, in order to further explore the possible neural mechanism of PSD in terms of altered brain network properties.

5. Conclusion

In this study, the brain network characteristics of PSD patients in both the cognitive task and the resting state were extracted using the fNIRS signals and compared with the network characteristics of non-PSD patients. The results showed that the differences of the network characteristics between the PSD and non-PSD patients were more distinct in the task state rather than the resting state. The altered brain network properties of the PSD patients demonstrated the reduced ability of the brain network to resist attacks and transmit information, and the enhanced network flexibility. The results of the classification between PSD and non-PSD patients further demonstrated the superiority of the network characteristics extracted in the task state on revealing the altered topography of the brain functional connectivity due to PSD. These findings demonstrated the feasibility and superiority of the brain network topography in the task state to explore the neural mechanism of PSD, which provides new insights into our understanding of PSD and new methods for the diagnosis of PSD.

Data availability statement

The raw data supporting the conclusions of this article will be made available by the authors, without undue reservation.

Ethics statement

The studies involving humans were approved by the Ethics Committee of the First Affiliated Hospital of Xi'an Jiaotong

University. The studies were conducted in accordance with the local legislation and institutional requirements. The participants provided their written informed consent to participate in this study.

Author contributions

YP and YZ conceptualized the study. JG, ZY, CF, JD, and SS performed the experiment. YZ and CL analyzed the data. YP, YZ, JQ, and JW drafted the manuscript. All authors revised the manuscript and approved the final version.

Funding

This work was supported by the STI 2030—Major Projects (grant no. 2022ZD0209800), the Qin Chuang Yuan Talent Project (grant no. QCYRCXM-2022-34), and the Natural Science Foundation of Shaanxi Province (grant no. 2021JM-279).

Conflict of interest

The authors declare that the research was conducted in the absence of any commercial or financial relationships that could be construed as a potential conflict of interest.

Publisher's note

References

Arbabshirani, M. R., Plis, S., Sui, J., and Calhoun, V. D. (2017). Single subject prediction of brain disorders in neuroimaging: promises and pitfalls. *Neuroimage* 145, 137–165. doi: 10.1016/j.neuroimage.2016.02.079

Balaev, V., Orlov, I., Petrushevsky, A., and Martynova, O. (2018). Functional connectivity between salience, default mode and frontoparietal networks in post-stroke depression. *J. Affect. Disord.* 227, 554–562. doi: 10.1016/j.jad.2017.11.044

Barch, D. M., Burgess, G. C., Harms, M. P., Petersen, S. E., Schlaggar, B. L., Corbetta, M., et al. (2013). Function in the human connectome: task-fMRI and individual differences in behavior. *Neuroimage* 80, 169–189. doi: 10.1016/j.neuroimage.2013.05.033

Boes, A. D., Prasad, S., Liu, H., Liu, Q., Pascual-Leone, A., Caviness, V. S. Jr., et al. (2015). Network localization of neurological symptoms from focal brain lesions. *Brain* 138, 3061–3075. doi: 10.1093/brain/awv228

Cole, M. W., Bassett, D. S., Power, J. D., Braver, T. S., and Petersen, S. E. (2014). Intrinsic and task-evoked network architectures of the human brain. *Neuron* 83, 238–251. doi: 10.1016/j.neuron.2014.05.014

Di, X., Gohel, S., Kim, E. H., and Biswal, B. B. (2013). Task vs. rest-different network configurations between the coactivation and the resting-state brain networks. *Front. Hum. Neurosci.* 7:493. doi: 10.3389/fnhum.2013.00493

Drysdale, L. G. A. T., Downar, J., Dunlop, K., Mansouri, F., Meng, Y., Fetcho, R. N., et al. (2017). Resting-state connectivity biomarkers define neurophysiological subtypes of depression. *Nat. Med.* 23, 28–38. doi: 10.1038/nm.4246

Egorova, N., Cumming, T., Shirbin, C., Veldsman, M., Werden, E., and Brodtmann, A. (2018). Lower cognitive control network connectivity in stroke participants with depressive features. *Transl. Psychiatry* 7:4. doi: 10.1038/s41398-017-0038-x

Ferrari, M., and Quaresima, V. (2012). A brief review on the history of human functional near-infrared spectroscopy (fNIRS) development and fields of application. *NeuroImage* 63, 921–935. doi: 10.1016/j.neuroimage.2012.03.049

Foster, B. L., Rangarajan, V., Shirer, W. R., and Parvizi, J. (2015). Intrinsic and task-dependent coupling of neuronal population activity in human parietal cortex. *Neuron* 86, 578–590. doi: 10.1016/j.neuron.2015.03.018

Fusar-Poli, P., Placentino, A., Carletti, F., Landi, P., Allen, P., Surguladze, S., et al. (2009). Functional atlas of emotional faces processing: a voxel-based meta-analysis of 105 functional magnetic resonance imaging studies. *J. Psychiatry Neurosci.* 34, 418–432. doi: 10.1111/j.1365-2850.2009.01434.x

Gard, M. G., and Kring, A. M. (2007). Sex differences in the time course of emotion. *Emotion* 7, 429–437. doi: 10.1037/1528-3542.7.2.429

Gerchen, M. F., Bernal-Casas, D., and Kirsch, P. (2014). Analyzing task-dependent brain network changes by whole-brain psychophysiological interactions: a comparison to conventional analysis. *Hum. Brain Mapp.* 35, 5071–5082. doi: 10.1002/hbm.22532

Gong, Q., and He, Y. (2015). Depression, neuroimaging and connectomics: a selective overview. *Biol. Psychiatry* 77, 223–235. doi: 10.1016/j.biopsych.2014.08.009

Gonzalez-Castillo, J., and Bandettini, P. A. (2018). Task-based dynamic functional connectivity: recent findings and open questions. *Neuroimage* 180, 526–533. doi: 10.1016/j.neuroimage.2017.08.006

Guo, J., Wang, J., Sun, W., and Liu, X. (2022). The advances of post-stroke depression: 2021 update. *J. Neurol.* 269, 1236–1249. doi: 10.1007/s00415-021-10597-4

Guo, S. Q., Zhao, G. Z., Li, S. T., Yao, Q., Han, L., Li, B., et al. (2022). Moxibustion for treating patients with post-stroke depression: a systematic review and meta-analysis. *Ann Palliat Med* 11, 85–97. doi: 10.21037/apm-21-3421

Ho, T. C., Connolly, C. G., Henje Blom, E., LeWinn, K. Z., Strigo, I. A., Paulus, M. P., et al. (2015). Emotion-dependent functional connectivity of the default mode network in adolescent depression. *Biol. Psychiatry* 78, 635–646. doi: 10.1016/j.biopsych.2014.09.002

Hong, K. S., and Khan, M. J. (2017). Hybrid brain-computer Interface techniques for improved classification accuracy and increased number of commands: a review. *Front. Neurorobot.* 11:35. doi: 10.3389/fnbot.2017.00035

Jenkins, L. M., Kendall, A. D., Kassel, M. T., Patron, V. G., Gowins, J. R., Dion, C., et al. (2018). Considering sex differences clarifies the effects of depression on facial emotion processing during fMRI. *J. Affect. Disord.* 225, 129–136. doi: 10.1016/j.jad.2017.08.027

Kaufmann, T., Alnaes, D., Brandt, C. L., Doan, N. T., Kauppi, K., Bettella, F., et al. (2017). Task modulations and clinical manifestations in the brain functional connectome in 1615 fMRI datasets. *Neuroimage* 147, 243–252. doi: 10.1016/j.neuroimage.2016.11.073

Klawohn, J., Santopetro, N. J., Meyer, A., and Hajcak, G. (2020). Reduced P300 in depression: evidence from a flanker task and impact on ERN, CRN, and Pe. *Psychophysiology* 57:e13520. doi: 10.1111/psyp.13520

Koyanagi, M., Yamada, M., Higashi, T., Mitsunaga, W., Moriuchi, T., and Tsujihata, M. (2021). The usefulness of functional near-infrared spectroscopy for the assessment of post-stroke depression. *Front. Hum. Neurosci.* 15:680847. doi: 10.3389/fnhum.2021.680847

Krienen, F. M., Yeo, B. T., and Buckner, R. L. (2014). Reconfigurable task-dependent functional coupling modes cluster around a core functional architecture. *Philos. Trans. R. Soc. Lond. Ser. B Biol. Sci.* 369:20130526. doi: 10.1098/rstb.2013.0526

Li, B., Liu, L., Friston, K. J., Shen, H., Wang, L., Zeng, L. L., et al. (2013). A treatment-resistant default mode subnetwork in major depression. *Biol. Psychiatry* 74, 48–54. doi: 10.1016/j.biopsych.2012.11.007

Li, H., Zhou, H., Yang, Y., Wang, H., and Zhong, N. (2017). More randomized and resilient in the topological properties of functional brain networks in patients with major depressive disorder. *J. Clin. Neurosci.* 44, 274–278. doi: 10.1016/j.jocn.2017.06.037

Lu Liu, M. X., Marshall, I. J., Wolfe, C. D. A., Wang, Y., and O'Connell, M. D. L. (2023). Prevalence and natural history of depression after stroke: a systematic review and meta-analysis of observational studies. *PLoS Med.* 20:e1004200. doi: 10.1371/journal.pmed.1004200

Luts, J., Ojeda, F., Van de Plas, R., De Moor, B., Van Huffel, S., and Suykens, J. A. (2010). A tutorial on support vector machine-based methods for classification problems in chemometrics. *Anal. Chim. Acta* 665, 129–145. doi: 10.1016/j.aca.2010.03.030

Matej Perovnik, T. R., Schindlbeck, K. A., and Eidelberg, D. (2023). Functional brain networks in the evaluation of patients with neurodegenerative disorders. *Nat. Rev. Neurol.* 19, 73–90. doi: 10.1038/s41582-022-00753-3

Meng, C., Brandl, F., Tahmasian, M., Shao, J., Manoliu, A., Scherr, M., et al. (2014). Aberrant topology of striatum's connectivity is associated with the number of episodes in depression. *Brain* 137, 598–609. doi: 10.1093/brain/awt290

Newman, M. E. J. (2002). Assortative mixing in networks. *Phys. Rev. Focus* 89:208701. doi: 10.1103/PhysRevLett.89.208701

Paolucci, S. (2017). Advances in antidepressants for treating post-stroke depression. *Expert. Opin. Pharmacother.* 18, 1011–1017. doi: 10.1080/14656566.2017.1334765

Polich, J. (2007). Updating P300: an integrative theory of P3a and P3b. *Clin. Neurophysiol.* 118, 2128–2148. doi: 10.1016/j.clinph.2007.04.019

Power, J. D., Fair, D. A., Schlaggar, B. L., and Petersen, S. E. (2010). The development of human functional brain networks. *Neuron* 67, 735–748. doi: 10.1016/j.neuron.2010.08.017

Rubinov, M., and Sporns, O. (2010). Complex network measures of brain connectivity: uses and interpretations. *Neuroimage* 52, 1059–1069. doi: 10.1016/j.neuroimage.2009.10.003

Shi, Y., Zeng, Y., Wu, L., Liu, W., Liu, Z., Zhang, S., et al. (2017). A study of the brain abnormalities of post-stroke depression in frontal lobe lesion. *Sci. Rep.* 7:13203. doi: 10.1038/s41598-017-13681-w

Shin, M., Sohn, M. K., Lee, J., Kim, D. Y., Shin, Y. I., Oh, G. J., et al. (2022). Post-stroke depression and cognitive aging: a multicenter, prospective cohort study. *J. Pers. Med.* 12:389. doi: 10.3390/jpm12030389

Taylor-Rowan, M., Momoh, O., Ayerbe, L., Evans, J. J., Stott, D. J., and Quinn, T. J. (2019). Prevalence of pre-stroke depression and its association with post-stroke depression: a systematic review and meta-analysis. *Psychol. Med.* 49, 685–696. doi: 10.1017/S0033291718002003

van Dinteren, R., Arns, M., Jongsma, M. L., and Kessels, R. P. (2014). Combined frontal and parietal P300 amplitudes indicate compensated cognitive processing across the lifespan. *Front. Aging Neurosci.* 6:294. doi: 10.3389/fnagi.2014.00294

Wang, Z., and Wang, R. (2014). Energy distribution property and energy coding of a structural neural network. *Front. Comput. Neurosci.* 8:14. doi: 10.3389/fncom.2014.00014

Wang, J., Wang, X., Xia, M., Liao, X., Evans, A., and He, Y. (2015). Corrigendum: GRETNA: a graph theoretical network analysis toolbox for imaging connectomics. *Front. Hum. Neurosci.* 9:458. doi: 10.3389/fnhum.2015.00458

Wang, Z., Xin, J., Wang, Z., Yao, Y., Zhao, Y., and Qian, W. (2021). Brain functional network modeling and analysis based on fMRI: a systematic review. *Cogn. Neurodyn.* 15, 389–403. doi: 10.1007/s11571-020-09630-5

Zhang, H., Benz, H. L., Bezerianos, A., Acharya, S., Crone, N. E., Maybhate, A., et al. (2010). Connectivity mapping of the human ECoG during a motor task with a time-varying dynamic Bayesian network. *Annu. Int. Conf. IEEE Eng. Med. Biol. Soc.* 2010, 130–133. doi: 10.1109/IEMBS.2010.5627179

Zhang, X. F., He, X., Wu, L., Liu, C. J., and Wu, W. (2019). Altered functional connectivity of amygdala with the Fronto-limbic-striatal circuit in temporal lobe lesion as a proposed mechanism for poststroke depression. *Am. J. Phys. Med. Rehabil.* 98, 303–310. doi: 10.1097/PHM.0000000000001081

Zhang, M., Zhou, H., Liu, L., Feng, L., Yang, J., Wang, G., et al. (2018). Randomized EEG functional brain networks in major depressive disorders with greater resilience and lower rich-club coefficient. *Clin. Neurophysiol.* 129, 743–758. doi: 10.1016/j.clinph.2018.01.017

Zheng, Y., Wang, G., and Wang, J. (2016). Is using threshold-crossing method and single type of features sufficient to achieve realistic application of seizure prediction? *Clin. EEG Neurosci.* 47, 305–316. doi: 10.1177/1550059415588658

Zheng, Y., and Xu, G. (2019). Quantifying mode mixing and leakage in multivariate empirical mode decomposition and application in motor imagery-based brain-computer interface system. *Med. Biol. Eng. Comput.* 57, 1297–1311. doi: 10.1007/s11517-019-01960-9

Zhu, X., Wang, X., Xiao, J., Liao, J., Zhong, M., Wang, W., et al. (2012). Evidence of a dissociation pattern in resting-state default mode network connectivity in first-episode, treatment-naive major depression patients. *Biol. Psychiatry* 71, 611–617. doi: 10.1016/j.biopsych.2011.10.035

frontiers | Frontiers in Neuroscience

TYPE Original Research
PUBLISHED 19 October 2023
DOI 10.3389/fnins.2023.1252732

Comparative analysis of group information-guided independent component analysis and independent vector analysis for assessing brain functional network characteristics in autism spectrum disorder

Junlin Jing[1], Benjamin Klugah-Brown[1]*, Shiyu Xia[1], Min Sheng[1] and Bharat B. Biswal[1,2]*

[1]The Clinical Hospital of Chengdu Brain Science Institute, MOE Key Laboratory for Neuroinformation, School of Life Science and Technology, University of Electronic Science and Technology of China, Chengdu, China, [2]Department of Biomedical Engineering, New Jersey Institute of Technology, Newark, NJ, United States

Introduction: Group information-guided independent component analysis (GIG-ICA) and independent vector analysis (IVA) are two methods that improve estimation of subject-specific independent components in neuroimaging studies. These methods have shown better performance than traditional group independent component analysis (GICA) with respect to intersubject variability (ISV).

Methods: In this study, we compared the patterns of community structure, spatial variance, and prediction performance of GIG-ICA and IVA-GL, respectively. The dataset was obtained from the publicly available Autism Brain Imaging Data Exchange (ABIDE) database, comprising 75 healthy controls (HC) and 102 Autism Spectrum Disorder (ASD) participants. The greedy rule was used to match components from IVA-GL and GIG-ICA in order to compare the similarities between the two methods.

Results: Robust correspondence was observed between the two methods the following networks: cerebellum network (CRN; $|r| = 0.7813$), default mode network (DMN; $|r| = 0.7263$), self-reference network (SRN; $|r| = 0.7818$), ventral attention network (VAN; $|r| = 0.7574$), and visual network (VSN; $|r| = 0.7503$). Additionally, the Sensorimotor Network demonstrated the highest similarity between IVA-GL and GIG-ICA (SOM: $|r| = 0.8125$). Our findings revealed a significant difference in the number of modules identified by the two methods (HC: $p < 0.001$; ASD: $p < 0.001$). GIG-ICA identified significant differences in FNC between HC and ASD compared to IVA-GL. However, in correlation analysis, IVA-GL identified a statistically negative correlation between FNC of ASD and the social total subscore of the classic Autism Diagnostic Observation Schedule (ADOS: pi = −0.26, $p = 0.0489$). Moreover, both methods demonstrated similar prediction performances on age within specific networks, as indicated by GIG-ICA-CRN ($R^2 = 0.91$, RMSE = 3.05) and IVA-VAN ($R^2 = 0.87$, RMSE = 3.21).

Conclusion: In summary, IVA-GL demonstrated lower modularity, suggesting greater sensitivity in estimating networks with higher intersubject variability. The improved age prediction of cerebellar-attention networks underscores their importance in the developmental progression of ASD. Overall, IVA-GL may be

EDITED BY
Takao Yamasaki,
Minkodo Minohara Hospital, Japan

REVIEWED BY
Tanu Wadhera,
Indian Institute of Information Technology, Una, India
Zhi-An Huang,
City University of Hong Kong, Hong Kong SAR, China
Junjie Zheng,
Affiliated Brain Hospital of Nanjing Medical University, China

*CORRESPONDENCE
Benjamin Klugah-Brown
✉ bklugah@gmail.com
Bharat B. Biswal
✉ bbiswal@gmail.com

RECEIVED 04 July 2023
ACCEPTED 02 October 2023
PUBLISHED 19 October 2023

CITATION
Jing J, Klugah-Brown B, Xia S, Sheng M and Biswal BB (2023) Comparative analysis of group information-guided independent component analysis and independent vector analysis for assessing brain functional network characteristics in autism spectrum disorder. *Front. Neurosci.* 17:1252732.
doi: 10.3389/fnins.2023.1252732

appropriate for investigating disorders with greater variability, while GIG-ICA identifies functional networks with distinct modularity patterns.

KEYWORDS

autism spectrum disorder, resting-state fMRI, intersubject variability, functional network connectivity, prediction

1. Introduction

Autism spectrum disorder (ASD) is a neurodevelopmental disorder that affects social communication and interaction and causes restricted, repetitive behaviors and interests. It is characterized by a diverse range of symptoms and severity levels, and its underlying causes are not yet fully understood. With the advancement of neuroimaging techniques, such as Electroencephalogram (EEG) and functional magnetic resonance imaging (fMRI), researchers have been able to gain new insights into the neural mechanisms of ASD. There are several studies that have proved the effectiveness of network hierarchical structure in ASD brain function using EEG data (Wadhera and Mahmud, 2022; 2023). Studies utilizing fMRI have revealed several brain regions and networks that exhibit atypical functioning in individuals with ASD, including the social brain network, default mode network, and mirror neuron system. Additionally, researchers have explored the functional network connectivity between different brain regions and how this connectivity may be disrupted in ASD.

Numerous fMRI studies have explored the neural underpinnings of ASD and have revealed changes in brain function and connectivity in various regions, including the prefrontal cortex, amygdala, and cerebellum. For instance (Kleinhans et al., 2008) found reduced prefrontal cortex activity during a social judgment task in children with ASD, indicating that this region may be crucial to social cognition impairments in ASD. Another study (Shukla et al., 2011) observed increased amygdala activity in response to emotional faces in children with ASD, indicating altered emotional processing. A recent review (Rafiee et al., 2022) the authors summarized the latest ASD developments on tasks and resting states. For instance, Lawrence et al. (2020) found more activity in lateral frontal cortex and insula activity compared to HC, indicating that these regions may be crucial to social reward in ASD. Another study Rausch et al. (2016) showed significantly reduced connectivity in visuospatial and superior parietal areas in ASD, supporting underconnectivity theory of autism. Although fMRI has yielded valuable insights into the neural basis of ASD and may help with its diagnosis and treatment, further research is necessary to fully comprehend the underlying neural mechanisms of ASD and their role in the disorder's development and progression.

There are a number of data-driven methods that are widely used for analyzing resting-state fMRI. Seed-based analysis is a method in which a voxel from a specific region of interest (ROI) is correlated with every voxel in the brain. This method has been used to identify functional connectivity networks in the brain (Biswal et al., 1995; Greicius et al., 2003). Machine learning is a statistical approach that can be used to learn from data and make predictions. It has been used in a growing number of ASD studies (Liu et al., 2021; Santana et al., 2022) to classify and predict brain disorders from fMRI data (Zhuang et al., 2018; Wang et al., 2022; Kunda et al., 2023).

Independent component analysis (ICA) (Mckeown et al., 1998; Damoiseaux et al., 2006) is a data driven method that has been widely used to identify and analyze brain networks. This approach of decomposing fMRI data into a linear mixture of independent components (ICs) allows researchers to identify components that are subsequently grouped as brain functional networks. Moreover, spatial ICA [sICA (Mckeown et al., 1998; Jafri et al., 2008)] has become a popular method (spatial dimension is higher than temporal dimension) accounting for spatial coherence to uncover spatially distributed data such as fMRI images and useful for identifying brain networks involved in resting-state functional connectivity. Nonetheless, temporal ICA (tICA) has also performed strongly in blind source separation (Biswal and Ulmer, 1999; Calhoun et al., 2001a; Smith et al., 2012).

Although ICA is widely used to analyze fMRI data, it has several limitations. Among these challenges is the need to modify the algorithm to account for the unique properties of fMRI data, such as high dimensionality, temporal autocorrelation, and noise properties. Model selection is also a critical factor in fMRI data analysis with ICA. Unlike other methods, the number of components to be extracted from the data is unknown *a priori* and must be estimated from the data. Various techniques can be used to determine the optimal number of components, including cross-validation, bootstrap resampling, and information criteria. Furthermore, interpretation of the results of ICA in fMRI studies requires expertise in neuroanatomy, cognitive neuroscience, and statistics. ICA can reveal complex patterns of neural activity that may be difficult to interpret without a deep understanding of brain function and organization. Finally, because fMRI studies typically involve multiple subjects, group-level analysis is required to identify common patterns of brain activity across individuals.

Group ICA (GICA) (Calhoun et al., 2001b; Svensén et al., 2002; Beckmann et al., 2009) is a variant of ICA specifically designed to identify common components in a group of subjects. The GICA is accomplished by applying the algorithm to decompose the fMRI data into independent components that are consistent across the group. In a commonly used implementation, a two-step approach is used in which each subject's data is first decomposed into independent components before being combined into a group level. In an alternative approach, all subjects' data is decomposed simultaneously using a single step. One of the strengths of GICA is its ability to reveal unique group-level functional networks that may not be easily visible in individual subjects. In addition, it can increase statistical power by pooling data from different subjects and reducing the effects of noise. Although GICA allows for the direct correlation of ICs between individuals in a group, it fails to capture intersubject variabilities (ISV). To address the ISV limitation of GICA, group information-guided independent component analysis (GIG-ICA) (Du and Fan, 2013; Du et al., 2016) and independent vector analysis (IVA) (Lee et al., 2008) were proposed.

IVA is a technique that maximizes both the independence between related components and the dependency between components of different subjects (Lee et al., 2008). IVA is achieved without the use of a back reconstruction phase by simultaneously calculating and optimizing ICs for each subject. This facilitates the computation of ICs at the group level and the interpretation of the relationship between ICs at the group and individual levels. Furthermore, IVA-GL (Lee et al., 2008; Anderson et al., 2012), an advanced version of IVA, can separate time-delayed and convolved signals using the Gaussian density model (IVA-G) and the Laplace density model (IVA-L) based on higher-order frequency dependencies. Previous studies (Dea et al., 2011; Michael et al., 2014) showed that IVA-GL outperformed GICA in capturing ISV in simulated fMRI data.

GIG-ICA is another technique that can obtain precise subject-specific functional networks by optimizing the independence of multiple components and improving the correspondence between each group-level IC and its associated subject-specific IC. The resulting subject-specific networks generated from the identified ICs have comparable physiological meanings, allowing for comparisons between subjects. Several studies have applied GIG-ICA to investigate functional networks in neurological diseases (Du et al., 2014, 2015, 2017; Zhi et al., 2018; Fattahi et al., 2021). These results imply that GIG-ICA can provide accurate subject-specific functional networks that are similar across participants and have physiological significance.

The advantages of GIG-ICA and IVA-GL over traditional GICA have been demonstrated in several studies (Ma et al., 2013; Michael et al., 2014; Du et al., 2016). For a comparative analysis, it was found that IVA-GL outperformed GIG-ICA in terms of identifying subject-specific signal sources as well as higher ISV though GIG-ICA detected a more stable modularity structure of FNC in healthy subjects (Du et al., 2017). Besides, IVA-GL has also been demonstrated in capturing variability, in disease subjects such as schizophrenia (Gopal et al., 2016).

In this study, we hypothesized that GIG-ICA and IVA-GL will show different brain network properties. To examine this, we compared the patterns of community structures of the FNC using features obtained from a case-control group comprising of ASD and HC. Additionally, we examined the differences in variance between the two methods to identify abnormal functional networks derived from the two groups. Finally, although network component features can be obtained from both GIG-ICA and IVA-GL to the best of our knowledge no studies have compared the prediction performance of both methods, here we used component features to predict age and WASI (three measures of IQ), respectively.

2. Methods and materials

This study obtained fMRI data from a publicly available Autism Brain Imaging Data Exchange (ABIDE) database (Di Martino et al., 2014). For the following analysis and prediction, we used 75 ASD patients and 102 healthy controls with ages ranging from 6.5 to 39.1 years old, scanned at New York University Langone Medical Center. ASD subjects were included based on the autism criteria in Diagnostic and Statistical Manual of Mental Disorders, 4th Edition, Text Revision (DSM-IV-TR) (American Psychiatric Association, 2000). Additionally, these subjects were acquired with a 3-T Siemens Allegra scanner. The main parameters of functional images for the resting-state are as follows: repetition time (TR)/Echo time (TE) = 2000/15 ms, flip angle = 90°, number of slices = 33, slice thickness = 4 mm, and voxel size = $3.0 \times 3.0 \times 4.0\,\text{mm}^3$. T1-weighted images were acquired with the following parameters: TR/TE = 2530/3.25 ms, flip angle = 7°, slice thickness = 1.33 mm, and voxel size = $1.3 \times 1.0 \times 1.3\,\text{mm}^3$. More details on the subject collection, exclusion criteria, and data parameters can be obtained from the website.[1]

2.1. Data preprocessing

We utilized Statistical Parametric Mapping 12 (SPM12) software[2] and Data Processing Assistant for Resting-State fMRI[3] to preprocess the T1-weighted images and rs-fMRI data, respectively. To preprocess the functional imaging, we took the following steps: (1) first ten time points were discarded to ensure stable magnetic resonance imaging signals at the beginning of the scan; (2) we performed head motion correction using rigid-body translation and rotation and then excluded subjects with a maximum motion greater than 3 mm or 3°; (3) trilinear interpolation with degrees of freedom was used to coregister the anatomical images with mean functional image; (4) we used the DARTEL algorithm to segment the T1-weighted image of each subject and obtained GM, WM, and CSF; (5) to reduce the residual effects of motion and other non-neuronal factors, we performed regression of the interference signal, including 24 head motion parameters, signals of WM and cerebrospinal fluid (CSF); (6) the rs-fMRI images were normalized from native space to the Montreal Neurological Institute (MNI) space with a voxel size of $3 \times 3 \times 3\,\text{mm}^3$; (7) all normalized images were smoothed with an 8 mm full width at half maximum Gaussian kernel (FWHM).

2.2. Networks component estimation

We used IVA-GL and GIG-ICA to estimate components for analysis in this work. They can be available in Group ICA for fMRI toolbox (GIFT).[4] Specifically, the main procedure steps of IVA-GL (Adali et al., 2014; Michael et al., 2014) are as follows: (1) performing subject-level PCA to each subject; (2) applying IVA-GL to estimate the SMs and TCs on each subject's data. For GIG-ICA (Du et al., 2017), there are mainly five steps: (1) performing subject-level PCA on each subject; (2) using group-level PCA on subject-level PCA data of the temporal concatenation; (3) applying Infomax algorithm (Bell and Sejnowski, 1995) on reduced data to obtain group ICs; (4) identifying and removing artifact group components, and then computing individual components using remaining non-artifact group ICs (Du et al., 2016); (5) estimating individual TCs. The estimated components are z-scored on IVA-GL and GIG-ICA after completing all steps.

To obtain the statistical threshold of components of the two methods and to reduce the noise of estimation, z-scored t-test maps were computed using the MANCOVAN toolbox for ASD and HC. Next, the correspondence of components was performed using the greedy rule between IVA-GL and GIG-ICA. The paired correlation matrix were implemented and then we choose valid

---

[1] http://fcon_1000.projects.nitrc.org/indi/abide/abide_I.html

[2] http://www.fil.ion.ucl.ac.uk/spm/software/spm12

[3] http://rfmri.org/DPARSF

[4] https://trendscenter.org/software/

ICs from the matrix by checking whether the correlation value is greater than the set threshold. Finally, after excluding the mismatched networks, we selected the common resting-state networks across both methods and named them based on the Automated Anatomical Labeling (AAL) atlas (Tzourio-Mazoyer et al., 2002). The higher-order and lower-order networks were then organized for subsequent analysis.

2.3. Functional network connectivity and its modularity analysis

To explore the potential differences in community structure between the two techniques, we employed the Brain Connectivity Toolbox (BCT[5]) to calculate modularity measures of the FNC matrix. First, we generated subject-specific FNC matrices by calculating Pearson correlation coefficients between the time courses (TCs) of paired networks, followed by computing the mean FNC matrix across ASD subjects. To enhance the efficiency of our analysis, we applied Fisher's r-to-z transformation to the original functional weight matrix. We utilized the Louvain algorithm, a modular community detection algorithm known for its efficiency and effectiveness (Blondel et al., 2008), to identify the hierarchical community structure and to determine the modularity Q value using the Girvan–Newman model (Girvan and Newman, 2002; Newman and Girvan, 2004), which reflects the quality of the community structure. A higher Q value represents a more stable modular structure. The modular segmentation results and corresponding Q value were used to analyze the FNC matrix. Finally, we performed a permutation test to calculate the group differences in module measures.

We used a two-sample t-test to examine the statistical difference of FNC, and the results were FDR corrected. This analysis helped determine if the two methods could capture FNC differences between ASD and HC. Additionally, we calculated the relationship between FNC and clinical measures using paired components of TCs. To consider both linear and nonlinear information, we employed a boosted method that leverages nonlinear information to enhance the linear effect (Motlaghian et al., 2022). The definition of the boosted method is as follows:

$$\mathrm{PC} + sign(\mathrm{PC}) \times \mathrm{NMI}$$

Where PC represents Pearson correlation and NMI represents normalized mutual information. In this case, the FNC matrix regressed the influence of gender, age and handedness scores. We have removed subjects that had abnormal or missing clinical measures. The Mahalanobis distance from the bivariate mean of the resampled data was used to identify and remove outliers from the data set (Samuel Schwarzkopf et al., 2012). Then, Shepherd's pi correlation was applied to the data after outlier removal to measure the correlation between the two variables (Samuel Schwarzkopf et al., 2012).

2.4. Estimating spatial differences

Differences in the spatial statistics between ASD and HC based on two methods, IVA-GL and GIG-ICA, were assessed using three aspects. Initially, a cluster-level two-sample t-test was conducted on z-score maps to determine differences in weighted amplitude between the two groups. The results were corrected for multiple comparisons using FDR correction. Based on the significant spatial differences in pairing components between the two methods, we also displayed the histogram of amplitude values using the voxel with the most remarkable difference for each subject. This allowed us to obtain the distribution differences between the two groups. Secondly, we calculated voxelwise differences in variance maps by subtracting the variance between groups (HCs – ASDs) for each component. Finally, since the variance distribution across voxels was non-normal between subjects, a nonparametric test was utilized to identify differences in variance maps for each component between ASDs and HCs. These statistical analyses enable the identification of not only the differences in mean and variance between ASD and HC but also the IVA-GL and GIG-ICA's characteristics in capturing variability. We also expected to discover significant differences between ASD and HC using these two methods. For instance, IVA-GL can reveal the variability of some networks, but GIG-ICA cannot, and vice versa.

2.5. Predictive model

Feature selection: to reduce the original spatial feature dimension of 54,263, we applied feature selection based on the CPM model (Shen et al., 2017), which considers the correlation between the connectivity matrix and behavioral measure. However, we used a stricter threshold value of $p < 0.001$ to determine the relationship between the original spatial networks and behavioral measures. This process resulted in obtaining a different number of voxels for each network associated with demographic variables (age and IQ), which were subsequently used for prediction.

LASSO model: the LASSO penalty regression is a linear model that is commonly used to estimate sparse coefficients (Friedman, 2010). This regression technique helps to prevent overfitting by applying a penalty function to compress the coefficients of variables. Mathematically, the minimized objective function of LASSO regression is:

$$\min_{\omega} \frac{1}{2N} \| X\omega - y \|_2^2 + \alpha \|\omega\|_1$$

Where N is the sample size, α is a constant, and ω is the coefficient vector. The whole training and prediction process was completed based on LassoCV package of sklearn in Python. Specifically, we performed a two-layer loop, with the outer loop using a leave-one-out cross-validation (LOOCV) and the inner loop using 10-fold cross-validations. In each outer loop, the optimal α value was found through the inner loop.

We employed a permutation test to assess the efficacy of our model in predicting target values, by generating an empirical null distribution to evaluate the correlation between predicted and target values. As the two datasets were not normally distributed, we utilized

---

[5] https://sites.google.com/site/bctnet/

TABLE 1 Demographics and clinical characteristics of subjects.

	HC ($N = 105$)	ASD ($N = 79$)	p-value
Gender (M/F)	65/10	76/26	0.047[a]
Age (mean ± SD)	14.84 ± 7.00	15.86 ± 6.33	0.311[b]
Handedness scores (mean ± SD)	40.65 ± 51.54	65.26 ± 27.51	0.000**[b]
FIQ (mean ± SD)	107.49 ± 16.45	113.23 ± 13.09	0.011*[b]
VIQ (mean ± SD)	105.44 ± 15.91	113.09 ± 12.33	0.001*[b]
PIQ (mean ± SD)	107.16 ± 20.70	110.25 ± 13.79	0.236[b]

HC, healthy control; ASD, autism spectrum disorders; M, male; F, female; FIQ, full intelligence quotient; VIQ, verbal intelligence quotient; PIQ, performance intelligence quotient (FIQ, VIQ, and PIQ are measured by Wechsler Abbreviated Scales of Intelligence; WASI). * represents the $p < 0.05$ and ** represents the $p < 0.001$.

[a] Chi-square.

[b] Two-sample t test.

Spearman's rank correlation for the permutation test, which involved rearranging the order of two independent samples 1,000 times. To evaluate our results, we also utilized root mean squared error (RMSE), a widely used metric for assessing predictions. Notably, RMSE provided a more meaningful understanding of the actual deviation, while the fixed range of correlation values made it easier to observe. Additionally, we employed the determination coefficient R^2 to reflect the regression fitting effect of the prediction model.

3. Results

Table 1 displays the demographic information of all subjects used in this study. There were relatively no significant age differences between the two groups ($p = 0.311$).

3.1. Spatial component selection and pairing

The analysis in IVA-GL and GIG-ICA used a relatively high model order of IC = 50, which has been previously demonstrated to produce reliable intrinsic component networks (ICNs) (Abou-Elseoud et al., 2010). To identify nonartifactual group components, a sorting procedure was combined with visual inspection, and fractional amplitude of low-frequency fluctuations (fALFF) and dynamic range were examined for all components. In these spectral measurements, the greater the value of the independent component representing the brain network, the lower the value of the noise component (Allen et al., 2012; Gopal et al., 2016). Finally, we only selected components with fALFF greater than 0.5 for further analysis.

Two different pairing strategies were used: (1) all components with an absolute correlation coefficient ($|r|$) greater than 0.5 were utilized for functional network connectivity (FNC) analysis and spatial differences analysis in group mean; (2) for the one-to-many case, the spatial components of IVA-GL were paired with those of GIG-ICA using high correlation coefficients, and the resulting components were used for difference analysis in variance maps of HCs and individuals with ASDs. Several networks and their corresponding correlation coefficients were obtained, including the Auditory network (AUD: $|r| = 0.6161$), Cerebellum network (CRN: $|r| = 0.7813$), Dorsal attention network (DAN: $|r| = 0.6479$), Default mode network (DMN: $|r| = 0.7263$), Motor network (MTN: $|r| = 0.6887$), Salience network (SN: $|r| = 0.6787$), Sensorimotor network (SOM: $|r| = 0.8125$), Self-reference network (SRN: $|r| = 0.7818$), Ventral attention network (VAN: $|r| = 0.7574$), and Visual network (VSN: $|r| = 0.7503$). The SOM network had the highest similarity between IVA-GL and GIG-ICA.

3.2. FNC and modularity analysis

The mean FNC matrix calculation of GIG-ICA and IVA-GL involves different numbers of matching components, which are 22 and 18, respectively. GIG-ICA exhibits stronger connection strength within the very crucial VSN network (please refer to meta-analytic database previous studies[6]), as shown in Figures 1A,D, with a maximum connection strength of 0.8, while IVA-GL only detects a maximum of 0.4. As shown in Figures 1B,E, GIG-ICA detected five and four modularities in HC and ASD, respectively. The five modules in HC identified by GIG-ICA mainly comprised of the basic function network (CRN) in module 1, low-order networks (DAN, MTN, SOM) in module 2, high-order networks (DMN) in module 3, interconnected networks (AUD, DMN, SN, SRN, VAN) in module 4 and VSN in module 5. For ASD, the four modules detected by GIG-ICA included CRN in module 1, DAN, DMN, MTN, and SOM in module 2, AUD, DMN, SN, SRN, and VAN in module 3, and VSN in module 4. On the other hand, IVA-GL detected two modularities in HC, including AUD, CRN, DMN, SN, and SRN in module 1 and CRN, DAN, DMN, MTN, SOM, VAN, and VSN in module 2. In ASD, IVA-GL detected three modularities, including AUD, CRN, DMN, SN, and SRN in module 1, DAN, DMN, MTN, SOM, and VAN in module 2, and CRN and VSN in module 3. Although GIG-ICA had a slightly higher Q value than IVA-GL (GIG-ICA: HC = 0.27, ASD = 0.29; IVA-GL: HC = 0.26, ASD = 0.25), the differences were small, and only provided global results.

To further explore the group differences in modules between GIG-ICA and IVA-GL, we conducted a permutation test (10,000 iterations, $p < 0.05$) for within-method and between-method comparison, as presented in Table 2. Our analysis revealed no significant differences in modularity measures between HC and ASD for both GIG-ICA and IVA-GL. Furthermore, the global modularity

---

[6] https://neuroquery.org/

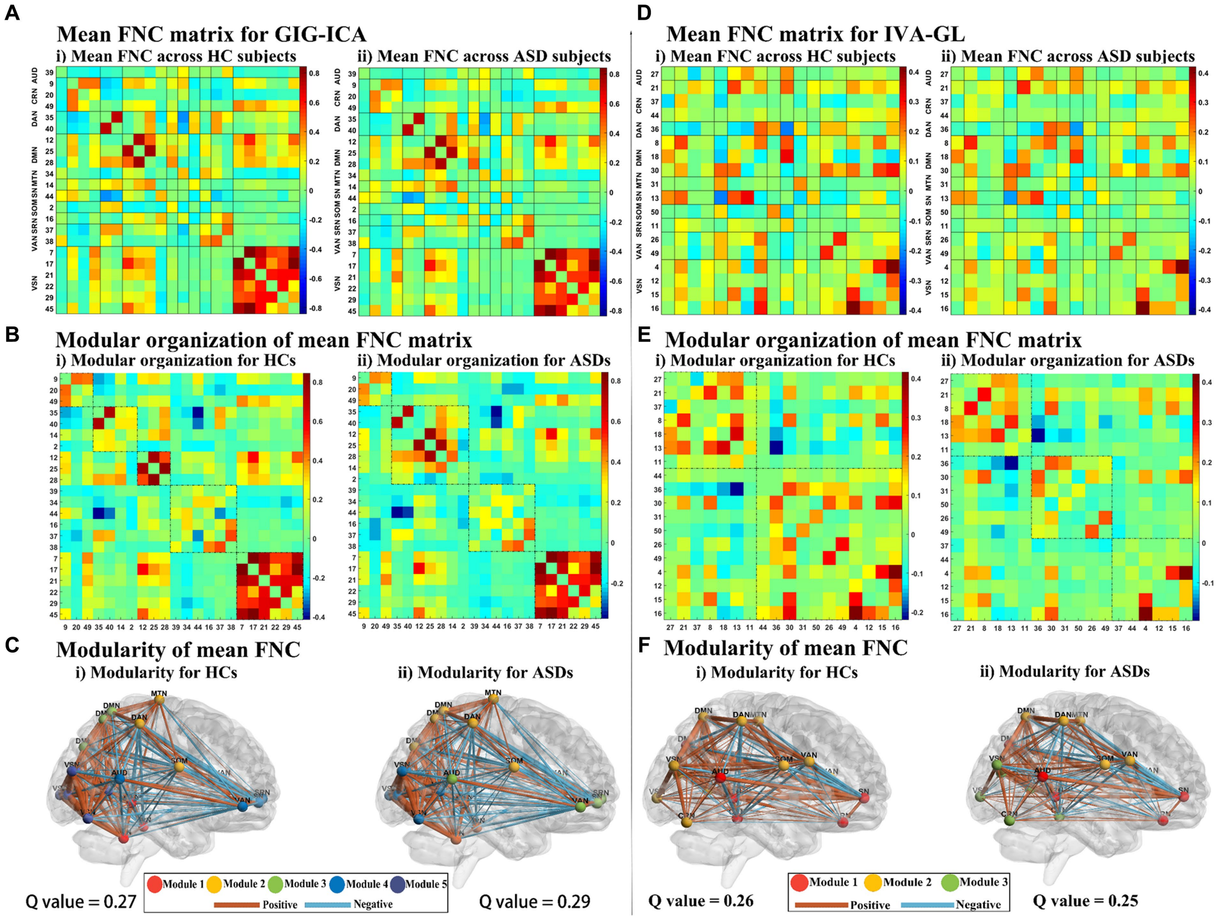

FIGURE 1
The mean FNC matrix of GIG-ICA and IVA-GL and their modularity results. **(A)** FNC correlation (averaged over ASD subjects). (i) and (ii) Show the functional network connectivity of pairing components for HC and ASD, respectively. On the left side of the FNC matrix are networks and their corresponding components, and the right side of the FNC matrix is the color bar, which represents the size of the correlation. **(B)** Modular organization of mean FNC matrix from GIG-ICA in HC and ASD. The dotted line in the matrix divides the network connectivity into multiple modules. **(C)** Modularity of the mean FNC from GIG-ICA in HC and ASD. The intrinsic networks of the modules and their functional connections were drawn in different colors, in which the thickness of the functional connections represents the connection strength. Similarly, **(D–F)** were the IVA-GL metrics corresponding to GIG-ICA.

TABLE 2 Group differences in modularity measures for GIG-ICA and IVA-GL.

	Modularity measures	HC mean (±std)	ASD mean (±std)	*p*-value
Within-method				
GIG-ICA	Global modularity *Q*	0.28 (±0.03)	0.28 (±0.04)	0.74
	Number of modules	3.28 (±0.58)	3.30 (±0.63)	0.71
IVA-GL	Global modularity *Q*	0.27 (±0.05)	0.27 (±0.06)	0.82
	Number of modules	2.95 (±0.61)	2.84 (±0.52)	0.15
Between-method	**Group**	**Methods**		***p*-value**
Global modularity *Q*	HC	GIG-ICA (0.28 (±0.03))	IVA-GL (0.27 (±0.05))	0.07
	ASD	IVA-GL (0.27 (±0.06))	GIG-ICA (0.28 (±0.04))	0.18
Number of modules	HC	GIG-ICA (3.28 (±0.58))	IVA-GL (2.95 (±0.61))	<0.001**
	ASD	IVA-GL (2.84 (±0.52))	GIG-ICA (3.30 (±0.63))	<0.001**

Q of GIG-ICA was not significantly different from that of IVA-GL in HC and ASD. However, we did observe significant differences in the number of modules between GIG-ICA and IVA-GL in both ASD and HC.

In Figure 2A, it was observed that GIG-ICA successfully detected significant FNC effects of HC – ASD with $p < 0.05$ and FDR correction, whereas IVA did not. GIG-ICA was able to identify differences in functional connections between VAN, CRN, AUD, SRN, and SN,

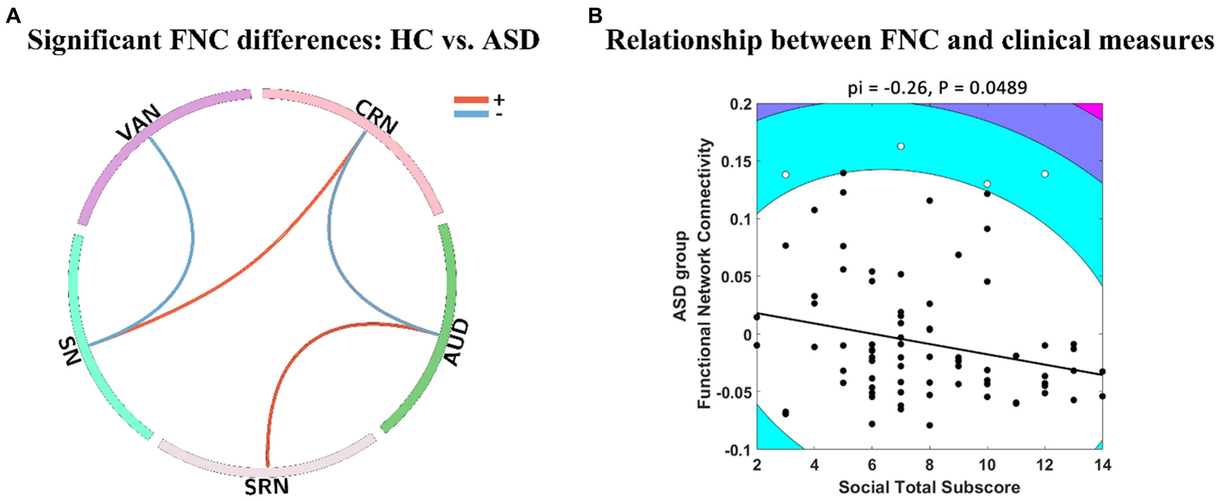

FIGURE 2
FNC analysis differences between GIG-ICA and IVA-GL. **(A)** Panel A shows significant FNC differences between HC and ASD ($p < 0.05$) using two-sample t-test in GIG-ICA. The line in the ring represents some significant FNC differences, where positive values indicate that HC is greater than ASD and vice versa. **(B)** Panel B illustrates negative relationship between group FNC across ASD and social total subscore of the classic ADOS in IVA-GL. The contour lines in the Shepherd's pi correlation map indicate the bootstrapped Mahalanobis distance from the bivariate mean of the resampled data. The black points represent the data included in the correlation analysis and the white points represent the outliers excluded from Shepherd's pi correlation analysis. The solid line represents the linear regression of the data after outlier removal and pi means Spearman correlation values after outlier removal. ADOS, autism diagnostic observation schedule.

where SN and CRN, SRN and AUD showed positive intensity (HC > ASD). Similarly, SN and VAN, AUD, and CRN showed negative intensity (ASD > HC). On the other hand, IVA-GL demonstrated that the mean FNC values in the ASD group were negatively correlated with the social total subscore of the classic Autism Diagnostic Observation Schedule (ADOS, which serves as a standard for diagnosing ASD), as presented in Figure 2B, while GIG-ICA did not find any significant relationship (pi = 0.18, $p = 0.2511$). However, our findings demonstrated significant FNC differences between HC and ASD. The IVA-GL showed a statistically negative correlation between the FNC of ASD and the ADOS. To summarize, GIG-ICA and IVA-GL had a complementary effect on the results of FNC statistical analysis.

3.3. Spatial statistical analysis

We utilized a two-sample t-test ($p < 0.05$) with FDR correction to compute spatial differences of mean, using z-scores t maps of nonartifact and paired components (Figure 3A). Results showed that GIG-ICA had significantly higher amplitudes and larger cluster size than IVA-GL, including CRN, DMN, SN, and VSN, respectively. Although GIG-ICA detected more activated areas, IVA-GL was better at identifying more important brain regions, such as the cerebellum. Significant components were matched between GIG-ICA and IVA-GL (DMN: $r = 0.6586$, SN: $r = 0.6787$) in Figure 3B. IVA-GL revealed both positive and negative DMN regions, while GIG-ICA only showed positive regions with a slight fluctuation range. On the other hand, GIG-ICA displayed a more prominent activation intensity in SN, different from IVA-GL. A histogram in Figure 3C showed the differences in weighted amplitudes of four components between HC and ASD of GIG-ICA and IVA-GL on the network, respectively, which included DMN and SN. Most voxels across subjects on SN had amplitude values between 1 and 2, while those of DMN was between 0 and 1, indicating that SN had more activities than DMN. The difference in DMN in Figure 3C was mainly evident in the distribution of ASD, while SN was concentrated in HC. These results provide significant insights into the neuroanatomy of autism.

Table 3 revealed that GIG-ICA detected more voxels compared to IVA-GL. The two-sample t-test p-values for each component at the voxel of maximum difference are as follows: SN of GIG-ICA: t-test $p\text{-value} = 6.79 \times 10^{-12}$ (HC < ASD); SN of IVA-GL: t-test $p\text{-value} = 1.65 \times 10^{-06}$ (HC < ASD); DMN of GIG-ICA: t-test $p\text{-value} = 2.36 \times 10^{-06}$ (HC > ASD); DMN of IVA-GL: t-test $p\text{-value} = 2.83 \times 10^{-06}$ (HC > ASD). The number of voxels showed significant changes after uncorrected and FDR correction, especially in DMN, with at least one cluster surviving correction. Given this situation, the uncorrected results were also presented in Table 3.

In addition, using the mean gray matter across subjects (Figure 4), a corresponding mask was created to calculate the spatial difference of variance maps based on the visual network. As anticipated, IVA-GL captured more variability than GIG-ICA, and ASD exhibited higher variance than HC, a noteworthy phenomenon. The findings suggest that autism is associated with a more intricate brain network activity than control.

A nonparametric test for variance differences between individuals with ASD and HC was conducted, examining the mean variance maps for all pairing components. In Figure 5, negative logarithm values of p and significant levels were shown, with blue and red dots representing IVA-GL and GIG-ICA, respectively. The third (CRN) and fourth (DAN) columns differed particularly between the two methods, especially in CRN. The majority of networks showed significant differences (ASD > HC), except for DMN (GIG-ICA: IC = 34, $p\text{-value} = 0.000$; IVA-GL:

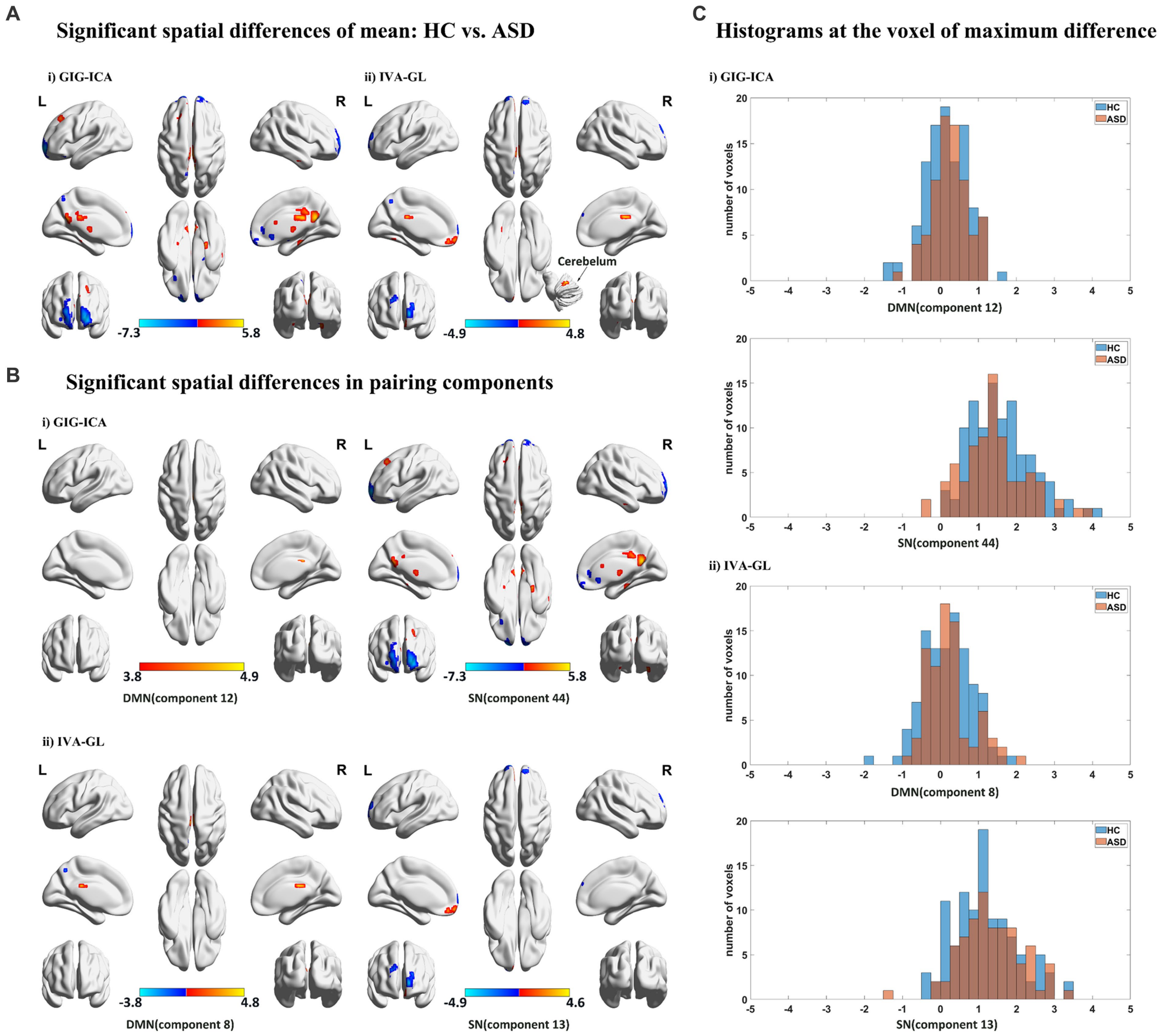

FIGURE 3
Spatial statistical analysis in mean based on GIG-ICA and IVA-GL. **(A)** Significant spatial effect ($p < 0.05$). Two sample t-test and FDR correction were performed and multi perspective spatial map was displayed. **(B)** Significant components of networks in HC vs. ASD ($p < 0.05$). Here are some statistically significant components, which are paired components in GIG-ICA and IVA-GL. **(C)** Histograms across subjects at cluster peak with significant difference, which come from the components with mean differences.

TABLE 3 Two-sample *t*-test for voxelwise group differences in the mean, based on matching components between GIG-ICA and IVA-GL.

Method	Matching components	Peak Foci/*T*-value	*p*-values (Unc)	NOV	*p*-values (Cor.)	NOV
GIG-ICA	44 (SN)	(−18, 57, −3)/−7.3418	0.015	872	0.006	592
	12 (DMN)	(3, −30, 24)/4.8750	0.019	251	0.000	23
IVA-GL	13 (SN)	(−18, 57, 3)/−4.9548	0.016	328	0.002	124
	8 (DMN)	(3, −21, 24)/4.8343	0.017	202	0.000	12

Unc, uncorrected; Cor, FDR-corrected; NOV, number of voxels.

IC = 18, p-value = 0.002) and VSN (GIG-ICA: IC = 22, p-value = 0.000; IVA-GL: IC = 12, p-value < 0.001). Overall, these results indicate that individuals with autism exhibit significantly higher variance than those without in CRN, DMN, VAN, and VSN.

3.4. Comparison of prediction for IVA-GL and GIG-ICA

The feature selection process was used to determine the number of voxels for each spatial network. The feature sizes for both methods'

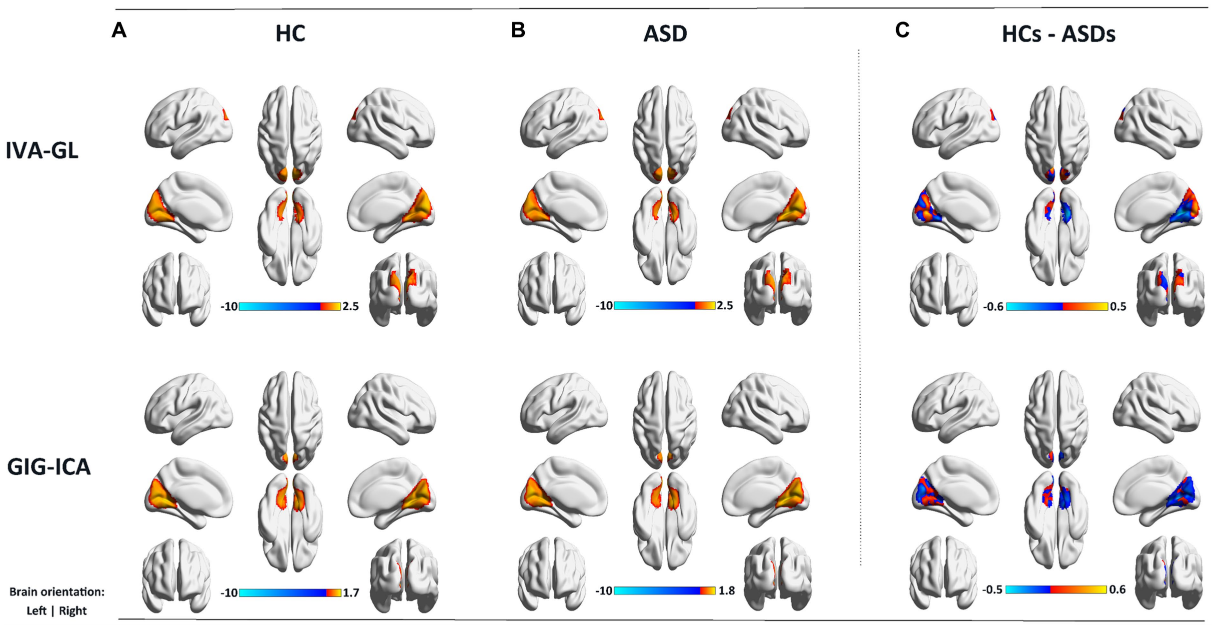

FIGURE 4
Variance maps for controls **(A)** and patients **(B)** as well as the difference **(C)** in the variance maps (HCs − ASDs) for visual network (VSN) for both IVA-GL and GIG-ICA.

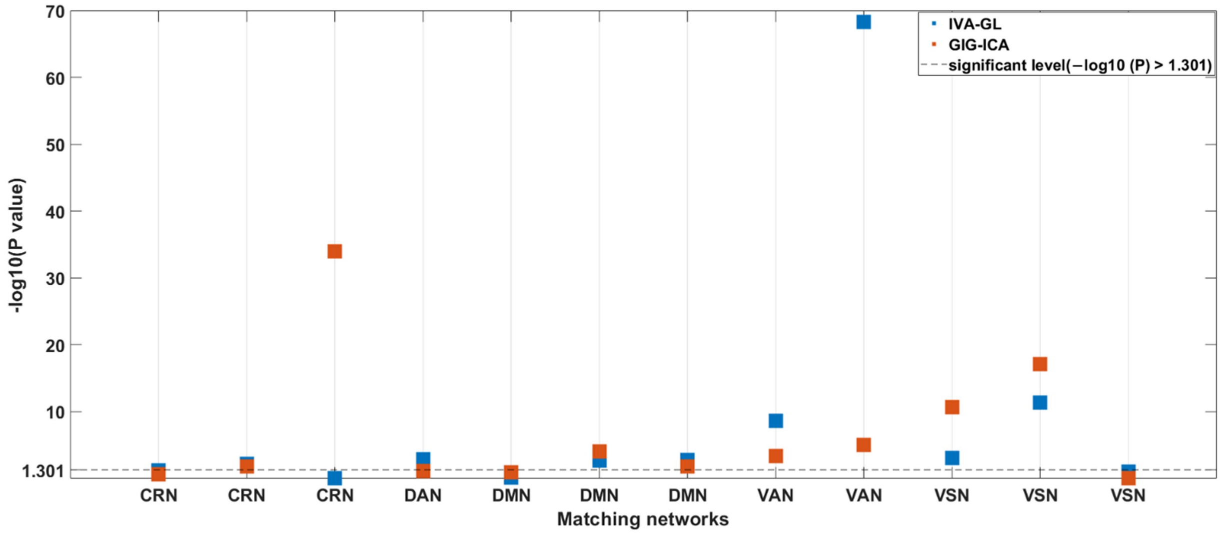

FIGURE 5
p-values for nonparametric test for difference in variance maps of HCs and ASDs for all matching components between two methods.

best-performing networks for predicting age were listed (GIG-ICA: CRN = 471; IVA-GL: VAN = 622); additional networks can be found in the Supplementary material. In terms of the determination coefficient R^2 in Table 4, the GIG-ICA method had better model fitting performance compared to IVA-GL. Permutation tests were used to calculate the correlation coefficient and *p*-values to evaluate the prediction results, and a regression plot between the predicted and observed values was shown in Figure 6. The root-mean-square error (RMSE) values for IVA-GL and GIG-ICA were also displayed in Table 4, with the smallest RMSE for IVA-GL in VAN and GIG-ICA in CRN. Notably, our results indicated which network is most suitable for predicting age using these two methods. Additionally, a paired *t*-test was conducted to detect any differences in prediction values

TABLE 4 **Comparison of GIG-ICA and IVA-GL in prediction performance.**

Method	Network	R^2	RMSE
GIG-ICA	CRN	0.91	3.05
IVA-GL	VAN	0.87	3.21

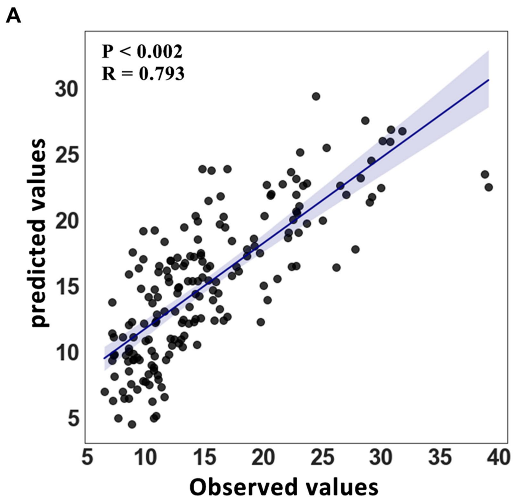

FIGURE 6
Regression model for age with 95% confidence interval. **(A)** Linear scatter plot between predicted value and observed value in VAN of IVA-GL. **(B)** A graph similar to IVA-GL for GIG-ICA's CRN.

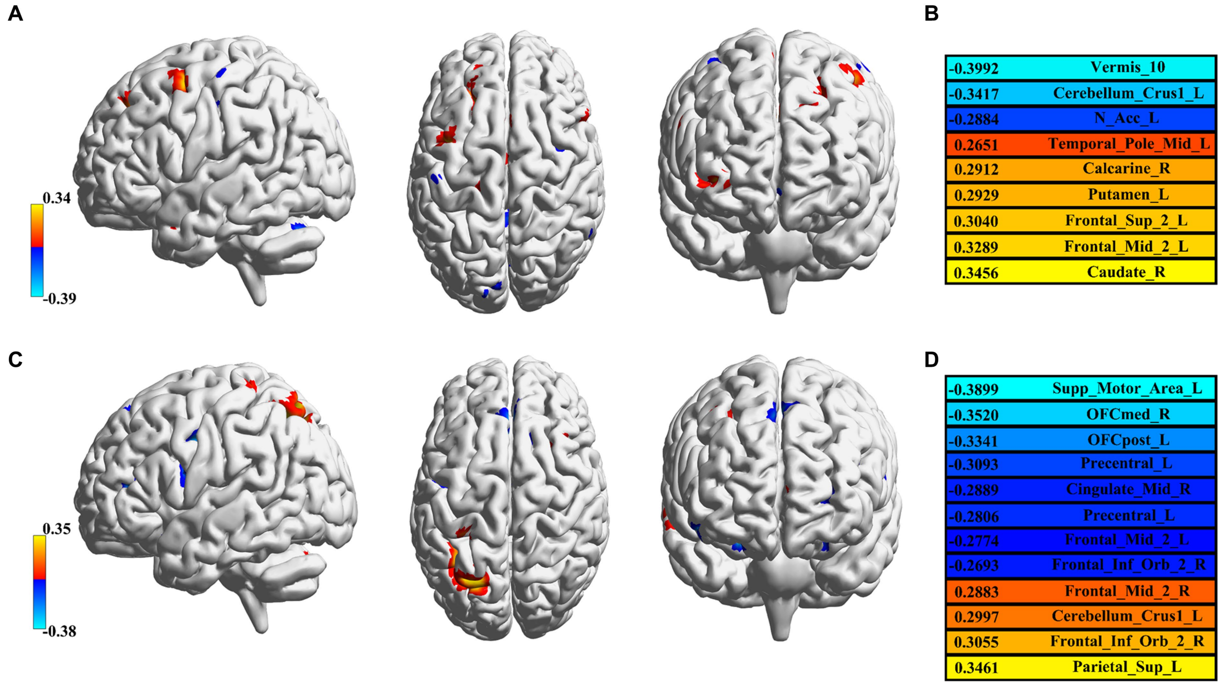

-0.3992	Vermis_10
-0.3417	Cerebellum_Crus1_L
-0.2884	N_Acc_L
0.2651	Temporal_Pole_Mid_L
0.2912	Calcarine_R
0.2929	Putamen_L
0.3040	Frontal_Sup_2_L
0.3289	Frontal_Mid_2_L
0.3456	Caudate_R

-0.3899	Supp_Motor_Area_L
-0.3520	OFCmed_R
-0.3341	OFCpost_L
-0.3093	Precentral_L
-0.2889	Cingulate_Mid_R
-0.2806	Precentral_L
-0.2774	Frontal_Mid_2_L
-0.2693	Frontal_Inf_Orb_2_R
0.2883	Frontal_Mid_2_R
0.2997	Cerebellum_Crus1_L
0.3055	Frontal_Inf_Orb_2_R
0.3461	Parietal_Sup_L

FIGURE 7
Feature visualization in GIG-ICA and IVA-GL. **(A)** CRN in GIG-ICA and its corresponding brain regions. **(B)** The list of detailed brain regions for GIG-ICA. **(C)** Corresponding brain regions for VAN in IVA-GL. **(D)** The list of detailed brain regions for IVA-GL. All brain regions are labeled according to the AAL atlas with each color in C and D corresponding to correlation values.

between IVA-GL and GIG-ICA, but the results showed no significant difference ($t = -0.09$, p-value = 0.92). The performance of all networks can be found in the Supplementary Table S1. To aid visualization, we presented brain maps in Figure 7 that displayed regions within the CRN and VAN that provided the most effective features for prediction.

However, compared to age, the three IQ measures might not be reliable predictors. For FIQ and VIQ, GIG-ICA outperforms IVA-GL (FIQ (RMSE: GIG-ICA-DMN = 7.22; IVA-CRN = 8.44); VIQ (RMSE: GIG-ICA-DMN = 7.66; IVA-VSN = 7.70)). However, for PIQ, IVA-GL surpasses GIG-ICA (RMSE: GIG-ICA-SOM = 8.99; IVA-VSN = 8.71). Additional details on these results are provided in Supplementary Table S1.

4. Discussion

This study investigated the potential differences between GIG-ICA and IVA-GL using resting-state data in ASD and HC. The study mainly focused on FNC measures (i.e., global modularity), spatial network differences (i.e., variance maps), and prediction performance (i.e., RMSE). We found that GIG-ICA and IVA-GL have different strengths when analyzing brain networks in HC and ASD. GIG-ICA can detect more regions and higher amplitudes, while IVA-GL is better at identifying abnormal brain regions in ASD. Both methods are equally effective at calculating the difference in variance maps between HC and ASD and demonstrated a complementary relationship in FNC analysis. Although GIG-ICA has better predictive performance, there was no significant statistical difference between the two methods.

4.1. FNC strengths and global modularity *Q*

The FNC strengths and global modularity *Q* in GIG-ICA were greater than those of IVA-GL. These findings align with a previous study (Du et al., 2017) that reported similar metrics in the HC dataset. However, we conducted additional statistical analyses to determine significant differences in the number of modules and global modularity *Q* within and between the two methods. We found no significant difference in the number of modules or global modularity *Q* between HC and ASD for within-method comparison. This contrasts with previous study in children (5–10 years) with ASD (Sigar et al., 2023), which found a significant difference. Given the wider age range (7.1–39.1 years) in our study, we speculate that there may be differences in the number of modules and global modularity *Q* between adult and child groups.

Regarding the between-method, we found significant differences in the number of modules between GIG-ICA and IVA-GL, regardless of HC or ASD. Given that GIG-ICA identifies more modules than IVA-GL, this result suggests that brain functional system obtained by GIG-ICA has higher integration and IVA-GL has higher segregation and result from that GIG-ICA can obtain more reliable networks compared to IVA-GL (Du et al., 2017). Additionally, it may also reflect that GIG-ICA has higher randomness of functional brain network (Rudie et al., 2013; Keown et al., 2017; Henry et al., 2018; Sigar et al., 2023). Our study further indicates no significant difference in global modularity *Q* between GIG-ICA and IVA-GL. Notably, GIG-ICA detected differences in FNC between HC and ASD, suggesting that it preserved the group relationship and identified potential differences. Similarly, IVA-GL identified a statistically negative correlation between the FNC of ASD and the ADOS, indicating its capability to extract ASD variability.

4.2. Spatial network differences

To investigate spatial variations in variance and mean, we employed various statistical measures to pair GIG-ICA and IVA-GL components. Although IVA-GL was previously used to analyze schizophrenia (Gopal et al., 2016), we assessed and compared the ability of the two methods to detect spatial network differences in ASD. During the pairing between the two methods, SN and DMN were found to be prominent, and we observed that GIG-ICA showed larger network areas and higher *t*-value differences, while IVA-GL identified cerebellar regions important to ASD. Our finding aligned with a prior investigation conducted by Du and colleagues, demonstrating that GIG-ICA is useful for evaluating coherent networks across subjects, whereas IVA-GL can estimate subject-specific networks (Du et al., 2017). Interestingly, both methods demonstrated similar amplitudes at the voxels of maximum difference. In terms of spatial variance analysis, IVA-GL detected more variability than GIG-ICA, consistent with previous studies comparing it with other methods (Lee et al., 2008; Michael et al., 2014; Laney et al., 2015). Moreover, we found that the group difference pattern (ASD > HC; ASD < HC) obtained from GIG-ICA was almost identical to IVA-GL, but there were differences in the statistical discrimination of some networks (CRN (GIG-ICA: IC = 49, p-value < 0.001; IVA-GL: IC = 44, p-value = 0.838), DAN (GIG-ICA: IC = 40, p-value = 0.074; IVA-GL: IC = 36, p-value = 0.001)), indicating that the two methods had comparable abilities to detect variance map differences.

4.3. Prediction performance

Using a regression model, GIG-ICA and IVA-GL were compared to determine which data-driven method was best for predicting age. Unlike typical feature selection methods in machine learning, we employed a statistical correlation method to identify the voxels most relevant to age and eliminated the effects of gender and handedness. To comprehensively evaluate the prediction results, we utilized a permutation test and the confidence coefficient R^2. The findings indicated no significant difference between the two methods in predicting age. Nevertheless, we displayed the predictive features of two networks in Figure 7. In GIG-ICA's CRN, the vermis and caudate was found to have the strongest negative and positive correlation with age, respectively. Similarly, for IVA-GL, the motor area correlated negatively with age, while the parietal was positively correlated. Additionally, the prediction accuracy for IQ is not as high as that for age, possibly because of the greater variance in its data.

4.4. Limitations

Despite the thorough evaluation of GIG-ICA and IVA-GL performance using various metrics, our study does have some limitations. Firstly, our subjects comprise different age groups, which might require an additional analysis to examine their differences. Since our study mainly focused on methodological differences, we did not investigate this aspect. Therefore, further studies will be required. Secondly, although a boosted method was used to calculate the FNC matrix, further research is needed to verify the effect of extracting network information. Considering that the *p*-value in Figure 2B is close to the statistically significant boundary, more work may be required to check its validity. Lastly, full IQ was determined by averaging the available performance and verbal IQ scores for each diagnostic group. Given the significant differences in FIQ and VIQ between the HC and ASD groups, the predictive characteristics might vary between them. While our comparison of prediction performance primarily focused on both methods of the two groups as a whole, further research may be necessary to delve deeper into the predictive characteristics of each group individually.

5. Conclusion

In conclusion, this study revealed that GIG-ICA and IVA-GL have distinct capabilities in identifying brain network modules in HC and ASD, with a complementary effect on FNC statistical analysis. GIG-ICA can detect more regions with higher amplitudes in spatial network differences, while IVA-GL can identify more networks associated with ASD. In addition, both methods can accurately determine the difference in variance maps between HC and ASD, with GIG-ICA having a better predictive performance (GIG-ICA-CRN ($R^2 = 0.91$, RMSE = 3.05, $R = 0.795$) and IVA-VAN ($R^2 = 0.87$, RMSE = 3.21, $R = 0.793$)), although not significantly different from IVA-GL ($t = -0.09$, p-value = 0.92). Finally, the study offers further insights into using different data-driven methods to examine neurological disorders of resting-state fMRI.

Data availability statement

Publicly available datasets were analyzed in this study. This data can be found at: http://fcon_1000.projects.nitrc.org/indi/abide/abide_I.html.

Author contributions

JJ, SX, and MS: organized and preprocessed the data. JJ and BK-B: formal analysis, statistical analysis and results, and writing the first draft. BK-B and BB: revision and editing. All authors contributed to the article and approved the submitted version.

Funding

This work was supported by the National Natural Science Foundation of China (NSFC82250410380 and NSFC62171101).

Conflict of interest

The authors declare that the research was conducted in the absence of any commercial or financial relationships that could be construed as a potential conflict of interest.

Publisher's note

Supplementary material

The Supplementary material for this article can be found online at: https://www.frontiersin.org/articles/10.3389/fnins.2023.1252732/full#supplementary-material

References

Abou-Elseoud, A., Starck, T., Remes, J., Nikkinen, J., Tervonen, O., and Kiviniemi, V. (2010). The effect of model order selection in group PICA. *Hum. Brain Mapp.* 31, 1207–1216. doi: 10.1002/hbm.20929

Adali, T., Anderson, M., and Fu, G. S. (2014). Diversity in independent component and vector analyses: identifiability, algorithms, and applications in medical imaging. *IEEE Signal Process. Mag.* 31, 18–33. doi: 10.1109/MSP.2014.2300511

Allen, E. A., Erhardt, E. B., Wei, Y., Eichele, T., and Calhoun, V. D. (2012). Capturing inter-subject variability with group independent component analysis of fMRI data: a simulation study. *NeuroImage* 59, 4141–4159. doi: 10.1016/j.neuroimage.2011.10.010

American Psychiatric Association. (2000). DSM-IV-TR. Diagnostic and Statistical Manual of Mental Disorder, Fourth Edition, Text Revision. American Psychiatric Association.

Anderson, M., Adali, T., and Li, X. L. (2012). Joint blind source separation with multivariate Gaussian model: algorithms and performance analysis. *IEEE Trans. Signal Process.* 60, 1672–1683. doi: 10.1109/TSP.2011.2181836

Beckmann, C., Mackay, C., Filippini, N., and Smith, S. (2009). Group comparison of resting-state FMRI data using multi-subject ICA and dual regression. *NeuroImage* 47:S148. doi: 10.1016/S1053-8119(09)71511-3

Bell, A. J., and Sejnowski, T. J. (1995). An information-maximization approach to blind separation and blind deconvolution. *Neural Comput.* 7, 1129–1159. doi: 10.1162/neco.1995.7.6.1129

Biswal, B. B., and Ulmer, J. L. (1999). Blind-source separation of multiple signal sources of fMIU data sets using independent component analysis. *Comparative Study* 23, 265–271. doi: 10.1097/00004728-199903000-00016

Biswal, B., Zerrin Yetkin, F., Haughton, V. M., and Hyde, J. S. (1995). Functional connectivity in the motor cortex of resting human brain using echo-planar MRI. *Magn. Reson. Med.* 34, 537–541. doi: 10.1002/mrm.1910340409

Blondel, V. D., Guillaume, J. L., Lambiotte, R., and Lefebvre, E. (2008). Fast unfolding of communities in large networks. *J. Stat. Mech. Theor. Exp.* 2008, 1–12. doi: 10.1088/1742-5468/2008/10/P10008

Calhoun, V. D., Adali, T., Pearlson, G. D., and Pekar, J. J. (2001a). Spatial and temporal independent component analysis of functional MRI data containing a pair of task-related waveforms. *Hum. Brain Mapp.* 13, 43–53. doi: 10.1002/hbm.1024

Calhoun, V. D., Adali, T., Pearlson, G. D., and Pekar, J. J. (2001b). A method for making group inferences from functional MRI data using independent component analysis. *Hum. Brain Mapp.* 14, 140–151. doi: 10.1002/hbm.1048

Damoiseaux, J. S., Rombouts, S. A. R. B., Barkhof, F., Scheltens, P., Stam, C. J., Smith, S. M., et al. (2006). Consistent resting-state networks across healthy subjects. *Proc. Natl. Acad. Sci.* 103, 13848–13853. doi: 10.1073/pnas.0601417103

Dea, JT, Anderson, M, Allen, E, Calhoun, VD, and Adali, T. IVA for multi-subject FMRI analysis: a comparative study using a new simulation toolbox. IEEE International Workshop on Machine Learning for Signal Processing, (2011)

Di Martino, A., Yan, C. G., Li, Q., Denio, E., Castellanos, F. X., Alaerts, K., et al. (2014). The autism brain imaging data exchange: towards a large-scale evaluation of the intrinsic brain architecture in autism. *Mol. Psychiatry* 19, 659–667. doi: 10.1038/mp.2013.78

Du, Y., Allen, E. A., He, H., Sui, J., Wu, L., and Calhoun, V. D. (2016). Artifact removal in the context of group ICA: a comparison of single-subject and group approaches. *Hum. Brain Mapp.* 37, 1005–1025. doi: 10.1002/hbm.23086

Du, Y., and Fan, Y. (2013). Group information guided ICA for fMRI data analysis. *NeuroImage* 69, 157–197. doi: 10.1016/j.neuroimage.2012.11.008

Du, Y., Lin, D., Yu, Q., Sui, J., Chen, J., Rachakonda, S., et al. (2017). Comparison of IVA and GIG-ICA in brain functional network estimation using fMRI data. *Front. Neurosci.* 11, 1–18. doi: 10.3389/fnins.2017.00267

Du, Y, Liu, J, Sui, J, He, H, Pearlson, GD, and Calhoun, VD. Exploring difference and overlap between schizophrenia, schizoaffective and bipolar disorders using resting-state brain functional networks. 2014 36th Annual International Conference of the IEEE Engineering in Medicine and Biology Society, EMBC 2014. (2014); 1517–1520.

Du, Y., Pearlson, G. D., Lin, D., Sui, J., Chen, J., Salman, M., et al. (2017). Identifying dynamic functional connectivity biomarkers using GIG-ICA: application to schizophrenia, schizoaffective disorder, and psychotic bipolar disorder. *Hum. Brain Mapp.* 38, 2683–2708. doi: 10.1002/hbm.23553

Du, Y., Pearlson, G. D., Liu, J., Sui, J., Yu, Q., He, H., et al. (2015). A group ICA based framework for evaluating resting fMRI markers when disease categories are unclear: application to schizophrenia, bipolar, and schizoaffective disorders. *NeuroImage* 122, 272–280. doi: 10.1016/j.neuroimage.2015.07.054

Fattahi, M., Zadeh, G. A. H., Asl, A. R. A., and Rostami, R. (2021). Dynamic functional connectivity in major depressive disorder with suicidal thoughts: an fMRI study. *Front. Biomed. Technol.* 8, 55–58. doi: 10.1109/ICBME54433.2021.9750309

Friedman, J. (2010). Regularization paths for generalized linear models via coordinate descent. *J. Stat. Softw.* 33, 1–22. doi: 10.18637/jss.v033.i01

Girvan, M., and Newman, M. E. J. (2002). Community structure in social and biological networks. *Proc. Natl. Acad. Sci. U. S. A.* 99, 7821–7826. doi: 10.1073/pnas.122653799

Gopal, S., Miller, R. L., Michael, A., Adali, T., Cetin, M., Rachakonda, S., et al. (2016). Spatial variance in resting fMRI networks of schizophrenia patients: an independent vector analysis. *Schizophr. Bull.* 42, 152–160. doi: 10.1093/schbul/sbv085

Greicius, M. D., Krasnow, B., Reiss, A. L., and Menon, V. (2003). Functional connectivity in the resting brain: a network analysis of the default mode hypothesis. *Proc. Natl. Acad. Sci. U. S. A.* 100, 253–258. doi: 10.1073/pnas.0135058100

Henry, T. R., Dichter, G. S., and Gates, K. (2018). Age and gender effects on intrinsic connectivity in autism using functional integration and segregation. *Biol Psychiatry Cogn Neurosci Neuroimaging.* 3, 414–422. doi: 10.1016/j.bpsc.2017.10.006

Jafri, M. J., Pearlson, G. D., Stevens, M., and Calhoun, V. D. (2008). A method for functional network connectivity among spatially independent resting-state components in schizophrenia. *NeuroImage* 39, 1666–1681. doi: 10.1016/j.neuroimage.2007.11.001

Keown, C. L., Datko, M. C., Chen, C. P., Maximo, J. O., Jahedi, A., and Müller, R. A. (2017). Network organization is globally atypical in autism: a graph theory study of intrinsic functional connectivity. *Biol Psychiatry Cogn Neurosci Neuroimaging.* 2, 66–75. doi: 10.1016/j.bpsc.2016.07.008

Kleinhans, N. M., Richards, T., Sterling, L., Stegbauer, K. C., Mahurin, R., Johnson, L. C., et al. (2008). Abnormal functional connectivity in autism spectrum disorders during face processing. *Brain* 131, 1000–1012. doi: 10.1093/brain/awm334

Kunda, M., Zhou, S., Gong, G., and Lu, H. (2023). Improving multi-site autism classification via site-dependence minimization and second-order functional connectivity. *IEEE Trans. Med. Imaging* 42, 55–65. doi: 10.1109/TMI.2022.3203899

Laney, J., Westlake, K. P., Ma, S., Woytowicz, E., Calhoun, V. D., and Adali, T. (2015). Capturing subject variability in fMRI data: a graph-theoretical analysis of GICA vs. IVA. *J. Neurosci. Methods* 247, 32–40. doi: 10.1016/j.jneumeth.2015.03.019

Lawrence, K. E., Hernandez, L. M., Eilbott, J., Jack, A., Aylward, E., Gaab, N., et al. (2020). Neural responsivity to social rewards in autistic female youth. *Transl. Psychiatry.* 10:178. doi: 10.1038/s41398-020-0824-8

Lee, J. H., Lee, T. W., Jolesz, F. A., and Yoo, S. S. (2008). Independent vector analysis (IVA): multivariate approach for fMRI group study. *NeuroImage* 40, 86–109. doi: 10.1016/j.neuroimage.2007.11.019

Liu, M., Li, B., and Hu, D. (2021). Autism spectrum disorder studies using fMRI data and machine learning: a review. *Front. Neurosci.* 15:697870. doi: 10.3389/fnins.2021.697870

Ma, S., Phlypo, R., and Calhoun, V. D. (2013). *Capturing group variability using IVA: a simulation study and graph-theoretical analysis, University of Maryland, Baltimore County, Department of CSEE, Baltimore, MD 21250 the mind research network and University of New Mexico, Department of ECE, Albuquerqu. Group (New York)*, 3128–3132.

Mckeown, M. J., Makeig, S., Brown, G. G., Jung, T., Kindermann, S. S., Bell, A. J., et al. (1998). Analysis of fMRI data by blind separation into independent spatial components. *Hum. Brain Mapp.* 6, 160–188. doi: 10.1002/(SICI)1097-0193(1998)6:3<160::AID-HBM5>3.0.CO;2-1

Michael, A. M., Anderson, M., Miller, R. L., Adali, T., and Calhoun, V. D. (2014). Preserving subject variability in group fMRI analysis: performance evaluation of GICA vs. *IVA. Front Syst Neurosci.* 8, 1–18. doi: 10.3389/fnsys.2014.00106

Motlaghian, S. M., Belger, A., Bustillo, J. R., Ford, J. M., Iraji, A., Lim, K., et al. (2022). Nonlinear functional network connectivity in resting functional magnetic resonance imaging data. *Hum. Brain Mapp.* 43, 4556–4566. doi: 10.1002/hbm.25972

Newman, M. E. J., and Girvan, M. (2004). Finding and evaluating community structure in networks. *Phys. Rev. E* 69:026113. doi: 10.1103/PhysRevE.69.026113

Rafiee, F., Rezvani Habibabadi, R., Motaghi, M., Yousem, D. M., and Yousem, I. J. (2022). Brain MRI in autism spectrum disorder: narrative review and recent advances. *J. Magn. Reson. Imaging* 55, 1613–1624. doi: 10.1002/jmri.27949

Rausch, A., Zhang, W., Haak, K. V., Mennes, M., Hermans, E. J., Van Oort, E., et al. (2016). Altered functional connectivity of the amygdaloid input nuclei in adolescents and young adults with autism spectrum disorder: a resting state fMRI study. *Mol. Autism.* 7, 1–13. doi: 10.1186/s13229-015-0060-x

Rudie, J. D., Brown, J. A., Beck-Pancer, D., Hernandez, L. M., Dennis, E. L., Thompson, P. M., et al. (2013). Altered functional and structural brain network organization in autism. *Neuroimage Clin.* 2, 79–94. doi: 10.1016/j.nicl.2012.11.006

Samuel Schwarzkopf, D., de Haas, B., and Rees, G. (2012). Better ways to improve standards in brain-behavior correlation analysis. *Front. Hum. Neurosci.* 6:200. doi: 10.3389/fnhum.2012.00200

Santana, C. P., de Carvalho, E. A., Rodrigues, I. D., Bastos, G. S., de Souza, A. D., and de Brito, L. L. (2022). Rs-fMRI and machine learning for ASD diagnosis: a systematic review and meta-analysis. *Sci. Rep.* 12:6030. doi: 10.1038/s41598-022-09821-6

Shen, X., Finn, E. S., Scheinost, D., Rosenberg, M. D., Chun, M. M., Papademetris, X., et al. (2017). Using connectome-based predictive modeling to predict individual behavior from brain connectivity. *Nat. Protoc.* 12, 506–518. doi: 10.1038/nprot.2016.178

Shukla, D. K., Keehn, B., Smylie, D. M., and Müller, R. A. (2011). Microstructural abnormalities of short-distance white matter tracts in autism spectrum disorder. *Neuropsychologia* 49, 1378–1382. doi: 10.1016/j.neuropsychologia.2011.02.022

Sigar, P., Uddin, L. Q., and Roy, D. (2023). Altered global modular organization of intrinsic functional connectivity in autism arises from atypical node-level processing. *Autism Res.* 16, 66–83. doi: 10.1002/aur.2840

Smith, S. M., Miller, K. L., Moeller, S., Xu, J., Auerbach, E. J., Woolrich, M. W., et al. (2012). Temporally-independent functional modes of spontaneous brain activity. *Proc Natl Acad Sci U S A* 109, 3131–6. doi: 10.1073/pnas.1121329109

Svensén, M., Kruggel, F., and Benali, H. (2002). ICA of fMRI group study data. *NeuroImage* 16, 551–563. doi: 10.1006/nimg.2002.1122

Tzourio-Mazoyer, N., Landeau, B., Papathanassiou, D., Crivello, F., Etard, O., Delcroix, N., et al. (2002). Automated anatomical labeling of activations in SPM using a macroscopic anatomical parcellation of the MNI MRI single-subject brain. *NeuroImage* 15, 273–289. doi: 10.1006/nimg.2001.0978

Wadhera, T, and Mahmud, M. Computing hierarchical complexity of the brain from electroencephalogram signals: a graph convolutional network-based approach, Proceedings of the International Joint Conference on Neural Networks. (2022); 1–6 July, 2022

Wadhera, T., and Mahmud, M. (2023). Brain functional network topology in autism spectrum disorder: a novel weighted hierarchical complexity metric for electroencephalogram. *IEEE J. Biomed. Health Inform.* 27, 1718–1725. doi: 10.1109/JBHI.2022.3232550

Wang, N., Yao, D., Ma, L., and Liu, M. (2022). Multi-site clustering and nested feature extraction for identifying autism spectrum disorder with resting-state fMRI. *Med. Image Anal.* 75:102279. doi: 10.1016/j.media.2021.102279

Zhi, D., Calhoun, V. D., Lv, L., Ma, X., Ke, Q., Fu, Z., et al. (2018). Aberrant dynamic functional network connectivity and graph properties in major depressive disorder. *Front. Psych.* 9, 558–561. doi: 10.3389/fpsyt.2018.00339

Zhuang, J, Dvornek, NC, Li, X, Ventola, P, and Duncan, JS. Prediction of severity and treatment outcome for ASD from fMRI. *Lecture notes in computer science (including subseries lecture notes in artificial intelligence and lecture notes in bioinformatics)*. (2018)

Frontiers in Neuroscience

TYPE Original Research
PUBLISHED 24 October 2023
DOI 10.3389/fnins.2023.1277733

EDITED BY
Takao Yamasaki,
Minkodo Minohara Hospital, Japan

REVIEWED BY
Martin Dietz,
Aarhus University, Denmark
Julia M. Stephen,
The Mind Research Network (MRN),
United States

*CORRESPONDENCE
Yoji Hirano
✉ yhouji@mac.com
Shunsuke Tamura
✉ bervafuta11@gmail.com

RECEIVED 15 August 2023
ACCEPTED 09 October 2023
PUBLISHED 24 October 2023

CITATION
Nakanishi S, Tamura S, Hirano S, Takahashi J, Kitajima K, Takai Y, Mitsudo T, Togao O, Nakao T, Onitsuka T and Hirano Y (2023) Abnormal phase entrainment of low- and high-gamma-band auditory steady-state responses in schizophrenia. *Front. Neurosci.* 17:1277733. doi: 10.3389/fnins.2023.1277733

Abnormal phase entrainment of low- and high-gamma-band auditory steady-state responses in schizophrenia

Shoichiro Nakanishi[1], Shunsuke Tamura[1,2]*, Shogo Hirano[1], Junichi Takahashi[1], Kazutoshi Kitajima[1], Yoshifumi Takai[1], Takako Mitsudo[1], Osamu Togao[3], Tomohiro Nakao[1], Toshiaki Onitsuka[1,4] and Yoji Hirano[1,2,5]*

[1]Department of Neuropsychiatry, Graduate School of Medical Sciences, Kyushu University, Fukuoka, Japan, [2]Department of Psychiatry, Division of Clinical Neuroscience, Faculty of Medicine, University of Miyazaki, Miyazaki, Japan, [3]Department of Molecular Imaging and Diagnosis, Graduate School of Medical Sciences, Kyushu University, Fukuoka, Japan, [4]National Hospital Organization Sakakibara Hospital, Mie, Japan, [5]Institute of Industrial Science, The University of Tokyo, Tokyo, Japan

Introduction: Gamma-band oscillatory deficits have attracted considerable attention as promising biomarkers of schizophrenia (SZ). Notably, a reduced auditory steady-state response (ASSR) in the low gamma band (40 Hz) is widely recognized as a robust finding among SZ patients. However, a comprehensive investigation into the potential utility of the high-gamma-band ASSR in detecting altered neural oscillations in SZ has not yet been conducted.

Methods: The present study aimed to assess the ASSR using magnetoencephalography (MEG) data obtained during steady-state stimuli at frequencies of 20, 30, 40, and 80 Hz from 23 SZ patients and 21 healthy controls (HCs). To evaluate the ASSR, we examined the evoked power and phase-locking factor (PLF) in the time-frequency domain for both the primary and secondary auditory cortices. Furthermore, we calculated the phase-locking angle (PLA) to examine oscillatory phase lead or delay in SZ patients. Taking advantage of the high spatial resolution of MEG, we also focused on the hemispheric laterality of low- and high-gamma-band ASSR deficits in SZ.

Results: We found abnormal phase delay in the 40 Hz ASSR within the bilateral auditory cortex of SZ patients. Regarding the 80 Hz ASSR, our investigation identified an aberrant phase lead in the left secondary auditory cortex in SZ, accompanied by reduced evoked power in both auditory cortices.

Discussion: Given that abnormal phase lead on 80 Hz ASSR exhibited the highest discriminative power between HC and SZ, we propose that the examination of PLA in the 80 Hz ASSR holds significant promise as a robust candidate for identifying neurophysiological endophenotypes associated with SZ. Furthermore, the left-hemisphere phase lead observed in the deficits of 80 Hz PLA aligns with numerous prior studies, which have consistently proposed that SZ is characterized by left-lateralized brain dysfunctions.

KEYWORDS

auditory steady-state response (ASSR), evoked power, gamma oscillation, magnetoencephalography (MEG), phase locking angle (PLA), phase locking factor (PLF), schizophrenia

1. Introduction

Gamma-band (30–100 Hz) oscillatory deficits have attracted considerable attention as a promising neurophysiological endophenotype of schizophrenia (SZ) due to their well-established association with various psychiatric symptoms and specific cognitive deficits observed in SZ (Uhlhaas and Singer, 2010; Hirano and Uhlhaas, 2021; Koshiyama et al., 2022; Onitsuka et al., 2022a,b,c; Sohal, 2022). Gamma-band oscillations are responsible for the temporal coordination of narrowly localized neural circuits throughout the brain (von Stein and Sarnthein, 2000; Fries et al., 2007; Buzsáki and Wang, 2012; Arnulfo et al., 2015; Buzsáki and Schomburg, 2015). In addition, they are well known to be generated by an appropriate balance between excitatory (E) and inhibitory (I) neurons, in which the excitatory output from pyramidal cells is precisely inhibited by fast-spiking inhibitory interneurons, such as parvalbumin (PV +) and somatostatin (SOM +) interneurons (Bartos et al., 2007; Sohal et al., 2009; Buzsáki and Wang, 2012). A prominent hypothesis concerning the pathophysiology of SZ proposes that *N*-methyl-D-aspartate receptors (NMDARs) on PV + neurons exhibit hypofunctionality, leading to diminished GABAergic signaling, excessive excitation of neurons, and subsequent deficits in gamma-band oscillations (Burgos and Lewis, 2008). Therefore, gamma-band oscillatory deficits are expected to serve as a potential biomarker related to altered E/I balance within the neural circuits in SZ (Gandal et al., 2012).

The auditory steady-state response (ASSR), which refers to the synchronized activity elicited by a click train or by amplitude-modulated sound, is frequently employed to evaluate gamma-band oscillatory deficits in SZ. A recent comprehensive review and meta-analysis investigating gamma-band ASSR deficits in SZ patients suggests that impairments in 40 Hz ASSR power and phase locking are pronounced and could serve as valuable probes for assessing neural circuit dysfunctions (Thuné et al., 2016; Onitsuka et al., 2022c). Numerous electroencephalography (EEG) studies have shown the deterioration of the gamma-band evoked power and phase-locking factor (PLF) (the degree of phase-locking evoked by stimuli) on 40 Hz ASSR, not only in chronic SZ patients (e.g., Kwon et al., 1999; Spencer et al., 2009; Kirihara et al., 2012) but also in first-episode SZ patients (e.g., Spencer et al., 2008; Tada et al., 2016) and subjects at clinical high risk for psychosis (Tada et al., 2016; Koshiyama et al., 2018). These recent findings provide compelling evidence that altered 40 Hz ASSR could serve as a neurophysiological marker with potential utility for early detection of psychosis.

Due to its remarkable temporal acuity and exceptional spatial resolution, magnetoencephalography (MEG) demonstrates remarkable proficiency in elucidating intricate neural dynamics (Hironaga et al., 2020; Tagawa et al., 2022). Several previous studies using MEG attempted to identify the brain regions responsible for gamma-band ASSR deficits in SZ (Hamm et al., 2011; Edgar et al., 2014, 2018; Murphy et al., 2020; Grent-‘t-Jong et al., 2021). Although most of these studies reported reduced evoked power or PLF on 40 Hz ASSR in the auditory cortex, Grent-‘t-Jong et al. (2021) found that subjects at clinical high risk for psychosis and patients with first-episode psychosis exhibited impaired 40 Hz ASSR power in subcortical regions such as the right thalamus and hippocampus. Likewise, leveraging the high spatial resolution of MEG, numerous studies have consistently reported a reduction in the laterality of the gamma-band ASSR in SZ (Teale et al., 2003, 2008; Maharajh et al., 2010; Tsuchimoto et al., 2011). Specifically, SZ patients demonstrated a weaker right hemisphere advantage in terms of 40-Hz ASSR evoked power and PLF when compared to healthy controls (HCs), indicating that SZ may be characterized by an abnormal hemispheric asymmetry in the 40-Hz ASSR.

Several recent studies focused on the gamma-band phase delay of the 40 Hz ASSR in SZ (Roach et al., 2019a,b, 2022; Yanagi et al., 2022). Notably, these studies revealed that gamma-band phase delay exhibited higher differential sensitivity to SZ (Roach et al., 2019b) and superior test–retest reliability (Roach et al., 2019a) compared to evoked power and PLF. In addition, Roach et al. (2022) identified a left-lateralized gamma-band delay in SZ by estimating 40 Hz ASSR within the bilateral auditory cortices using EEG data. However, EEG lacks adequate spatial resolution, necessitating a reassessment of the laterality pattern of gamma-band phase delay in SZ using MEG, which offers better spatial resolution than EEG. In addition to the examination of 40 Hz ASSR, it may be worthwhile to consider the high-gamma-band (80 Hz) ASSR as a possible neurophysiological marker for SZ (Onitsuka et al., 2022c). A limited number of studies (Hamm et al., 2011; Tsuchimoto et al., 2011; Parker et al., 2019) have revealed that patients with SZ exhibit decreased evoked power and PLF not only in the 40 Hz range but also in the 80 Hz range of ASSRs. Notably, our previous MEG study (Tsuchimoto et al., 2011) showed that evoked power and PLF of the 80 Hz ASSR demonstrated greater differential sensitivity to SZ patients compared to those of the 20, 30, and 40 Hz ASSRs. Moreover, early auditory deficits within the auditory cortices are known to play a crucial role in the pathophysiology of SZ (Javitt and Sweet, 2015; Dondé et al., 2023). Hence, it would be of great interest to investigate whether SZ patients exhibit reduced evoked power and PLF and a phase delay in the 80 Hz ASSR within the primary and secondary auditory cortex.

The objective of the present MEG study is to investigate whether SZ patients exhibit abnormal phase entrainment, characterized by either a lead or delay, in both low- and high-gamma-band ASSRs within the auditory cortices. Additionally, we aimed to explore the laterality pattern of gamma-band phase entrainment (leads or delays) in SZ. We utilized MEG to measure ASSRs during 20, 30, 40, and 80 Hz click trains in both SZ patients and HCs. Our analysis focused on examining evoked power, PLF, and the degree of phase delay relative to the expected phase angle (phase-locking angle, PLA) in the bilateral primary (Heschl's gyrus)

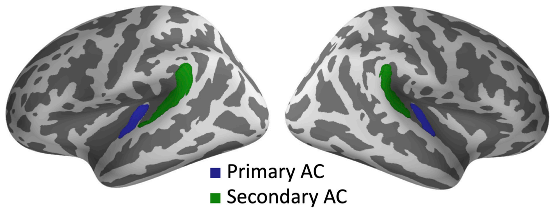

FIGURE 1
Regions of interest for source analysis of ASSRs. The green and blue areas indicate the primary and secondary auditory cortices, respectively, in both hemispheres. AC, auditory cortex.

and secondary auditory cortices (the planum temporale of the superior temporal gyrus) (**Figure 1**).

2. Materials and methods

2.1. Participants

Twenty-three SZ patients (10 males) and 21 HCs (10 males) participated in this study. All SZ patients were recruited from Kyushu University Hospital, and they were diagnosed based on the SCID-DSM V (First, 2002). The HC participants were recruited from the local community in Fukuoka City, and they and their first-degree relatives were free of Axis I psychiatric disorders. The exclusion criteria for both groups were as follows: (1) history of neurological illness or major head trauma that could result in abnormal electroencephalography results; (2) history of electroconvulsive therapy; (3) history of alcohol or drug dependence in their lifetime; (4) history of alcohol or drug abuse within the previous 5 years; or (5) a verbal intelligence quotient below 75. This study received approval from the Research Ethics Board of the Faculty of Medicine, Kyushu University (approval number 29038) and was carried out in accordance with the latest version of the Declaration of Helsinki. All the participants gave informed consent before the experiment.

Four SZ patients and 3 HC participants were excluded from data analysis because the MEG data were affected greatly by external magnetic noise (the exclusion criteria are stated in the description of MEG preprocessing). Finally, we employed the data of nineteen SZ patients (9 males with a mean age of 35.9 years) and 18 HCs (7 males with a mean age of 32.2 years). All participants were right-handed and did not have difficulty in listening to the stimuli used in this study. The symptoms of SZ patients were assessed by the Positive and Negative Syndrome Scale (PANSS) (Kay et al., 1987). Eighteen out of the 19 patients were receiving antipsychotics, with a mean daily dose equivalent to 499.12 mg of chlorpromazine (Inada and Inagaki, 2015). The mean illness duration in SZ patients was approximately 8.26 years. More detailed demographic and clinical characteristics are described in **Table 1**.

2.2. Stimuli and apparatus

We used four types of click-train sounds with different train frequencies for the ASSR task. The 20, 30, 40, and 80 Hz click-train sounds with 500-ms duration were created using a 1-ms rectangle click sound. Each click-train sound was presented repetitively with an interstimulus interval of 500 ms until we obtained 200 trials with a peak amplitude less than amplitude criteria (gradiometer amplitude >3,000 fT/cm, magnetometer amplitude >3,000 fT) during online MEG recording. The order of employing the four frequencies was randomized across the participants. All stimuli were generated using a signal generator (Waveform Generator 7075, Hioki, Nagano, Japan) and presented to both ears of the participants through inserted earphones (ER-3A, Etymotic Research, IL, USA). The sound pressure level of these stimuli was set to 80 dB.

The MEG signals were acquired using a 306-channel system consisting of 204 planar-type gradiometers and 102 magnetometers (Neuromag, Elekta, Helsinki, Finland). The MEG signals were recorded at a sampling rate of 1 kHz with an online bandpass filter of 0.01–330 Hz. Since the magnetometers are sensitive to external noises, we used only the MEG signals of the gradiometers for data analysis. Before the recording, four head position indicator (HPI) coils were attached to the scalp, and the three fiducial points (the nasion and the left and right auricular points) of the head, the HPI positions, and approximately 200 head-surface points were measured using a three-dimensional digitizer. The accurate location of the head with regards to the sensor array was measured by the HPI coils.

T1-weighted structural images were obtained using a three-dimensional turbo field echo sequence using a 3T magnetic resonance imaging (MRI) scanner (Achieva TX, Philips, Best, Netherlands). The imaging parameters were as follows: repetition time = 8.2 ms, echo time = 3.8 ms, flip angle = 8°, field of view = 24 cm × 24 cm, number of echoes = 1, matrix = 240 × 240,

TABLE 1 Demographic and clinical characteristics of healthy control (HC) and schizophrenia (SZ) groups.

	Schizophrenia (n = 19)		Healthy control (n = 18)		*df*	t or χ^2	*p*
	Mean	SD	Mean	SD			
Age (years)	35.9	10.9	32.2	14.1	32.9	−0.58	0.57
Sex (M/F)	9/10		7/11		1	0.04	0.85
SES	3.6	1	2.2	0.7	28.3	−4.55	<0.01
Parental SES	2.4	0.85	2.9	1.2	31.9	1.58	0.12
Education years	13.8	20.6	15.1	2	33.8	1.89	0.07
PANSS positive	19.6	7.2					
PANSS negative	23.2	8.8					
PANSS general	44.1	17.1					
Duration of illness (years)	8.3	8.9					
Medication dose (CPZ equiv., mg)	499.12	299.28					

The data are given as the mean ± standard deviation. Socioeconomic status (SES) and Positive and Negative Syndrome Scale (PANSS) data were not available for 1 and 3 patients, respectively.

inversion time = 1025.9 ms, number of slices = 190, and slice thickness = 1 mm. The MR images were aligned using the intercommissural line and the sagittal sulcus to correct head tilt. We constructed whole-brain source space from individual MRI data and created a boundary element model (BEM) of the brain using FreeSurfer 7.1.1. The coregistration of the MEG and MRI data was conducted based on the head position data obtained through the HPI coils and 3-D digitizer.

2.3. MEG pre-processing

We employed MNE-python 0.23.0[1] and Python 3.9.6[2] to perform MEG data analysis. To remove noise from MEG sensors, we first applied an oversampled temporal projection to the MEG data (Larson and Taulu, 2017). Second, we removed external noise from the MEG data and corrected head movements using the temporal extension of Signal-Space Separation (Nenonen et al., 2012). Third, we applied a high-pass filter of 1 Hz and a notch filter of 60 Hz and its harmonics (120, 180, 240, and 300 Hz) to MEG data. Finally, we removed artifacts caused by eye movement and electrocardiograms by applying an independent component analysis to the filtered data.

Using the artifact-free MEG data, we created epochs with 1500 ms duration, starting at 500 ms prior to stimulus onset and lasting for 1000 ms after stimulus-onset, separately for each stimulus condition (20, 30, 40, or 80 Hz). The epochs were rejected if the peak-to-peak amplitude of their waveform exceeded 5000 fT/cm. The four SZ patients and 3 HC participants were excluded from further analysis as described above because the number of epochs did not reach 200 in any of the four stimulus conditions. To avoid adverse effect of difference in the number of accepted epochs on time-frequency analysis results, 200 epochs selected from accepted epochs for each stimulus condition were submitted to further analysis. We also created evoked-subtracted epochs for each stimulus condition by subtracting an averaged evoked waveform from the waveform of each epoch.

2.4. Time-frequency analysis in source space

We calculated time-frequency representations (PLF, PLA, and evoked power) of ASSRs in the bilateral primary and secondary auditory cortices for each stimulus condition. The PLF measures the degree to which an oscillatory phase synchronizes across trials and ranges from 0 (random distribution) to 1 (perfect phase locking). The PLA is defined as the degree to which a certain participant's oscillatory phase leads or lags relative to group (HC)-averaged phase angles of stimulus-evoked oscillations (Roach et al., 2019b). The evoked power is the spectrotemporal power of event-related activity. The primary and secondary auditory cortices are considered to correspond to the anterior transverse temporal gyrus and the planum temporale of the superior temporal gyrus, respectively, in the Destrieux atlas (Destrieux et al., 2010). Therefore, we defined these regions in both hemispheres as the regions of interest (ROIs) in this study (**Figure 1**).

The detailed procedure of source-level time-frequency analysis was as follows. First, we calculated a complex representation at each time-frequency point (time range from −500 to 1000 ms with 1 ms steps and frequency range from 10 to 100 Hz with 1 Hz steps) for each epoch or each evoked-subtracted epoch at each sensor by applying a Morlet wavelet transform ($\sigma = 7.0$) to the MEG signal. The norm of the obtained complex representation was changed to 1. The complex representations in source space were estimated from those in sensor space using noise-normalized minimum norm estimation (MNE), executed with dynamic statistical parametric mapping (dSPM) (Dale et al., 2000). For source estimation, we first constructed the forward solution, which models the propagation of the magnetic field from each brain region (mesh-patterned 8192 vertices were marked in the brain) to each sensor and was calculated based on the BEM of the brain. We next computed an inverse operator, which was used for estimation of the source-level complex representations from each epoch or each evoked-subtracted epoch, using the forward solution and a noise-covariance matrix calculated from pre-stimulus period (from –400 to –100 ms) signals of epochs or evoked-subtracted epochs.

For each vertex in source space, the averaged time-frequency complex representation across epochs was calculated. The norms of the averaged time-frequency complex representations were obtained as the time-frequency PLF. The time-frequency PLA was obtained for each vertex by re-expressing the angle of the averaged complex representation as its difference from an expected angle at each time-frequency point. According to Roach et al. (2019b), we defined a group-averaged angle of the HC group as the expected angle. To evaluate the time-frequency evoked power at each vertex on source space, we first obtained total and induced power values at each time-frequency point by calculating the averaged squared absolute values of the complex representations across epochs and evoked-subtracted epochs, respectively. The difference between the time-frequency total and induced powers was obtained as the time-frequency evoked power. The time-frequency PLF, PLA, and evoked power, which were obtained in each vertex, were averaged across vertices on each ROI. Regarding the time-frequency evoked power, a baseline correction was applied in each frequency point by subtracting a time-averaged evoked power in the pre-stimulus period (from –400 to –100 ms) from the evoked power at each time point.

2.5. Statistical analysis

The demographic variables [age, sex, socioeconomic status (SES), and education years] were compared between the HC and SZ groups using unpaired Welch's *t*-tests or chi-square tests.

For statistical analysis of PLF and evoked power, we computed their mean values across time-frequency ranges, ranging from 30 to 530 ms and from 5 Hz below to 5 Hz above the train frequency for each stimulus condition. The obtained PLF and evoked power were subjected to three-way repeated-measures analyses of variance (rmANOVAs) with hemisphere (left/right) and ROI (first/secondary auditory cortex) as within-subjects factors

---

[1] https://mne.tools/0.23/index.html

[2] https://www.python.org/

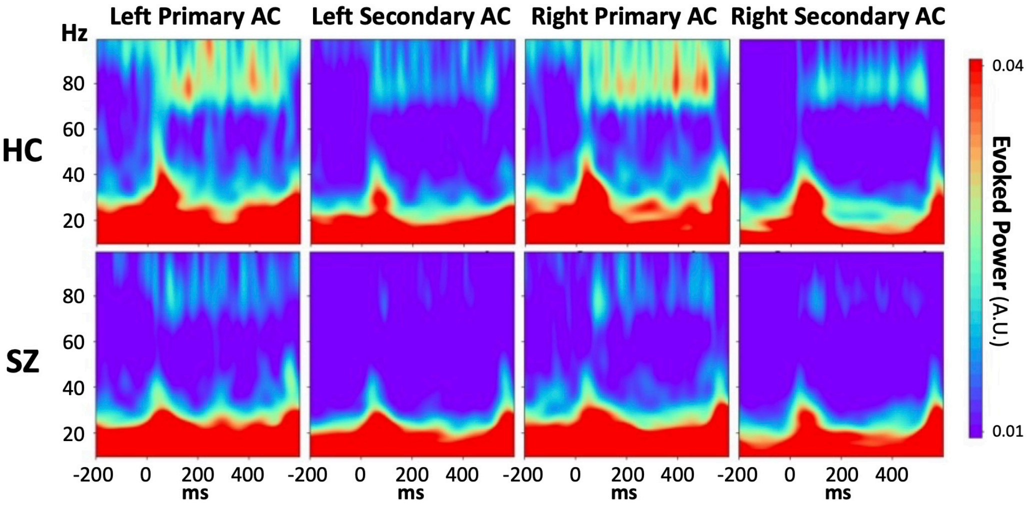

FIGURE 2
The grand average time-frequency maps of the evoked power during 80 Hz stimulation in each HC (**upper** line) or SZ (**lower** line) group for each region of interest. From left, the columns show the maps derived from the left primary auditory cortex, the left secondary auditory cortex, the right primary auditory cortex, and the right secondary auditory cortex. The color bar shows the values of the evoked power, in which red indicates a higher value and blue indicates a lower value. HC, healthy control; SZ, schizophrenia; AC, auditory cortex.

and group (SZ/HC) as a between-subject factor separately for each stimulus condition (20, 30, 40, or 80 Hz).

We conducted a statistical analysis of the PLA following the previous study of Roach et al. (2019b). The time-averaged (200–400 ms) PLA at a frequency that was the same as the train frequency was obtained and converted to a z score based on the mean and standard deviation of the HC group for each stimulus condition, each hemisphere, and each ROI. Three-way rmANOVAs were performed for the z scored PLA value in the same way as statistical analyses of PLF and evoked power. The *post hoc* analyses were conducted for 40 and 80 Hz conditions as follows. For the 40 Hz condition, the unpaired t-test was conducted between HC and SZ groups on the averaged z-scale PLA across ROIs and hemispheres. Regarding the 80 Hz PLA, two-way rmANOVAs were conducted with group and hemisphere as factors for each ROI. In addition, unpaired t-tests were performed between the two groups for the z-scored PLA, separately for the left and right secondary auditory cortices.

The optimal sensitivity and specificity of gamma-band ASSR measures to differentiate between HC and SZ groups were determined via receiver operating characteristic (ROC) analysis to discuss a clinical applicability of these measures as a diagnostic or therapeutic tool in the future. Specifically, we conducted ROC analysis with each analysis index with a significant group difference (averaged evoked power across ROIs and hemispheres in the 80 Hz condition, averaged z-scale PLA across ROIs and hemispheres in the 40 Hz condition, or averaged z-scale PLA across ROIs in the 80 Hz condition) as a discriminant value. The ROC curve was drawn based on a trapezoidal rule. The effect size (Cohen's d) was also calculated using the analysis indices used for the ROC analysis.

The relationships of gamma-band ASSR to clinical symptoms were examined using Spearman's rank correlation analysis. We calculated Spearman's correlations between the analysis indices with significant group differences and PANSS subscales (General, Positive, and Negative scales).

3. Results

3.1. Demographic data

There were no significant group differences in age ($t = -0.58$, $p = 0.57$) or sex ($\chi^2 = 0.04$, $p = 0.85$). The SES of the SZ group was significantly higher than that of the HC group ($t = -4.55$, $p < 0.01$), while there were no significant group differences in parental SES ($t = 1.58$, $p = 0.12$) or years of education ($t = 1.89$, $p = 0.07$).

3.2. PLF and evoked power

Supplementary Figures 1, 2 show group-averaged time-frequency PLFs and evoked powers, respectively, separately for each stimulus condition, each hemisphere, and each ROI. Regarding the PLF, we found neither a significant main effect of group nor group-related interactions in any stimulus condition, although the 80 Hz PLF was inclined to be lower in the SZ group than in the HC group. In terms of the evoked power, we found a significant reduction in 80 Hz evoked power in the SZ group (**Figure 2**). The three-way rmANOVA revealed a significant main effect of group ($F = 4.42$, $p = 0.04$) and no significant group-related interactions. We further conducted an unpaired t-test on the averaged evoked power values across ROIs and hemispheres as a *post hoc* analysis and confirmed that the evoked power during 80 Hz stimulation was significantly lower for the SZ group than for the HC group ($t = -2.07$, $p = 0.049$, Cohen's $d = 0.71$) (**Figure 2**). While the evoked power at 20 and 40 Hz in the left primary auditory cortex showed a tendency to be higher and lower, respectively, in

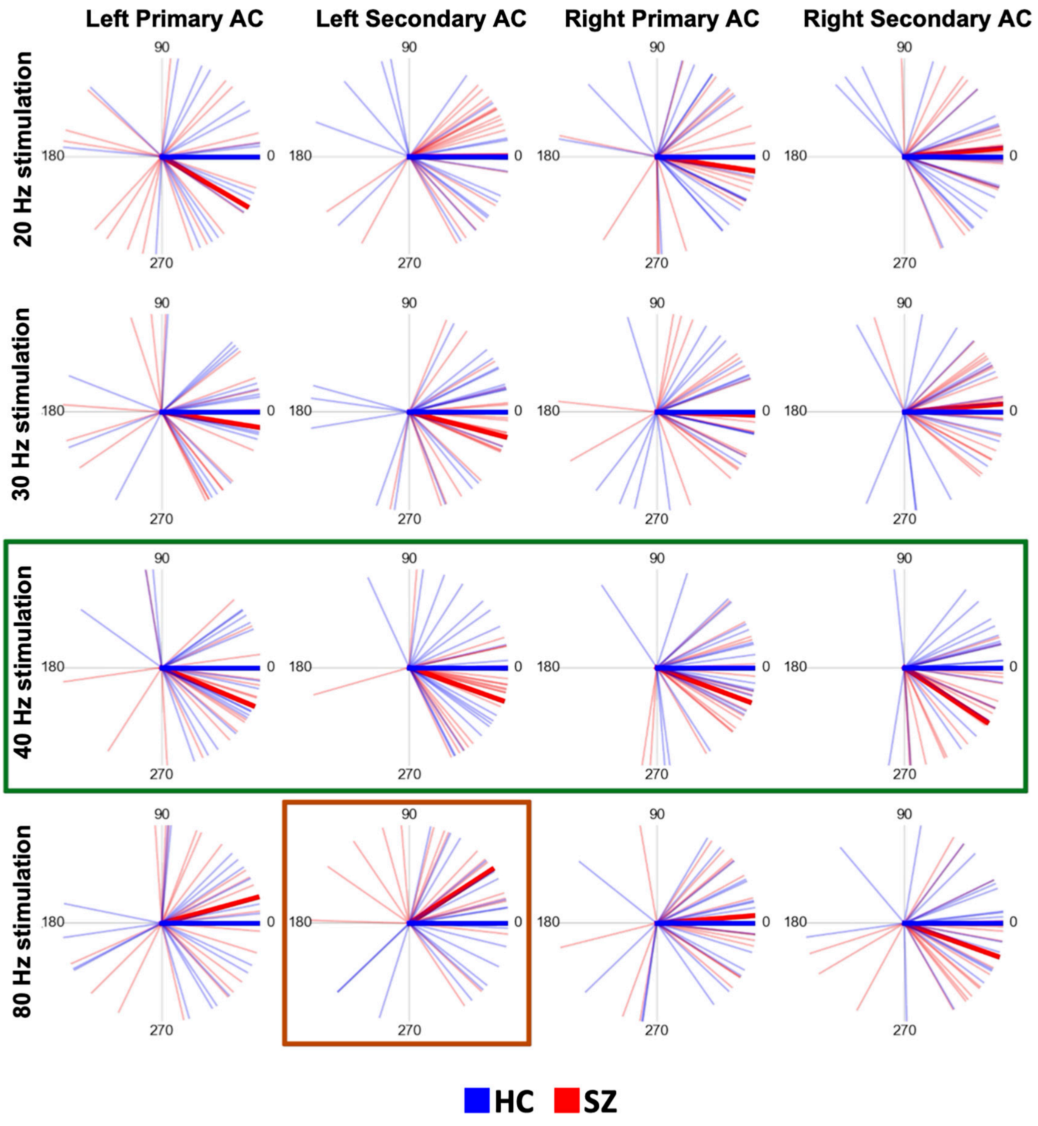

FIGURE 3
The time-averaged (200–400 ms) PLAs plotted on the polar coordinate of each subject and the grand average time-averaged PLA in each group (SZ or HC) at each stimulation frequency for each stimulus condition and each region of interest. In each plot, each thin red line indicates the time-averaged PLA of each SZ subject, each thin blue line indicates each HC subject, the thick red line indicates the grand average in the SZ group, and the thick blue line indicates the grand average in the HC group. The numbers placed circularly indicate angles (unit: degree). Each of the 4 plots on a horizontal line shows the plots derived at each stimulation frequency. Each column shows the plots in the same way as in **Figure 2**. In this figure, the thick green lines highlight the time-averaged PLAs at the 40 Hz stimulation, emphasizing that the SZ group had significant phase lags compared to the HC. The thick red lines highlight the time-averaged PLAs under 80 Hz stimulation in the left secondary auditory cortex, emphasizing that the SZ group had a significant phase lead compared to the HC group. HC, healthy control; SZ, schizophrenia; AC, auditory cortex; PLA, phase-locking angle.

the SZ group than in the HC group, no significant main effect of group or group-related interactions was observed, except for the 80 Hz condition. The detailed results of the rmANOVAs on PLF and evoked power can be found in **Supplementary Tables 1**, **2**, respectively.

3.3. PLA

Figure 3 shows the circular plots of individual PLAs at latencies of 200–400 ms separately for each stimulus condition, each hemisphere, and each ROI. The 40 Hz phase lags were clearly observed for the SZ group in both the primary and secondary auditory cortices of both hemispheres. The three-way rmANOVA on z-scored 40 Hz PLA showed that there was a significant main effect of group ($F = 4.97$, $p = 0.03$) with no group-related interactions. A *post-hoc* t-test confirmed that the SZ group had significantly lower values of z-scored 40 Hz PLA than the HC group ($t = -2.21$, $p = 0.03$, Cohen's $d = 0.75$). On the other hand, the phase lead was observed on 80 Hz ASSR in the left secondary auditory cortex in the SZ group compared to HC. In the three-way rmANOVA on the z-scored 80 Hz PLA, we found a significant group × hemisphere × ROI interaction ($F = 6.04$, $p = 0.02$). The *post hoc* analyses revealed a significant interaction between

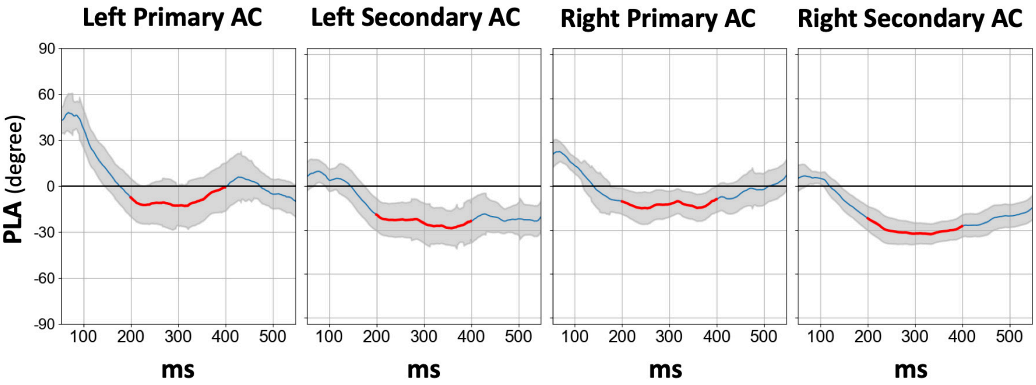

FIGURE 4
The grand average time course difference of 40 Hz PLA in the SZ group for each hemisphere and each ROI compared to HC, in which the PLA in SZ was subtracted from the PLA in HC. The thick red line in each time course indicates the time range used for statistical analysis of the PLA (200–400 ms). HC, healthy control; SZ, schizophrenia; AC, auditory cortex; PLA, phase-locking angle; ROI, regions of interest.

group and hemisphere specifically in the secondary auditory cortex ($F = 11.08$, $p < 0.01$), while no significant interaction was observed in the primary auditory cortex. In the left secondary auditory cortex, the z-scored 80 Hz PLA was significantly higher in the SZ group than in the HC group ($t = 3.04$, $p < 0.01$, Cohen's $d = 1.03$). Conversely, there was no significant group difference found in the right secondary auditory cortex ($t = -1.54$, $p = 0.13$). No main effect of group or group-related interactions was observed for the 20 Hz or 30 Hz conditions. The detailed results of the three-way rmANOVAs and the *post hoc* two-way rmANOVAs for the 80 Hz condition on the z-scored PLA are shown in Supplementary Table 3.

Figure 4 displays the temporal profile of the 40 Hz PLA in the SZ group separately for each hemisphere and ROI. In the SZ group, we observed a phase delay starting at approximately 150 ms latency, persisting for over 200 ms across all hemispheres and ROIs. Conversely, a phase lead was observed at latencies preceding 100 ms, particularly in the primary auditory cortex. To further explore this, we conducted an additional statistical analysis focusing on the 30–100 ms PLA range. However, the three-way rmANOVA did not reveal any significant main effect of group or any group-related interactions (see Supplementary Table 4 for details). The time course of the 80 Hz PLA in the SZ group on the left secondary auditory cortex is also shown in Figure 5. Notably, the 80 Hz PLA in the SZ group showed abnormal phase lead throughout most of the ASSR stimulation, with occasional instances of phase delay around a latency of 200 ms.

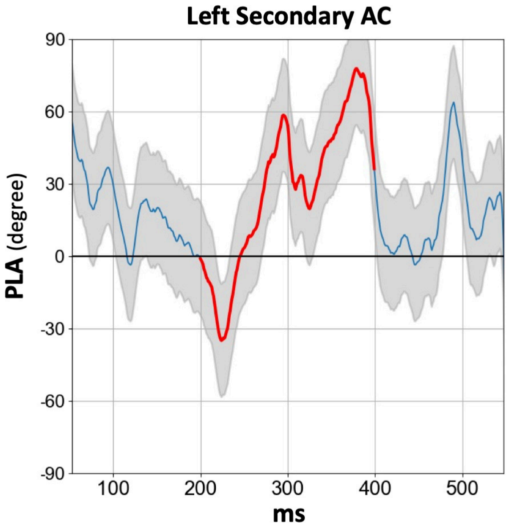

FIGURE 5
The grand average time course of 80 Hz PLA in the SZ group on the left secondary auditory cortex. The thick red line in each time course indicates the time range used for statistical analysis of the PLA (200–400 ms). HC, healthy control; SZ, schizophrenia; AC, auditory cortex; PLA, phase-locking angle.

3.4. ROC analysis

We conducted ROC curve analyses to explore the discriminant value of ASSR measures. The left panel of Figure 6 shows the ROC curve for the averaged 80 Hz evoked power across ROIs and hemispheres, aiming to distinguish between the HC and SZ groups. The area under the curve (AUC) of this ROC curve was 0.74 [95% confidence interval (CI): 0.58–0.90]. The middle and right panel of Figure 6 shows the ROC curve for averaged z-scale 80 Hz PLA on the left secondary auditory cortex and averaged z-scale 40 Hz PLA across ROIs and hemispheres, respectively. The AUCs of the ROC curves for 80 Hz and 40 Hz PLA were 0.754 (95% CI: 0.60–0.91) and 0.705 (95% CI: 0.53–0.88), respectively. The obtained AUC values from 80 Hz evoked power, 40 Hz PLA, and 80 Hz PLA indicate acceptable discrimination between the HC and SZ groups (Hosmer et al., 2013).

3.5. Correlations of gamma-band ASSR measures with clinical symptoms

The 80 Hz evoked power was not significantly correlated with PANSS subscores (positive: rho = 0.34, $p = 0.18$; negative: rho = −0.08, $p = 0.77$; general: rho = −0.03 $p = 0.93$). Similarly, no significant associations were found between z-scored PLA and

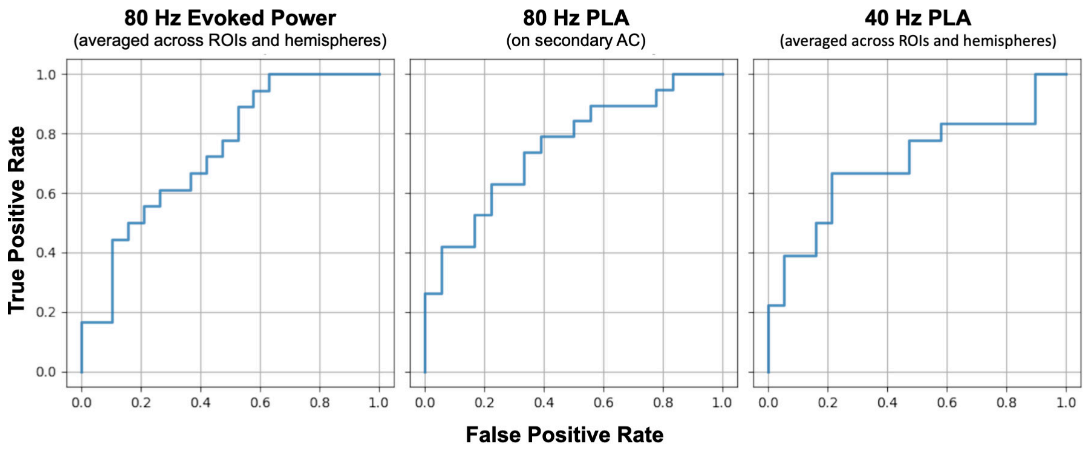

FIGURE 6
Comparison of receiver operating characteristic (ROC) curves between SZ and HC groups for 80 Hz evoked power **(left)**, 80 Hz phase lead **(middle)**, and 40 Hz phase delay **(right)**. HC, healthy control; SZ, schizophrenia; AC, auditory cortex; PLA, phase-locking angle; ROI, regions of interest.

PANSS subscales for both 40 Hz (positive: rho = 0.43, $p = 0.09$; negative: rho = 0.11, $p = 0.67$; general: rho = 0.19, $p = 0.46$) and 80 Hz conditions (positive: rho = 0.06, $p = 0.82$, negative score: rho = −0.07, $p = 0.79$, general score: rho = −0.04, $p = 0.88$).

4. Discussion

The present study aimed to explore potential abnormalities in phase entrainment of low and high gamma-band ASSRs in patients with SZ, with a particular focus on hemispheric laterality. Our results revealed the presence of abnormal phase delay in the bilateral auditory cortices of SZ patients during the 40 Hz ASSR. In contrast, we observed an abnormal phase lead specifically localized to the left secondary auditory cortex during the 80 Hz ASSR, demonstrating higher discriminability between HC and SZ when compared to the other indices. Our findings suggest that left-lateralized deficits in the 80 Hz ASSR are a neurophysiological endophenotype of SZ.

4.1. Reduced 80 Hz evoked power in SZ patients

We detected reduced 80 Hz evoked power in SZ patients in source space by applying MNE-dSPM to MEG data, as with several previous MEG studies (Hamm et al., 2011; Tsuchimoto et al., 2011). In addition, we revealed that 80 Hz evoked power had higher discriminative power between the HC and SZ groups than 20, 30, or 40 Hz evoked power. Therefore, 80 Hz ASSR stimulation can be a robust tool to assess neural oscillatory deficits in SZ. High-gamma-band activity in the brain is considered to play critical roles in several cognitive functions, such as memory and language processing (e.g., Gaona et al., 2011; Kucewicz et al., 2014; Tamura and Hirano, 2023). Notably, our previous study (Tamura and Hirano, 2023) reported that high-gamma-band activity in the auditory cortex is closely involved with accurate processing of speech temporal information. Therefore, it is expected that assessing high-gamma-band activity in SZ patients would clarify the brain mechanisms underlying their cognitive dysfunctions, although we have to develop experimental paradigms requiring more cognitive demand compared to the ASSR paradigm in future studies. On the other hand, there was no group difference in 80 Hz PLF, although sensor-level analysis in our previous study revealed reduced evoked power and PLF at sensors surrounding auditory cortices in SZ patients (Tsuchimoto et al., 2011). One possibility is that this inconsistency might be attributed to the difference in cortical distributions between evoked power and PLF on 80 Hz ASSR. Specifically, an EEG study by Tada et al. (2021) reported that 80 Hz evoked power was localized to the auditory cortex in both hemispheres, while 80 Hz PLF was distributed in broad brain regions ranging from the temporal to frontal areas.

4.2. Phase delay of the 40 Hz ASSR in SZ patients

Similar to several previous studies (Roach et al., 2019a,b, 2022; Yanagi et al., 2022), we successfully confirmed the presence of a significant phase delay during 40 Hz ASSR in SZ patients. In addition, we observed that the 40 Hz PLA exhibited greater sensitivity to differentiate SZ compared to both 40 Hz evoked power and PLF. This result supports the utility of the PLA as a measure to detect gamma-band oscillatory deficits in SZ. When examining the time course of the 40 Hz PLA, we found that, when compared to the HC group, the SZ group showed a phase lead prior to approximately 150 ms, followed by a phase delay after a latency of approximately 150 ms. Notably, there were no significant group differences observed in the early latency phase lead. It is worth noting that the ASSR comprises two distinct components: a transient component (0–100 ms) and a sustained component (over 150 ms), which are believed to have distinct neural mechanisms (Ross et al., 2002; Ross and Pantev, 2004; Ding and Simon, 2009). Therefore, we propose that the observed 40 Hz phase lead and delay in the SZ group may indicate disruptions in both the transient and sustained components of 40 Hz ASSR.

However, we were unable to replicate the left-lateralized 40 Hz phase delay observed in a previous EEG study (Roach et al., 2022).

In our study, we employed MEG with superior spatial resolution to EEG to assess the laterality of PLA deficits in gamma-band ASSRs. Notably, Edgar et al. (2017) practically confirmed that MEG has an advantage in detecting hemispheric laterality in 40 Hz ASSR compared to EEG. Our use of distributed source analysis (MNE-dSPM) is preferable to dipole source analysis, as gamma-band PLFs are known to originate from broad cortical sources (Tada et al., 2021). Therefore, it is plausible that our findings regarding the laterality of 40 Hz PLA deficits are more reliable than those of the previous study.

4.3. Left-lateralized phase lead of the 80 Hz ASSR in SZ patients

Patients with SZ exhibited an abnormal phase lead during the 200–400 ms latencies in the 80 Hz ASR, with a larger effect size compared to the phase delay observed in 40 Hz ASSR. This finding, in conjunction with the results of 80 Hz evoked power, underscores the value of utilizing 80 Hz ASSR stimulation. However, it is crucial to note that at these latencies, not only phase lead but also phase delay were observed in SZ. The phase angle in the high gamma-band ASSR might exhibit temporal instability, warranting further investigations to determine the optimal time range for assessing abnormal phase lead in SZ.

Furthermore, it is noteworthy that the abnormal phase lead observed in 80 Hz ASSR was specific to the left secondary auditory cortex. Consistent with our findings, there exists a substantial body of evidence from other studies demonstrating structural and functional abnormalities in the auditory cortex, particularly in the left hemisphere (Hajek et al., 1997; Kasai et al., 2003; Spencer et al., 2009; Hirano et al., 2010, 2015, 2020; Kompus et al., 2011; Kühn and Gallinat, 2012; Modinos et al., 2013; Shinn et al., 2013). This suggests that left-lateralized brain dysfunction might be a characteristic feature of SZ. Based on the hypothesis proposing that gamma-band oscillatory activity in the left auditory cortex plays a critical role in speech information processing with high temporal resolution (Poeppel, 2003; Poeppel et al., 2008), it is plausible that deficits in this activity could be linked to language dysfunction specific to SZ (Meyer et al., 2021). In future studies, given MEG's remarkable temporal acuity and excellent spatial resolution, it would be intriguing to examine gamma-band PLA deficits focusing on subcortical areas such as the brainstem and thalamus because they were detected as signal sources of 80 Hz ASSR (Farahani et al., 2017, 2019).

4.4. Molecular mechanisms

As outlined in the Introduction, gamma-band oscillations are well known to reflect reciprocal interactions between excitatory and inhibitory neurons (E/I balance) (Bartos et al., 2007; Sohal et al., 2009; Buzsáki and Wang, 2012). Specifically, γ-aminobutyric acid (GABA)ergic and *N*-methyl-D-aspartate (NMDA) receptor antagonists have been shown to affect stimulus-phase-locked and non-phase-locked activities on gamma-band ASSRs (Vohs et al., 2012; Sullivan et al., 2015; Sivarao et al., 2016; Yamazaki et al., 2020). Nevertheless, the majority of preclinical studies have focused on exploring molecular mechanisms associated with reduced evoked power and PLF in the 40 Hz ASSR. As far as we know, there have been no studies focusing on high-gamma-band ASSR and its associated phase lead or delay. Therefore, further translational studies investigating high gamma-band activities are warranted.

4.5. Auditory dysfunctions in SZ

Among various perceptual and cognitive deficits, early auditory deficits play a crucial role in the pathophysiology of SZ (Javitt and Sweet, 2015; Dondé et al., 2023). A recent conceptual review (Dondé et al., 2023) highlights the utility of auditory measures for treatment targets and translational biomarker research. Alternation of gamma-band ASSR is one of the most prominent neurophysiological markers for early auditory deficits in SZ (Hirano and Uhlhaas, 2021; Onitsuka et al., 2022c). In addition, the gamma-band ASSR is well-known to reflect temporal processing ability in the auditory system (Baltus and Herrmann, 2015; Dimitrijevic et al., 2016). As described above, auditory-evoked high gamma-band activity in the left hemisphere is crucial in speech-temporal information processing (Tamura and Hirano, 2023). Thus, investigating auditory dysfunctions in SZ using the ASSR paradigm is useful for detecting impaired auditory temporal information processing in SZ.

4.6. Limitations

We obtained several meaningful findings concerning low- and high-gamma-band oscillatory dysfunctions in SZ patients; however, there are several limitations in the present study. First, the number of participants included in each group is relatively modest. Consequently, further studies with a larger sample size are warranted to validate the utility of 80 Hz ASSR stimulation and PLA measurement. Second, possibly due to the limited sample size, we were unable to observe reduced PLF and evoked power on 40 Hz ASSR in SZ patients. Third, during the MEG recording, the majority of patients were under antipsychotic medication, which leaves the possibility of antipsychotic influence on our reported results, although significant correlations of gamma-band ASSR measures with CPZ equivalent dose were not observed (40 Hz PLA: $rho = 0.07$, $p = 0.79$; 80 Hz evoked power: $rho = -0.17$, $p = 0.50$; 80 Hz PLA: $rho = 0.06$, $p = 0.80$). It is necessary to conduct additional research targeting untreated drug-free patients in future studies to evaluate 80 Hz ASSR and PLA with the effects of antipsychotic medication eliminated. Fourth, aberrant observations of the 80 Hz ASSR and PLA in SZ, as revealed from our investigation, currently lack clarity regarding their disease specificity. Consequently, prospective validation will necessitate the execution of large-scale cross-disease EEG or MEG investigations. Fifth, while our present study predominantly focused on analyzing the auditory cortex due to our implementation of a passive listening task that primarily engages early sensory functions, it would be crucial to investigate the ASSR in other areas by adapting tasks such as the attentional modulation paradigm that requires higher-order cognitive processes in future studies. Sixth, while assessing the dynamic time-course of PLA to detect abnormal entrainment is crucial, our technical constraints hindered us from employing a statistical approach that could retain temporal information within circular data. The emergence of analytical methods that take into account the dynamic time-course of PLA is anticipated. Last, we could not find a clear relationship between the gamma-band PLA measure and clinical symptoms, consistent with previous studies examining gamma-band PLA in SZ. We speculate that abnormal gamma-band phase lead or delay may serve as a trait marker rather than a state marker.

5. Conclusion

Considering the prominent phase-lead abnormality of the 80 Hz ASSR, which demonstrated the highest discriminative power between HC and SZ, we propose that a comprehensive investigation of PLA during the 80 Hz ASSR paradigm holds significant promise as a robust candidate for identifying neurophysiological endophenotypes associated with SZ. Moreover, the prominent left-hemisphere phase lead observed in the deficits of 80 Hz PLA aligns with numerous prior studies, which have consistently proposed that SZ is characterized by left-lateralized brain dysfunctions. To further explore whether this measure is a promising endophenotype related to the onset, the robustness of our findings ought to be confirmed through longitudinal investigations involving a larger sample size of first-episode SZ. Notably, to enhance the elucidation of its neural dynamics, the utilization of distributed source analysis alongside MEG data would facilitate the comprehensive exploration of gamma-band oscillatory functions across cerebral regions.

Data availability statement

The datasets presented in this article are not readily available because the data that support the findings of this study are not openly available due to reasons of sensitivity and are available from the corresponding author upon reasonable request. Data are located in controlled access data storage at Kyushu University. Requests to access the datasets should be directed to YH, yhouji@gmail.com.

Ethics statement

The studies involving humans were approved by the Research Ethics Board of the Faculty of Medicine, Kyushu University (approval number 29038). The studies were conducted in accordance with the local legislation and institutional requirements. The participants provided their written informed consent to participate in this study.

Author contributions

SN: Data curation, Formal analysis, Investigation, Methodology, Visualization, Writing – original draft, Software. ST: Data curation, Formal analysis, Investigation, Methodology, Software, Visualization, Writing – original draft, Conceptualization, Resources, Supervision, Validation, Writing – review and editing. SH: Formal analysis, Resources, Supervision, Writing – review and editing, Project administration. JT: Writing – review and editing, Data curation, Investigation. KK: Data curation, Investigation, Writing – review and editing. YT: Data curation, Investigation, Writing – review and editing. TM: Data curation, Investigation, Writing – review and editing. OT: Data curation, Writing – review and editing, Methodology, Software, Supervision. TN: Supervision, Writing – review and editing, Funding acquisition, Resources. TO: Funding acquisition, Resources, Supervision, Writing – review and editing, Conceptualization, Methodology, Project administration. YH: Conceptualization, Funding acquisition, Methodology, Project administration, Resources, Supervision, Writing – review and editing, Data curation, Formal analysis, Investigation, Validation, Visualization, Writing – original draft.

Funding

The author(s) declare financial support was received for the research, authorship, and/or publication of this article. This research was supported in part by the Japan Society for the Promotion of Science (JSPS) KAKENHI under grant numbers JP20K22286 (ST), JP21K13753 (ST), JP18K07602 (SH), JP22K07617 (TO), JP18K07604 (YH), JP19H03579 (YH), JP19H00630 (YH), JP20KK0193 (YH), JP21H02851 (YH); AMED grant numbers JP19dm0207069 (TO) and JP19dm0107124h0004 (YH); and the SIRS Research Fund Award (YH).

Acknowledgments

We thank all the participants for their contribution to this research.

Conflict of interest

The authors declare that the research was conducted in the absence of any commercial or financial relationships that could be construed as a potential conflict of interest.

Publisher's note

Supplementary material

The Supplementary Material for this article can be found online at: https://www.frontiersin.org/articles/10.3389/fnins.2023.1277733/full#supplementary-material

References

Arnulfo, G., Hirvonen, J., Nobili, L., Palva, S., and Palva, J. M. (2015). Phase and amplitude correlations in resting-state activity in human stereotactical EEG recordings. *Neuroimage* 112, 114–127. doi: 10.1177/1535759719843301

Baltus, A., and Herrmann, C. S. (2015). Auditory temporal resolution is linked to resonance frequency of the auditory cortex. *Int. J. Psychophysiol.* 98, 1–7. doi: 10.1016/j.ijpsycho.2015.08.003

Bartos, M., Vida, I., and Jonas, P. (2007). Synaptic mechanisms of synchronized gamma oscillations in inhibitory interneuron networks. *Nat. Rev. Neurosci.* 8, 45–56. doi: 10.1038/nrn2044

Burgos, G. G., and Lewis, D. A. (2008). GABA neurons and the mechanisms of network oscillations: Implications for understanding cortical dysfunction in schizophrenia. *Schizophr. Bull.* 34, 944–961. doi: 10.1093/schbul/sbn070

Buzsáki, G., and Schomburg, E. W. (2015). What does gamma coherence tell us about inter-regional neural communication? *Nat. Neurosci.* 18, 484–489. doi: 10.1038/nn.3952

Buzsáki, G., and Wang, X. J. (2012). Mechanisms of gamma oscillations. *Annu. Rev. Neurosci.* 35, 203–225. doi: 10.1146/annurev-neuro-062111-150444

Dale, A. M., Liu, A. K., Fischl, B. R., Buckner, R. L., Belliveau, J. W., Lewine, J. D., et al. (2000). Dynamic statistical parametric mapping: Combining fMRI and MEG for high-resolution imaging of cortical activity. *Neuron* 26, 55–67. doi: 10.1016/s0896-6273(00)81138-1

Destrieux, C., Fischl, B., Dale, A. M., and Halgren, E. (2010). Automatic parcellation of human cortical gyri and sulci using standard anatomical nomenclature. *Neuroimage* 53, 1–15. doi: 10.1016/j.neuroimage.2010.06.010

Dimitrijevic, A., Alsamri, J., John, M. S., Purcell, D., George, S., and Zeng, F. G. (2016). Human envelope following responses to amplitude modulation: Effects of aging and modulation depth. *Audiology* 37, 322–335. doi: 10.1097/AUD.0000000000000324

Ding, N., and Simon, J. Z. (2009). Neural representations of complex temporal modulations in the human auditory cortex. *J. Neurophysiol.* 102, 2731–2743. doi: 10.1152/jn.00523.2009

Dondé, C., Kantrowitz, J. T., Medalia, A., Alice, S. M., Balla, A., Sehatpour, P., et al. (2023). Early auditory processing dysfunction in schizophrenia: Mechanisms and implications. *Neurosci. Biobehav. Rev.* 148:105098. doi: 10.1016/j.neubiorev.2023.105098

Edgar, J. C., Chen, Y. H., Lanza, M., Howell, B., Chow, V. Y., Heiken, K., et al. (2014). Cortical thickness as a contributor to abnormal oscillations in schizophrenia? *Neuroimage Clin.* 4, 122–129. doi: 10.1016/j.nicl.2013.11.004

Edgar, J. C., Fisk, C. L. IV, Chen, Y., Stone-Howell, B., Hunter, M. A., Huang, M., et al. (2017). By our bootstraps: Comparing methods for measuring auditory 40 Hz steady-state neural activity. *Psychophysiology* 54, 1110–1127. doi: 10.1111/psyp.12876

Edgar, J. C., Fisk, C. L. IV, Chen, Y., Stone-Howell, B., Liu, S., Hunter, M. A., et al. (2018). Identifying auditory cortex encoding abnormalities in schizophrenia: The utility of low-frequency versus 40 Hz steady-state measures. *Psychophysiology* 55:e13074. doi: 10.1111/psyp.13074

Farahani, E. D., Goossens, T., Wouters, J., and van Wieringen, A. (2017). Spatiotemporal reconstruction of auditory steady-state responses to acoustic amplitude modulations: Potential sources beyond the auditory pathway. *Neuroimage* 148, 240–253. doi: 10.1016/j.neuroimage.2017.01.032

Farahani, E. D., Wouters, J., and van Wieringen, A. (2019). Contributions of non-primary cortical sources to auditory temporal processing. *Neuroimage* 191, 303–314. doi: 10.1016/j.neuroimage.2019.02.037

First, M. B. (2002). The DSM series and experience with DSM-IV. *Psychopathology* 35, 67–71.

Fries, P., Nikolić, D., and Singer, W. (2007). The gamma cycle. *Trends. Neurosci.* 30, 309–316. doi: 10.1016/j.tins.2007.05.005

Gandal, M. J., Sisti, J., Klook, K., Ortinski, P., Leitman, V., Liang, Y., et al. (2012). GABAB-mediated rescue of altered excitatory-inhibitory balance, gamma synchrony and behavioral deficits following constitutive NMDAR-hypofunction. *Transl. Psychiatry* 2:e142. doi: 10.1038/tp.2012.69

Gaona, C. M., Sharma, M., Freudenburg, Z. V., Breshears, J. D., Bundy, D. T., Roland, J., et al. (2011). Nonuniform high-gamma (60-500 Hz) power changes dissociate cognitive task and anatomy in human cortex. *J. Neurosci.* 9, 2091–2100. doi: 10.1523/JNEUROSCI.4722-10.2011

Grent-'t-Jong, T., Gajwani, R., Gross, J., Gumley, A. I, Krishnadas, R., Lawrie, S. M., et al. (2021). 40-Hz auditory steady-state responses characterize circuit dysfunctions and predict clinical outcomes in clinical high-risk for psychosis participants: A magnetoencephalography study. *Biol. Psychiatry* 90, 419–429. doi: 10.1016/j.biopsych.2021.03.018

Hajek, M., Huonker, R., Boehle, C., Hans-Peter, V., Nowak, H., and Sauer, H. (1997). Abnormalities of auditory evoked magnetic fields and structural changes in the left hemisphere of male schizophrenics—a magnetoencephalographic magnetic resonance imaging study. *Biol. Psychiatry* 42, 609–616. doi: 10.1016/s0006-3223(96)00428-3

Hamm, J. P., Gilmore, C. S., Picchetti, N. A., Sponheim, S. R., and Clementz, B. A. (2011). Abnormalities of neuronal oscillations and temporal integration to low-and high-frequency auditory stimulation in schizophrenia. *Biol. Psychiatry* 69, 989–996. doi: 10.1016/j.biopsych.2010.11.021

Hirano, Y., and Uhlhaas, P. J. (2021). Current findings and perspectives on aberrant neural oscillations in schizophrenia. *Psychiatry Clin. Neurosci.* 75, 358–368. doi: 10.1111/pcn.13300

Hirano, Y., Hirano, S., Maekawa, T., Obayashi, C., Oribe, N., Monji, A., et al. (2010). Auditory gating deficit to human voices in schizophrenia: A MEG study. *Schizophr. Res.* 117, 61–67. doi: 10.1016/j.schres.2009.09.003

Hirano, Y., Oribe, N., Kanba, S., Onitsuka, T., Nestor, P. G., and Spencer, K. M. (2015). Spontaneous gamma activity in schizophrenia. *JAMA Psychiatry* 72, 813–821. doi: 10.1001/jamapsychiatry.2014.2642

Hirano, Y., Oribe, N., Onitsuka, T., Kanba, S., Nestor, P. G., Hosokawa, T., et al. (2020). Auditory cortex volume and gamma oscillation abnormalities in schizophrenia. *Clin. EEG Neurosci.* 51, 244–251. doi: 10.1177/1550059420914201

Hironaga, N., Takei, Y., Mitsudo, T., Kimura, T., and Hirano, Y. (2020). Prospects for future methodological development and application of magnetoencephalography devices in psychiatry. *Front. Psychiatry* 11:863. doi: 10.3389/fpsyt.2020.00863

Hosmer, D. W., Lemeshow, S., and Sturdivant, R. X. (2013). "Assessing the fit of the model," in *Applied logistic regression*, 3rd Edn, eds W. A. Shewhart and S. S. Wilks (Hoboken, NJ: Wiley), 173–181.

Inada, T., and Inagaki, A. (2015). Psychotropic dose equivalence in Japan. *Psychiatry Clin. Neurosci.* 69, 440–447. doi: 10.1111/pcn.12275

Javitt, D. C., and Sweet, R. A. (2015). Auditory dysfunction in schizophrenia: Integrating clinical and basic features. *Nat Rev Neurosci.* 16, 535–550. doi: 10.1038/nrn4002

Kasai, K., Shenton, M. E., Salisbury, D. F., Hirayasu, Y., Lee, C. U., Ciszewski, A. A., et al. (2003). Progressive decrease of left superior temporal gyrus gray matter volume in patients with first-episode schizophrenia. *Am. J. Psychiatry.* 160, 156–164. doi: 10.1176/appi.ajp.160.1.156

Kay, S. R., Fiszbein, A., and Opler, L. A. (1987). The positive and negative syndrome scale (PANSS) for schizophrenia. *Schizophr. Bull.* 13, 261–276. doi: 10.1093/schbul/13.2.261

Kirihara, K., Rissling, A. J., Swerdlow, N. R., Braff, D. L., and Light, G. A. (2012). Hierarchical organization of gamma and theta oscillatory dynamics in schizophrenia. *Biol. Psychiatry* 71, 873–880. doi: 10.1016/j.biopsych.2012.01.016

Kompus, K., Westerhausen, R., and Hugdahl, K. (2011). The "paradoxical" engagement of the primary auditory cortex in patients with auditory verbal hallucinations: A meta-analysis of functional neuroimaging studies. *Neuropsychologia* 49, 3361–3369. doi: 10.1016/j.neuropsychologia.2011.08.010

Koshiyama, D., Kirihara, K., Tada, M., Nagai, T., Fujioka, M., Ichikawa, E., et al. (2018). Electrophysiological evidence for abnormal glutamate-GABA association following psychosis onset. *Transl. Psychiatry* 8:211. doi: 10.1038/s41398-018-0261-0

Koshiyama, D., Miyakoshi, M., Tanaka-Koshiyama, K., Sprock, J., and Light, G. A. (2022). High-power gamma-related delta phase alteration in schizophrenia patients at rest. *Psychiatry Clin. Neurosci.* 76, 179–186. doi: 10.1111/pcn.13331

Kucewicz, M. T., Cimbalnik, J., Matsumoto, J. Y., Brinkmann, B. H., Bower, M. R., Vasoli, V., et al. (2014). High frequency oscillations are associated with cognitive processing in human recognition memory. *Brain* 137, 2231–2244. doi: 10.1093/brain/awu149

Kühn, S., and Gallinat, J. (2012). Quantitative meta-analysis on state and trait aspects of auditory verbal hallucinations in schizophrenia. *Schizophr. Bull.* 38, 779–786. doi: 10.1093/schbul/sbq152

Kwon, J. S., O'Donnell, B. F., Wallenstein, G. V., Greene, R. W., Hirayasu, Y., Nestor, P. G., et al. (1999). Gamma frequency–range abnormalities to auditory stimulation in schizophrenia. *Arch. Gen. Psychiatry* 56, 1001–1005. doi: 10.1001/archpsyc.56.11.1001

Larson, E., and Taulu, S. (2017). Reducing sensor noise in MEG and EEG recordings using oversampled temporal projection. *IEEE Trans. Biomed. Eng.* 65, 1002–1013. doi: 10.1109/TBME.2017.2734641

Maharajh, K., Teale, P., Rojas, D. C., and Reite, M. L. (2010). Fluctuation of gamma-band phase synchronization within the auditory cortex in schizophrenia. *Clin. Neurophysiol.* 121, 542–548. doi: 10.1016/j.clinph.2009.12.010

Meyer, L., Lakatos, P., and He, Y. (2021). Language dysfunction in schizophrenia: Assessing neural tracking to characterize the underlying disorder (s)? *Front. Neurosci.* 15:640502. doi: 10.3389/fnins.2021.640502

Modinos, G., Costafreda, S. G., van Tol, M. J., McGuire, P. K., Aleman, A., and Allen, P. (2013). Neuroanatomy of auditory verbal hallucinations in schizophrenia: A quantitative meta-analysis of voxel-based morphometry studies. *Cortex* 49, 1046–1055. doi: 10.1016/j.cortex.2012.01.009

Murphy, N., Ramakrishnan, N., Walker, C. P., Polizzotto, N. R., and Cho, R. Y. (2020). Intact auditory cortical cross-frequency coupling in early and chronic schizophrenia. *Front. Psychiatry* 11:507. doi: 10.3389/fpsyt.2020.00507

Nenonen, J., Nurminen, J., Kičić, D., Bikmullina, R., Lioumis, P., Jousmäki, V., et al. (2012). Validation of head movement correction and spatiotemporal signal space separation in magnetoencephalography. *Clin. Neurophysiol.* 123, 2180–2191. doi: 10.1016/j.clinph.2012.03.080

Onitsuka, T., Hirano, Y., Nakazawa, T., Ichihashi, K., Miura, K., Inada, K., et al. (2022a). Toward recovery in schizophrenia: Current concepts, findings, and future research directions. *Psychiatry Clin. Neurosci.* 76, 282–291. doi: 10.1111/pcn.13342

Onitsuka, T., Hirano, Y., Nemoto, K., Hashimoto, N., Kushima, I., Koshiyama, D., et al. (2022b). Trends in big data analyses by multicenter collaborative translational research in psychiatry. *Psychiatry Clin. Neurosci.* 76, 1–14. doi: 10.1111/pcn.13311

Onitsuka, T., Tsuchimoto, R., Oribe, N., Spencer, K. M., and Hirano, Y. (2022c). Neuronal imbalance of excitation and inhibition in schizophrenia: A scoping review of gamma-band ASSR findings. *Psychiatry Clin. Neurosci.* 76, 610–619. doi: 10.1111/pcn.13472

Parker, D. A., Hamm, J. P., McDowell, J. E., Keedy, S. K., Gershon, E. S., Ivleva, E. I., et al. (2019). Auditory steady-state EEG response across the schizo-bipolar spectrum. *Schizophr. Res.* 209, 218–226. doi: 10.1016/j.schres.2019.04.014

Poeppel, D. A. (2003). The analysis of speech in different temporal integration windows: Cerebral lateralization as 'asymmetric sampling in time'. *Speech Commun.* 41, 245–255. doi: 10.1016/S0167-6393(02)00107-3

Poeppel, D. A., Idsardi, W. J., and Van Wassenhove, V. (2008). Speech perception at the interface of neurobiology and linguistics. *Philos. Trans. R. Soc. Lond. B Biol. Sci.* 363, 1071–1086. doi: 10.1098/rstb.2007.2160

Roach, B. J., D'Souza, D. C., Ford, J. M., and Mathalon, D. H. (2019a). Test-retest reliability of time-frequency measures of auditory steady-state responses in patients with schizophrenia and healthy controls. *Neuroimage Clin.* 23:101878. doi: 10.1016/j.nicl.2019.101878

Roach, B. J., Ford, J. M., and Mathalon, D. H. (2019b). Gamma band phase delay in schizophrenia. *Biol. Psychiatry Cogn. Neurosci. Neuroimaging* 4, 131–139. doi: 10.1016/j.bpsc.2018.08.011

Roach, B. J., Hirano, Y., Ford, J. M., Spencer, K. M., and Mathalon, D. H. (2022). Phase delay of the 40 Hz auditory steady-state response localizes to left auditory cortex in schizophrenia. *Clin. EEG Neurosci.* 54, 370–378. doi: 10.1177/15500594221130896

Ross, B., and Pantev, C. (2004). Auditory steady-state responses reveal amplitude modulation gap detection thresholds. *J. Acoust. Soc. Am.* 115, 2193–2206. doi: 10.1121/1.1694996

Ross, B., Picton, T. W., and Pantev, C. (2002). Temporal integration in the human auditory cortex as represented by the development of the steady-state magnetic field. *Hear. Res.* 165, 68–84. doi: 10.1016/s0378-5955(02)00285-x

Shinn, A. K., Baker, J. T., Cohen, B. M., and Öngür, D. (2013). Functional connectivity of left Heschl's gyrus in vulnerability to auditory hallucinations in schizophrenia. *Schizophr. Res.* 143, 260–268. doi: 10.1016/j.schres.2012.11.037

Sivarao, D. V., Chen, P., Senapati, A., Yang, Y., Fernandes, A., Benitex, Y., et al. (2016). 40 Hz auditory steady-state response is a pharmacodynamic biomarker for cortical NMDA receptors. *Neuropsychopharmacology* 41, 2232–2240. doi: 10.1038/npp.2016.17

Sohal, V. S. (2022). Transforming discoveries about cortical microcircuits and gamma oscillations into new treatments for cognitive deficits in schizophrenia. *Am. J. Psychiatry* 179, 267–276. doi: 10.1176/appi.ajp.20220147

Sohal, V. S., Zhang, F., Yizhar, O., and Deisseroth, K. (2009). Parvalbumin neurons and gamma rhythms enhance cortical circuit performance. *Nature* 459, 698–702. doi: 10.1038/nature07991

Spencer, K. M., Niznikiewicz, M. A., Nestor, P. G., Shenton, M. E., and McCarley, R. W. (2009). Left auditory cortex gamma synchronization and auditory hallucination symptoms in schizophrenia. *BMC Neurosci.* 10:85. doi: 10.1186/1471-2202-10-85

Spencer, K. M., Salisbury, D. F., Shenton, M. E., and McCarley, R. W. (2008). Gamma-band auditory steady-state responses are impaired in first episode psychosis. *Biol. Psychiatry* 64, 369–375. doi: 10.1016/j.biopsych.2008.02.021

Sullivan, E. M., Timi, P., Hong, L. E., and O'Donnell, P. (2015). Effects of NMDA and GABA-A receptor antagonism on auditory steady-state synchronization in awake behaving rats. *Int. J. Neuropsychopharmacol.* 18:yu118. doi: 10.1093/ijnp/pyu118

Tada, M., Kirihara, K., Ishishita, Y., Takasago, M., Kunii, N., Uka, T., et al. (2021). Global and parallel cortical processing based on auditory gamma oscillatory responses in humans. *Cereb. Cortex* 31, 4518–4532. doi: 10.1093/cercor/bhab103

Tada, M., Nagai, T., Kirihara, K., Koike, S., Suga, M., Araki, T., et al. (2016). Differential alterations of auditory gamma oscillatory responses between pre-onset high-risk individuals and first-episode schizophrenia. *Cereb. Cortex* 26, 1027–1035. doi: 10.1093/cercor/bhu278

Tagawa, M., Takei, Y., Kato, Y., Suto, T., Hironaga, N., Ohki, T., et al. (2022). Disrupted local beta band networks in schizophrenia revealed through graph analysis: A magnetoencephalography study. *Psychiatry Clin. Neurosci.* 76, 309–320. doi: 10.1111/pcn.13362

Tamura, S., and Hirano, Y. (2023). Cortical representation of speech temporal information through high gamma-band activity and its temporal modulation. *Cereb. Cortex* 33, 8773–8782. doi: 10.1093/cercor/bhad158

Teale, P., Carlson, J., Rojas, D., and Reite, M. (2003). Reduced laterality of the source locations for generators of the auditory steady-state field in schizophrenia. *Biol. Psychiatry* 54, 1149–1153. doi: 10.1016/s0006-3223(03)00411-6

Teale, P., Collins, D., Maharajh, K., Rojas, D. C., Kronberg, E., and Reite, M. (2008). Cortical source estimates of gamma band amplitude and phase are different in schizophrenia. *Neuroimage* 42, 1481–1489. doi: 10.1016/j.neuroimage.2008.06.020

Thuné, H., Recasens, M., and Uhlhaas, P. J. (2016). The 40-Hz auditory steady-state response in patients with schizophrenia: A meta-analysis. *JAMA Psychiatry* 73, 1145–1153. doi: 10.1001/jamapsychiatry.2016.2619

Tsuchimoto, R., Kanba, S., Hirano, S., Oribe, N., Ueno, T., Hirano, Y., et al. (2011). Reduced high and low frequency gamma synchronization in patients with chronic schizophrenia. *Schizophr. Res.* 133, 99–105. doi: 10.1016/j.schres.2011.07.020

Uhlhaas, P. J., and Singer, W. (2010). Abnormal neural oscillations and synchrony in schizophrenia. *Nat. Rev. Neurosci.* 11, 100–113. doi: 10.1038/nrn2774

Vohs, J. L., Chambers, R. A., O'Donnell, B. F., Krishnan, G. P., and Morzorati, S. L. (2012). Auditory steady state responses in a schizophrenia rat model probed by excitatory/inhibitory receptor manipulation. *Int. J. Psychophysiol.* 86, 136–142. doi: 10.1016/j.ijpsycho.2012.04.002

von Stein, A., and Sarnthein, J. (2000). Different frequencies for different scales of cortical integration: From local gamma to long range alpha/theta synchronization. *Int. J. Psychophysiol.* 38, 301–313. doi: 10.1016/s0167-8760(00)00172-0

Yamazaki, M., Honda, S., Tamaki, K., Irie, M., and Mihara, T. (2020). Effects of (+)-bicuculline, a GABAa receptor antagonist, on auditory steady state response in free-moving rats. *PLoS One* 15:e0236363. doi: 10.1371/journal.pone.0236363

Yanagi, M., Tsuchiya, A., Hosomi, F., Terada, T., Ozaki, S., Shirakawa, O., et al. (2022). Evaluating delay of gamma oscillations in patients with schizophrenia using evoked response audiometry system. *Sci. Rep.* 12:11327. doi: 10.1038/s41598-022-15311-6

frontiers | Frontiers in Neuroscience

TYPE Original Research
PUBLISHED 09 November 2023
DOI 10.3389/fnins.2023.1277690

EDITED BY
Zhiyong Zhao,
Zhejiang University, China

REVIEWED BY
Wenxin Niu,
Tongji University, China
Lanxin Ji,
New York University, United States

*CORRESPONDENCE
Wenyu Jiang
✉ wenyu_jiang@163.com

RECEIVED 15 August 2023
ACCEPTED 19 October 2023
PUBLISHED 09 November 2023

CITATION
Wu P, Wang C, Wei M, Li Y, Xue Y, Li X, Jiang J, Bi Y, Dai J and Jiang W (2023) Prefrontal cortex functional connectivity changes during verbal fluency test in adults with short-term insomnia disorder: a functional near-infrared spectroscopy study.
Front. Neurosci. 17:1277690.
doi: 10.3389/fnins.2023.1277690

Prefrontal cortex functional connectivity changes during verbal fluency test in adults with short-term insomnia disorder: a functional near-infrared spectroscopy study

Peirong Wu[1], Chaowen Wang[2], Mindong Wei[2], Yijiang Li[3], Yuan Xue[2], Xinrong Li[1], Jianfan Jiang[1], Yinuo Bi[2], Jian Dai[4] and Wenyu Jiang[1]*

[1]Department of Neurological Rehabilitation, Jiangbin Hospital of Guangxi Zhuang Autonomous Region, Nanning, China, [2]Cognitive Rehabilitation Center, Jiangbin Hospital of Guangxi Zhuang Autonomous Region, Nanning, China, [3]Faculty of Science and Engineering, University of Nottingham Ningbo, Ningbo, China, [4]Department of Clinical Psychology, Jiangbin Hospital of Guangxi Zhuang Autonomous Region, Nanning, China

Background: Individuals suffering from short-term insomnia disorder (SID) experience difficulties in falling or staying asleep, often leading to daytime fatigue and impaired concentration. However, the underlying mechanisms of SID remain unclear. This study aims to investigate the alterations in brain activation patterns and functional connectivity in patients with SID.

Methods: The study enrolled a total of 31 adults diagnosed with SID and 31 healthy controls (HC). Functional near-infrared spectroscopy (fNIRS) was utilized to assess the concentrations of oxyhemoglobin (Oxy-Hb) and functional connectivity in the prefrontal cortex of each participant while performing the verbal fluency test (VFT) task.

Results: In the VFT task, no significant difference was found between the SID group and the HC group in terms of integral values, centroid values, and mean Oxy-Hb variations. These findings suggest that both groups exhibit similar hemodynamic responses. However, the functional connectivity analysis revealed significant differences in inter-channel connectivity strength between the two groups. The SID group showed significantly lower average inter-channel connectivity strength compared to the HC group. Moreover, six channel pairs (right frontopolar cortex – left frontopolar cortex, left orbitofrontal cortex – left temporopolar cortex, left temporopolar cortex – left frontopolar cortex, left frontopolar cortex-Ch38, left frontopolar cortex – right pre-motor and supplementary motor cortex, and left frontopolar cortex – right dorsolateral prefrontal cortex) exhibited significantly higher connectivity strength in the HC group compared to the SID group (FDR corrected, $p<0.05$). Specifically, channel 27 exhibited the highest frequency of significant connectivity across different channel pairs, occurring five times in total. The channel pair Ch27-Ch39, representing left frontopolar cortex and right dorsolateral prefrontal cortex, exhibited a negative correlation with PSQI scores ($r=-0.422$, $p=0.018$).

Conclusion: Our findings suggest that patients with SID may exhibit altered brain connectivity during the VFT task, as measured by fNIRS. These results provide valuable insights into the functional brain differences associated with SID. Further research is needed to validate and expand upon these findings.

KEYWORDS

functional near-infrared spectroscopy, short-term insomnia disorder, verbal fluency test, functional connectivity, prefrontal cortex

1. Introduction

According to a White paper on healthy sleep published on the internet in 2023, over 60% of the Chinese population suffers from sleep-related issues. Insufficient sleep has been associated with memory decline, weakened immunity, negative emotions, and increased risk of endocrine disorders and cardiovascular diseases (Bin Heyat et al., 2021). Insomnia, a prevalent sleep disorder, is characterized by difficulties falling asleep, sleep maintenance problems, early waking, and impaired daytime functioning (Patel et al., 2018). Short-term insomnia disorder (SID) is diagnosed when symptoms persist for less than 3 months (Vargas et al., 2020). Approximately 27% of the population experiences SID annually, with about 72% recovering without any treatment. However, a subset of people with persistent symptoms progress to chronic insomnia disorder (CID; LeBlanc et al., 2009). Despite sharing similar clinical symptoms, SID and CID exhibit distinct pathophysiological bases and clinical characteristics, such as etiology, incidence, symptom severity. While SID arises from acute hyperarousal, CID is more likely due to prolonged exposure to hyperarousal and poor sleep patterns, leading to a "conditioned" arousal (Vargas et al., 2020). Thus, SID and CID should not be considered different stages of a single disease, and CID should not be solely explained by a single pattern of hyperarousal. Therefore, studying SID contributes to a deeper understanding of its unique pathophysiological basis and clinical characteristics, in order to provide more individualized and effective interventions for this condition, and to avoid simply regarding SID as an early stage of CID, thus offering better treatment and management strategies for patients.

Investigators are increasingly focusing on the neuropathological mechanism of insomnia and tailoring clinical treatments accordingly. Neuroimaging studies have demonstrated that the prefrontal cortex (PFC) as a critical brain region involved sleep regulation and maintenance (Perrier et al., 2015; Anastasiades et al., 2022). The PFC becomes progressively deactivated during the transition from wakefulness to non-rapid eyes movement (NREM) sleep, and this deactivation intensifies with deeper NREM sleep, subsequently reactivating during sleep (Muzur et al., 2002). Moreover, sleep deprivation has been found to impair brain network function in the PFC, highlighting its vulnerability to insomnia (Mukli et al., 2021). Previous neuroimaging studies have shown that individuals with primary insomnia exhibit the following: (1) increased overall brain metabolism during wakefulness and sleep (Nofzinger et al., 2004), (2) decreased relative metabolism in the PFC compared to other brain region during wakefulness (Nofzinger et al., 2004), and (3) reduced PFC response during verbal fluency test (VFT) task compared to healthy individuals (Gong et al., 2022).

The VFT task is a widely utilized assessment tool for evaluating language and executive control abilities in individuals with neurological and psychiatric disorders (Xu et al., 2023). These abilities are closely linked to fundamental cognitive functions such as working memory, motivation, and attention. Published NIRS studies have demonstrated that patients with CID exhibit abnormal prefrontal activation during the VFT task (Sun et al., 2017; Gong et al., 2022). Based on this evidence, it is logical to hypothesize that the cognitive decline observed in individuals with insomnia is associated with dysfunction in the prefrontal cortex (PFC). Consequently, the integration of NIRS and the VFT task allows for the assessment of PFC function and identification of cognitive impairment in individuals with insomnia.

However, the majority of research conducted on insomnia thus far has primarily focused on patients with CID, whereas less attention has been directed towards SID and its underlying mechanisms remain unclear. In recent years, functional near-infrared spectroscopy (fNIRS), a non-invasive optical imaging technique used to monitor cerebral cortex oxygenation and dynamics, has been extensively employed to observe brain activity patterns in various diseases, leading to a better understanding of the mechanisms underlying neuropsychiatric impairments. Compared to other neuroimaging methods, fNIRS offers the advantages of portability, cost-effectiveness, and relative insensitivity to movement, making it suitable for assessing brain activity in different environments. By utilizing fNIRS to evaluate of PFC activity in individuals suffering from SID, it may be possible to explore the underlying mechanisms of SID and provide valuable insights for clinical interventions.

The present study aims to utilize fNIRS to investigate the changes in PFC activation and functional connectivity in patients with SID during a verbal fluency test (VFT) task. Additionally, the study seeks to explore the relationship between these alterations and impaired sleep quality.

2. Materials and methods

2.1. Participants

For this research, a total of 31 patients with SID and 31 gender-, age-and education-matched healthy controls (HC) were recruited from the community. The sleep quality of all participants in the past month was assessed using the Pittsburgh Sleep Quality Index (PSQI). Cognitive status was evaluated using the Montreal Cognitive Assessment (MoCA), while anxiety and depression levels were measured using the Hamilton Anxiety Rating Scale (HAMA) and Hamilton Depression Rating Scale ($HAMD_{24}$), respectively.

The inclusion criteria for the SID group were as follows: (1) meeting the diagnostic criteria of short-term insomnia disorder outlined in third edition of the International Classification of Sleep

Disorders (ICSD-3; Medicine AAoS, 2014), with insomnia occurring at least 3 days per week for a duration of 1 week to 3 months; (2) PSQI score > 7 (Buysse et al., 1989); (3) MoCA score > 26; (4) right-handedness. The exclusion criteria included: (1) taking neuropsychiatric drugs within past 3 months; (2) presence of cognitive impairment, emotional disorders, neuropsychiatric disorders, or any serious physical illnesses. Control volunteers with similar social backgrounds and PSQI scores ≤7 were enrolled, except for left-handers and individuals with neurological or psychiatric illnesses.

The study protocol was approved by the Ethics Committee of Jiangbin Hospital of Guangxi Zhuang Autonomous Region. All individuals involved in the study were fully informed about the study and provided written informed consent.

2.2. Verbal fluency test

The verbal fluency test (VFT) task was conducted to elicit the cerebral cortex activation. The entire test was conducted in a quiet and comfortable environment. Prior to initiating the formal test, all participants were provided with detailed instructions regarding the task procedure and were given an opportunity to practice. The VFT task consisted of three consecutive trials: a 30-s pre-task baseline, a 60-s task period, and a 70-s post-task baseline (as illustrated in Figure 1A). During the pre-task baseline, participants were instructed to repeatedly count from 1 to 5. In the task period, participants were required to generate as many words as possible using the Chinese characters "白" (representing white), "北" (representing north), and "大" (representing big). Lastly, during the post-task baseline, participants again repeated the act of counting from 1 to 5 repeatedly. To prevent periods of silence, the given three characters were changed every 20 s during the 60-s task period. The total number of correct words generated was recorded as a measure of task performance.

2.3. NIRS measurement

The changes in hemoglobin (Hb) concentration were measured using a multi-channel NIRS instrument (NirScan-6000C, Danyang Huichuang Medical Equipment Co., Ltd., China) that utilized laser diodes emitting two wavelengths (730 and 850 nm) during the VFT task. The sampling frequency was set at 11 Hz. A total of 31 probes (comprising 15 sources and 16 detectors) were positioned at a fixed distance of 3 cm. The placement of these probes followed the 10/20 international electrode placement system, with the FPz channel serving as the center of detector D3, and the lowest probes positioned along the Fp1-Fp2 line. Each pair of sources and detectors formed a channel, allowing for the observation of hemoglobin concentration information at a depth of 2–3 cm beneath the scalp. A total of 48 channels were created, symmetrically distributed across the bilateral PFC and temporal cortex of each participant (Figures 1B,C). The channels and corresponding brain areas are detailed in Supplementary Table 1.

2.4. Data processing and analysis

The processing of near-infrared spectroscopy data was conducted using NirSpark software (Huichuang, China), which has been used in previous research (Li et al., 2020). Preprocessing steps involved an initial inspection of the raw data by an expert to identify and discard poor-quality signals. Participants with more than five bad channels

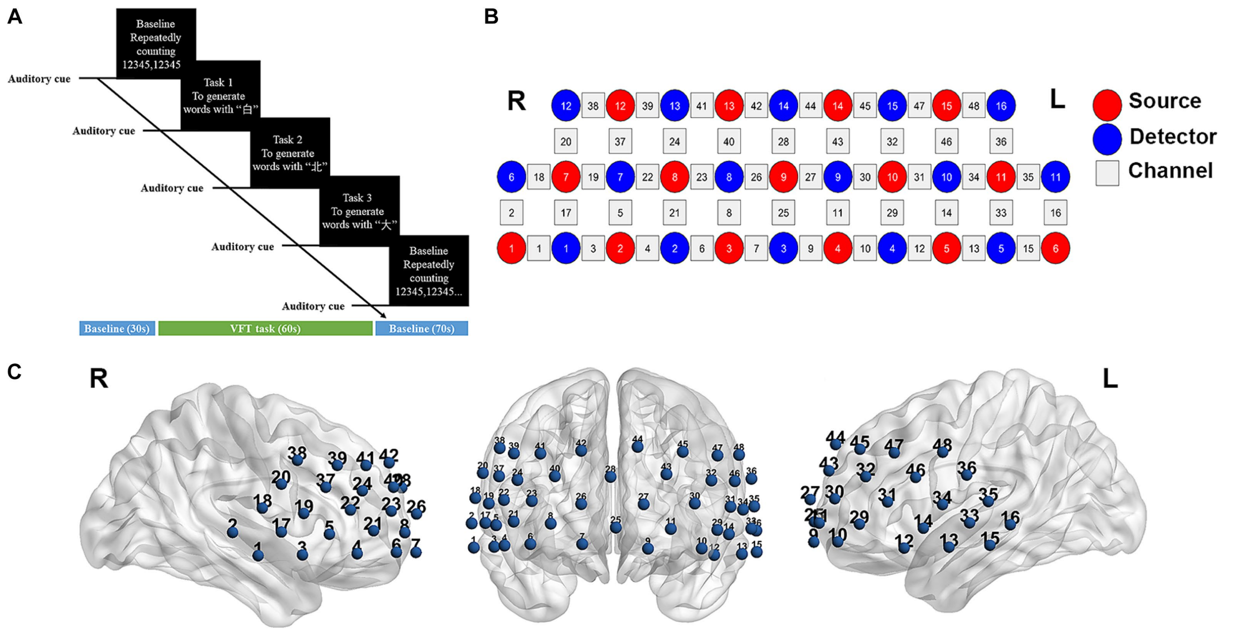

FIGURE 1
fNIRS data acquisition. **(A)** The task procedure of verbal fluency test (VFT). **(B)** Measurement points of the 48-channel NIRS system. Red and blue circles represent light source and detector, respectively. Gray squares represent the location of each probes pair (channel). **(C)** Three-dimensional detection regions of 48 channels. L, left; R, right.

were excluded from further analysis. Motion artifacts were addressed using a spline interpolation algorithm, a commonly employed method for correcting localized artifacts. Motion artifacts typically manifest as sudden jumps or cliff-like changes caused by the relative displacement of the scalp and the probe (Sutoko et al., 2020). Physiological noise, such as respiration, cardiac activity, and low-frequency signal drift, were mitigated through band-pass filtering set between 0.01 and 0.1 Hz. The modified Beer–Lambert law was employed to calculate relative changes in both oxygenated hemoglobin (Oxy-Hb) and deoxygenated hemoglobin (Deoxy-Hb) concentrations (Xia et al., 2022). Among the two, Oxy-Hb has a higher signal-to-noise ratio and was analyzed as the primary index for observing hemodynamic changes (Hoshi et al., 2001).

The start time of the VFT task period was set as "0 s," and the hemodynamic response function (HRF) was defined with an initial time of −10 s and an end time of 115 s (Liu et al., 2022). Specifically, "−10–0 s" represented the pre-baseline state, while "0–60s" corresponded to the duration of the block paradigm, and "60–115 s" represented the post-baseline period. For each channel, the integral value and centroid value were calculated to capture the time-course changes and quantitatively describe the waveform characteristics of the NIRS signal. The integral value indicated the magnitude of the signal changes during the 60s task period, while the centroid value represented the time point corresponding to half of the area under the positive change curve of the NIRS spectrum for the entire task period (from −10 to 115 s). Additionally, the average change in Oxy-Hb was analyzed for each channel during the 60s task period. By calculated hemoglobin concentration across all channels for each participant, we obtained the average hemoglobin concentration at the group level. Moreover, functional connectivity (FC) values were derived through Pearson correlation analysis of the time series data for each channel pair. And then Fisher's r-to-z transformation was conducted for improving the normality (Li et al., 2023). This produced a correlation matrix of dimensions 48 × 48 for each participant.

2.5. Statistics analysis

Clinical data, neuropsychological test scores and VFT performance were analyzed using SPSS 17.0 (SPSS Inc., Chicago, IL, USA). Initially, the Kolmogorov–Smirnov test was employed to ascertain the normality of the quantitative data. Subsequently, inter-group comparisons were carried out based on the distribution of data: data that followed a normal distribution underwent statistical analysis using independent t-tests, while data with a non-normal distribution were assessed using the Mann–Whitney U test. The gender variable, treated as binary, was evaluated using the chi-squared test. Statistical significance was defined as $p < 0.05$.

The Near-infrared spectroscopy data was analyzed using NirSpark software. GraphPad Prism 8.0, BrainNetViewer and Photoshop CS6 were used for generating figures. A two-sample t-test was applied to compare the hemodynamic changes and FC values between the two groups, aiming to identify patterns brain activation and connection. False discovery rate (FDR) correction was applied to the fNIRS data. Statistical significance was defined as $p < 0.05$. Additionally, the mean Oxy-Hb changes or mean FC values were extracted from channels that exhibited statistical differences, and correlation analysis with PSQI scores was performed using Pearson's method.

3. Results

3.1. Demographic and clinical characteristics

No significant difference was found in age, gender, years of education, VFT performance and MoCA total scores between the SID group and HC group ($p > 0.05$). However, the SID group exhibited significantly higher PSQI scores compared to the HC group ($p < 0.05$). Although the HAMA and HAMD scores of the SID group were also significantly higher than those of the HC group ($p < 0.05$), it is noteworthy that neither group met the criteria for clinical diagnosis of anxiety or depression. Please refer to Table 1 for a comprehensive summary of these findings.

3.2. Hemodynamic response during the VFT task

During the VFT task, no significant difference was observed in the integral values, centroid values or mean Oxy-Hb changes between the two groups ($p > 0.05$, FDR corrected).

Through FC analysis, two oxy-Hb correlation matrix maps were obtained for the SID group and HC group (Figures 2A,B). The mean strength of channel-to-channel connectivity was found to be significantly lower in the SID group compared to the HC group (0.217 ± 0.125 vs. 0.297 ± 0.142, $p < 0.0001$; Figure 2C). Furthermore, as shown in Figure 2D, the SID group exhibited significantly decreased FC strength in six pairs of channels compared to the HC group: Ch8-Ch27, Ch11-Ch14, Ch14-Ch27, Ch27-Ch38, Ch27-Ch39, and Ch27-Ch41 ($p < 0.05$, FDR corrected). Notably, channel 27 (corresponding to the left frontopolar cortex) appeared most frequently (5 times) in the channels displaying differential connectivity. Conversely, no channel pair with significantly higher connectivity was observed in the SID group. Please refer to Table 2 for detailed information regarding the differential channel pairs and their corresponding brain regions.

TABLE 1 Comparison of clinical data and neuropsychological scores between the two groups.

Characteristics	SID group	HC group	*p* value
Gender (M/F)	12/19	15/16	0.609[a]
Age (years)	43.74 ± 15.61	43.19 ± 14.91	0.888
Education (years)	12.23 ± 3.47	11.63 ± 3.54	0.510
Duration (months)	1.88 ± 0.69	/	/
VFT performance	8.42 ± 2.23	9.26 ± 2.14	0.137
PSQI scores	10.03 ± 1.97	4.42 ± 2.14	<0.001
MoCA total scores	27.71 ± 1.37	27.84 ± 1.34	0.710
HAMA scores	1.13 ± 1.28	0.55 ± 0.85	0.040
HAMD$_{24}$ scores	1.74 ± 1.63	0.48 ± 0.85	<0.001

SID, short-term insomnia disorder; HC, heathy control; VFT, verbal fluency test; PSQI, Pitsburgh sleep quality index; MoCA, Montreal Cognitive Assessment; HAMA, Hamilton Anxiety Rating Scale; HAMD$_{24}$, Hamilton Depression Rating Scale. $p < 0.05$ indicates statistical significance. [a]χ^2 test for sex (n). Independent t-test for the other data (means ± SD).

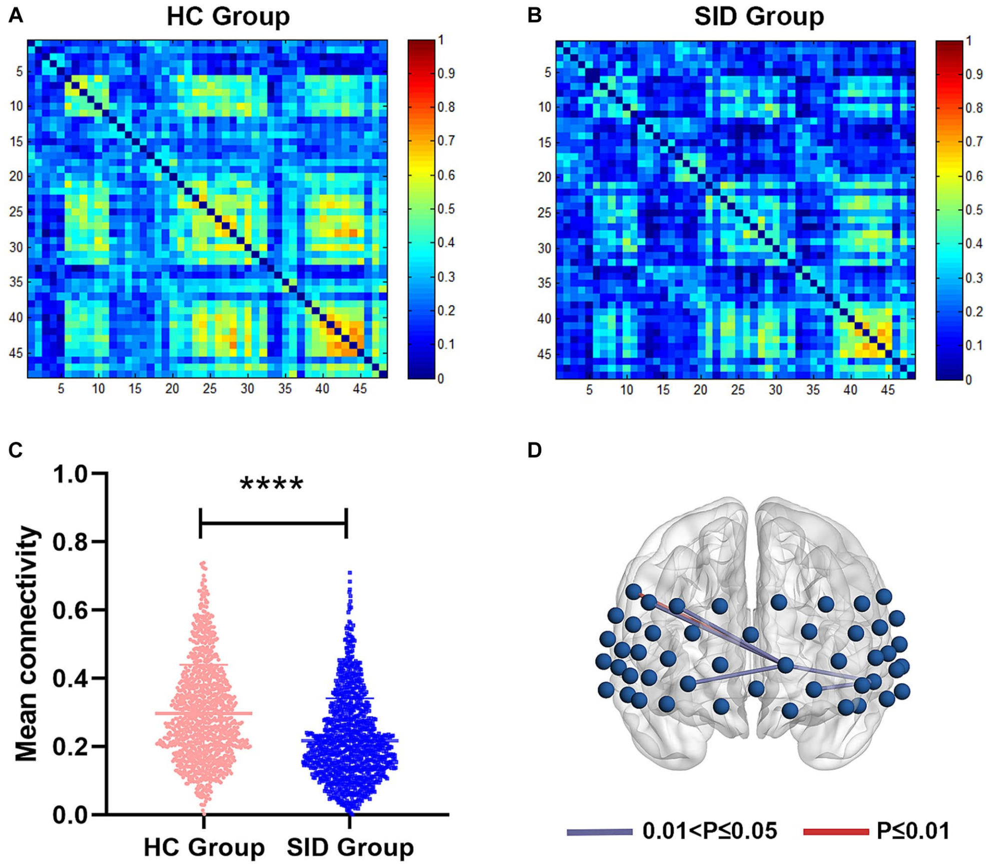

FIGURE 2
Functional connectivity between two groups. **(A,B)** The average functional connectivity strength of 48 channels in HC group and SID group, respectively. **(C)** Comparisons of mean connectivity strength of 48 channels between two groups. **(D)** Six channel pairs had significantly higher connectivity in HC group than SID group (FDR corrected $p < 0.05$). HC, healthy control; SID, short-term insomnia disorder. ****$p < 0.0001$.

TABLE 2 **Channel pairs with significant differences in connectivity strength between groups (mean ± SD).**

Channel pairs	Brain regions	Connectivity strength		*t*	*p* (FDR corrected)
		SID group	HC group		
Ch8-Ch27	RFPC-LFPC	0.15 ± 0.39	0.52 ± 0.34	3.968	0.044
Ch11-Ch14	LOFC-LTPC	−0.02 ± 0.35	0.34 ± 0.35	4.136	0.044
Ch14-Ch27	LTPC-LFPC	0.01 ± 0.37	0.37 ± 0.34	3.908	0.044
Ch27-Ch38	LFPC-RPMC/SMA	0.03 ± 0.43	0.50 ± 0.32	4.923	0.007
Ch27-Ch39	LFPC-RDPFC	0.22 ± 0.34	0.52 ± 0.26	3.964	0.044
Ch27-Ch41	LFPC-RDPFC	0.18 ± 0.40	0.54 ± 0.31	3.946	0.044

SD, standard deviation; SID, short-term insomnia disorder; HC, healthy control; RFPC, right frontopolar cortex; LFPC, left frontopolar cortex; LOFC, left orbitofrontal cortex; LTPC, left temporopolar cortex; RPMC/SMA, right pre-motor and supplementary motor cortex; RDPFC, right dorsolateral prefrontal cortex; FDR, false discovery rate.

3.3. Correlations with clinical characteristics

The FC values of the differential channel pairs for each participant were extracted and subjected to a Pearson correlation analysis with PSQI scores. As shown in Figure 3, the channel pair Ch27-Ch39, representing the left frontopolar cortex (LFPC) and right dorsolateral prefrontal cortex (RDPFC), exhibited a significant negative correlation with PSQI scores ($r = -0.422$, $p = 0.018$). This finding suggested that decreased connectivity between the LFPC and the RDPFC is associated with higher PSQI scores and poorer sleep quality.

4. Discussion

In order to unravel the pathophysiological mechanisms underlying short-term insomnia disorder, the present study utilized fNIRS to investigate the hemodynamic response and functional connectivity characteristics in the prefrontal cortex of patients with

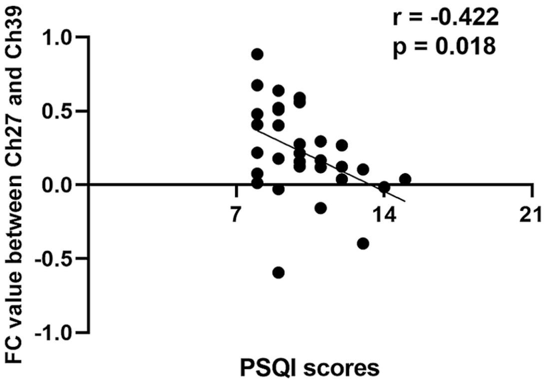

FIGURE 3
Correlation analysis between channel pair Ch27-Ch39 functional connectivity values and PSQI scores in short-term insomnia disorder group. FC, functional connectivity; Ch, channel; PSQI, Pitsburgh sleep quality index.

SID during VFT task. Furthermore, we observed whether these changes were correlated with poor sleep quality. To our knowledge, this study represents the first report to employ fNIRS combined with a cognitive task in the SID patients.

No significant differences in terms of integral values, centroid values, and mean Oxy-Hb variations were found between the SID group and the HC group in the VFT task, suggesting similar hemodynamic responses in both groups. However, our findings contrast with those of a previous study that reported significantly hypoactivated frontopolar cortex and right dorsolateral prefrontal cortex in individuals with chronic insomnia during the VFT task (Gong et al., 2022). This disparity may be attributed to variations in the severity of insomnia symptoms (as measured by PSQI scores: 16.1 ± 2.4 vs. 10.03 ± 1.97) and the duration of insomnia (25.4 ± 23.2 months vs. 1.88 ± 0.69 months) within the populations under investigation. This could be due to the fact that SID has a relatively smaller impact on brain activation patterns compared to chronic insomnia, which likely accounts for the similar performance of individuals with SID and healthy controls during the VFT task.

Insomnia has been recognized as a disorder associated with abnormal brain network connectivity (Nardone et al., 2020). Through functional connectivity analysis, we observed a notable decrease in connection strength between the left frontopolar cortex (LFPC) and several other brain regions in patients with SID. These regions include the right frontopolar cortex (RFPC), left temporopolar cortex (LTPC), right pre-motor and supplementary motor cortex (RPMC/SMA), and right dorsolateral prefrontal cortex (RDPFC). Similar to our research findings, Mukli et al. (2021) utilized fNIRS technology to investigate changes in prefrontal functional brain networks in 10 healthy young males following sleep deprivation, and reported a significant decrease in the number of functional connections in the overall network response. Additional investigations conducted using fNIRS (Bu et al., 2017), functional magnetic resonance imaging (fMRI; Wang et al., 2022) and electroencephalography (EEG; Verweij et al., 2014) have also reported diminished connectivity in the prefrontal cortex after sleep deprivation. These findings suggest that even short-term sleep disorder can exert adverse effects on the synchronized interactions among brain regions. The dorsolateral prefrontal cortex is a crucial region for maintaining working memory and executive function (Vartanian et al., 2014). The RPMC/SMA and temporopolar cortex also play a crucial role in executive function (Xu et al., 2020; Godefroy et al., 2023). The functional connectivity abnormalities in these regions may indicate cognitive decline. In turn, it is possible that one of the functions of sleep is to autonomously regulate the connectivity of the prefrontal brain network, thereby optimizing cognitive performance.

Evidence derived from studies conducted on non-human primates suggests that the FPC possesses various outgoing connections, such as those with the cingulate gyrus and superior temporal gyrus, as well as incoming connections from regions like the amygdala, thalamus, and basal forebrain (Petrides and Pandya, 2007; Burman et al., 2011). These connections provide support for the proposition that the FPC serves as a vital hub for integrating cognitive processes across multiple domains. In this study, we observed notable reduction in connectivity between the FPC and the other brain regions in SID patients. This finding suggest that lack of sleep may disrupt the functional network of the FPC, potentially leading to difficulties in maintaining normal cognitive activities.

Furthermore, our study revealed a negative correlation between FC values of the LFPC and the RDPFC with PSQI scores. This suggests that decreased connectivity between the LFPC and the RDPFC is associated with poorer sleep quality. Consistent with previous findings, patients with SID exhibit reduced activation in the FPC and the RDPFC during verbal fluency tasks, indicating a potential relationship between dysfunction in these regions and sleep disorders. Additionally, Hermesdorf et al. (2021) has observed that arousal might interfere with the transition to quiet slow-wave sleep and lead to a reduction in the volume of gray matter in the FPC. Therefore, it is plausible that the FPC not only plays a role in cognitive processes but also is involved in sleep maintenance.

The RDPFC has also been implicated in regulating normal sleep patterns. Jiang et al. (2013) used low-frequency repetitive transcranial magnetic stimulation (rTMS) to stimulate the dorsolateral prefrontal cortex (DLPFC) in the treatment of patients with SID and found significant improvements in stage III sleep and REM sleep cycles. One possible mechanism is that low-frequency rTMS stimulation of the DLPFC promotes the secretion of melatonin, brain serotonin, and norepinephrine, thereby maintaining normal sleep–wake cycles. We hypothesize that the decline in functional connectivity between the FPC and the RDPFC may lead to a reduction in reduced secretion of sleep-regulating hormones, ultimately resulting in the overactivation of the hypothalamic–pituitary–adrenal (HPA) and hypothalamic–pituitary-thyroid (HPT) axes, consequently causing a hyperarousal state in insomnia patients. Restoring this abnormal functional connection may help decrease arousal levels, improve sleep quality, and enhance daytime functioning. However, further investigation is required to determine the precise mechanisms through which these abnormal functional connectivity patterns contribute to sleep disorders.

This study utilizes fNIRS technology to evaluate the prefrontal cortex function in individuals diagnosed with SID, aiming to obtain a more comprehensive comprehension of the neural mechanisms and biomarkers implicated in insomnia. The utilization of fNIRS offers valuable insights into the underlying pathophysiological processes associated with insomnia, thereby facilitating the development of more precise and dependable diagnostic and assessment tools. The abnormal prefrontal pathways identified in this study could potentially serve as new targets for further transcranial stimulation treatments. Future research could validate the effectiveness of these new targets, providing information for the development of personalized treatment approaches.

4.1. Limitations

Several limitations in our study should be acknowledged. Firstly, participant selection was solely based on subjective questionnaires, which may have introduced bias, as objective parameters such as polysomnography data were not included. Secondly, the absence of significant differences in brain activation patterns between the two groups may be attributed to the small sample size. Thus, future studies should consider expanding the sample size to enhance the robustness of our findings. Thirdly, it is important to note that fNIRS technology only measures cortical activity on the surface and is unable to detect subcortical structures that are beyond the reach of near-infrared light. Hence, combining fNIRS with complementary imaging techniques such as EEG and MRI would improve both the temporal and spatial resolution of our investigations. Fourthly, considering that SID may impact multiple cognitive domains, it would be beneficial to include other assessments in addition to the VFT task in future studies to achieve a more comprehensive cognitive evaluation.

5. Conclusion

Patients with short-term insomnia disorder showed aberrant functional connectivity pattern in the prefrontal cortex during VFT task. Notably, the disruption in connectivity strength between the LFPC and the RDPFC was found to be significantly correlated with the severity of sleep disturbances. By employing fNIRS technology, it becomes possible to detect and diagnose individuals with SID at an early stage, thereby mitigating the risk of disease progression effectively.

Data availability statement

The raw data supporting the conclusions of this article will be made available by the authors, without undue reservation.

Ethics statement

The studies involving humans were approved by Ethics Committee of Jiangbin Hospital of Guangxi Zhuang Autonomous Region. The studies were conducted in accordance with the local legislation and institutional requirements. Written informed consent for participation in this study was provided by the participants' legal guardians/next of kin.

Author contributions

PW: Conceptualization, Formal analysis, Methodology, Visualization, Writing – original draft. CW: Data curation, Investigation, Writing – original draft. MW: Data curation, Investigation, Writing – original draft. YL: Methodology, Software, Writing – original draft. YX: Data curation, Investigation, Writing – original draft. XL: Resources, Writing – original draft. JJ: Writing – original draft, Resources. YB: Investigation, Software, Writing – original draft. JD: Writing – review & editing, Resources. WJ: Conceptualization, Funding acquisition, Writing – review & editing.

Funding

The author(s) declare financial support was received for the research, authorship, and/or publication of this article. The study was supported by the grant from the Guangxi Medical and Health Foundation for Development and Application of Appropriate Technology (grant no. S2018092), the Guangxi science and Technology Base and special talents (Guike AD20238075), and the Nanning Qingxiu District Science and Technology Plan Project (grant no. 2018037).

Acknowledgments

We appreciate the assistance provided by Ying Zhao in data analysis.

Conflict of interest

The authors declare that the research was conducted in the absence of any commercial or financial relationships that could be construed as a potential conflict of interest.

Publisher's note

Supplementary material

The Supplementary material for this article can be found online at: https://www.frontiersin.org/articles/10.3389/fnins.2023.1277690/full#supplementary-material

References

Anastasiades, P. G., de Vivo, L., Bellesi, M., and Jones, M. W. (2022). Adolescent sleep and the foundations of prefrontal cortical development and dysfunction. *Prog. Neurobiol.* 218:102338. doi: 10.1016/j.pneurobio.2022.102338

Bin Heyat, M. B., Akhtar, F., Ansari, M. A., Khan, A., Alkahtani, F., Khan, H., et al. (2021). Progress in detection of insomnia sleep disorder: a comprehensive review. *Curr. Drug Targets* 22, 672–684. doi: 10.2174/1389450121666201027125828

Bu, L., Zhang, M., Li, J., Li, F., Liu, H., and Li, Z. (2017). Effects of sleep deprivation on phase synchronization as assessed by wavelet phase coherence analysis of prefrontal tissue oxyhemoglobin signals. *PLoS One* 12:e0169279. doi: 10.1371/journal.pone.0169279

Burman, K. J., Reser, D. H., Richardson, K. E., Gaulke, H., Worthy, K. H., and Rosa, M. G. (2011). Subcortical projections to the frontal pole in the marmoset monkey. *Eur. J. Neurosci.* 34, 303–319. doi: 10.1111/j.1460-9568.2011.07744.x

Buysse, D. J., Reynolds, C. F. 3rd, Monk, T. H., Berman, S. R., and Kupfer, D. J. (1989). The Pittsburgh sleep quality index: a new instrument for psychiatric practice and research. *Psychiatry Res.* 28, 193–213. doi: 10.1016/0165-1781(89)90047-4

Godefroy, O., Aarabi, A., Dorchies, F., Barbay, M., Andriuta, D., Diouf, M., et al. (2023). Functional architecture of executive processes: evidence from verbal fluency and lesion mapping in stroke patients. *Cortex* 164, 129–143. doi: 10.1016/j.cortex.2023.03.013

Gong, H., Sun, H., Ma, Y., Tan, Y., Cui, M., Luo, M., et al. (2022). Prefrontal brain function in patients with chronic insomnia disorder: a pilot functional near-infrared spectroscopy study. *Front. Neurol.* 13:985988. doi: 10.3389/fneur.2022.985988

Hermesdorf, M., Szentkiralyi, A., Teismann, H., Teismann, I., Young, P., and Berger, K. (2021). Sleep characteristics, cognitive performance, and gray matter volume: findings from the BiDirect study. *Sleep* 44:zsaa209. doi: 10.1093/sleep/zsaa209

Hoshi, Y., Kobayashi, N., and Tamura, M. (2001). Interpretation of near-infrared spectroscopy signals: a study with a newly developed perfused rat brain model. *J. Appl. Physiol.* 90, 1657–1662. doi: 10.1152/jappl.2001.90.5.1657

Jiang, C. G., Zhang, T., Yue, F. G., Yi, M. L., and Gao, D. (2013). Efficacy of repetitive transcranial magnetic stimulation in the treatment of patients with chronic primary insomnia. *Cell Biochem. Biophys.* 67, 169–173. doi: 10.1007/s12013-013-9529-4

LeBlanc, M., Mérette, C., Savard, J., Ivers, H., Baillargeon, L., and Morin, C. M. (2009). Incidence and risk factors of insomnia in a population-based sample. *Sleep* 32, 1027–1037. doi: 10.1093/sleep/32.8.1027

Li, Q., Feng, J., Guo, J., Wang, Z., Li, P., Liu, H., et al. (2020). Effects of the multisensory rehabilitation product for home-based hand training after stroke on cortical activation by using NIRS methods. *Neurosci. Lett.* 717:134682. doi: 10.1016/j.neulet.2019.134682

Li, H., Fu, X., Lu, L., Guo, H., Yang, W., Guo, K., et al. (2023). Upper limb intelligent feedback robot training significantly activates the cerebral cortex and promotes the functional connectivity of the cerebral cortex in patients with stroke: a functional near-infrared spectroscopy study. *Front. Neurol.* 14:1042254. doi: 10.3389/fneur.2023.1042254

Liu, X., Cheng, F., Hu, S., Wang, B., Hu, C., Zhu, Z., et al. (2022). Cortical activation and functional connectivity during the verbal fluency task for adolescent-onset depression: a multi-channel NIRS study. *J. Psychiatr. Res.* 147, 254–261. doi: 10.1016/j.jpsychires.2022.01.040

Medicine AAoS *International classification of sleep disorders. 3rd* Darien, IL: American Academy of Sleep Medicine (2014).

Mukli, P., Csipo, T., Lipecz, A., Stylianou, O., Racz, F. S., Owens, C. D., et al. (2021). Sleep deprivation alters task-related changes in functional connectivity of the frontal cortex: a near-infrared spectroscopy study. *Brain Behav.* 11:e02135. doi: 10.1002/brb3.2135

Muzur, A., Pace-Schott, E. F., and Hobson, J. A. (2002). The prefrontal cortex in sleep. *Trends Cogn. Sci.* 6, 475–481. doi: 10.1016/S1364-6613(02)01992-7

Nardone, R., Sebastianelli, L., Versace, V., Brigo, F., Golaszewski, S., Pucks-Faes, E., et al. (2020). Effects of repetitive transcranial magnetic stimulation in subjects with sleep disorders. *Sleep Med.* 71, 113–121. doi: 10.1016/j.sleep.2020.01.028

Nofzinger, E. A., Buysse, D. J., Germain, A., Price, J. C., Miewald, J. M., and Kupfer, D. J. (2004). Functional neuroimaging evidence for hyperarousal in insomnia. *Am. J. Psychiatry* 161, 2126–2128. doi: 10.1176/appi.ajp.161.11.2126

Patel, D., Steinberg, J., and Patel, P. (2018). Insomnia in the elderly: a review. *J. Clin. Sleep Med.* 14, 1017–1024. doi: 10.5664/jcsm.7172

Perrier, J., Clochon, P., Bertran, F., Couque, C., Bulla, J., Denise, P., et al. (2015). Specific EEG sleep pattern in the prefrontal cortex in primary insomnia. *PLoS One* 10:e0116864. doi: 10.1371/journal.pone.0116864

Petrides, M., and Pandya, D. N. (2007). Efferent association pathways from the rostral prefrontal cortex in the macaque monkey. *J. Neurosci.* 27, 11573–11586. doi: 10.1523/JNEUROSCI.2419-07.2007

Sun, J. J., Liu, X. M., Shen, C. Y., Zhang, X. Q., Sun, G. X., Feng, K., et al. (2017). Reduced prefrontal activation during verbal fluency task in chronic insomnia disorder: a multichannel near-infrared spectroscopy study. *Neuropsychiatr. Dis. Treat.* 13, 1723–1731. doi: 10.2147/NDT.S136774

Sutoko, S., Monden, Y., Tokuda, T., Ikeda, T., Nagashima, M., Funane, T., et al. (2020). Atypical dynamic-connectivity recruitment in attention-deficit/hyperactivity disorder children: an insight into task-based dynamic connectivity through an fNIRS study. *Front. Hum. Neurosci.* 14:3. doi: 10.3389/fnhum.2020.00003

Vargas, I., Nguyen, A. M., Muench, A., Bastien, C. H., Ellis, J. G., and Perlis, M. L. (2020). Acute and chronic insomnia: what has time and/or hyperarousal got to do with it? *Brain Sci.* 10:71. doi: 10.3390/brainsci10020071

Vartanian, O., Bouak, F., Caldwell, J. L., Cheung, B., Cupchik, G., Jobidon, M.-E., et al. (2014). The effects of a single night of sleep deprivation on fluency and prefrontal cortex function during divergent thinking. *Front. Hum. Neurosci.* 8:214. doi: 10.3389/fnhum.2014.00214

Verweij, I. M., Romeijn, N., Smit, D. J., Piantoni, G., Van Someren, E. J., and van der Werf, Y. D. (2014). Sleep deprivation leads to a loss of functional connectivity in frontal brain regions. *BMC Neurosci.* 15:88. doi: 10.1186/1471-2202-15-88

Wang, Y., Dai, C., Shao, Y., Wang, C., and Zhou, Q. (2022). Changes in ventromedial prefrontal cortex functional connectivity are correlated with increased risk-taking after total sleep deprivation. *Behav. Brain Res.* 418:113674. doi: 10.1016/j.bbr.2021.113674

Xia, W., Dai, R., Xu, X., Huai, B., Bai, Z., Zhang, J., et al. (2022). Cortical mapping of active and passive upper limb training in stroke patients and healthy people: a functional near-infrared spectroscopy study. *Brain Res.* 1788:147935. doi: 10.1016/j.brainres.2022.147935

Xu, S. Y., Lu, F. M., Wang, M. Y., Hu, Z. S., Zhang, J., Chen, Z. Y., et al. (2020). Altered functional connectivity in the motor and prefrontal cortex for children with Down's syndrome: an fNIRS study. *Front. Hum. Neurosci.* 14:6. doi: 10.3389/fnhum.2020.00006

Xu, H., Wang, Y., Wang, Y. M., Cao, Y. Q., Li, P. F., Hu, Y. X., et al. (2023). Insomniacs show greater prefrontal activation during verbal fluency task compared to non-insomniacs: a functional near-infrared spectroscopy investigation of depression in patients. *BMC Psychiatry* 23:217. doi: 10.1186/s12888-023-04694-z

Frontiers in Neuroscience

TYPE Original Research
PUBLISHED 11 December 2023
DOI 10.3389/fnins.2023.1308551

EDITED BY
Zhiyong Zhao,
Zhejiang University, China

REVIEWED BY
Chao Li,
The First Affiliated Hospital of China Medical University, China
Lanxin Ji,
New York University, United States
Zhengyuan Yang,
University of Macau, China

*CORRESPONDENCE
Yao Zhu
✉ Yaoz88@outlook.com
Xuzhou Li
✉ lixuzhou@ynnu.edu.cn;
✉ xuzhouli_ecnupsy@126.com

†These authors have contributed equally to this work

RECEIVED 06 October 2023
ACCEPTED 24 November 2023
PUBLISHED 11 December 2023

CITATION
Zhu Y, Huang T, Li R, Yang Q, Zhao C, Yang M, Lin B, the DIRECT Consortium and Li X (2023) Distinct resting-state effective connectivity of large-scale networks in first-episode and recurrent major depression disorder: evidence from the REST-meta-MDD consortium. *Front. Neurosci.* 17:1308551. doi: 10.3389/fnins.2023.1308551

Distinct resting-state effective connectivity of large-scale networks in first-episode and recurrent major depression disorder: evidence from the REST-meta-MDD consortium

Yao Zhu[1]*†, Tianming Huang[2]†, Ruolin Li[3], Qianrong Yang[4], Chaoyue Zhao[1], Ming Yang[1], Bin Lin[5], the DIRECT Consortium and Xuzhou Li[4]*

[1]School of Psychology and Cognitive Science, East China Normal University, Shanghai, China, [2]Department of General Psychiatry, Shanghai Changning Mental Health Center, Shanghai, China, [3]Department of Radiology, Children's Hospital of Philadelphia, Philadelphia, PA, United States, [4]Faculty of Education, Yunnan Normal University, Kunming, Yunnan, China, [5]Department of Radiology, The Second Affiliated Hospital, Zhejiang University School of Medicine, Hangzhou, China

Introduction: Previous studies have shown disrupted effective connectivity in the large-scale brain networks of individuals with major depressive disorder (MDD). However, it is unclear whether these changes differ between first-episode drug-naive MDD (FEDN-MDD) and recurrent MDD (R-MDD).

Methods: This study utilized resting-state fMRI data from 17 sites in the Chinese REST-meta-MDD project, consisting of 839 patients with MDD and 788 normal controls (NCs). All data was preprocessed using a standardized protocol. Then, we performed a granger causality analysis to calculate the effectivity connectivity (EC) within and between brain networks for each participant, and compared the differences between the groups.

Results: Our findings revealed that R-MDD exhibited increased EC in the fronto-parietal network (FPN) and decreased EC in the cerebellum network, while FEDN-MDD demonstrated increased EC from the sensorimotor network (SMN) to the FPN compared with the NCs. Importantly, the two MDD subgroups displayed significant differences in EC within the FPN and between the SMN and visual network. Moreover, the EC from the cingulo-opercular network to the SMN showed a significant negative correlation with the Hamilton Rating Scale for Depression (HAMD) score in the FEDN-MDD group.

Conclusion: These findings suggest that first-episode and recurrent MDD have distinct effects on the effective connectivity in large-scale brain networks, which could be potential neural mechanisms underlying their different clinical manifestations.

KEYWORDS

major depressive disorder, first-episode and recurrent, resting-state fMRI, brain networks, effective connectivity

Introduction

Major depressive disorder (MDD) is a prevalent and debilitating psychiatric disorder that affects 4.7% of the global population and is the second leading cause of disability worldwide (Ferrari et al., 2013). Neuroimaging studies have made significant efforts to explore the pathology underlying MDD. Abnormal functional connectivity (FC) within and between large-scale intrinsic brain networks (Yan et al., 2019; Liu et al., 2021; Sun et al., 2022a,b), such as the default mode network (DMN), executive control network (ECN), and salience network (SN), has been found in MDD using resting-state functional magnetic resonance imaging (rs-fMRI). This reflects that the synchronized spontaneous activity among anatomically distinct networks is potentially linked to rumination dysfunction (Hamilton et al., 2015), cognitive impairment (Clark et al., 2009), and emotional dysregulation (Zhao et al., 2021) in patients with MDD. However, inconsistencies in the FC of several networks like DMN, including increases, decreases, both increases and decreases, and no significant changes, have been reported in prior studies of brain networks in MDD (Yan et al., 2019). This may be related to low sensitivity and reliability, as well as limited statistical power due to small sample sizes (Button et al., 2013; Chen et al., 2018), leading to the pathophysiology of MDD remaining unknown.

According to the ICD-10, MDD can be classified as first-episode or recurrent depression (Hiller et al., 1994). The risk of relapse in MDD is directly proportional to the number of episodes (de Jonge et al., 2018). Compared to first-episode MDD, recurrent MDD exhibits more severe depressive and somatic symptoms, greater impairments in verbal memory, executive function, and mental representation processing (Roca et al., 2011; Nigatu et al., 2015), as well as higher medical costs (Kamlet et al., 1995; Biesheuvel-Leliefeld et al., 2012). Therefore, distinguishing the neuropathological mechanisms of first-episode and recurrent MDD is important for developing new and effective treatment protocols. A prior large-sample study found FC reduction of DMN in recurrent but not in first-episode MDD, which was associated with duration of illness rather than medication usage, suggesting this alteration is related to symptom severity (Yan et al., 2019). Another study revealed that compared with healthy controls, both first-episode and recurrent MDD showed reduced FC in the DMN and affective network, whereas the decrease in cognitive control network only occurred in first-episode MDD (Sun et al., 2022a,b). Compared with recurrent MDD, first-episode MDD showed hypoconnectivity in the DMN, dorsal attention network (DAN), and somatomotor network (Liu et al., 2021). However, these FC findings did not consider the direction of information communication between networks.

Effective connectivity (EC) represents the direct or indirect causal effect of one brain region on another (Deshpande et al., 2011; Deshpande and Xiaoping, 2012). In EC methods, Granger causality analysis (GCA) is a relatively data-driven analytical method that does not require the design of a complicated task. It is more convenient for clinical application than model-driven Structural equation modeling (SEM) and Dynamic causal modeling (DCM) (Seminowicz et al., 2004; Schlösser et al., 2008). GCA analyzes the direction of information flow between brain areas using time series of information processing and can depict resting-state directional brain networks (Jiao et al., 2014). A prior study has demonstrated that the EC measure may play a more important role than FC in exploring alterations in disease brains and afford better mechanistic interpretability (Geng et al., 2018). Studies on MDD have reported abnormal EC in several brain regions such as the amygdala (de Almeida et al., 2009), prefrontal cortex (Hamilton et al., 2011), and insula (Iwabuchi et al., 2014; Kandilarova et al., 2018), as well as in networks such as DMN, SN, and DAN (Guo et al., 2020; Li et al., 2020; Wang et al., 2022). However, the similarities and differences of EC between first-episode and recurrent MDD in large-scale networks have been less studied using GCA.

In this study, we obtained resting-state fMRI data from 839 patients with MDD and 788 matched normal controls (NCs) from the Chinese REST-meta-MDD project. We used GCA to explore alterations in the EC within and between brain networks in first-episode and recurrent MDD. We also estimated the correlation between EC and clinical assessments. Our hypothesis was that the two MDD subgroups would show different changes in intra- and inter-network EC.

Methods

Participants

We utilized rs-fMRI data from the REST-meta-MDD consortium (Chen et al., 2023), comprising 1,300 MDD patients and 1,128 NCs across 23 sites. Each participant underwent a T1-weighted structural scan and an rs-fMRI scan. The patient inclusion criteria, as reported in the study (Yan et al., 2019), were as follows: (1) 18 years < age < 65 years; (2) education >5 years; (3) fulfillment of the Diagnostic and Statistical Manual of Mental Disorders-IV criteria for MDD; and (4) a total score of ≥8 on the 17-item Hamilton Depression Rating Scale (HAMD) at the time of scanning. The exclusion criteria included: (1) any contraindications for undergoing MRI; (2) poor spatial normalization, coverage, or excessive head motion; (3) incomplete information; and (4) sites with fewer than 10 patients in either group. Consequently, we obtained data from 839 MDD patients and 788 NCs across 17 sites. In terms of subgroups, we compared 227 first-episode drug-naïve (FEDN) patients with 388 matched NCs from five sites, 189 recurrent MDD patients with 423 matched NCs from six sites, and 117 FEDN patients with 72 recurrent MDD patients from two sites. The HAMD and Hamilton Anxiety Rating Scale (HAMA) were employed to assess depression and anxiety symptoms in each patient, respectively.

All data were identified and anonymized. Local Institutional Review Boards approved all contributing studies, and participants signed a written informed consent at each local institution.

fMRI preprocessing

All rs-fMRI scans were preprocessed at each site utilizing the identical DPARSF protocol as reported in Yan et al. (2019). Specifically, the initial 10 volumes were discarded and slice-timing correction was performed. Subsequently, a rigid body transformation was used to realign the time series of images for each subject. After that, individual T1-weighted images were co-registered to the mean functional image using a 6 degrees-of-freedom linear transformation without re-sampling, and then segmented into gray matter (GM), white matter (WM), and cerebrospinal fluid (CSF). Following this, transformations from individual native space to MNI space were computed using the Diffeomorphic Anatomical Registration Through Exponentiated Lie algebra (DARTEL) tool (Ashburner, 2007) and applied to individual functional images. The Friston 24-parameter model, WM, and CSF signals were removed from normalized data through linear regression. Lastly, a linear trend was included as a regressor to account for drifts in the BOLD signal and temporal band-pass filtering (0.01–0.1 Hz) was applied to all time series.

Effective connectivity analysis

We used the DOS-160 atlas (Dosenbach et al., 2010) to segment the brain into 160 regions of interest (ROIs) involved in six networks: cingulo-opercular network (CON), FPN, DMN, sensorimotor network (SMN), visual network (VN), and cerebellum network (CN) (Figure 1). We extracted the averaged time series for each ROI and calculated the EC between any paired ROIs using the GCA method. Then, we computed intra- and inter-network EC by averaging the connectivities between ROIs belonging to the same or different networks, respectively, and the averaged EC with each ROI or network as a seed.

Statistical analysis

We employed a linear mixed model (LMM) (West et al., 2022) to compare differences in EC between MDD and NC, FEDN and NC, recurrent MDD and NC, and FEDN and recurrent MDD, respectively. The model was following: $y \sim 1 + \text{Diagnosis} + \text{Age} + \text{Sex} + \text{Education} + \text{Motion} + (1|\text{Site}) + (\text{Diagnosis}\ |\text{Site})$, in which y represents the EC value. This yields t and p values for the fixed effect of Diagnosis (Yan et al., 2019). To test relationships between EC and clinical assessments, we replaced the 'y' in the LMM with HAMD or HAMA scores, respectively. The multiple comparisons were corrected using false discovery rate (FDR) correction ($p < 0.05$).

Results

Characteristics of participants

As shown in Table 1, two MDD subgroups had no significant differences than NCs in age and gender ($p > 0.05$), but showed lower education than NCs ($p < 0.001$). Recurrent MDD showed a longer duration of illness than FEDN ($p < 0.001$). FEDN and recurrent MDD showed no significant differences in age, gender, and education ($p > 0.05$). Total MDD (mixture of FEDN and recurrent MDD) showed significant differences in education ($p < 0.001$) and gender ($p = 0.005$) but not age ($p > 0.05$) compared with NCs.

Between-group differences in EC of large-scale brain networks

As shown in Figures 2, 3, total MDD showed decreased afferent EC to the CN, increased efferent EC from the FPN, and increased EC from SMN to FPN compared with NCs. When MDD was divided into two subgroups, FEDN showed increased EC from SMN to FPN compared to NCs, and decreased EC from SMN to VN relative to recurrent MDD. Recurrent MDD showed stronger efferent EC in the ventral lateral prefrontal cortex (vlPFC) with all other regions in the whole brain relative to both NCs and FEDN, and decreased afferent to the CN and efferent EC from the SMN compared with NCs. The FEDN showed no significant difference in seed-based network EC compared to NCs, and the recurrent MDD showed no significant difference in inter-network EC compared to NCs.

Correlation

The EC from CON to SMN showed a significant negative correlation ($p = 0.004$, $R = -0.20$) with the HAMD score in the FEDN group (Figure 4). No significant correlations were observed in the total MDD and recurrent MDD groups. There was no significant correlations between EC and the HAMA score in all groups.

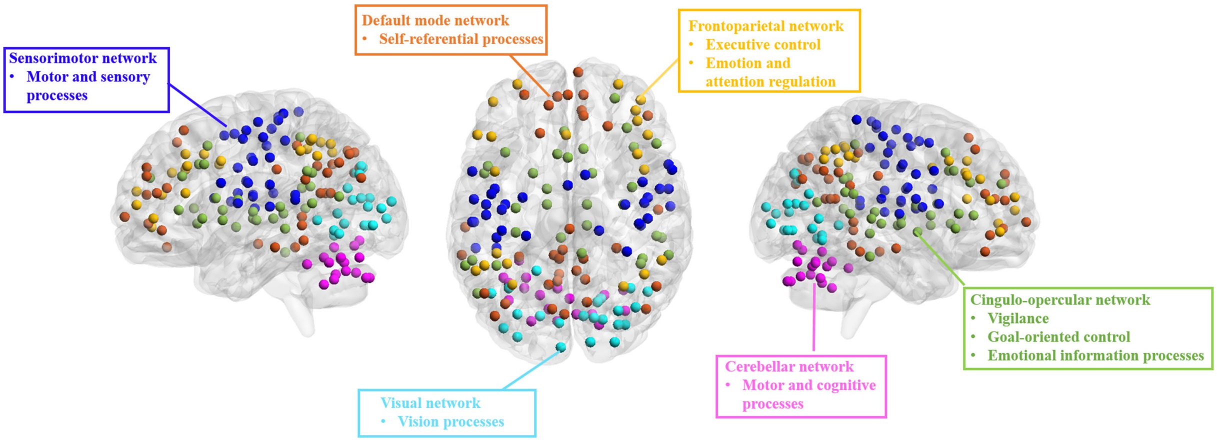

FIGURE 1
Brain networks from DOS-160 atlas used in the present study. DMN, default mode network; FPN, fronto-parietal network; CON, cingulo-opercular network; SMN, sensorimotor network; VN, visual network; CN, cerebellum network.

TABLE 1 Demographic characteristics of participants.

	MDD vs NC			FEDN vs NC			RMDD vs NC			FEDN vs RMDD		
	MDD (N = 848)	NC (N = 794)	p-value	FEDN (N = 232)	NC (N = 394)	p-value	RMDD (N = 189)	NC (N = 427)	p-value	FEDN (N = 119)	RMDD (N = 72)	p-value
Age	34.3 ± 11.5	34.4 ± 13.0	0.313	32.7 ± 10.4	35.7 ± 14.2	0.154	35.4 ± 12.5	37.1 ± 14.1	0.333	35.4 ± 11.3	36.3 ± 12.7	0.865
Sex (male, *n*%)	474(36.5%)	474(42.1%)	0.005	78(33.6%)	152(38.6%)	0.214	78(41.3%)	167(39.1%)	0.613	40(33.6%)	30(41.7%)	0.263
Education	12.0 ± 3.4	13.6 ± 3.4	<0.001	12.2 ± 3.4	13.6 ± 3.6	<0.001	11.7 ± 3.2	13.4 ± 3.8	<0.001	11.5 ± 3.4	12.0 ± 3.5	0.270
Head Motion	0.07 ± 0.04	0.07 ± 0.04	0.920	0.06 ± 0.03	0.07 ± 0.04	0.455	0.07 ± 0.04	0.07 ± 0.04	0.910	0.06 ± 0.03	0.07 ± 0.03	0.566
Duration (month)	38.4 ± 60.6	NA	NA	17.7 ± 30.8	NA	NA	92.7 ± 86.1	NA	NA	27.0 ± 39.5	88.7 ± 80.1	<0.001
Site	17	17	1.000	5	5	1.000	6	6	1.000	2	2	1.000
HAMD	21.7 ± 6.6	NA	NA	22.5 ± 5.4	NA	NA	17.7 ± 7.8	NA	NA	22.1 ± 4.2	21.3 ± 5.8	0.371
HAMA	19.2 ± 8.9	NA	NA	21.9 ± 9.3	NA	NA	13.9 ± 10.5	NA	NA	11.2 ± 8.3	11.4 ± 10.5	0.342

Discussion

This study used GCA to explore alterations in EC within and between resting-state networks in FEDN and recurrent MDD patients in a large-sample Chinese population. We found that: (1) recurrent and total MDD showed altered EC in the FPN, SMN, and CN compared to NCs, while FEDN and total MDD showed altered inter-network EC from SMN to FPN compared to NCs; (2) two MDD subgroups showed significant differences in intra-network EC of the vlPFC within the FPN and in inter-network EC from SMN to VN; (3) the EC from CON to SMN showed a significant negative correlation with the HAMD score in FEDN but not in recurrent MDD group. These findings suggest that the EC among large-scale brain networks at rest was disrupted in patients with MDD, and that recurrent MDD exhibited different effective connections from FEDN.

The previous studies demonstrated that repetitive transcranial magnetic stimulation to the vlPFC reduced individual depersonalization symptoms (American Psychiatric Association, 2013; Jay et al., 2016). Increased activity in this region is linked with increased fronto-insula/limbic inhibitory regulation (Lemche et al., 2007) and may represent an increased effort to regulate emotions or be indicative of deficits in this area (Langenecker et al., 2007). Compared with healthy controls and MDD patients, bipolar disorder (BD) patients showed increased ventral prefrontal cortical responses to both positive and negative emotional expressions (Lawrence et al., 2004). A prior magnetic resonance spectroscopy study found that recurrent MDD showed more metabolite abnormalities in the ventral frontal cortex compared with both first-episode MDD and controls (Portella et al., 2011). A recent functional near-infrared spectroscopy study demonstrated different neurofunctional activity in frontal regions in FEDN and recurrent MDD, which linked between the level of complexity activation in these regions and cognitive impairment severity of patients (Yang et al., 2023). Another recent fMRI study reported that recurrent MDD had higher spontaneous brain activity in the prefrontal cortex compared to first-episode depression, which showed a positive correlation with depressive symptom severity (Sun et al., 2022a,b). Effective connectivity analysis revealed mutually propagating activation in ventral prefrontal cortex in people with MDD, which predicted higher levels of depressive rumination (Hamilton et al., 2011). Consistently, our study found that recurrent MDD had increased EC in the vlPFC compared with both FEDN and NCs, suggesting more severe depressive symptoms in recurrent patients, possibly associated with depersonalization, emotional regulation, and rumination.

Recent studies have demonstrated that the cerebellum plays a significant role in motor control, cognition, and emotion (Balasubramanian et al., 2021; Su et al., 2021). For example, Liu et al. (2012) found disrupted FC of the CN in adults with major depression, which could be associated with emotional disturbances and cognitive deficits. Liu et al. (2022) reported altered EC of the CN in patients with MDD, which was correlated with deficits in spatial–visual attention and psychomotor disorders. The FPN, also referred to as the executive network, plays a pivotal role in control function, execution, and emotion processing. It is strongly associated with cognitive problems in depression, especially those concerning executive functions. Dysfunctions within the FPN are likely connected to ineffective transmission of information between parietal and prefrontal regions (Brzezicka, 2013). Studies also reported alterations in FC strengths in

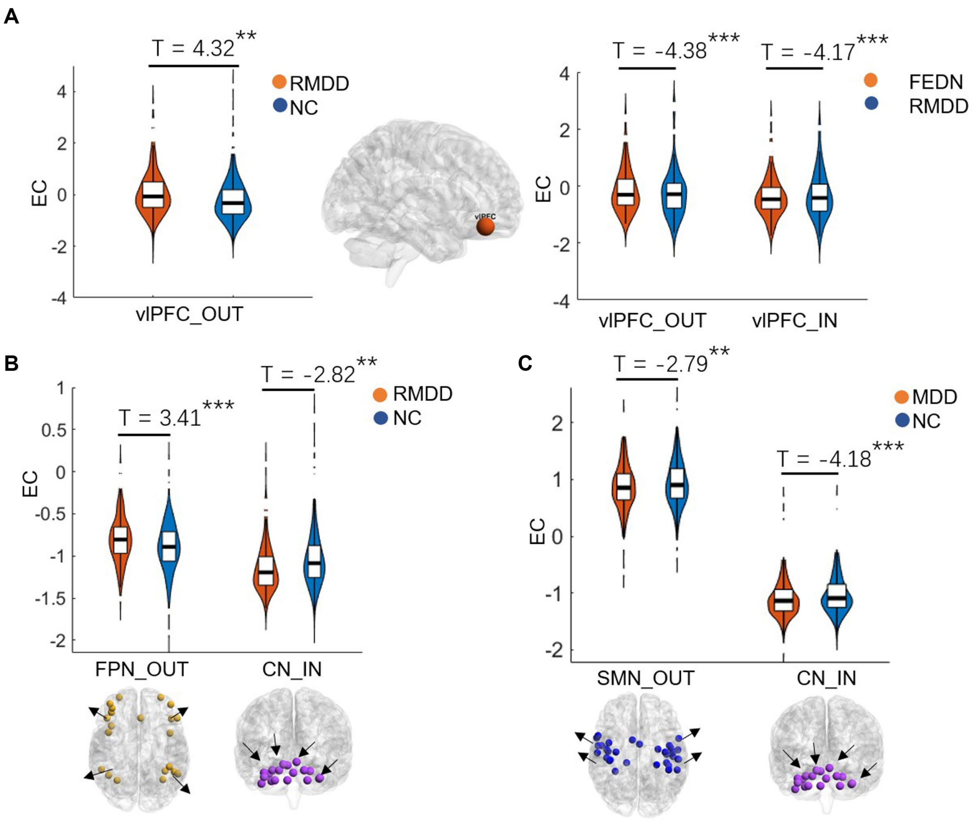

FIGURE 2
Differences between groups in effective connectivity of brain networks. FEDN, first-episode drug-naïve; RMDD, recurrent major depression disorder; vlPFC, ventral lateral prefrontal cortex; FPN, fronto-parietal network; SMN, sensorimotor network; CN, cerebellum network. **$p < 0.05$; ***$p < 0.001$.

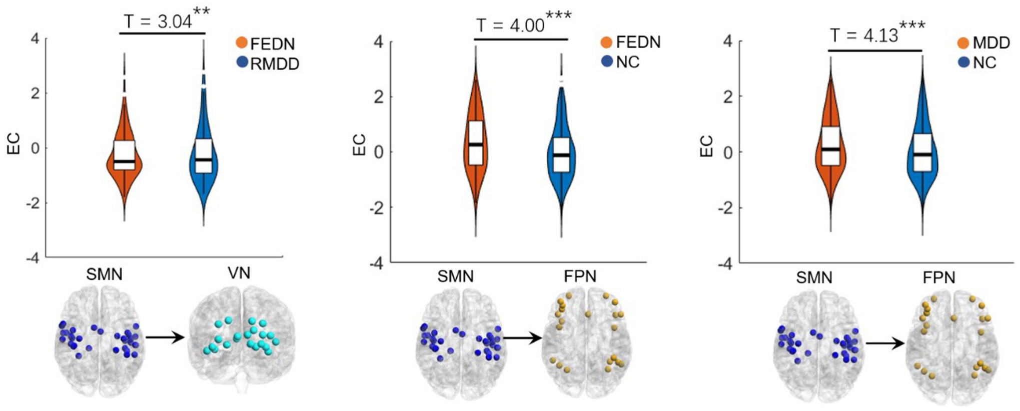

FIGURE 3
Inter-network differences in effective connectivity between groups. FEDN, first-episode drug-naïve; RMDD, recurrent major depression disorder; FPN, fronto-parietal network; SMN, sensorimotor network; VN, visual network. **$p < 0.05$; ***$p < 0.001$.

the frontal and sensorimotor networks (Pang et al., 2020) and disrupted interhemispheric coordination in SMN in MDD patients (Zhang et al., 2023). Moreover, individuals with long-duration MDD showed increased FC in the FPN compared to those with short-duration MDD (Sheng et al., 2022). Similarly, the present study found altered EC of the FPN, CN, and SMN in total MDD and recurrent MDD but not in FEDN, which could be associated with functional impairments of cognitive processing, perception and information integration (Lu et al., 2020), and treatment response-related changes in depression (Dichter et al., 2015). These findings may serve as a potentially effective biomarker for recurrent MDD.

Many studies have found significantly altered connections in low-order networks such as the SMN and VN in MDD patients (Wei et al., 2015; Sambataro et al., 2017). The sensorimotor

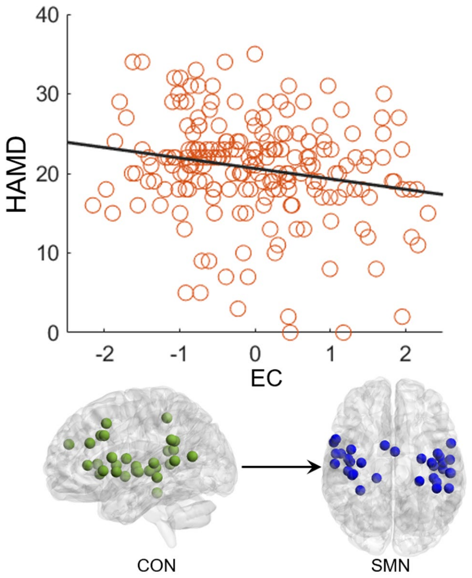

FIGURE 4
Correlation between effective connectivity and HAMD score. The effective connectivity from CON to SMN shows a significant negative correlation with the HAMD score in the FEDN group.

cortex is a brain region that has attracted much attention in depression research (Ray et al., 2021). Several sensorimotor interventions, including light, music, and physical exercise are known to modulate mood and depressive symptoms (Canbeyli, 2013). Depression gives rise to sensorimotor alterations such as psychomotor retardation or agitation and feelings of fatigue, which are part of the diagnostic criteria for depression (Guha, 2014). Previous studies have found alterations of FC and cerebral blood flow in the SMN related to psychomotor retardation in patients with depression (Yin et al., 2018; Yu et al., 2019), while task-based fMRI studies showed differential reactions of the visual cortex in depression (Rosa et al., 2015; Le et al., 2017). Lu et al. (2020) found reduced between-network FC in auditory and visual networks associated with depression. Kang et al. (2018) demonstrated abnormal primary somatosensory area-thalamic FC in MDD. Moreover, abnormal ECs among the FPN, VN, and SMN networks have been reported to be related to visual attention and cognitive behavior deficits in MDD patients (Kang et al., 2018). Therefore, the present study observed increased EC from SMN to FPN in both total MDD and FEDN compared to NCs, which may be compensation for sensory impairments, psychomotor retardation, and cognitive dysfunction of patients. In addition, a recent study uncovered that the ECs in sensorimotor cortices may serve as a promising and quantifiable candidate marker of depression severity and treatment response (Ray et al., 2021). Another study found that changes in information flow direction from SMN before and after electroconvulsive therapy were significantly correlated with improvement in depressive symptoms in MDD patients (Kyuragi et al., 2023). A small-sample study found that patients with recurrent MDD showed remarkably different effective connections compared to patients with first-episode MDD, especially related to the attention network (Wang et al., 2022). Thus, the increased EC from the SMN to the VN in recurrent MDD relative to FEDN in the present study may be associated with depression severity and treatment of patients. Furthermore, the EC from CON to SMN negatively correlated with the HAMD score may serve as a biomarker to predict the severity of MDD.

Limitations

The present study has several limitations. First, the correlation analysis relied solely on HAMD scores of depression. There are a large number of rating scales for assessing depression severity, and each with its own advantages and limitations. Thus, the present neuroimaging findings could be further validated with a combination of observer rating scales and objective behavioral measures of depression (Lahnakoski et al., 2020). Second, we were unclear about the medication history of the recurrent MDD patients, and therefore the present findings are in need of replication. Third, MDD patients in the present study were the Chinese populations, which might not be generalized to other regions or populations. Fourth, the use of LMM should be discussed with regard to its potential limitations, such as its comparison to other methods or its applicability to this specific study. Finally, as a cross-sectional study, changes in connections with disease progression cannot be thoroughly reflected by the limited nodes. Further efforts, such as intervention studies with comparisons before and after medication, are required to draw valid conclusions on the impact of EC.

Conclusion

The present study used the GCA method to investigate differences in EC of large-scale brain networks in FEDN and recurrent MDD patients. We found that recurrent MDD showed altered EC in the FPN, SMN, and CN, while FEDN showed altered inter-network EC from SMN to FPN compared with NCs. Meanwhile, the ECs within FPN and from SMN to VN displayed significant differences between two MDD subgroups. Moreover, the EC from CON to SMN showed a significant negative correlation with HAMD scores in FEDN but not recurrent MDD group. These findings suggest that first-episode and recurrent MDD may have different effective connectivity patterns among large-scale brain networks, which may serve as potential biomarkers for diagnosing MDD.

Data availability statement

Publicly available datasets were analyzed in this study. This data can be found here: http://rfmri.org/REST-meta-MDD.

Author contributions

YZ: Writing – original draft, Methodology, Software, Writing – review & editing. TH: Methodology, Writing – original draft. RL: Writing – original draft, Writing – review & editing. QY: Writing

– original draft, Writing – review & editing. CZ: Writing – review & editing, Methodology, Software. MY: Writing – review & editing, Methodology, Software. BL: Writing – review & editing, Formal analysis. XL: Writing – review & editing.

Funding

The author(s) declare financial support was received for the research, authorship, and/or publication of this article. This study was supported by Innovation Team Program in Philosophy and Social Science of Yunnan Province (Research on psychological adaptation and development of China's ethnic minority students in border areas).

Conflict of interest

The authors declare that the research was conducted in the absence of any commercial or financial relationships that could be construed as a potential conflict of interest.

Publisher's note

References

American Psychiatric Association. (2013). *Diagnostic and statistical manual of mental disorders: DSM-5* (American psychiatric association Washington, DC).

Ashburner, J. (2007). A fast diffeomorphic image registration algorithm. *NeuroImage* 38, 95–113. doi: 10.1016/j.neuroimage.2007.07.007

Balasubramanian, M., Mulkern, R. V., Neil, J. J., Maier, S. E., and Polimeni, J. R. (2021). Probing in vivo cortical myeloarchitecture in humans via line-scan diffusion acquisitions at 7 T with 250–500 micron radial resolution. *Magn. Reson. Med.* 85, 390–403. doi: 10.1002/mrm.28419

Biesheuvel-Leliefeld, K. E. M., Kersten, S., van der Horst, H. E., van Schaik, A., Bockting, C. L. H., Bosmans, J. E., et al. (2012). Cost-effectiveness of nurse-led self-help for recurrent depression in the primary care setting: design of a pragmatic randomised controlled trial. *BMC Psychiatry* 12, 1–9. doi: 10.1186/1471-244X-12-59

Brzezicka, A. (2013). Integrative deficits in depression and in negative mood states as a result of fronto-parietal network dysfunctions. *Acta Neurobiol. Exp.* 73, 313–325.

Button, K. S., Ioannidis, J. P. A., Mokrysz, C., Nosek, B. A., Flint, J., Robinson, E. S. J., et al. (2013). Power failure: why small sample size undermines the reliability of neuroscience. *Nat. Rev. Neurosci.* 14, 365–376. doi: 10.1038/nrn3475

Canbeyli, R. (2013). Sensorimotor modulation of mood and depression: in search of an optimal mode of stimulation. *Front. Hum. Neurosci.* 7:428. doi: 10.3389/fnhum.2013.00428

Chen, X., Bin, L., Wang, Y.-W., Li, X.-Y., Wang, Z.-H., Li, H.-X., et al. (2023). The complexity of functional connectivity profiles of the Subgenual anterior cingulate cortex and dorsal lateral prefrontal cortex in major depressive disorder: a DIRECT consortium study. *bioRxiv*. doi: 10.1101/2023.03.09.531726

Chen, X., Bin, L., and Yan, C.-G. (2018). Reproducibility of R-fMRI metrics on the impact of different strategies for multiple comparison correction and sample sizes. *Hum. Brain Mapp.* 39, 300–318. doi: 10.1002/hbm.23843

Clark, L., Chamberlain, S. R., and Sahakian, B. J. (2009). Neurocognitive mechanisms in depression: implications for treatment. *Annu. Rev. Neurosci.* 32, 57–74. doi: 10.1146/annurev.neuro.31.060407.125618

de Almeida, J., Cardoso, R., Versace, A., Mechelli, A., Hassel, S., Quevedo, K., et al. (2009). Abnormal amygdala-prefrontal effective connectivity to happy faces differentiates bipolar from major depression. *Biol. Psychiatry* 66, 451–459. doi: 10.1016/j.biopsych.2009.03.024

de Jonge, M., Bockting, C. L. H., van Oppen, P., Van, H. L., Peen, J., Kikkert, M. J., et al. (2018). The association between the number of previous episodes and modifiable vulnerability factors in remitted patients with recurrent depression. *PLoS One* 13:e0206495. doi: 10.1371/journal.pone.0206495

Deshpande, G., Santhanam, P., and Xiaoping, H. (2011). Instantaneous and causal connectivity in resting state brain networks derived from functional MRI data. *NeuroImage* 54, 1043–1052. doi: 10.1016/j.neuroimage.2010.09.024

Deshpande, G., and Xiaoping, H. (2012). Investigating effective brain connectivity from fMRI data: past findings and current issues with reference to granger causality analysis. *Brain Connect.* 2, 235–245. doi: 10.1089/brain.2012.0091

Dichter, G. S., Gibbs, D., and Smoski, M. J. (2015). A systematic review of relations between resting-state functional-MRI and treatment response in major depressive disorder. *J. Affect. Disord.* 172, 8–17. doi: 10.1016/j.jad.2014.09.028

Dosenbach, N. U. F., Nardos, B., Cohen, A. L., Fair, D. A., Power, J. D., Church, J. A., et al. (2010). Prediction of individual brain maturity using fMRI. *Science* 329, 1358–1361. doi: 10.1126/science.1194144

Ferrari, A. J., Charlson, F. J., Norman, R. E., Flaxman, A. D., Patten, S. B., Vos, T., et al. (2013). The epidemiological modelling of major depressive disorder: application for the global burden of disease study 2010. *PLoS One* 8:e69637. doi: 10.1371/journal.pone.0069637

Geng, X., Junhai, X., Liu, B., and Shi, Y. (2018). Multivariate classification of major depressive disorder using the effective connectivity and functional connectivity. *Front. Neurosci.* 12:38. doi: 10.3389/fnins.2018.00038

Guha, Martin. (2014). 'Diagnostic and statistical manual of mental disorders: DSM-5′, *Ref. Rev.*, American Psychiatric Publishing, Inc., Arlington, VA

Guo, M., Wang, T., Zhang, Z., Chen, N., Li, Y., Wang, Y., et al. (2020). Diagnosis of major depressive disorder using whole-brain effective connectivity networks derived from resting-state functional MRI. *J. Neural Eng.* 17:056038. doi: 10.1088/1741-2552/abbc28

Hamilton, J. P., Chen, G., Thomason, M. E., Schwartz, M. E., and Gotlib, I. H. (2011). Investigating neural primacy in major depressive disorder: multivariate granger causality analysis of resting-state fMRI time-series data. *Mol. Psychiatry* 16, 763–772. doi: 10.1038/mp.2010.46

Hamilton, J. P., Farmer, M., Fogelman, P., and Gotlib, I. H. (2015). Depressive rumination, the default-mode network, and the dark matter of clinical neuroscience. *Biol. Psychiatry* 78, 224–230. doi: 10.1016/j.biopsych.2015.02.020

Hiller, W., Dichtl, G., Hecht, H., Hundt, W., Mombour, W., and von Zerssen, D. (1994). Evaluating the new ICD-10 categories of depressive episode and recurrent depressive disorder. *J. Affect. Disord.* 31, 49–60. doi: 10.1016/0165-0327(94)90126-0

Iwabuchi, S. J., Peng, D., Fang, Y., Jiang, K., Liddle, E. B., Liddle, P. F., et al. (2014). Alterations in effective connectivity anchored on the insula in major depressive disorder. *Eur. Neuropsychopharmacol.* 24, 1784–1792. doi: 10.1016/j.euroneuro.2014.08.005

Jay, E.-L., Nestler, S., Sierra, M., McClelland, J., Kekic, M., and David, A. S. (2016). Ventrolateral prefrontal cortex repetitive transcranial magnetic stimulation in the treatment of depersonalization disorder: a consecutive case series. *Psychiatry Res.* 240, 118–122. doi: 10.1016/j.psychres.2016.04.027

Jiao, Z.-Q., Zou, L., Cao, Y., Qian, N., and Ma, Z.-H. (2014). Effective connectivity analysis of fMRI data based on network motifs. *J. Supercomput.* 67, 806–819. doi: 10.1007/s11227-013-1010-z

Kamlet, M. S., Paul, N., Greenhouse, J., Kupfer, D., Frank, E., and Wade, M. (1995). Cost utility analysis of maintenance treatment for recurrent depression. *Control. Clin. Trials* 16, 17–40. doi: 10.1016/0197-2456(94)00020-4

Kandilarova, S., Stoyanov, D., Kostianev, S., and Specht, K. (2018). Altered resting state effective connectivity of anterior insula in depression. *Front. Psych.* 9:83. doi: 10.3389/fpsyt.2018.00083

Kang, L., Zhang, A., Sun, N., Liu, P., Yang, C., Li, G., et al. (2018). Functional connectivity between the thalamus and the primary somatosensory cortex in major depressive disorder: a resting-state fMRI study. *BMC Psychiatry* 18, 1–8. doi: 10.1186/s12888-018-1913-6

Kyuragi, Y., Oishi, N., Yamasaki, S., Hazama, M., Miyata, J., Shibata, M., et al. (2023). Information flow and dynamic functional connectivity during electroconvulsive therapy in patients with depression. *J. Affect. Disord.* 328, 141–152. doi: 10.1016/j.jad.2023.02.060

Lahnakoski, J. M., Forbes, P. A. G., McCall, C., and Schilbach, L. (2020). Unobtrusive tracking of interpersonal orienting and distance predicts the subjective quality of social interactions. *R. Soc. Open Sci.* 7:191815. doi: 10.1098/rsos.191815

Langenecker, S. A., Kennedy, S. E., Guidotti, L. M., Briceno, E. M., Own, L. S., Hooven, T., et al. (2007). Frontal and limbic activation during inhibitory control predicts treatment response in major depressive disorder. *Biol. Psychiatry* 62, 1272–1280. doi: 10.1016/j.biopsych.2007.02.019

Lawrence, N. S., Williams, A. M., Surguladze, S., Giampietro, V., Brammer, M. J., Andrew, C., et al. (2004). Subcortical and ventral prefrontal cortical neural responses to facial expressions distinguish patients with bipolar disorder and major depression. *Biol. Psychiatry* 55, 578–587. doi: 10.1016/j.biopsych.2003.11.017

Le, T. M., Borghi, J. A., Kujawa, A. J., Klein, D. N., and Leung, H.-C. (2017). Alterations in visual cortical activation and connectivity with prefrontal cortex during working memory updating in major depressive disorder. *NeuroImage Clin.* 14, 43–53. doi: 10.1016/j.nicl.2017.01.004

Lemche, E., Surguladze, S. A., Giampietro, V. P., Anilkumar, A., Brammer, M. J., Sierra, M., et al. (2007). Limbic and prefrontal responses to facial emotion expressions in depersonalization. *Neuroreport* 18, 473–477. doi: 10.1097/WNR.0b013e328057deb3

Li, G., Liu, Y., Zheng, Y., Li, D., Liang, X., Chen, Y., et al. (2020). Large-scale dynamic causal modeling of major depressive disorder based on resting-state functional magnetic resonance imaging. *Hum. Brain Mapp.* 41, 865–881. doi: 10.1002/hbm.24845

Liu, J., Fan, Y., Zeng, L.-L., Liu, B., Yumeng, J., Wang, M., et al. (2021). The neuroprogressive nature of major depressive disorder: evidence from an intrinsic connectome analysis. *Transl. Psychiatry* 11:102. doi: 10.1038/s41398-021-01227-8

Liu, D.-Y., Xuan, J., Gao, Y., Han, J.-F., Li, Z., Xi-Wen, H., et al. (2022). From molecular to behavior: higher order occipital cortex in major depressive disorder. *Cereb. Cortex* 32, 2129–2139. doi: 10.1093/cercor/bhab343

Liu, L., Zeng, L.-L., Li, Y., Ma, Q., Li, B., Shen, H., et al. (2012). Altered cerebellar functional connectivity with intrinsic connectivity networks in adults with major depressive disorder. *PLoS One* 7:e39516. doi: 10.1371/journal.pone.0039516

Lu, F., Cui, Q., Huang, X., Li, L., Duan, X., Chen, H., et al. (2020). Anomalous intrinsic connectivity within and between visual and auditory networks in major depressive disorder. *Prog. Neuro-Psychopharmacol. Biol. Psychiatry* 100:109889. doi: 10.1016/j.pnpbp.2020.109889

Nigatu, Y. T., Bültmann, U., and Sijmen, A.%J BMC Public Health Reijneveld (2015). The prospective association between obesity and major depression in the general population: does single or recurrent episode matter? *BMC Public Health* 15, 1–8. doi: 10.1186/s12889-015-1682-9

Pang, Y., Zhang, H., Cui, Q., Yang, Q., Fengmei, L., Chen, H., et al. (2020). Combined static and dynamic functional connectivity signatures differentiating bipolar depression from major depressive disorder. *Aust. N. Z. J. Psychiatry* 54, 832–842. doi: 10.1177/0004867420924089

Portella, M. J., de Diego-Adeliño, J., Gómez-Ansón, B., Morgan-Ferrando, R., Vives, Y., Puigdemont, D., et al. (2011). Ventromedial prefrontal spectroscopic abnormalities over the course of depression: a comparison among first episode, remitted recurrent and chronic patients. *J. Psychiatr. Res.* 45, 427–434. doi: 10.1016/j.jpsychires.2010.08.010

Ray, D., Bezmaternykh, D., Mel'nikov, M., Friston, K. J., and Das, M. (2021). Altered effective connectivity in sensorimotor cortices is a signature of severity and clinical course in depression. *Proc. Natl. Acad. Sci.* 118:e2105730118. doi: 10.1073/pnas.2105730118

Roca, M., Armengol, S., García-García, M., Rodriguez-Bayón, A., Ballesta, I., Serrano, M. J., et al. (2011). Clinical differences between first and recurrent episodes in depressive patients. *Compr. Psychiatry* 52, 26–32. doi: 10.1016/j.comppsych.2010.04.011

Rosa, M. J., Portugal, L., Hahn, T., Fallgatter, A. J., Garrido, M. I., Shawe-Taylor, J., et al. (2015). Sparse network-based models for patient classification using fMRI. *NeuroImage* 105, 493–506. doi: 10.1016/j.neuroimage.2014.11.021

Sambataro, F., Visintin, E., Doerig, N., Brakowski, J., Holtforth, M. G., Seifritz, E., et al. (2017). Altered dynamics of brain connectivity in major depressive disorder at-rest and during task performance. *Psychiatry Res. Neuroimaging* 259, 1–9. doi: 10.1016/j.pscychresns.2016.11.001

Schlösser, R. G. M., Wagner, G., Koch, K., Dahnke, R., Reichenbach, J. R., and Sauer, H. (2008). Fronto-cingulate effective connectivity in major depression: a study with fMRI and dynamic causal modeling. *NeuroImage* 43, 645–655. doi: 10.1016/j.neuroimage.2008.08.002

Seminowicz, D. A., Mayberg, H. S., McIntosh, A. R., Goldapple, K., Kennedy, S., Segal, Z., et al. (2004). Limbic–frontal circuitry in major depression: a path modeling metanalysis. *NeuroImage* 22, 409–418. doi: 10.1016/j.neuroimage.2004.01.015

Sheng, W., Cui, Q., Jiang, K., Chen, Y., Tang, Q., Wang, C., et al. (2022). Individual variation in brain network topology is linked to course of illness in major depressive disorder. *Cereb. Cortex* 32, 5301–5310. doi: 10.1093/cercor/bhac015

Su, L.-D., Fang-Xiao, X., Wang, X.-T., Cai, X.-Y., and Shen, Y. (2021). Cerebellar dysfunction, cerebro-cerebellar connectivity and autism spectrum disorders. *Neuroscience* 462, 320–327. doi: 10.1016/j.neuroscience.2020.05.028

Sun, J., Chen, L., He, J., Zhongming, D., Ma, Y., Wang, Z., et al. (2022a). Altered brain function in first-episode and recurrent depression: a resting-state functional magnetic resonance imaging study. *Front. Neurosci.* 16:876121. doi: 10.3389/fnins.2022.876121

Sun, J., Zhongming, D., Ma, Y., Chen, L., Wang, Z., Guo, C., et al. (2022b). Altered functional connectivity in first-episode and recurrent depression: a resting-state functional magnetic resonance imaging study. *Front. Neurol.* 13:1822. doi: 10.3389/fneur.2022.922207

Wang, Y., Chen, X., Liu, R., Zhang, Z., Zhou, J., Feng, Y., et al. (2022). Disrupted effective connectivity of the default, salience and dorsal attention networks in major depressive disorder: a study using spectral dynamic causal modelling of resting-state fMRI. *J. Psychiatry Neurosci.* 47, E421–E434. doi: 10.1503/jpn.220038

Wei, M., Qin, J., Yan, R., Bi, K., Liu, C., Yao, Z., et al. (2015). Association of resting-state network dysfunction with their dynamics of inter-network interactions in depression. *J. Affect. Disord.* 174, 527–534. doi: 10.1016/j.jad.2014.12.020

West, Brady T, Welch, Kathleen B, and Galecki, Andrzej T. (2022). *Linear mixed models: a practical guide using statistical software* (Crc Press), Boca Raton, FL.

Yan, C.-G., Chen, X., Li, L., Castellanos, F. X., Bai, T.-J., Bo, Q.-J., et al. (2019). Reduced default mode network functional connectivity in patients with recurrent major depressive disorder. *Proc. Natl. Acad. Sci.* 116, 9078–9083. doi: 10.1073/pnas.1900390116

Yang, T., Wang, H., Dai, H., Hui, J., Zhang, J., Li, J., et al. (2023). The fNIRS evaluation of frontal and temporal lobe cortical activation in Chinese first-episode medication-naïve and recurrent depression during a verbal fluency task. *Front. Psych.* 14:1132666. doi: 10.3389/fpsyt.2023.1132666

Yin, Y., Wang, M., Wang, Z., Xie, C., Zhang, H., Zhang, H., et al. (2018). Decreased cerebral blood flow in the primary motor cortex in major depressive disorder with psychomotor retardation. *Prog. Neuro-Psychopharmacol. Biol. Psychiatry* 81, 438–444. doi: 10.1016/j.pnpbp.2017.08.013

Yu, M., Linn, K. A., Shinohara, R. T., Oathes, D. J., Cook, P. A., Duprat, R., et al. (2019). Childhood trauma history is linked to abnormal brain connectivity in major depression. *Proc. Natl. Acad. Sci.* 116, 8582–8590. doi: 10.1073/pnas.1900801116

Zhang, C., Jing, H., Yan, H., Li, X., Liang, J., Zhang, Q., et al. (2023). Disrupted interhemispheric coordination of sensory-motor networks and insula in major depressive disorder. *Front. Neurosci.* 17:1135337. doi: 10.3389/fnins.2023.1135337

Zhao, Y., Zhang, F., Zhang, W., Chen, L., Chen, Z., Lui, S., et al. (2021). Decoupling of gray and white matter functional networks in medication-naïve patients with major depressive disorder. *J. Magn. Reson. Imaging* 53, 742–752. doi: 10.1002/jmri.27392

Frontiers in Neuroscience

TYPE Original Research
PUBLISHED 05 January 2024
DOI 10.3389/fnins.2023.1286340

OPEN ACCESS

EDITED BY
Takao Yamasaki,
Minkodo Minohara Hospital, Japan

REVIEWED BY
Naoya Oribe,
Hizen Psychiatric Center (NHO), Japan
Jamie Hershaw,
Traumatic Brain Injury Center of Excellence,
United States

*CORRESPONDENCE
Zhandong Liu
✉ zhandongliu@ccmu.edu.cn

RECEIVED 31 August 2023
ACCEPTED 07 December 2023
PUBLISHED 05 January 2024

CITATION
Liu X, Liu S, Ren R, Wang X, Han C and Liu Z (2024) A cross-sectional study exploring the relationship between symptoms of anxiety/depression and P50 sensory gating in adult patients diagnosed with chronic fatigue syndrome/myalgic encephalomyelitis.
Front. Neurosci. 17:1286340.
doi: 10.3389/fnins.2023.1286340

A cross-sectional study exploring the relationship between symptoms of anxiety/depression and P50 sensory gating in adult patients diagnosed with chronic fatigue syndrome/myalgic encephalomyelitis

Xinyi Liu[1], Sitong Liu[1], Runtao Ren[1], Xue Wang[2], Chunyu Han[2] and Zhandong Liu[1]*

[1]Department of Neurology, Health Care Centre, Beijing Friendship Hospital, Capital Medical University, Beijing, China, [2]Department of Neurology, Beijing Friendship Hospital, Capital Medical University, Beijing, China

Introduction: Chronic fatigue syndrome (CFS) is a clinical disease that affects multiple body systems. It is characterized by persistent or recurring fatigue, which may be linked to immune, neuroendocrine, and energy metabolism dysfunctions. Individuals with CFS may experience pain, sleep disorders, anxiety, and depression. This research analyzed the fundamental characteristics of anxiety/depression symptoms in patients with CFS and investigated the association between these symptoms and the P50 SG (sensory gate) ratio.

Methods: Two hundred and forty-nine subjects fulfilled the CDC-1994 criteria for CFS and were included in the study. The subjects successively completed the Symptom CheckList-90-Revised (SCL-90-R), Hamilton Anxiety Rating Scale-14 (HAMA-14), and Hamilton Depression Rating Scale-24 (HAMD-24). Auditory-evoked potential P50 were measured using the 128-lead-electroencephalograph.

Result: According to HAMA and HAMD, 17.3% ($n = 43$) of the patients did not exhibit anxiety/depression, with a threshold score of 7 and 7 for HAMA and HAMD. When the threshold score was 14 and 20 respectively, 43.3% ($n = 108$) of the patients did not exhibit anxiety/depression. The SCL-90-R results indicated that 69.5% ($n = 173$) of these individuals with the score arranging from 0 to 160 did not present mental problems. There was a correlation between somatization scores and P50 SG ratio in the overall sample and no anxiety or depression (NAOD) group delimited by 14 and 20, respectively, ($p < 0.05$). Regression analysis showed that anxiety and depression were risk factors associated with an abnormal P50 SG ratio.

Discussion: A significant correlation exists between the P50 SG ratio and clinical symptoms such as fatigue, anxiety, and depression. Abnormalities in brain function among patients with CFS may play a crucial role in the pathogenesis of the condition, leading to their classification as being prone to functional neurological disorders. The P50 SG ratio cannot be used as a diagnostic marker for CFS but show some significance on the mechanism, classification, treatment, and prognosis of CFS.

KEYWORDS

chronic fatigue syndrome/myalgic encephalomyelitis, anxiety, depression, auditory evoked potential P50, functional neurological disorder

1 Introduction

Chronic fatigue syndrome/myalgic encephalomyelitis (CFS/ME) is a debilitating disease involving persistent or recurrent fatigue. The persistent and unmitigable symptoms of CFS have seriously affected the daily life and work of patients. Although many clinicians consider CFS a neurological disease, its complex features intersect with those of other systemic diseases, such as irritable bowel syndrome, hyperventilation syndrome, and polymyalgia rheumatica (Teodoro et al., 2018). There is considerable controversy over CFS/ME, as some scholars consider it a mental disorder similar to anxiety and depression (Manu et al., 1988; Roy-Byrne et al., 2002). This controversy stems from the fact that it is primarily diagnosed based on symptoms, and the United States CDC 1994 diagnostic criteria are most widely used (Fukuda et al., 1994). According to research reports, the global incidence rate of CFS has shown a rapid upward trend approximate to 1% in recent years (Prins et al., 2006). CFS is challenging to treat and highly disabling, severely impacting patients' quality of life. With the increase in social pressure and the influence of the environmental, infectious diseases, and other factors, the incidence of CFS in China has significantly increased (Haider et al., 2023), with its persistent and unmitigable symptoms affecting people's daily activities and work. Hence, CFS is a significant problem endangering social public health.

The fatigue dimension shown by patients with CFS has physical and mental implications. The main manifestations are anxiety, depression, irritability, and emotional instability. Its mechanisms may be related to immunity, neuroendocrine, and energy metabolism (Carruthers et al., 2011; Clayton, 2015). For a long time, the relationship between CFS and anxiety/depression could not be explained, as the three have differences and similarities (Sáez-Francàs et al., 2012; Wright et al., 2021). Studies have shown that CFS, anxiety, and depression may show the same trend of oxidative stress immunity, inflammation, and endocrine changes (Kennedy et al., 2005). However, the degree of biological changes in CFS, anxiety, and depression significantly differ (Shungu et al., 2012). Cockshell et al. reported that fatigue in patients with CFS was not associated with depression (Cockshell and Mathias, 2013). However, these conditions undergo dynamic changes throughout their course, necessitating the need for ongoing patient monitoring. The underlying mechanism linking fatigue with anxiety and depressive symptoms in patients with CFS warrants further investigation.

Abnormal brain function has been reported in both anxiety/depression and CFS, and significant progress in this aspect has been made with the development of neuroimaging technology (Barnden et al., 2015; Klumpp and Shankman, 2018). Some scholars believe that "cortical diencephalic syndrome," a stress-induced abnormality in brain function, can be classified as a subtype of CFS. CFS patients exhibit distinct cerebral morphology, cerebral blood flow (CBF), cerebral functional connectivity, and cerebral metabolism on MRI. Numerous imaging studies have confirmed reduced CBF and abnormalities in gray and white matter signals among CFS patients. Currently, several scholars employ multimodal MRI technology to investigate the correlation between symptoms and changes in brain function, as well as systematically evaluate the effects of pharmacological, cognitive, physical, and other treatments. Above those have laid the groundwork for further research on whether the pathogenesis of CFS is associated with abnormal brain function (Xue and Liu, 2015).

Therefore, using objective indicators closely related to brain function to measure CFS and anxiety/depression symptoms is reasonable. Information processing by the human brain is regularly transmitted from the lower to the higher central nervous system, and the average human brain has a selection and filtering process for external stimulus information called sensory gating (SG). The P50 auditory evoked potential is a widely used neuroelectrophysiological examination method in research for the detection of SG, especially related with cognitive domain and emotional disorders (Harrison et al., 2019). However, there is still a lack of using P50 SG in the research field of CFS. Therefore, we are interested in checking abnormal brain function in CFS patients by examining the correlation between symptoms of anxiety or depression with the P50 SG ratio. Furthermore, we aim to explore the usage of this indicator for diagnosis and prognostic assessment. The findings of this study may provide more information for the potential of the P50 SG ratio as an objective, non-invasive diagnostic tool.

2 Materials and methods

2.1 Participants and inclusion/exclusion criteria

For this three-year cross-sectional study (from August 2019 to August 2022), data from patients with CFS at the Neuroscience Clinic of the Department of Neurology at Beijing Friendship Hospital was collected. The Human Research Ethics Committee of Beijing Friendship Hospital, affiliated with Capital Medical University, approved the study. Written informed consent was obtained from all eligible and enrolled patients.

The inclusion criteria were (Teodoro et al., 2018) individuals 14–70 years old (Roy-Byrne et al., 2002) CFS diagnosed according to the CDC-1994 criteria (Manu et al., 1988) absence of fatigue due to other causes, including encephalitis, stroke, brain tumor, diabetes or metabolic syndrome (Fukuda et al., 1994) no history of anxiety, depression, or other psychiatric or neurological disorders (Prins et al., 2006) no prior use of antipsychotic medication (Haider et al., 2023) demonstrated ability to read and understand research documents as

---

Abbreviations: CFS, chronic fatigue syndrome; ME, myalgic encephalomyelitis; SCL-90-R, Symptom CheckList-90-Revised; HAMA-14, Hamilton Anxiety Rating Scale-14; HAMD-24, Hamilton Depression Rating Scale-24; CZ, central zero; NAOD, no anxiety or depression; OA, only anxiety; OD, only depression; AAD, anxiety and depression; NA, no anxiety; MHA, may have anxiety; TMBA, there must be anxiety; MBSA, may be severe anxiety; TMBOA, there must be obvious anxiety.

assessed by researchers; and (Clayton, 2015) have no prior diagnosis of hearing impairment or demonstrate no abnormalities in preliminary hearing tests. The exclusion criteria were (Teodoro et al., 2018) schizophrenia diagnosis (Roy-Byrne et al., 2002) previously diagnosed emotional disorders with or without clinical treatment (Manu et al., 1988) drug addiction (Fukuda et al., 1994) severe organ dysfunction, and (Prins et al., 2006) diagnosed with hearing impairment or demonstrate abnormalities in preliminary hearing tests. Three hundred and thirty-five individuals were assessed for eligibility; 249 met the inclusion criteria and were enrolled (Figure 1).

2.2 Measures

The participants' sociodemographic data were collected. Age, sex, and educational level were obtained at the first visit. All participants voluntarily sought treatment for the first time at the Neurology Department's Fatigue and Depression Clinic. Participants were asked if they had had any infectious diseases such as colds, flu, and bacterial or viral infections before becoming ill, to which they answered "yes" or "no." All eligible participants completed the following questionnaires.

2.2.1 Symptom CheckList-90-Revised

Derogatis' Symptom CheckList-90-Revised (SCL-90-R) is one of the most widely used measures of psychological distress (Derogatis, 1994). The inventory assesses a wide range of self-reported psychological problems and symptoms of psychopathology. SCL-90-R programs are simple, less invasive, and readily acceptable by patients early in the visit (Preti et al., 2019). Another advantage of SCL-90-R is its ability to distinguish and quantify psychosomatic symptoms from clinical manifestations (Achenbach et al., 2016). Each questionnaire item (90 in total) is scored on a five-point scale (0–4). It is then scored and interpreted based on nine primary symptom domains and three general indicators of psychological distress. The primary symptom dimensions include anxiety, depression, hostility, interpersonal sensitivity, obsessive-compulsive, paranoid ideation, phobic anxiety, psychotics, and somatization. The global indices comprise the global severity index, overall positive symptoms, and the positive symptom distress index. A total score exceeding 160 points suggests mild psychological distress, scores surpassing 200 points indicate moderate psychological issues, and scores exceeding 250 points demonstrate significant psychological difficulties.

2.2.2 Hamilton Anxiety Rating Scale-14

The Hamilton Anxiety Rating Scale (HAMA) was presented as a rating scale for the severity of anxiety neurosis (Hamilton, 1959). The HAMA is a clinician-based questionnaire comprising 14 symptom-defined elements; it covers psychological and somatic symptoms, comprising anxious mood, tension, fears, insomnia, 'intellectual' (poor memory/difficulty concentrating),

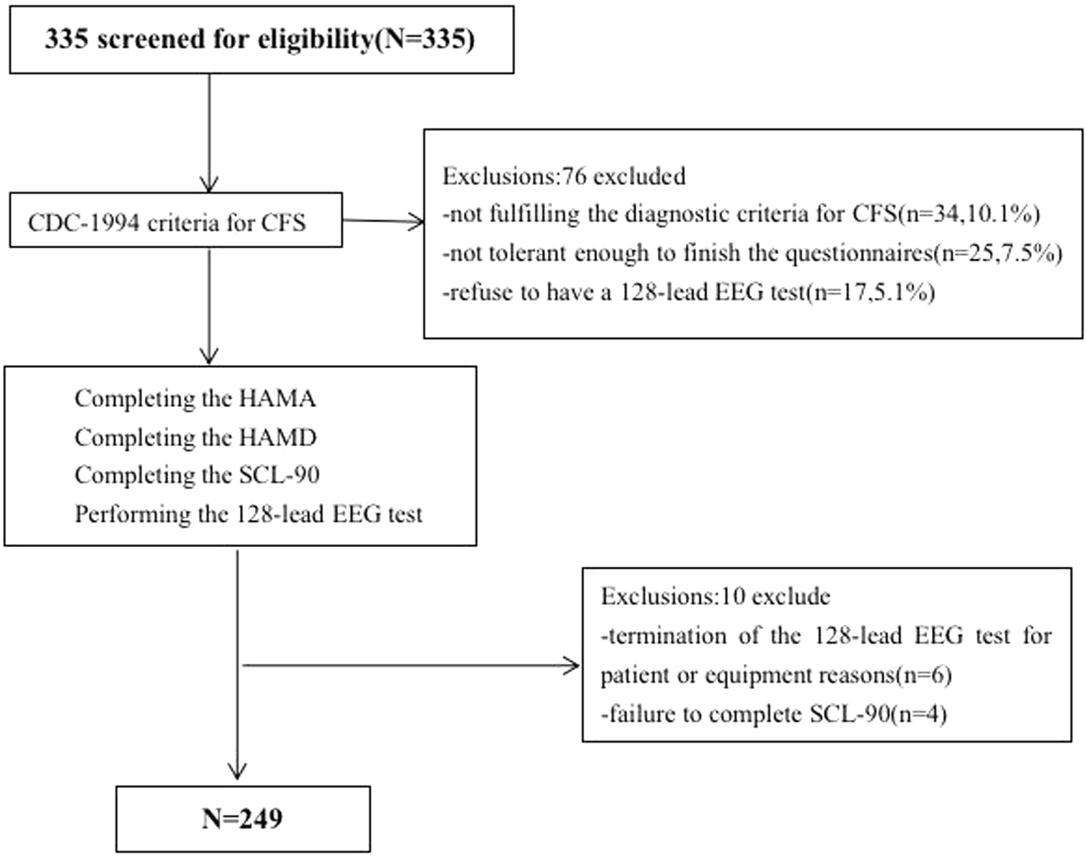

FIGURE 1
Web diagram of the study sample. CFS, chronic fatigue syndrome; HAMA, Hamilton Anxiety Rating Scale; HAMA, Hamilton Depression Rating Scale; SCL-90-R, Symptom CheckList-90-Revised Scale.

depressed mood (including anhedonia), somatic symptoms (including aches and pains, stiffness, bruxism), sensory (tinnitus, blurred vision), cardiovascular, respiratory symptoms (chest tightness, choking), gastrointestinal symptoms, genitourinary symptoms, autonomic symptoms (dry mouth, tension headache), and observed behavior during the interview (restless, fidgety). Each item is scored on an essential numeric scoring of 0 (not present) to 4 (severe); a score > 29 points is considered severe anxiety, >21 points indicates significant anxiety, >14 points indicates anxiety, 8–14 points indicates a tendency for anxiety, and ≤ 7 points indicates no anxiety. The general boundary value for the HAMA-l4 is 14 points.

2.2.3 Hamilton Depression Rating Scale-24

The Hamilton Depression Rating Scale (HAMD), developed by Hamilton in 1960, is the most commonly used scale in the clinical evaluation of depression (Hamilton, 1960; Addington et al., 1996). The HAMD can be summarized into seven-factor structures: anxiety/somatization, weight, cognitive impairment, day and night change, blockage, sleep disorder, and sense of despair. We utilize the following severity ranges for the HAMD: no depression (0–7), a tendency for mild depression (Derogatis, 1994; Kennedy et al., 2005; Carruthers et al., 2011; Sáez-Francàs et al., 2012; Shungu et al., 2012; Cockshell and Mathias, 2013; Barnden et al., 2015; Xue and Liu, 2015; Achenbach et al., 2016; Klumpp and Shankman, 2018; Harrison et al., 2019; Preti et al., 2019; Wright et al., 2021), moderate depression (Hamilton, 1959, 1960; Addington et al., 1996; Wang et al., 2002, 2010; Cella et al., 2013; Frémont et al., 2013; Crawley, 2014; Faro et al., 2016; Jackson and Mac Leod, 2017; Salk et al., 2017; Herrera et al., 2018; Zhao, 2018; Qin et al., 2020), and severe depression (≥35).

2.3 SG P50 acquisition

Auditory evoked potentials were recorded using a 128-lead high-density electrophysiological EEG recorder MagstimEGI GES 300 provided by Magstim Inc. The recording electrodes were positioned according to the GSN-HydroCel-128, specifically targeting the Cz point. The impedances of all electrodes are below 50 kΩ. The experiment was conducted at a sampling frequency of 500 Hz. The experiment employed an auditory conditioned stimulus (S1) - test stimulus (S2) paradigm. The test took place in a shielded, soundproof room where participants sat in a relaxed, awake, and focused state. The background illumination was set to 2 lux. Prior to the test, participants received uniform instructions. A microcomputer program delivered groups of sound stimuli as conditioned stimulus S1 and test stimulus S2, with a 500 ms interval between stimuli and an intensity of 80 dB. Fifty groups were presented, separated by 10-s intervals. The input signal was amplified using an amplifier. The P50 component induced by the S1 stimulus was referred to as the conditioned stimulus wave (S1-P50), while the P50 component induced by the S2 stimulus was labeled as the test stimulus wave (S2-P50). Collected indicators included the amplitude (μV), and the amplitude difference and ratio between S1-P50 and S2-P50. Amplitude refers to the difference between the peak of the P50 wave and the preceding trough. The amplitude of both S1 and S2 is measured using this method. Previous studies have confirmed that the P50 SG ratio among healthy people typically falls below 50% (Wang et al., 2002). In this study, we chose a threshold of 50% to analyze the EEG changes in CFS patients based on this established norm.

MATLAB and the Net Station 4.3 version toolbox, an open-source software, were utilized for data pre-processing, which involved bandpass filtering from 0.1 to 30 Hz. Re-referencing was performed by averaging the values of all recording electrodes. Independent component analysis (ICA) was used to eliminate eye movements, and motion artifacts were manually removed. The epoch was extracted from 100 ms prior to the onset of S1 to 400 ms after the onset of S2. The initial 100 ms was utilized for baseline correction. The EEG data from each participant were averaged across all trials. The maximum positive peak, representing the P50 amplitude, was automatically extracted 30–90 ms after the onset of stimulation (Wang et al., 2010).

2.4 Statistical analysis

Statistical analyses were performed using SPSS V.26 (IBM, Armonk, NY, United States) and GraphPad Prism (version 9; GraphPad Software, San Diego, CA). Descriptive analyses were used to assess the demographic and clinical characteristics. General characteristics and P50 SG information were expressed as means and standard deviation. Spearman test was employed to assess correlations between variables. Furthermore, binary logistic regression analysis was performed for confirming the influence of various factors on P50 SG. All items on the scale were utilized, and various anxiety/depression groups were considered as factors of exposure to investigate their influence on the ratio of P50 SG. $p < 0.05$ were considered significant.

2.5 Grouping and abbreviations

2.5.1 Grouping

In the subsequent subgroup analysis, anxiety and depression are assessed using HAMA and HAMD scales. Scores ranging from 0 to 7 on both scales indicate the absence of anxiety or depression. In HAMA, scores between 8 and 14 indicate the presence of anxiety, while in HAMD, scores between 8 and 20 indicate mild depression (Qin et al., 2020). Neither score can definitively indicate the presence of anxiety or depression; thus, we assign them similar interpretations within our subgroup analysis.

2.5.2 Abbreviations

Only in HAMA: NA (0–7) - no anxiety; MHA (8–14) - may have anxiety; TMBA (15–20) - there must be anxiety; MBSA (21–28) - may be severe anxiety; TMBOA (≥29) - there must be obvious anxiety.

Combine HAMA and HAMD delimited by 7/7: NAOD (0–7 in both HAMD and HAMA) - no anxiety or depression; OA (0–7 in HAMD and ≥ 8 in HAMA) - only anxiety; OD (≥8 in HAMD and 0–7 in HAMA) - only depression; AAD (≥8 in both HAMD and HAMA) - anxiety and depression.

Combine HAMA and HAMD delimited by 14/20: NAOD (0–20 in HAMD and 0–14 in HAMA) - no anxiety or depression; OA (0–20 in HAMD and ≥ 15 in HAMA) - only anxiety; OD (≥21 in HAMD and 0–14 in HAMA) - only depression; AAD (≥21 in HAMD and ≥ 15 in HAMA) - anxiety and depression.

TABLE 1 Demographic and clinical characteristics of participants.

Individual characteristics	*n*	%
Gender		
Male	109	43.8
Female	140	56.2
Age		
≤30	58	23.3
31–40	54	21.7
41–50	37	14.9
≥50	100	40.2
Educational level		
Illiteracy	2	0.8
Primary school	8	3.2
Junior high school	32	12.8
Senior high school	36	14.5
Junior college	42	16.9
Undergraduate course	93	37.3
Postgraduate course	34	13.7
Doctor's degree or above	2	0.8
SCL-90		
0–160	173	69.5
161–200	29	11.6
201–249	27	10.8
>250	20	8.0
HAMD		
0–7	52	20.9
8–20	83	33.3
21–34	88	35.3
>35	26	10.4
HAMA		
0–7	48	19.3
8–14	60	24.1
15–20	61	24.5
21–28	52	20.9
>29	28	11.2
P50 SG ratio		
≤50	108	43.4
>50	141	56.6

3 Results

3.1 General characteristics of participants

We describe the basic information and give a preliminary description of the degree of anxiety and depression and whether the P50 SG ratio is >50% (Table 1). The mean age of all subjects was 43.88 ± 15.47 years, and older patients (≥50 years old) accounted for the highest proportion (40.2%) during the age subgroups. A total of 43.8% of the subjects were male. Of the participants, 247 (99.1%) received education. Of these, 129 (51.8%) participants received undergraduate education or above. More than half of the subjects (56.6%) had an abnormal P50 SG ratio. All the participants were right-handed, and the EEG data was collected at the CZ (Central Zero) point; therefore, the results of P50 SG ratio in this study were not affected by this factor. The CFS patients were classified into two groups based on their P50 SG ratio: P50% ≤ 50and P50% > 50. We compiled the mean and standard deviation of S1 and S2 for both groups (Figure 2). The data from both groups was averaged and used to generate waveform and energy spectrum maps that highlighted significant differences between the two groups (Figures 3, 4). The spectrum graphs shows that different P50 SG ratio characteristics of the two groups in certain brain regions (bilateral occipital, central parietal).

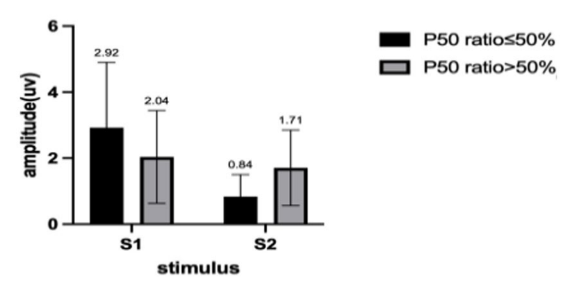

FIGURE 2
The mean and standard deviation of both sets of S1 and S2.

Since in this version of HAMA and HAMD, 0–7 points both represent absolute absence of anxiety/depression, 8–14 points may have anxiety in HAMA, 8–20 may have depression in HAMD, we choose 7/7 for the first and 14/20 for the second analysis. With the score of 7/7 as the threshold for anxiety/depression, there were 43 patients without anxiety or depression, accounting for 17.3%. If we saw reference to score of 14/20, there were 108 patients without anxiety/depression, accounting for 43.4%. However, based on the results of SCL-90-R, among those 173 people here, 69.5% showed no mental problems (Figure 5). Then, we did a grouping analysis. Before this step, we conducted normality analysis on all continuous variables, and all continuous variables did not satisfy normal distribution.

We also conducted non-parametric tests on the P50 SG ratio of different variable groups (Table 2). Normal distribution was not met after grouping owing to the small sample size of some groups and subgroups. We chose the Kruskal–Wallis test of the non-parametric tests for comparisons of significant differences in the P50 SG ratio between different groups. The results showed no significant difference in P50 SG ratio between age, sex, HAMD, SCL-90, and anxiety/depression groups divided by 7/7 ($p > 0.05$, Table 2).

However, in the HAMA and anxiety/depression groups divided by 14/20, some groups had significant differences in the P50 SG ratio ($p < 0.05$, Table 2). The P50 SG ratio of the HAMA group were significantly different between the NA and TMBOA groups ($p < 0.05$, Table 3). There was a significant difference in the P50 SG ratio between the NAOD and AAD groups with the threshold of 14/20 ($p < 0.05$, Table 4).

Finally, we conducted a correlation analysis, which analyzed the correlation between the P50 SG ratio and the variables of each scale (Table 5). We also conducted multi-angle analysis by grouping (Table 5). We discussed the correlation between the P50 SG ratio and other variables from the total sample, the normal P50 SG ratio sample,

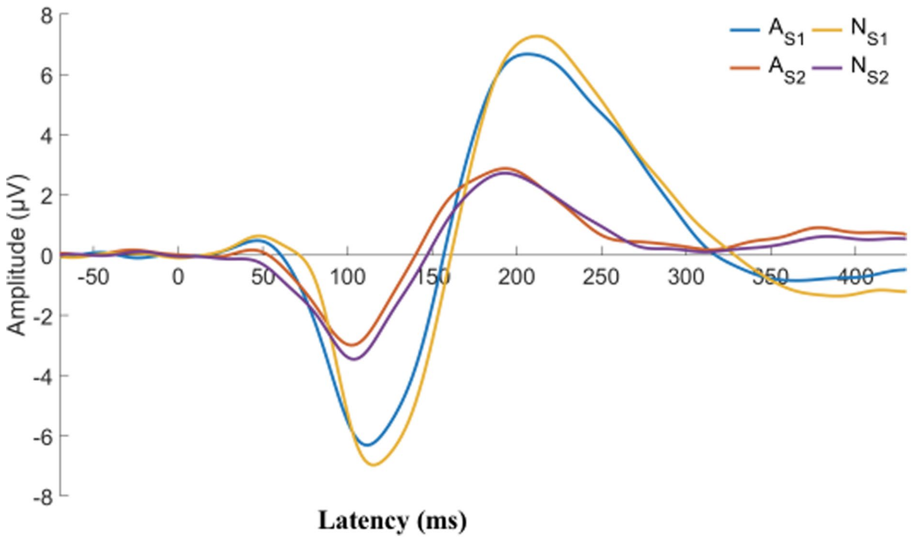

FIGURE 3
CFS patients were classified into two groups, normal and abnormal, based on their P50 SG ratio. The displayed graph illustrates the average S1 and S2 waveform for both groups. A, abnormal (P50 SG ratio > 50%); N, normal (P50 SG ratio ≤ 50%).

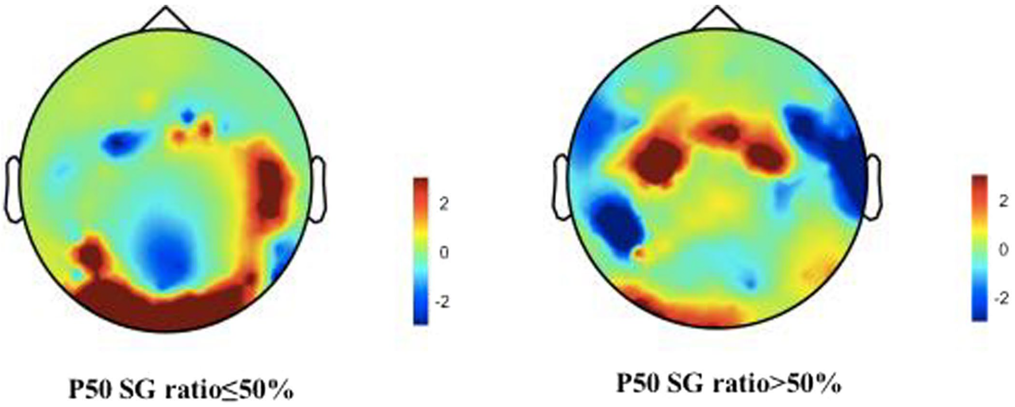

FIGURE 4
Brain activities in both normal and abnormal P50 SG ratio groups of CFS patients. A representation of "topographies" at the peak of P50 response illustrates the spatial distribution of brain activity, displays differences in mean energy spectral density. The diagram depicts the disparity in brain energy levels between the two groups. The figure showed that the energy accumulation in brain lobes may be different in both normal and abnormal P50 SG ratio groups of CFS patients.

the abnormal P50 SG ratio sample, and the anxiety/depression sample divided by 7/7 and 14/20. In the overall sample, the somatization scores in the HAMA and HAMD were correlated with the P50 SG ratio, and the somatization scores in HAMD were associated with P50 SG ratio in the OD group delimited by 14/20 and the AAD group delimited by 7/7 and 14/20 ($p < 0.05$, Table 5). In the NAOD group delimited by 14/20, the somatization scores in HAMA are also associated with the P50 SG ratio. Among the general population, sense of despair, hostility, and paranoid ideation were correlated with the P50 SG ratio ($p < 0.05$, Table 5). Regarding the correlation between P50 SG ratio and anxiety and depression symptoms that this study focuses on, the overall characteristics of the results of other groups are as follows: the greater the levels of anxiety and depression symptoms, the greater the correlation is. When comparing the 14/20 groups with the 7/7 groups, the correlation is greater with the group exhibiting more symptoms (Table 5).

In the regression analysis of each item on the three scales, solely the hopelessness score in HAMD emerged as a risk factor for an abnormal P50 SG ratio. However, other factors showed no significance. The following binary logistic regression analysis of P50 SG ratio showed that the OA and AAD groups delimited by 14/20 in different groups significantly influenced the P50 SG ratio ($p < 0.05$, Table 6).

4 Discussion

The concept of CFS continues to receive widespread attention, and fatigue is becoming a major public health problem. Its

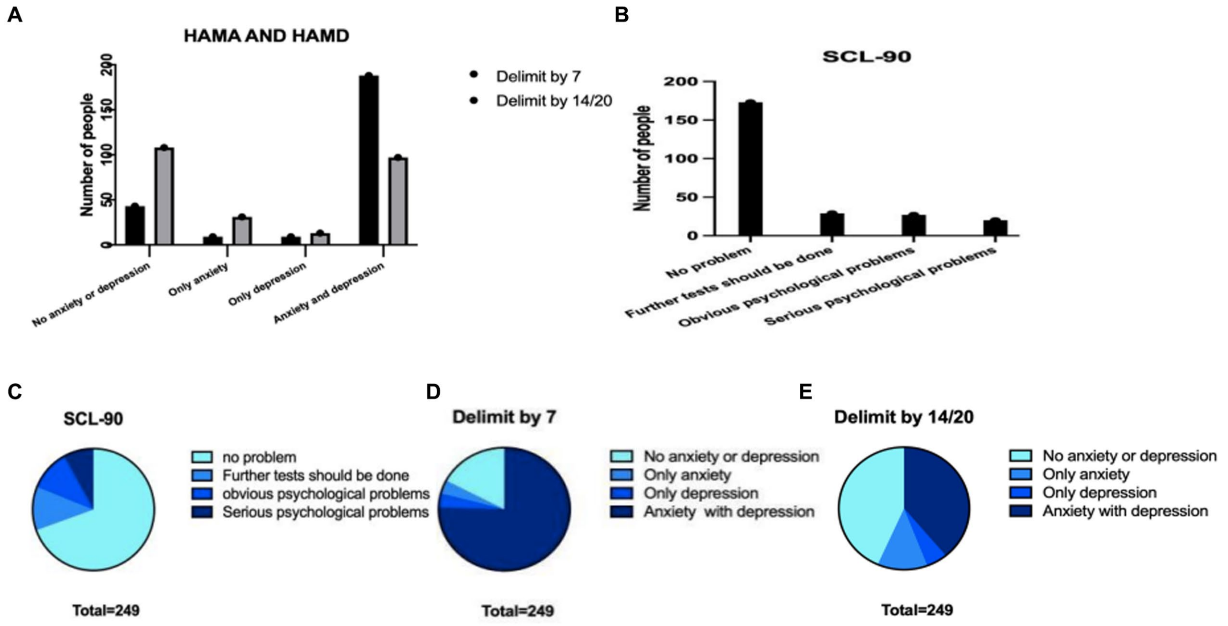

FIGURE 5
The characteristics of the three scales in the total population were compared with the data differences obtained from different scales. **(A)** Number of HAMA and HAMD patients with different dividing lines **(B)** number of patients with different SCL-90 scores **(C)** proportions of different parts of SCL-90 **(D)** the proportion of patients with different degrees of HAMA and HAMD scales divided by 7 **(E)** the proportion of patients with different degrees of HAMA and HAMD scales divided by 14.

TABLE 2 Non-parametric tests for differences in P50 values between different variable groups.

The K-W test	Total = 249	*N* (%)	Degrees of freedom	*p* value
Age	The youth	58 (23.3)	3	0.764
	Young and middle-aged	54 (21.7)		
	The middle-aged	37 (14.9)		
	The middle-aged and elderly	100 (40.2)		
Gender	Male	109 (43.8)	1	0.079
	Female	140 (56.2)		
Anxiety (HAMA)	No anxiety	48 (19.3)	4	*0.032*
	May have anxiety	60 (24.1)		
	There must be anxiety	61 (24.5)		
	There must be obvious anxiety	52 (20.9)		
	May be severe anxiety	28 (11.2)		
Depression (HAMD)	No depression	52 (20.9)	3	0.055
	Maybe mild depression	83 (33.3)		
	Must be depressed	88 (35.3)		
	Severe depression	26 (10.4)		
SCL-90	No problem	173 (69.5)	3	0.353
	Further tests should be done	29 (11.6)		
	Obvious psychological problems	27 (10.8)		
	Serious psychological problems	20 (8.0)		
Anxiety/depression(divided by 7)	No anxiety and depression	43 (17.3)	3	0.092
	Only anxiety	9 (3.6)		
	Only depression	9 (3.6)		
	Anxiety with depression	188 (75.5)		
Anxiety/depression (divided by 14/20)	No anxiety and depression	108 (43.4)	3	*0.024*
	Only anxiety	31 (12.4)		
	Only depression	13 (5.2)		
	Anxiety with depression	97 (39.0)		

$p < 0.05$ in italics was considered to be different between groups.

TABLE 3 Pairwise comparison for the P50 SG ratio of anxiety degree groups.

Sample 1-sample 2	Test statistics	Standard error	Standard test statistics	Significance	Adj. significance[a]
NA-MHA	−16.796	13.946	−1.204	0.228	1.000
NA-TMBA	−16.973	13.895	−1.222	0.222	1.000
NA-MBSA	−32.926	17.126	−1.923	0.055	0.545
NA-TMBOA	−44.037	14.415	−3.055	0.002	*0.023*
MHA-TMBA	−0.177	13.094	−0.014	0.989	1.000
MHA-MBSA	−16.130	16.483	−0.979	0.328	1.000
MHA-TMBOA	−27.241	13.645	−1.996	0.046	0.459
TMBA-MBSA	−15.953	16.439	−0.970	0.332	1.000
TMBA-TMBOA	−27.064	13.593	−1.991	0.046	0.465
MBSA-TMBOA	11.111	16.881	0.658	0.510	1.000

Each row tests the null hypothesis that sample 1 and sample 2 have the same distribution. Progressive significance was shown (two-sided test). The significance level was 0.05. [a]Significance values have been adjusted by Bonferroni correction for a number of tests. NA, no anxiety; MHA, may have anxiety; TMBA, there must be anxiety; MBSA, may be severe anxiety; TMBOA, there must be obvious anxiety. $p < 0.05$ in italics was considered to be different between groups.

TABLE 4 Pairwise comparison for the P50 SG ratio of anxiety and depression groups (divided by 14/20).

Sample 1-sample 2	Test statistics	Standard error	Standard test statistics	Significance	Adj. significance[a]
NAOD-OD	−16.220	14.674	−1.105	0.269	1.000
NAOD-AAD	−29.949	10.074	−2.973	0.003	*0.018*
NAOD-OA	−30.307	21.142	−1.433	0.152	0.910
OD-AND	−13.729	14.859	−0.924	0.356	1.000
OD-OA	−14.087	23.796	0.423	0.554	1.000
AAD-OA	0.358	21.270	0.335	0.987	1.000

Each row tests the null hypothesis that sample 1 and sample 2 have the same distribution. Progressive significance was shown (two-sided test). The significance level was 0.05. [a]Significance values have been adjusted by Bonferroni correction for a number of tests. NAOD, no anxiety or depression; OA, only anxiety; OD, only depression; AAD, anxiety and depression. $p < 0.05$ in italics was considered to be different between groups.

TABLE 5 The correlation analysis results of P50 value and various variables.

Spearman nonparametric test			Total ($N = 249$)	P50 normal ($N = 108$)	P50 abnormal ($N = 141$)	AAD delimited by 7 ($N = 188$)	NAOD on delimited by 14/20 ($N = 108$)	OD delimited by 14/20 ($N = 13$)	AAD delimited by 14/20 ($N = 97$)
	Somatic symptoms	Sig. (Double tail)	0.012*				0.022*		
	Psychological symptoms	Sig. (Double tail)	0.003**			0.035*	0.023*		0.030*
	HAMA total points	Sig. (Double tail)	0.002**			0.025*	0.013*		0.040*
	Anxiety/somatization	Sig. (Double tail)	0.002**			0.004**		0.048*	0.016*
	Weight	Sig. (Double tail)		0.033*					
	Cognitive impairment	Sig. (Double tail)				0.003**	0.009**		0.006**
	Day and night change	Sig. (Double tail)			0.032*				0.038*
	Blockage	Sig. (Double tail)			0.039*	0.002**	0.017*		0.003**
	Sense of Despair	Sig. (Double tail)	0.001**			0.002**	0.044*		0.013*
	HAMD total points	Sig. (Double tail)	0.001**			0.001**			0.003**
	Interpersonal sensitivity	Sig. (Double tail)						0.038*	
	Depression	Sig. (Double tail)						0.036*	
	Hostility	Sig. (Double tail)	0.018*					0.048*	
	Paranoid ideation	Sig. (Double tail)	0.019*						

*At level 0.05 (two-tailed), the correlation was significant. **At level 0.01 (two-tailed), the correlation was significant. NAOD, no anxiety or depression; OA, only anxiety; OD, only depression; AAD, anxiety and depression.

etiology and pathogenesis remain unclear, resulting in a lack of specific treatments, possibly due to the involvement of multiple systems and difficulty distinguishing CFS symptoms from those of anxiety and depression (Zhao, 2018). To our knowledge, few studies have investigated the relationship between fatigue and anxiety/depression. This cross-sectional study analyzes anxiety/depression in a population of patients with CFS. It explores the distribution characteristics of anxiety/depression symptoms in this population and the correlation of the P50 SG ratio with different symptoms.

The incidence rate of CFS varies significantly according to country, sex, age, and educational background (Crawley, 2014; Faro et al., 2016; Herrera et al., 2018). Our results show that CFS is more common in women (56.2%), people older than 50 years old (40.2%), and people with relatively high education levels, similar to the characteristics of previous findings (Frémont et al., 2013). The participants were highly educated and more concerned about their health, which may explain why they actively sought help in the fatigue clinic of the general hospital.

The fatigue dimension of CFS patients exists in the physical and mental aspects, mainly manifested as anxiety, depression, irritability, and emotional instability (Cella et al., 2013; Jackson and Mac Leod, 2017; Salk et al., 2017). We first evaluated the SCL-90 scale for this population. SCL-90 has a comprehensive dimension and a specific ability to distinguish physical and mental symptoms, which has good reliability and validity in Chinese populations (Chen and Li, 2003; Sun et al., 2017; Dang et al., 2021). The results of the SCL-90 scale among the outpatient population indicated a comparatively low prevalence of psychological issues and a comparatively high prevalence of physical or somatic symptoms. These findings prompt our hypothesis that CFS may manifest as a distinct condition, separate from anxiety, depression, and other emotional disorders. Some patients with CFS may solely experience physical symptoms without comorbid emotional symptoms. After checking the widely used the HAMA and HAMD (Zhang et al., 2020; Zimmerman et al., 2020), we observed that the data from the HAMA, HAMD, and SCL-90 exhibited distinct trends regarding the assessment of emotional disorders (Figure 5). This confirmed that most patients with CFS had anxiety (69.5%) and depression (79%) according to HAMA and HAMD, suggesting that people with CFS have a high rate of comorbidity with anxiety/depression (Leong et al., 2022). While many patients experience noticeable mental symptoms like anxiety or depression, they tend to perceive their condition primarily in terms of physical problems. This perception aligns with the clinical profile of most of these patients, who initially seek treatment at non-psychiatric hospitals. The SCL-90 results reflect that most patients present for physical symptoms such as fatigue without revealing obvious psychiatric problems, which is not inconsistent.

We now discuss the possible reasons for this different trend between those scales. The HAMA and HAMD are rating scales of the physician's assessment, while the SCL-90 is a self-rating scale. There are differences in the evaluation subjects. In addition, the scales have specific differences in the classification of different symptoms, which may be one of the reasons for the difference in results (Carrozzino et al., 2020). Moreover, the characteristics of our outpatients are, the general hospital neurology outpatients some clinicians consider psychological problems, patients do not recognize, they usually feel that they are the existence of physical disease. This phenomenon has been reported in the literature (Wang et al., 2022).

Although the exact underlying mechanism of fatigue in individuals with CFS remains unclear, it is believed to involve the central fatigue predominantly, as this is primarily associated with stress (Aleksandrov et al., 2016). However, the pathogenesis of CFS in cases associated with other factors, such as viral infection, may be more intricate. Some studies have demonstrated that muscle fatigue affecting the central fatigue will further weaken the SG (Evstigneeva et al., 2010; Aleksandrov et al., 2016). The normal brain filters out non-important information and selects useful information. Through this gating, valuable information is absorbed and transmitted to the higher brain to avoid an overload of information intake (Wang et al., 2009). The S2 to S1 ratio is the commonly used metric to separate patients from controls (Smith et al., 1994; Jiang et al., 2015; Xie and Liang, 2015). In the present study, more than half of the population (56.6%) had an abnormal P50 SG ratio. In our total sample, correlation analysis revealed that the P50 SG ratio was associated with somatization symptoms in HAMA and HAMD, suggesting a potential correlation between P50 SG and fatigue ($p < 0.05$, Table 5). Patients with CFS with no anxiety/depression delimited by 7/7 showed no apparent correlation between P50 SG and somatic symptoms. However, when the grouping method was modified by adjusting the cutoff to 14/20 and adding patients with potential symptoms of anxiety/depression, a correlation was observed. These findings suggest that as the symptoms of anxiety/depression worsen in CFS patients, the degree of brain function abnormalities becomes increasingly apparent. This was initially attributed to an association with anxiety/depression, but it is more reasonable to associate it with physical symptoms. Since there is no reliable measure for evaluating fatigue, the data in this study cannot provide further insights into the relationship between fatigue and physical symptoms. However, in scale classification, fatigue is categorized as a physical symptom. Therefore, the presence of P50 SG ratio abnormalities in these patients should be interpreted as an indication of increasingly pronounced brain function abnormalities as anxiety/depression and fatigue worsen in patients with CFS.

Previous studies have reported that abnormalities in P50 SG ratio are likely associated with anxiety and depression in patients (Xie and Liang, 2015). Our data further support these findings. The P50 SG ratio in patients with schizophrenia is influenced by depression (Li et al., 2023). The literature has shown that P50 SG ratio levels are correlated with anxiety, depression, and cognitive function (Sussman et al., 2014). In our study, regression analysis showed that among the influencing factors in different anxiety/depression groups, the OA and AAD groups delimited by 14/20 impacted P50 SG ratio. The abnormal influence of P50 SG ratio may contribute to dysregulated brain function, potentially leading to heightened anxiety/depression in certain patients. This study revealed additional dimensions of the HAMA and HAMD, including cognition, fear, hostility, and paranoia (Table 5). With the subgroup of NAOD going from 7/7 with no anxiety and depression symptoms at all to 14/20 with possible anxiety and depression symptoms, the percentage of patients with abnormal P50 SG ratio responses increased from 17.3 to 43.4%, the symptoms of anxiety and depression were significantly intensified, and a significant correlation was observed. It is plausible that with the progression of the disease, abnormal brain function manifests an increasing number of psychiatric symptoms. Furthermore, among the 43 patients in the NAOD group delimited by 7/7, 20 tested positive for P50 SG ratio (data not provided in Table 2), the differences in P50 SG ratio degree observed may not solely be attributable to anxiety and depression, but may also be significantly associated with the sleep problems among patients suffering from CFS, which this study was not addressed. These previously unexplored characteristics of the NAOD groups offer new avenues for investigation. Our findings demonstrate the possible

TABLE 6 Binary logistic regression analysis.

Variable in the equation									
		B	Standard error	Wald	Degree of freedom	Significance	Exp(B)	95% confidence interval for EXP(B)	
								The upper limit	The floor limit
Step 1[a]	NAOD			8.155	3	0.043			
	OA	−0.802	0.287	7.793	1	*0.005*	0.448	0.255	0.787
	OD	−0.552	0.418	1.748	1	0.186	0.576	0.254	1.305
	AAD	−0.147	0.609	0.058	1	0.809	0.863	0.262	2.846
	Constant	0.617	0.213	8.400	1	*0.004*	1.853		

NAOD, no anxiety or depression; OA, only anxiety; OD, only depression; AAD, anxiety and depression. [a]Variables entered in step 1: anxiety and depression group. $p < 0.05$ in italics was considered to be different between groups.

application of the objective P50 SG test to differenate CFS patients with anxiety or depression (Figure 4).

SG of P50 auditory-evoked potentials has been previously suggested in other literature to contribute to stimulus selection and information processing and may further affect cognition and emotion. The specific mechanism may be related to cholinergic regulation and hippocampal-mediated preattention channels (Adler et al., 1993; Freedman et al., 1994, 1996). P50 SG inhibition may involve activity across brain networks. Previous experiments have found that P50 SG ratio can change the rhythm of the entire cerebral cortex with the reduction of beta waves (Javitt and Freedman, 2015), and a higher P50 SG ratio than normal indicates a weaker ability to process information. This could be the underlying pathophysiological mechanism responsible for the abnormal P50 SG ratio observed in patients with CFS.

This study had some limitations. First CSF patients with anxiety/depression history (diagnosed and treated before they were recruited in our study) were not enrolled. All of them were treated with certain kinds of medications for their symptoms, which could disturb the measurement of P50 SG (Oranje et al., 2011). In addition, we only got few patients of this kind (total number was less than 5). However, excluding these patients may affect the evaluation of correlation coefficient.

The jumpy nature of the scale scoring method hampers accurate grading of symptom severity, leading to a decrease in grouping accuracy. Moreover, the data exhibited poor normality, thereby impacting the analysis of the results to an extent. Furthermore, This study employs a cross-sectional design, focusing on symptoms and EEG physiological markers among individuals diagnosed with CFS. Further exploration of their precise relationships necessitates additional cohort studies. The absence of reliable fatigue symptom scales or other measurement tools also hinders further research on CFS.

Considering the intricate etiology of CFS and the nature of symptom-based diagnostic criteria, some heterogeneity among the patients included in this study was expected. Nevertheless, most patients exhibited discernible abnormalities in P50 SG ratio that were closely associated with clinical symptoms, encompassing fatigue, emotion, cognition, and overall well-being.

The findings of this study indicate that abnormal brain function potentially plays a vital role in CFS pathogenesis. Furthermore, a positive correlation between the number of symptoms exhibited by the P50 index and clinical symptoms was observed, reinforcing the significance of this association. Consequently, in light of the study findings, we posit that CFS patients exhibiting the higher P50 SG ratio should be categorized into distinct subtypes or subgrouped within the functional neurological disorders spectrum to promote additional exploration of their central fatigue mechanisms.

Data availability statement

The original contributions presented in the study are included in the article/supplementary material, further inquiries can be directed to the corresponding author.

Ethics statement

The studies involving humans were approved by The Human Research Ethics Committee of Beijing Friendship Hospital, affiliated with Capital Medical University. The studies were conducted in accordance with the local legislation and institutional requirements. Written informed consent for participation was not required from the participants or the participants' legal guardians/next of kin in accordance with the national legislation and institutional requirements.

Author contributions

XL: Writing – original draft, Data curation, Formal analysis, Investigation, Methodology, Supervision, Validation, Writing – review & editing. SL: Data curation, Formal analysis, Visualization, Writing – review & editing. RR: Data curation, Writing – review & editing. XW: Formal analysis, Writing – original draft, Writing – review & editing. CH: Writing – review & editing. ZL: Writing – review & editing.

Funding

The author(s) declare financial support was received for the research, authorship, and/or publication of this article.

Fund project: Capital Health Development Research Project (2018-1-221); National priority. R&D Program Science and Technology Winter Olympics Special (2019YFF0301700).

Acknowledgments

We express our gratitude to the authors, reviewers, and editors for their dedication and contribution to this study. Additionally, we extend our appreciation to each patient for their invaluable patience and cooperation during the completion of all the tests. We would like to thank Editage (www.editage.cn) for English language editing.

Conflict of interest

The authors declare that the research was conducted in the absence of any commercial or financial relationships that could be construed as a potential conflict of interest.

Publisher's note

References

Achenbach, T. M., Ivanova, M. Y., Rescorla, L. A., Turner, L. V., and Althoff, R. R. (2016). Internalizing/externalizing problems: review and recommendations for clinical and research applications. *J. Am. Acad. Child Adolesc. Psychiatry* 55, 647–656. doi: 10.1016/j.jaac.2016.05.012

Addington, D., Addington, J., and Atkinson, M. (1996). A psychometric comparison of the Calgary depression scale for schizophrenia and the Hamilton depression rating scale. *Schizophr. Res.* 19, 205–212. doi: 10.1016/0920-9964(95)00070-4

Adler, L. E., Hoffer, L. D., Wiser, A., and Freedman, R. (1993). Normalization of auditory physiology by cigarette smoking in schizophrenic patients. *Am. J. Psychiatry* 150, 1856–1861. doi: 10.1176/ajp.150.12.1856

Aleksandrov, A. A., Dmitrieva, E. S., Stankevich, L. N., Knyazeva, V. M., and Shestakova, A. N. (2016). The development of muscle fatigue suppresses auditory sensory gating (P50) during sustained contraction. *Front. Syst. Neurosci.* 10:44. doi: 10.3389/fnsys.2016.00044

Barnden, L. R., Crouch, B., Kwiatek, R., Burnet, R., and Del Fante, P. (2015). Evidence in chronic fatigue syndrome for severity-dependent upregulation of prefrontal myelination that is independent of anxiety and depression. *NMR Biomed.* 28, 404–413. doi: 10.1002/nbm.3261

Carrozzino, D., Patierno, C., Fava, G. A., and Guidi, J. (2020). The Hamilton rating scales for depression: a critical review of Clinimetric properties of different versions. *Psychother. Psychosom.* 89, 133–150. doi: 10.1159/000506879

Carruthers, B. M., van de Sande, M. I., De Meirleir, K. L., Klimas, N. G., Broderick, G., Mitchell, T., et al. (2011). Myalgic encephalomyelitis: international consensus criteria. *J. Intern. Med.* 270, 327–338. doi: 10.1111/j.1365-2796.2011.02428.x

Cella, M., White, P. D., Sharpe, M., and Chalder, T. (2013). Cognitions, behaviours and co-morbid psychiatric diagnoses in patients with chronic fatigue syndrome. *Psychol. Med.* 43, 375–380. doi: 10.1017/S0033291712000979

Chen, S. L., and Li, L. J. (2003). Re-testing reliability, validity and norm applicatility of SCL-90. *Chin J Nerv Ment Dis.* 13, 79–83. doi: 10.1007/s11769-003-0089-1

Clayton, E. W. (2015). Beyond myalgic encephalomyelitis/chronic fatigue syndrome: an IOM report on redefining an illness. *JAMA* 313, 1101–1102. doi: 10.1001/jama.2015.1346

Cockshell, S. J., and Mathias, J. L. (2013). Cognitive deficits in chronic fatigue syndrome and their relationship to psychological status, symptomatology, and everyday functioning. *Neuropsychology* 27, 230–242. doi: 10.1037/a0032084

Crawley, E. (2014). The epidemiology of chronic fatigue syndrome/myalgic encephalitis in children. *Arch. Dis. Child.* 99, 171–174. doi: 10.1136/archdischild-2012-302156

Dang, W., Xu, Y., Ji, J., Wang, K., Zhao, S., Yu, B., et al. (2021). Study of the SCL-90 scale and changes in the Chinese norms. *Front. Psych.* 11:524395. doi: 10.3389/fpsyt.2020.524395

Derogatis, LR. *Symptom Checklist-90-R: Administration, Scoring & Procedure Manual for the Revised Version of the SCL-90.* Minneapolis, MN: National Computer Systems (1994)

Evstigneeva, M. D., Alexandrov, A. A., Mathiassen, S. E., and Lyskov, E. (2010). Muscle contraction force and fatigue: effects on mismatch negativity. *Neuroreport* 21, 1152–1156. doi: 10.1097/WNR.0b013e328340cc66

Faro, M., Sàez-Francás, N., Castro-Marrero, J., Aliste, L., Fernández de Sevilla, T., and Alegre, J. (2016). Gender differences in chronic fatigue syndrome. *Reumatol Clin.* 12, 72–77. doi: 10.1016/j.reuma.2015.05.007

Freedman, R., Adler, L. E., Bickford, P., Byerley, W., Coon, H., Cullum, C. M., et al. (1994). Schizophrenia and nicotinic receptors. *Harv. Rev. Psychiatry* 2, 179–192. doi: 10.3109/10673229409017136

Freedman, R., Adler, L. E., Myles-Worsley, M., Nagamoto, H. T., Miller, C., Kisley, M., et al. (1996). Inhibitory gating of an evoked response to repeated auditory stimuli in schizophrenic and normal subjects. Human recordings, computer simulation, and an animal model. *Arch. Gen. Psychiatry* 53, 1114–1121. doi: 10.1001/archpsyc.1996.01830120052009

Frémont, M., Coomans, D., Massart, S., and De Meirleir, K. (2013). High-throughput 16S rRNA gene sequencing reveals alterations of intestinal microbiota in myalgic encephalomyelitis/chronic fatigue syndrome patients. *Anaerobe* 22, 50–56. doi: 10.1016/j.anaerobe.2013.06.002

Fukuda, K., Straus, S. E., Hickie, I., Sharpe, M. C., Dobbins, J. G., and Komaroff, A. (1994). The chronic fatigue syndrome: a comprehensive approach to its definition and study. International chronic fatigue syndrome study group. *Ann. Intern. Med.* 121, 953–959. doi: 10.7326/0003-4819-121-12-199412150-00009

Haider, S., Janowski, A. J., Lesnak, J. B., Hayashi, K., Dailey, D. L., Chimenti, R., et al. (2023). A comparison of pain, fatigue, and function between post-COVID-19 condition, fibromyalgia, and chronic fatigue syndrome: a survey study. *Pain* 164, 385–401. doi: 10.1097/j.pain.0000000000002711

Hamilton, M. (1959). The assessment of anxiety states by rating. *Br. J. Med. Psychol.* 32, 50–55. doi: 10.1111/j.2044-8341.1959.tb00467.x

Hamilton, M. (1960). A rating scale for depression. *J. Neurol. Neurosurg. Psychiatry* 23, 56–62. doi: 10.1136/jnnp.23.1.56

Harrison, L. A., Kats, A., Williams, M. E., and Aziz-Zadeh, L. (2019). The importance of sensory processing in mental health: a proposed addition to the research domain criteria (RDoC) and suggestions for RDoC 2.0. *Front. Psychol.* 10:103. doi: 10.3389/fpsyg.2019.00103

Herrera, S., de Vega, W. C., Ashbrook, D., Vernon, S. D., and McGowan, P. O. (2018). Genome-epigenome interactions associated with Myalgic encephalomyelitis/chronic fatigue syndrome. *Epigenetics* 13, 1174–1190. doi: 10.1080/15592294.2018.1549769

Jackson, H., and Mac Leod, A. K. (2017). Well-being in chronic fatigue syndrome: relationship to symptoms and psychological distress. *Clin. Psychol. Psychother.* 24, 859–869. doi: 10.1002/cpp.2051

Javitt, D. C., and Freedman, R. (2015). Sensory processing dysfunction in the personal experience and neuronal machinery of schizophrenia. *Am. J. Psychiatry* 172, 17–31. doi: 10.1176/appi.ajp.2014.13121691

Jiang, W. H., Zhang, W., Zhao, X. W., Sun, D. W., Chen, X. S., Song, L. S., et al. (2015). Three-year follow up of event-related potentials PPI, P50 and color map of N400 during the rehabilitation of first episode schizophrenia patients. *Natl Med China.* 95, 3813–3817. doi: 10.3760/cma.j.issn.0376-2491.2015.47.004

Kennedy, G., Spence, V. A., McLaren, M., Hill, A., Underwood, C., and Belch, J. J. (2005). Oxidative stress levels are raised in chronic fatigue syndrome and are associated with clinical symptoms. *Free Radic. Biol. Med.* 39, 584–589. doi: 10.1016/j.freeradbiomed.2005.04.020

Klumpp, H., and Shankman, S. A. (2018). Using event-related potentials and startle to evaluate time course in anxiety and depression. *Biol Psychiatry Cogn Neurosci Neuroimaging.* 3, 10–18. doi: 10.1016/j.bpsc.2017.09.004

Leong, K. H., Yip, H. T., Kuo, C. F., and Tsai, S. Y. (2022). Treatments of chronic fatigue syndrome and its debilitating comorbidities: a 12-year population-based study. *J. Transl. Med.* 20:268. doi: 10.1186/s12967-022-03461-0

Li, S., Yu, B., Wang, D., Xia, L., Wang, L., Chen, D., et al. (2023). P50 sensory gating, cognitive deficits and depressive symptoms in first-episode antipsychotics-naïve schizophrenia. *J. Affect. Disord.* 324, 153–161. doi: 10.1016/j.jad.2022.12.143

Manu, P., Lane, T. J., and Matthews, D. A. (1988). The frequency of the chronic fatigue syndrome in patients with symptoms of persistent fatigue. *Ann. Intern. Med.* 109, 554–556. doi: 10.7326/0003-4819-109-7-554

Oranje, B., Wienberg, M., and Glenthoj, B. Y. (2011). A single high dose of escitalopram disrupts sensory gating and habituation, but not sensorimotor gating in healthy volunteers. *Psychiatry Res.* 186, 431–436. doi: 10.1016/j.psychres.2010.09.019

Preti, A., Carta, M. G., and Petretto, D. R. (2019). Factor structure models of the SCL-90-R: replicability across community samples of adolescents. *Psychiatry Res.* 272, 491–498. doi: 10.1016/j.psychres.2018.12.146

Prins, J. B., van der Meer, J. W., and Bleijenberg, G. (2006). Chronic fatigue syndrome. *Lancet* 367, 346–355. doi: 10.1016/S0140-6736(06)68073-2

Qin, X., Sun, J., Wang, M., Lu, X., Dong, Q., Zhang, L., et al. (2020). Gender differences in dysfunctional attitudes in major depressive disorder. *Front. Psych.* 11:86. doi: 10.3389/fpsyt.2020.00086

Roy-Byrne, P., Afari, N., Ashton, S., Fischer, M., Goldberg, J., and Buchwald, D. (2002). Chronic fatigue and anxiety/depression: a twin study. *Br. J. Psychiatry* 180, 29–34. doi: 10.1192/bjp.180.1.29

Sáez-Francàs, N., Alegre, J., Calvo, N., Antonio Ramos-Quiroga, J., Ruiz, E., Hernández-Vara, J., et al. (2012). Attention-deficit hyperactivity disorder in chronic fatigue syndrome patients. *Psychiatry Res.* 200, 748–753. doi: 10.1016/j.psychres.2012.04.04111

Salk, R. H., Hyde, J. S., and Abramson, L. Y. (2017). Gender differences in depression in representative national samples: Meta-analyses of diagnoses and symptoms. *Psychol. Bull.* 143, 783–822. doi: 10.1037/bul0000102

Shungu, D. C., Weiduschat, N., Murrough, J. W., Mao, X., Pillemer, S., Dyke, J. P., et al. (2012). Increased ventricular lactate in chronic fatigue syndrome. III. Relationships to cortical glutathione and clinical symptoms implicate oxidative stress in disorder pathophysiology. *NMR Biomed.* 25, 1073–1087. doi: 10.1002/nbm.2772

Smith, D. A., Boutros, N. N., and Schwarzkopf, S. B. (1994). Reliability of P50 auditory event-related potential indices of sensory gating. *Psychophysiology* 31, 495–502. doi: 10.1111/j.1469-8986.1994.tb01053.x

Sun, X. Y., Li, Y. X., Yu, C. Q., and Li, L. M. (2017). Reliability and validity of depression scales of Chinese version: a systematic review. *Zhonghua Liu Xing Bing Xue Za Zhi* 38, 110–116. doi: 10.3760/cma.j.issn.0254-6450.2017.01.021

Sussman, E. S., Chen, S., Sussman-Fort, J., and Dinces, E. (2014). The five myths of MMN: redefining how to use MMN in basic and clinical research. *Brain Topogr.* 27, 553–564. doi: 10.1007/s10548-013-0326-6

Teodoro, T., Edwards, M. J., and Isaacs, J. D. (2018). A unifying theory for cognitive abnormalities in functional neurological disorders, fibromyalgia and chronic fatigue syndrome: systematic review. *J. Neurol. Neurosurg. Psychiatry* 89, 1308–1319. doi: 10.1136/jnnp-2017-3178236

Wang, H. X., Bai, P. S., and Chen, X. S. (2002). Application of sensory gating P 50 in the study of schizophrenia. *Chin J Psychiatry.* 35, 125–128. doi: 10.3760/j:issn:1006-7884.2002.02.025

Wang, Y., Fang, Y. R., Chen, X. S., Chen, J., Wu, Z. G., Yuan, C. M., et al. (2009). A follow-up study on features of sensory gating P50 in treatment-resistant depression patients. *Chin. Med. J.* 122, 2956–2960. doi: 10.3760/cma.j.issn.0366-6999.2009.24.007

Wang, H. X., Ma, X., and Zhen, W. F. (2010). Follow-up study on auditory sensory gating P 50 in schizophrenia patients with homicide. *Chin J Neuropsychiatr Disord* 36, 153–156. doi: 10.3969/j.issn.1002-0152.2010.03.007

Wang, J., Zhu, E., Ai, P., Liu, J., Chen, Z., Wang, F., et al. (2022). The potency of psychiatric questionnaires to distinguish major mental disorders in Chinese outpatients. *Front. Psych.* 13:1091798. doi: 10.3389/fpsyt.2022.1091798

Wright, A., Fisher, P. L., Baker, N., O'Rourke, L., and Cherry, M. G. (2021). Perfectionism, depression and anxiety in chronic fatigue syndrome: a systematic review. *J. Psychosom. Res.* 140:110322. doi: 10.1016/j.jpsychores.2020.11032210

Xie, Z. B., and Liang, M. L. (2015). Characteristics of cognitive potential P 300 and sensory gating P50 in patients with anxiety disorders. *Sichuan Ment Health.* 28, 25–22. doi: 10.11886/j.issn.1007-3256.2015.01.008

Xue, Q. M., and Liu, Z. D. (2015). Cortical diencephalic syndrome caused by long-term stress state. *J Clin Psychosomat Dis.* 21, 110–113. doi: 10.3969/j.Issn.1672-187X.2015.01.038-0110-04

Zhang, B., Cui, C., Yu, H., and Li, G. (2020). Association between ZNF184 and symptoms of Parkinson's disease in southern Chinese. *Neurol. Sci.* 41, 2121–2126. doi: 10.1007/s10072-020-04309-5

Zhao, C. X. (2018). Research status of chronic fatigue syndrome. *J. Heze Univ.* 40, 60–64. doi: 10.16393/j.cnki.37-1436/z.2018.05.014

Zimmerman, M., Thompson, J. S., Diehl, J. M., Balling, C., and Kiefer, R. (2020). Is the DSM-5 anxious distress specifier interview a valid measure of anxiety in patients with generalized anxiety disorder: a comparison to the Hamilton anxiety scale. *Psychiatry Res.* 286:112859. doi: 10.1016/j.psychres.2020.112859

frontiers | Frontiers in Neuroscience

TYPE Original Research
PUBLISHED 26 January 2024
DOI 10.3389/fnins.2023.1321365

Radiation-induced glymphatic dysfunction in patients with nasopharyngeal carcinoma: a study using diffusion tensor image analysis along the perivascular space

Xingyou Zheng[1†], Jianchun Peng[2†], Qing Zhao[3,4], Li Li[5], Jian-ming Gao[6], Keyang Zhou[2], Bei Tan[2], Lingling Deng[2]* and Youming Zhang[3,4]*

[1]Department of Medical Imaging, The Fourth Hospital of Changsha, Changsha, Hunan, China, [2]Department of Radiology, The Second Affiliated Hospital, Hengyang Medical School, University of South China, Hengyang, Hunan, China, [3]Department of Radiology, Xiangya Hospital, Central South University, Changsha, China, [4]National Clinical Research Center for Geriatric Diseases, Xiangya Hospital, Central South University, Changsha, Hunan, China, [5]Sun Yat-sen University Cancer Center, State Key Laboratory of Oncology in South China, Collaborative Innovation Center for Cancer Medicine, Guangzhou, China, [6]Department of Radiation Oncology, Sun Yat-sen University Cancer Center, State Key Laboratory of Oncology in South China, Collaborative Innovation Center for Cancer Medicine, Guangzhou, China

Radiation encephalopathy (RE) refers to radiation-induced brain necrosis and is a life-threatening complication in patients with nasopharyngeal carcinoma (NPC) after radiotherapy (RT), and radiation-induced pre-symptomatic glymphatic alterations have not yet been investigated. We used diffusion tensor image analysis along the perivascular space (DTI-ALPS) index to examine the pre-symptomatic glymphatic alterations in NPC patients following RT. A total of 109 patients with NPC consisted of Pre-RT ($n = 35$) and Post-RT ($n = 74$) cohorts were included. The post-RT NPC patients, with normal-appearing brain structure at the time of MRI, were further divided into Post-RT-RE- ($n = 58$) and Post-RT-RE+ ($n = 16$) subgroups based on the detection of RE in follow-up. We observed lower DTI-ALPS $_{\text{left}}$ index, DTI-ALPS $_{\text{right}}$ index and DTI-ALPS $_{\text{whole brain}}$ index in post-RT patients than that in pre-RT patients ($p < 0.05$). We further found that post-RT-RE+ patients demonstrated significantly lower DTI-ALPS $_{\text{right}}$ ($p = 0.013$), DTI-ALPS $_{\text{whole brain}}$ ($p = 0.011$) and marginally lower DTI-ALPS $_{\text{left}}$ ($p = 0.07$) than Post-RT $_{\text{non-RE}}$ patients. Significant negative correlations were observed between the maximum dosage of radiation-treatment (MDRT) and DTI-ALPS $_{\text{left}}$ index ($p = 0.003$) as well as DTI-ALPS $_{\text{whole brain}}$ index ($p = 0.004$). Receiver operating characteristic (ROC) curve analysis showed that DTI-ALPS $_{\text{whole brain}}$ index exhibited good performance (AUC = 0.706) in identifying patients more likely developing RE. We concluded that glympathic function was impaired in NPC patients following RT and DTI-ALPS index may serve as a novel imaging biomarker for diagnosis of RE.

KEYWORDS

radiation encephalopathy, glymphatic function, DTI-ALPS index, nasopharyngeal carcinoma, imaging biomarker radiation encephalopathy

OPEN ACCESS

EDITED BY
Zhiyong Zhao,
Zhejiang University, China

REVIEWED BY
Lanxin Ji,
New York University, United States
Yun Jung Bae,
Seoul National University Bundang Hospital,
Republic of Korea

*CORRESPONDENCE
Youming Zhang
✉ zhangym0820@csu.edu.cn
Lingling Deng
✉ 2023020148@usc.edu.cn

†These authors have contributed equally to this work

RECEIVED 13 October 2023
ACCEPTED 29 November 2023
PUBLISHED 26 January 2024

CITATION
Zheng X, Peng J, Zhao Q, Li L, Gao J-M, Zhou K, Tan B, Deng L and Zhang Y (2024) Radiation-induced glymphatic dysfunction in patients with nasopharyngeal carcinoma: a study using diffusion tensor image analysis along the perivascular space.
Front. Neurosci. 17:1321365.
doi: 10.3389/fnins.2023.1321365

Introduction

Nasopharyngeal carcinoma (NPC) is a malignancy of the nasopharynx cavity; it has a distinctive geographical distribution in east and Southeast Asia (Chen et al., 2019). Radiotherapy (RT) is one of the most important treatments for locally advanced NPC, which is highly sensitive to ionizing radiation (Kang et al., 2022). Although RT has led to great improvements in disease control and survival (Chua et al., 2016), radiation-related complications inevitably occur months, or even years, after RT treatment (Chen et al., 2019). Radiation-induced brain injury (RBI) is one of the most common radiation-induced complications. It has recently become a research focus for physicians because of its unclear pathological mechanisms and wide range of neuropsychiatric symptoms (such as cognitive decline and epilepsy) that worsen over time (Kang et al., 2022). RBI is pathophysiologically divided into three phases including acute reaction period (few days to few weeks), early delayed radiation period (1–6 months), and late delayed radiation period (6 months to few years) (Lin et al., 2017), while its clinical course is largely consisted of reversible (brain structures are normal-appearing after RT) and irreversible stages (MRI-detected brain necrosis, also known as radiation encephalopathy [RE]). Given that the progress of RBI into the irreversible phase leads to serious brain necrosis, more severe clinical symptoms and poor treatment outcomes, an investigation into the pathogenesis of RBI during the reversible phase is crucial for the early prevention of RE.

Many pre-symptomatic studies have reported that RBI is characterized by structural and functional alterations throughout the whole brain, rather than being confined to the temporal lobes only. For example, using advanced magnetic resonance imaging (MRI) sequences, several morphological and functional studies have reported altered gray matter volume, cortical thickness, local brain activity, and functional connectivity in brain regions not only within the temporal lobes (such as the inferior temporal gyrus and medial temporal lobe), but also outside the radiation field (such as the precentral gyrus and regions in the default mode network) (Lv et al., 2014; Lin et al., 2017; Ding et al., 2018; Zhang et al., 2020; Zhang W. et al., 2021). Moreover, numerous animal studies investigating the potential molecular substrates of RBI have reported that ionizing radiation-related inflammatory factors (including interleukin-1β, interferon-γ, and tumor necrosis factor-α) play an important role in blood–brain barrier (BBB) permeability, microvascular diameter, neuronal apoptosis, and glial proliferation (Raju et al., 2000; Yuan et al., 2003; Hwang et al., 2006; Wilson et al., 2009; Stielke et al., 2012; Yang et al., 2017), which in turn result in macroscopic structural and functional abnormalities. An excessive accumulation of inflammatory waste and the resulting neuroinflammatory pathology suggest that the removal of brain waste may be impeded (Lv et al., 2021). The glymphatic system—a perivascular network that exchanges brain metabolites between interstitial fluid and cerebrospinal fluid—is an emerging system responsible for the clearance of brain metabolic waste. Together with the well-known function of the glymphatic system, the presence of altered macroscopic brain structure and function and microscopic inflammatory waste accumulation in RBI suggests that an in-depth investigation into radiation-induced glymphatic system dysfunction may help our understanding of the potential neural mechanisms of this injury.

Diffusion tensor image analysis along the perivascular space (DTI-ALPS) is a non-invasive imaging method for quantitatively measuring the capacity of the glymphatic system (Taoka et al., 2017). This real-time method can evaluate glymphatic changes without using contrast agent, and is based on the knowledge that the direction of the perimedullary vein space is perpendicular to association and projection fibers (Taoka et al., 2017; Chen et al., 2021). Experimental evidence shows that DTI-ALPS findings are strongly correlated with results using the intrathecal method of glymphatic measurement, and a lower DTI-ALPS index is associated with poorer glymphatic clearance of waste products (Taoka and Naganawa, 2020; Shen et al., 2022). The DTI-ALPS index has thus been used to assess glymphatic system alterations in disorders such as neurodegenerative conditions, sleep disorders, and cerebrovascular disease (Chen et al., 2021; Lee et al., 2022; Zhang et al., 2022; Qin et al., 2023). However, few DTI-APLS studies have been conducted to investigate the alterations in activity of glymphatic system in RBI.

Given that neuroinflammatory pathology, vascular vulnerability, and the resulting deposits of neurotoxic agents in brain tissue have been reported after RT, we hypothesized that the glymphatic drainage system would be impaired in RT-treated patients with NPC. Furthermore, we predicted that these glymphatic impairments would be independent of radiation dose. To test our hypotheses, we first used DTI-APLS to measure glymphatic activity alterations in patients with NPC after RT, using DTI data. We then assessed the associations between the DTI-APLS index and radiation dose to confirm that glymphatic functional changes were likely induced by RT.

Materials and methods

Subjects

In the present study, 109 patients with NPC were included (74 in the post-RT group and 35 in the pre-RT group). The post-RT group was further divided into two subgroups based on the occurrence of RE in the follow-up (interval between RT and DTI examination <12 months): post-RT without RE (post-RT-RE−, $n = 58$) and post-RT with RE (post-RT-RE+, $n = 16$). Notably, NPC patients displayed normal-appearing brain morphology on the MRI scans at the beginning of our study. They were diagnosed with RE in the years of MRI follow-up after DTI examinations.

Figure 1 illustrates the whole technical route and main research contents of the present study. This study was approved by the Medical Research Ethics Committee of our hospital, and written informed consent was obtained from all subjects.

The RT and chemotherapy treatment information has been documented in our previous work (Zhang et al., 2018; Zhang Y. M. et al., 2021; Kang et al., 2022). In brief, intensity-modulated RT and two-dimensional conventional RT were applied to the post-RT patients. For patients staged IIb to IVa–b, concurrent chemoradiotherapy with/without neoadjuvant/adjuvant chemotherapy were administered. Detailed RT and chemotherapy information (Zhao et al., 2021) is provided in the Supplementary material. The 8th edition of the Union for International Cancer Control/American Joint Committee on Cancer Tumor, Node, Metastasis (TNM) system was used to

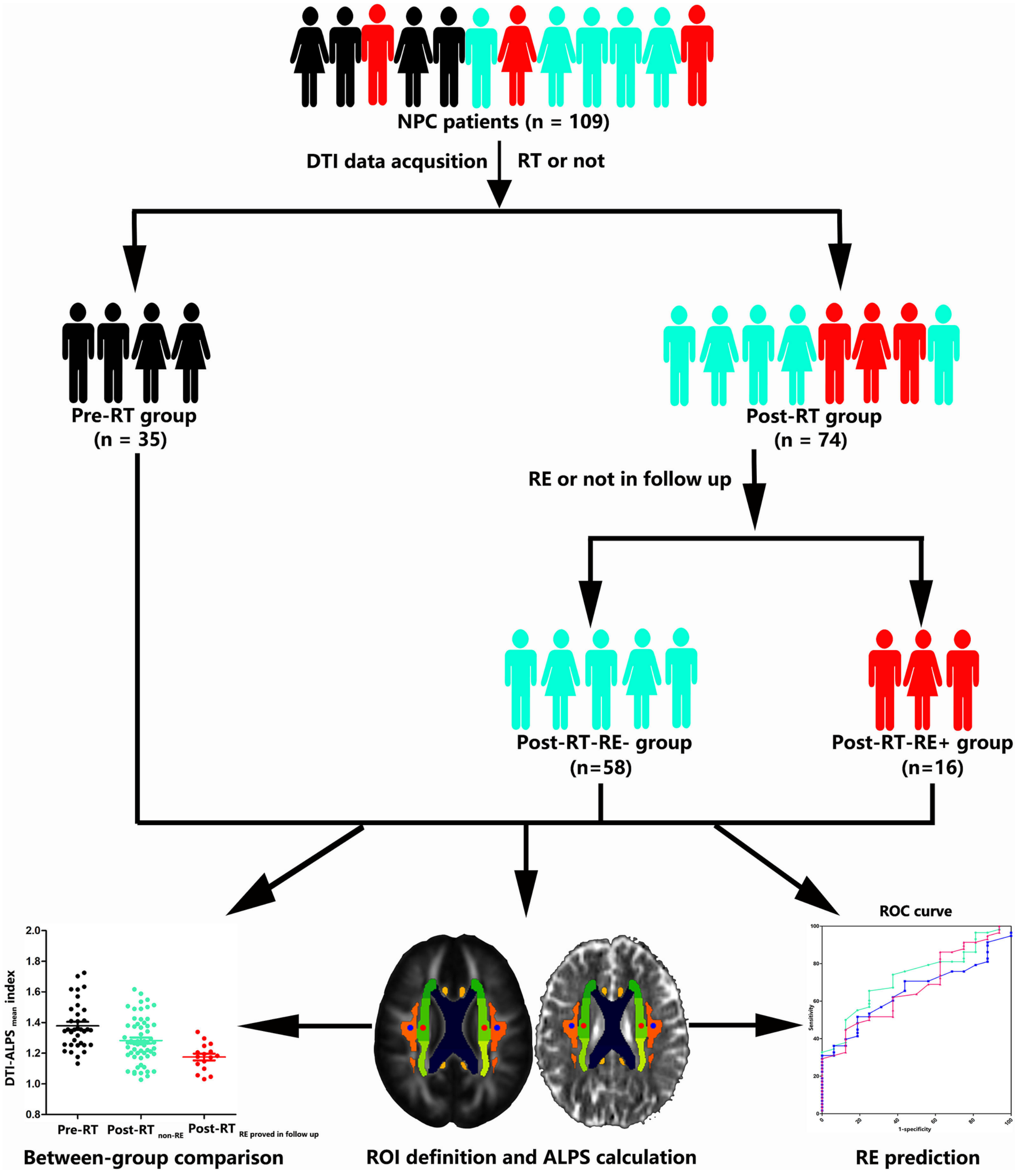

FIGURE 1
Skeleton diagram for grouping and analysis of the enrolled NPC patients. NPC, nasopharyngeal carcinoma; DTI, diffusion tensor imaging; RT, radiotherapy; RE, radiation encephalopathy; DTI-ALPS, diffusion tensor image analysis along the perivascular space; ROI, region of interest; ROC, receiver operator characteristic curve.

determine the clinical stages of NPC lesions (Pan et al., 2016). Patients were enrolled if they met the following criteria: (1) pathologically confirmed NPC; (2) MRI detection of normal-appearing brain imaging; (3) right-handedness; (4) age < 68 years; and (5) Karnofsky Performance Status score > 80. Patients were excluded if they had: (1) MRI detection of brain invasion, orbital apex involvement or intracranial cranial nerve extension; (2) brain tumors or infectious disease (such as abscess); (3) history of head trauma or surgery; (4) history of neurological or psychiatric diseases; (5); severe brain atrophy (specific definition can be found in the supplementary materials); (6) contraindications (such as claustrophobia) for MRI scanning; (7) severe small vessel

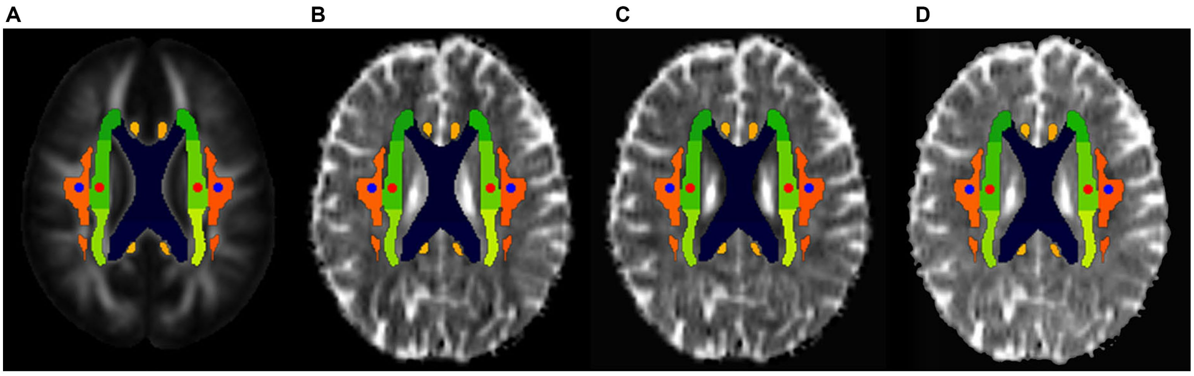

FIGURE 2
ROI selections for the DTI-ALPS index calculation. The placement of the ROIs (circles with a diameter of 5 mm) was determined on the color-coded fractional anisotropy (FA) maps, and these ROIs were placed in the bilateral projection fibers (blue circles) and association fibers (red circles) in FA atlas, respectively **(A)**. Then, these ROIs were placed on the diffusivity maps (spatially normalized) in the direction of the *x*-axis **(B)**, *y*-axis **(C)**, and *z*-axis **(D)**.

disease (deep and periventricular white matter hyperintensities, Fazekas score > 1); or (8) other substantial intracranial diseases (such as cerebral hemorrhage or stroke).

MRI acquisition

MRI data were obtained on a Siemens Magnetom Tim Trio 3 T scanner. The DTI sequence was included in the present study for the subsequent DTI-ALPS data analysis. DTI data were collected transversely with an echo-planar imagingsequence using the following parameters: field of view = 256 mm × 256 mm, number of axial slices = 85, acquisition matrix = 128 × 128, slice thickness/gap = 2/0 mm, voxel size = 2 mm × 2 mm × 2 mm, repetition time = 10,800 ms, echo time = 87 ms, one image with b = 0 s/mm2, 30 images with b = 1,000 s/mm2, and number of excitations = 1.

DTI data preprocessing

The main steps for DTI data preprocessing were as follows. First, we evaluated the artifacts (such as total geometric distortion, signal loss, and volume motion) and corrected the origin positions of all diffusion-weighted images. All diffusion-weighted image preprocessing was performed using FSL (FMRIB Software Library Package 6.0.1) (Smith et al., 2004).[1] Non-brain voxels were extracted using BET and underwent motion correction and eddy current correction using FSL. The resulting data were then DTI fitted using FMRIB's Diffusion toolbox to generate fractional anisotropy (FA) and mean diffusivity maps. Next, diffusivity maps of each subject were obtained using FSL software in the direction of the x-axis (right–left; Dxx), y-axis (anterior–posterior, Dyy), and z-axis (inferior–superior, Dzz).

DTI-ALPS calculation

The DTI-ALPS index is widely used in neurological disorders, including brain injury. An improved ALPS calculation method (Zhang W. et al., 2021) was used to calculate the ALPS index. Specifically, we first registered the diffusion maps obtained in the x-axis (right–left; Dxx), y-axis (anterior–posterior, Dyy), and z-axis (inferior–superior, Dzz) directions into the standard FA map template of the ICBM-DTI-81 Atlas.[2] Previous studies have generally used susceptibility-weighted imaging to assist in selecting the position of the uppermost layer of the lateral ventricle body perpendicular to the medullary vein, to obtain different diffusion coefficients to calculate the ALPS. However, because most patients have the same direction of medullary veins in the uppermost layer of the lateral ventricle body, regions of interest (ROIs) can be placed using DTI images only, without relying on susceptibility-weighted imaging. Using a standard color-coded FA map, spherical ROIs measuring 5 mm in diameter were placed in the projection and association areas at the level of the bilateral lateral ventricle body (Figure 2). The ROI positions were visually confirmed for each patient. If needed, manual corrections were performed by slightly moving the ROIs. Subsequent extractions of the diffusion coefficients of these ROIs on the x-, y-, and z-axes were performed in the subsequent analysis. In the projection fiber area, the main fibers run along the z-axis direction, while the x-and y-axes are perpendicular to the main fibers. By contrast, in the association fiber area, the main fibers run in the direction of the y-axis, and the x-and z-axes are perpendicular to the main fibers. The ALPS index was therefore derived from the ratio of the average values of x-axis diffusivity in the projection fiber area (Dx_proj) and the x-axis diffusivity in the association fiber area (Dx_assoc) to the average values of the y-axis diffusivity in the projection fiber area (Dy_proj) and the z-axis diffusivity in the association fiber area (Dz_assoc), as follows:

---

[1] http://www.fmrib.ox.ac.uk/fsl

[2] https://www.loni.usc.edu/research/atlases

$$ALPS-index=\frac{meanDx\_proj,Dx\_assoc}{meanDy\_proj,Dz\_assoc}$$

In the present study, the left, right, and the average ALPS index values across hemispheres (DTI-ALPS$_{wholebrain}$) were evaluated separately.

Statistical analysis

Clinical data analysis

We used a number of statistics to depict different data types. Specifically, we used the mean and standard deviation to describe quantitative clinical data with normal distribution; the median and interquartile range were reported when clinical data were non-normally distributed. Qualitative clinical data were presented using frequencies. We compared intergroup differences in clinical stage, sex, and RT technique using the chi-squared test, and compared intergroup differences in age using one-way analysis of variance. For the post-RT subgroups, we compared intergroup differences in maximum temporal lobe RT dosage and the interval between RT and DTI examination using a two-sample *t*-test. For all analyses, $p < 0.05$ was considered significant.

DTI-ALPS analysis

Intergroup differences in the DTI-ALPS index were compared at three levels: the DTI-ALPS index in the left hemisphere (DTI-ALPS$_{left}$), the DTI-ALPS index in the right hemisphere (DTI-ALPS$_{right}$), and the average DTI-ALPS index across hemispheres (DTI-ALPS$_{wholebrain}$). We compared the intergroup differences in DTI-ALPS$_{left}$, DTI-ALPS$_{right}$, and DTI-ALPS$_{wholebrain}$ using one-way analysis of variance. *Post hoc* tests were performed using the least significant difference method. For all analyses, $p < 0.05$ was considered significant.

A correlation analysis was used to explore the relationship between the DTI-ALPS index (including DTI-ALPS$_{left}$, DTI-ALPS$_{right}$, and DTI-ALPS$_{wholebrain}$) and the ipsilateral maximum dosage of radiation-treatment (MDRT); $p < 0.05$ was considered significant.

A receiver operating characteristic (ROC) curve was used to assess the RE diagnostic performance of the DTI-ALPS index. In terms of diagnostic performance, area under the curve (AUC) values between 0.9 and 1.0 are considered excellent, values between 0.7 and 0.9 are considered good, and values between 0.6 and 0.7 are considered fair (El Khouli et al., 2009). The cut-off value was equal to the maximum of Youden's index, which was calculated as (sensitivity + specificity) − 1.

Results

Clinical parameters

This study consisted of 86 male and 23 female patients with NPC. Ages ranged from 22 to 67 (mean 45.61) years. Tumor stage ranged from T1N1M0 to T4N3M0 in the pre-RT and post-RT-RE− groups, and from T1N0M0 to T4N2M0 in the post-RT-RE+ group. No significant differences were observed between the pre-RT, post-RT-RE−, and post-RT-RE+ groups in age ($p = 0.091$), sex ($p = 0.211$), or clinical stage ($p = 0.304$). In the post-RT group, there were no significant differences between the post-RT-RE− and post-RT-RE+ subgroups in the time interval between RT and DTI examination ($p = 0.278$), RT technique ($p = 0.955$), or MDRT to the left ($p = 0.744$) or right ($p = 0.683$) temporal lobes. In the post-RT-RE+ group, brain necrotic lesions in the left, right, and bilateral temporal lobes were observed in seven, four, and five patients, respectively (Table 1). The time interval between DTI examination and the diagnosis of RE is 34.37 ± 14.68 months.

DTI-ALPS index

For DTI-ALPS$_{wholebrain}$, significant intergroup differences were observed between the pre-RT, post-RT-RE−, and post-RT-RE+ groups ($p < 0.001$). Subsequent *post hoc* testing revealed that DTI-ALPS$_{wholebrain}$ was significantly lower in the post-RT-RE+ group than in the pre-RT ($p < 0.001$) and post-RT-RE− ($p = 0.011$) groups. Moreover, DTI-ALPS$_{wholebrain}$ was significantly lower in the post-RT-RE− group than in the pre-RT group ($p = 0.002$) (Figure 3A).

For DTI-ALPS$_{left}$, significant intergroup differences were observed between the pre-RT, post-RT-RE−, and post-RT-RE+ groups ($p = 0.021$). Subsequent *post hoc* testing revealed that DTI-ALPS$_{left}$ was significantly lower in the post-RT-RE+ group than in the pre-RT group ($p = 0.006$). Furthermore, a marginally significant difference in DTI-ALPS$_{left}$ was observed between the post-RT-RE+ and post-RT-RE− groups ($p = 0.07$). No significant differences were observed between the pre-RT and post-RT-RE− groups ($p = 0.133$) (Figure 3B).

For DTI-ALPS$_{right}$, significant intergroup differences were observed between the pre-RT, post-RT-RE−, and post-RT-RE+ groups ($p < 0.001$). Subsequent *post hoc* testing revealed that DTI-ALP$_{right}$ was significantly lower in the post-RT-RE+ group than in the pre-RT ($p < 0.001$) and post-RT-RE− ($p = 0.013$) groups. Moreover, DTI-ALPS$_{right}$ was significantly lower in the post-RT-RE− group than in the pre-RT group ($p = 0.001$) (Figure 3C).

Correlation analysis

In the post-RT group, there was a significant negative correlation between DTI-ALPS$_{left}$ and ipsilateral MDRT ($r = -0.472$, 95% confidence interval [−0.688, −0.179], $p = 0.003$). There was also a significant negative correlation between DTI-ALPS$_{wholebrain}$ and left-side MDRT ($r = -0.460$, 95% confidence interval [−0.680, −0.164], $p = 0.004$). No significant correlations were observed between DTI-ALPS$_{right}$ or DTI-ALPS$_{wholebrain}$ and right-side MDRT ($p = 0.854$ and 0.150, respectively).

ROC analysis

The mean, left, and right ALPS indexes were used to evaluate the diagnostic performance of RE. The AUC value was 0.706 for the mean ALPS index ($p = 0.009$), 0.616 for the left ALPS index ($p = 0.139$), and 0.685 for the right ALPS index ($p = 0.018$). The AUC value of the

TABLE 1 Demographic and clinical data of patients with NPC.

Clinical features	Pre-RT group (*n* = 35)	Post-RT-RE-group (*n* = 58)	Post-RT-RE+ group (*n* = 16)	*p* value
Age (years) mean ± SD	46.71 ± 9.02	43.95 ± 8.43	49.19 ± 10.04	0.079
Sex, n				
Male	26	45	15	0.269
Female	9	13	1	
Clinical staging #				
I/II, *n*	3[a]	7[b]	4[c]	0.240
III/IV, *n*	25[a]	42[b]	9[c]	
Cervical lymphatic involvement				
N0	4[a]	2[b]	1[c]	0.290
N1-3	24[a]	47[b]	13[c]	
Time intervals between RT and DTI examinations (month)	NA	6.81 ± 4.47	9.00 ± 9.81	0.397
RT technology				
IMRT, *n*	NA	48	13	0.888
others, *n*	NA	10	3	
Chemotherapy or not				
No	NA	2[b]	1[c]	0.662
Yes	NA	46[b]	13[c]	
Maximum dosage of RT for temporal lobes (Gy)				
Left	NA	66.91 ± 7.56[#]	68.89 ± 6.79*	0.268
Right	NA	66.84 ± 7.59[#]	67.82 ± 10.26*	0.789
The location of RE				
Right, *n*	NA	NA	4 (25.00)	NA
Left, *n*	NA	NA	7 (43.75)	
Bilateral, *n*	NA	NA	5 (31.25)	

NA denotes not available; a–c denote 7, 9, and 3 patients' clinical stageing were not available from medical records; #denotes radiation dose of 35 patients were available; *denotes radiation dose of 7 patients were available.

ALPS$_{\text{wholebrain}}$ index was the highest, with a cut-off value of 1.22, sensitivity of 67.2%, and specificity of 72.2% (Figure 4).

Discussion

To our knowledge, the present report details the first attempt to use the DTI-ALPS index to examine the effects of RT on the glymphatic clearance system in patients with NPC. Patients with NPC in the post-RT group (comprising both the post-RT-RE− and post-RT-RE+ subgroups) had a significantly lower DTI-ALPS index than those in the pre-RT group, suggesting that glymphatic function is impaired in NPC patients following RT. Notably, patients with NPC in the post-RT-RE+ subgroup had significantly lower DTI-ALPS$_{\text{right}}$ and DTI-ALPS$_{\text{wholebrain}}$ values and marginally lower DTI-ALPS$_{\text{left}}$ values than post-RT-RE− patients; further ROC analysis revealed that the DTI-ALPS$_{\text{wholebrain}}$ index was able to effectively differentiate NPC patients who developed RE in the follow-up from those who did not. These findings suggest that the DTI-ALPS index may serve as a potential biomarker for the early diagnosis of RE. In addition, the significant correlations between the MDRT and the DTI-ALPS index indicate that the insufficient clearance system function was likely induced by RT. Together, these findings may contribute to a better understanding of the underlying neural mechanisms of RE.

Compared with patients in the pre-RT group, those in the post-RT group had a significantly lower DTI-ALPS index. This finding is consistent with that of a recent diffusion-weighted imaging study in which the diffusion-weighted imaging-ALPS index was significantly lower in the post-radiation group than in the control group (Taoka et al., 2023). A decreased DTI-ALPS index may thus indicate glymphatic system insufficiency in patients with NPC following RT. Anatomically and physiologically, the glymphatic system runs parallel to central nervous system vasculature in a perivascular space that is enclosed by astrocytic endfeet; it mediates substrate exchange between cerebrospinal fluid and interstitial fluid (ISF) to remove extracellular waste (Radford et al., 2015; Plog and Nedergaard, 2018; Hablitz and Nedergaard, 2021). Any pathophysiological processes or molecular events that affect structural components of the glymphatic system can result in the decreased removal of neurotoxic metabolites (Iliff et al., 2013; Radford et al., 2015; Mogensen et al., 2021; Wei et al., 2023). Interestingly, the pathophysiological hallmark of RBI is tightly linked to an altered tissue microenvironment consisting of overloaded inflammatory factors (such as tumor necrosis factor-α, cell adhesion molecules, and cytokines), BBB disruption, glial cell apoptosis, and

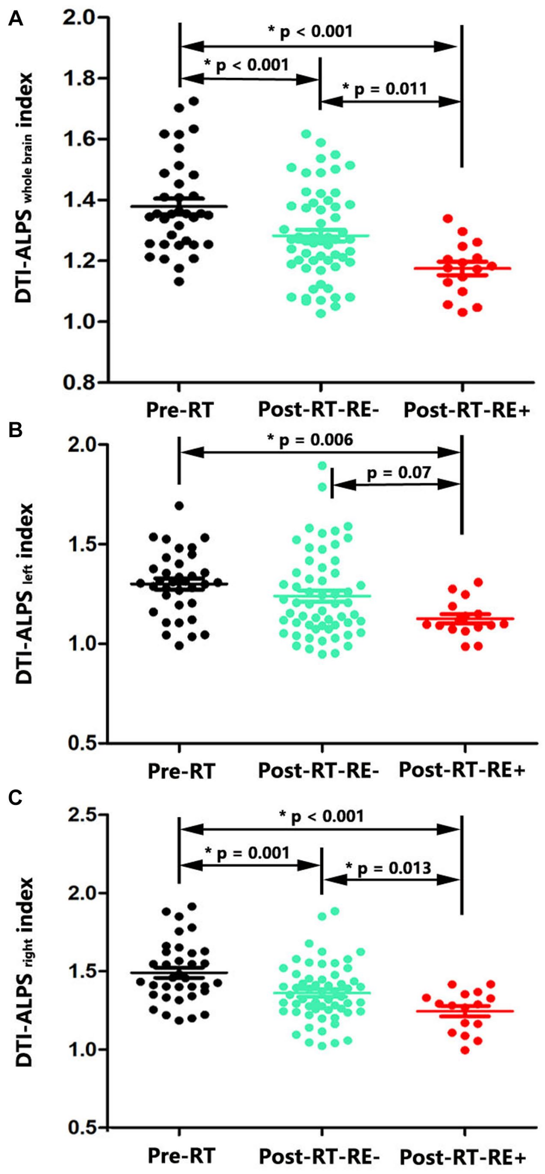

FIGURE 3
Between-group differences in DTI-ALPS index. Significant reductions of DTI-ALPS $_{\text{whole brain}}$ index were observed in the pairwise comparisons of Post-RT-RE+ vs. Pre-RT (*p* < 0.001), Post-RT-RE-vs. Pre-RT (*p* < 0.001), and Post-RT-RE+ vs. Post-RT-RE- (*p* = 0.011) **(A)**. Compared with the Pre-RT group, patients in Post-RT-RE+ displayed significant reduction of DTI-ALPS $_{\text{left}}$ index (*p* = 0.006). Compared with the Post-RT-RE-group, patients in Post-RT-RE+ group showed marginally significant reduction of DTI-ALPS $_{\text{left}}$ index (*p* = 0.07) **(B)**. Significant reductions of DTI-ALPS $_{\text{right}}$ index were observed in the pairwise comparisons of Post-RT-RE+ vs. Pre-RT (*p* < 0.001), Post-RT-RE-vs. Pre-RT (*p* = 0.001), and Post-RT-RE+ vs. Post-RT-RE- (*p* = 0.013) **(C)**.

varying degrees of vascular damage (Raju et al., 2000; Yuan et al., 2003; Wilson et al., 2009; Yang et al., 2017). These factors are related to pathological reactions, such as the perivascular accumulation of superfluous inflammatory substances, endothelial apoptosis-related BBB leakage, and vascular defect-induced pulse pressure disruption, and are reportedly the key contributors to insufficient glymphatic clearance (Kress et al., 2014; Verheggen et al., 2018; Ekenze et al., 2023; Kern et al., 2023). Together with the observation that pathogenic factors are interrelated in RBI, it is therefore tempting to speculate that the impaired glymphatic function in post-RT patients in the present study may be the result of multiple superimposed insults from diverse molecular events or pathological processes.

Our findings of the lowest DTI-ALPS index in post-RT-RE+ patients, and of its impressive predictive performance for RE, are of particular interest. Such findings indicate that the DTI-ALPS index may serve as a potential biomarker for the early diagnosis of RE/brain necrosis (if glymphatic function worsens) in post-radiation NPC patients. Early RBI may be regarded as a pathological state characterized by a dynamic balance of damage and repair; brain necrosis can occur when this balance is disrupted (Steel et al., 1986; Yang et al., 2017). Findings from numerous animal models indicate that self-healing systems can be activated immediately after RT to protect against neurological deterioration through the inhibition or reduction of RT-related oxidative stress and apoptosis (Wang et al., 2016; Soria et al., 2019). As a self-healing system, the glymphatic system may exert its neuroprotective effects on damaged brain tissue by enhancing its drainage function, to remove metabolic neurotoxic products (Dai et al., 2023). Such a role may also be supported by a study of a healthy population showing that increased glymphatic clearance, driven by physical activity, plays an essential role in maintaining a healthy brain throughout aging (Vecchio et al., 2018). It is thus reasonable to speculate that progressive glymphatic impairments might be the key drivers for the phenoconversion from reversible RBI to clinically irreversible radiation-induced brain necrosis/RE. However, the probable reasons for our observation of the most severe glymphatic impairments in post-RT-RE+ patients remain unknown and require further investigation. Nonetheless, the glymphatic system may be a novel therapeutic target for alleviating the neuropsychiatric symptoms of RE.

Our findings of significant negative correlations between the MDRT and the DTI-ALPS index indicate that a higher ipsilateral maximum RT dosage is associated with a lower DTI-ALPS index. This expected finding implies that glymphatic functional impairments are mainly induced by RT, and is in line with one recent whole-brain radiation study showing that the ALPS index has a weak negative correlation with biologically equivalent RT doses (Taoka et al., 2023). Moreover, using rat models, several studies have reported that increased single or total radiation doses result in elevated inflammatory factors (such as tumor necrosis factor-α, interferon-γ, and interleukin-1β), cellular debris, and BBB permeability, and have a negative effect on perivascular astrocyte survival (Chiang et al., 1993; Raju et al., 2000; Yuan et al., 2003; Yang et al., 2017). Coincidentally, as reported in previous studies, these RT-related pathological events can in turn aggravate glymphatic system dysfunction through possible mechanisms that include inadequate competence in dealing with overloaded waste, turbulent convective flux through the interstitium along the central nervous system vasculature, and aquaporin-4 depolarization in damaged astrocytic endfeet (Kress et al., 2014; Jessen et al., 2015; Radford et al., 2015). The proposed hypothesis, that the observed glymphatic dysfunction is mainly driven by ionizing radiation exposure in patients with NPC, is therefore both etiologically and pathologically reasonable.

Several limitations of the present study should be mentioned. First, the DTI-ALPS index cannot assess whole-brain glymphatic function because it is based on the orthogonal geometric relationship between projection and association fibers and medullary arteries

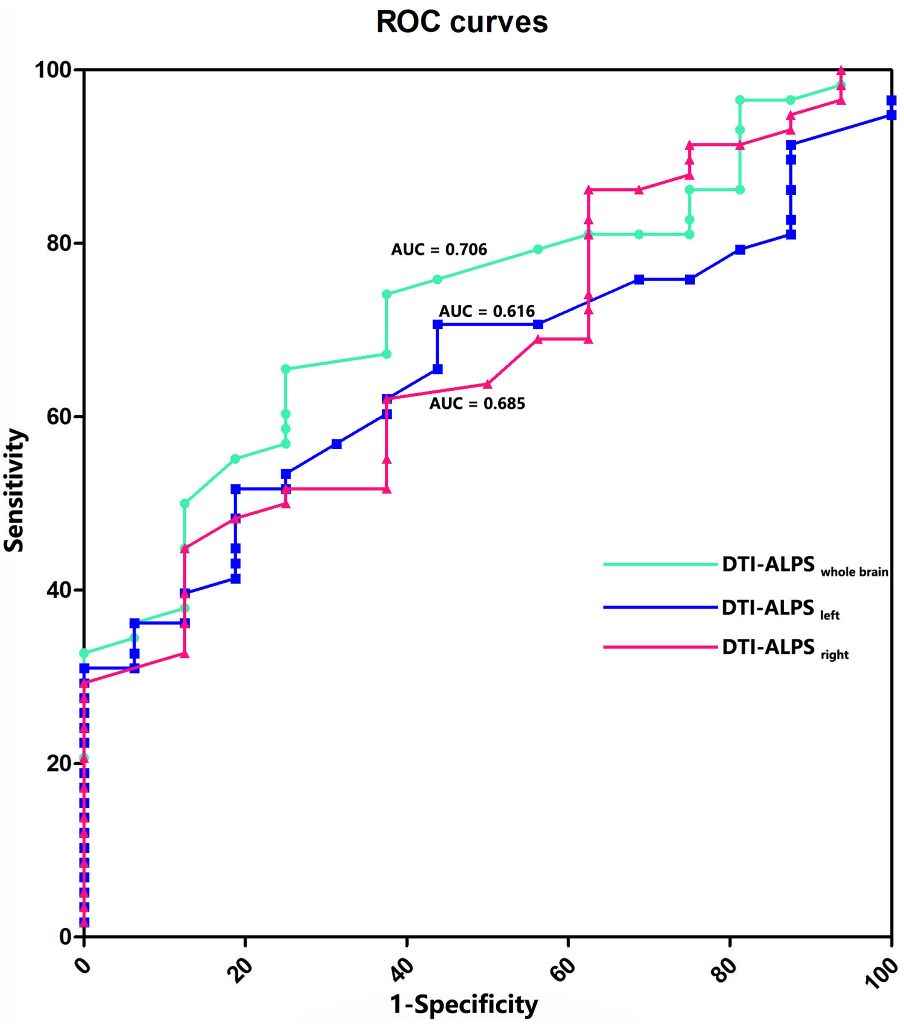

FIGURE 4
ROC curves for prediction of RE. The AUC value is 0.706 for the whole brain ALPS index ($p = 0.009$), 0.616 for the left ALPS index ($p = 0.139$), and 0.685 for the right ALPS index ($p = 0.018$).

and veins in the lateral ventricle body (Taoka et al., 2017; Kamagata et al., 2022). The DTI-ALPS index thus warrants cautious interpretation and further investigation. Nevertheless, considering that RBI can occur not only in the temporal lobe, but also in almost all areas of the brain, the DTI-ALPS index measured at the lateral ventricle level may reflect—at least to some extent—important RT-related pathological processes. Second, several confounding factors (such as chemotherapeutic agents, varying radiation fields and potential small vessel disease) were present in the present study. Because their negative confounding effects were unable to be completely eliminated, the reliability of our results may be compromised. Third, the lack of sufficient biological and cognitive data weakens the interpretability of our findings. Fourth, a relatively small sample size, such as that of the current study, may lower the statistical power and result in false-negative error, which then lowers our confidence to reach a definitive conclusion. Fifth, although the between-group difference of cervical lymphatic metastases in post-RT NPC patients were not significant, their potential confounding effects on glymphatic changes could not be ruled out. Finally, the cross-sectional study design impeded investigations into temporal alterations in the glymphatic clearance network at different stages of RBI. Given the aforementioned limitations of our study, future longitudinal investigations with large sample sizes and comprehensive multimodal data are warranted to further validate our findings.

Conclusion

A radiation-induced reduction in the DTI-ALPS—a potential biomarker for the early diagnosis of RE—was observed in patients with NPC, indicating that glymphatic dysfunction may contribute to the pathogenesis of RBI.

Data availability statement

The original contributions presented in the study are included in the article/Supplementary material, further inquiries can be directed to the corresponding author.

Ethics statement

The studies involving humans were approved by Medical Research Ethics Committee of Xiangya hospital, Central South University. The studies were conducted in accordance with the local legislation and institutional requirements. The participants provided their written informed consent to participate in this study.

Author contributions

XZ: Data curation, Formal analysis, Methodology, Writing – original draft. JP: Software, Writing – original draft. QZ: Investigation, Conceptualization. LL: Conceptualization, Supervision, Writing – review & editing. J-mG: Data curation, Supervision, Writing – review & editing. KZ: Investigation, Writing – review & editing. BT: Investigation, Writing – review & editing. LD: Formal analysis, Investigation, Writing – review & editing. YZ: Conceptualization, Data curation, Funding acquisition, Investigation, Supervision, Writing – review & editing.

Funding

The author(s) declare financial support was received for the research, authorship, and/or publication of this article. This study was supported in part by the National Natural Science Foundation of China (Grant/Award No. 82001784), the Youth Science Foundation of Xiangya Hospital (Grant/Award No. 2019Q16), and the Natural Science Foundation (Youth Science Foundation Project) of Hunan Province (Grant/Award No. 2021JJ41054).

Acknowledgments

We thank all the study participants for their efforts and enthusiasm for our clinical research. We thank Bronwen Gardner, PhD, from Liwen Bianji (Edanz) (www.liwenbianji.cn/), for editing the English text of a draft of this manuscript.

Conflict of interest

The authors declare that the research was conducted in the absence of any commercial or financial relationships that could be construed as a potential conflict of interest.

Publisher's note

Supplementary material

The Supplementary material for this article can be found online at: https://www.frontiersin.org/articles/10.3389/fnins.2023.1321365/full#supplementary-material

References

Chen, Y. P., Chan, A. T. C., Le, Q. T., Blanchard, P., Sun, Y., and Ma, J. (2019). Nasopharyngeal carcinoma. *Lancet* 394, 64–80. doi: 10.1016/S0140-6736(19)30956-0

Chen, H. L., Chen, P. C., Lu, C. H., Tsai, N. W., Yu, C. C., Chou, K. H., et al. (2021). Associations among cognitive functions, plasma DNA, and diffusion tensor image along the perivascular space (DTI-ALPS) in patients with Parkinson's disease. *Oxidative Med. Cell. Longev.* 2021:4034509. doi: 10.1155/2021/4034509

Chiang, C. S., McBride, W. H., and Withers, H. R. (1993). Radiation-induced astrocytic and microglial responses in mouse brain. *Radiother. Oncol.* 29, 60–68. doi: 10.1016/0167-8140(93)90174-7

Chua, M. L. K., Wee, J. T. S., Hui, E. P., and Chan, A. T. C. (2016). Nasopharyngeal carcinoma. *Lancet* 387, 1012–1024. doi: 10.1016/S0140-6736(15)00055-0

Dai, Z., Yang, Z., Li, Z., Li, M., Sun, H., Zhuang, Z., et al. (2023). Increased glymphatic system activity in patients with mild traumatic brain injury. *Front. Neurol.* 14:1148878. doi: 10.3389/fneur.2023.1148878

Ding, Z., Zhang, H., Lv, X. F., Xie, F., Liu, L., Qiu, S., et al. (2018). Radiation-induced brain structural and functional abnormalities in presymptomatic phase and outcome prediction. *Hum. Brain Mapp.* 39, 407–427. doi: 10.1002/hbm.23852

Ekenze, O., Pinheiro, A., Demissie, S., Charidimou, A., Beiser, A. S., Vasan, R. S., et al. (2023). Inflammatory biomarkers and MRI visible perivascular spaces: the Framingham heart study. *Neurobiol. Aging* 127, 12–22. doi: 10.1016/j.neurobiolaging.2023.03.001

El Khouli, R. H., Macura, K. J., Barker, P. B., Habba, M. R., Jacobs, M. A., and Bluemke, D. A. (2009). Relationship of temporal resolution to diagnostic performance for dynamic contrast enhanced MRI of the breast. *J. Magn. Reson. Imaging* 30, 999–1004. doi: 10.1002/jmri.21947

Hablitz, L. M., and Nedergaard, M. (2021). The glymphatic system: a novel component of fundamental neurobiology. *J. Neurosci.* 41, 7698–7711. doi: 10.1523/JNEUROSCI.0619-21.2021

Hwang, S. Y., Jung, J. S., Kim, T. H., Lim, S. J., Oh, E. S., Kim, J. Y., et al. (2006). Ionizing radiation induces astrocyte gliosis through microglia activation. *Neurobiol. Dis.* 21, 457–467. doi: 10.1016/j.nbd.2005.08.006

Iliff, J. J., Wang, M., Zeppenfeld, D. M., Venkataraman, A., Plog, B. A., Liao, Y., et al. (2013). Cerebral arterial pulsation drives paravascular CSF-interstitial fluid exchange in the murine brain. *J. Neurosci.* 33, 18190–18199. doi: 10.1523/JNEUROSCI.1592-13.2013

Jessen, N. A., Munk, A. S., Lundgaard, I., and Nedergaard, M. (2015). The glymphatic system: a beginner's guide. *Neurochem. Res.* 40, 2583–2599. doi: 10.1007/s11064-015-1581-6

Kamagata, K., Andica, C., Takabayashi, K., Saito, Y., Taoka, T., Nozaki, H., et al. (2022). Association of MRI indices of glymphatic system with amyloid deposition and cognition in mild cognitive impairment and Alzheimer disease. *Neurology* 99, e2648–e2660. doi: 10.1212/WNL.0000000000201300

Kang, Y. F., Chen, R. T., Ding, H., Li, L., Gao, J. M., Liu, L. Z., et al. (2022). Structure-function decoupling: a novel perspective for understanding the radiation-induced brain injury in patients with nasopharyngeal carcinoma. *Front. Neurosci.* 16:915164. doi: 10.3389/fnins.2022.915164

Kern, K. C., Nasrallah, I. M., Bryan, R. N., Reboussin, D. M., and Wright, C. B. (2023). Intensive systolic blood pressure treatment remodels brain perivascular spaces: a secondary analysis of the systolic pressure intervention trial (SPRINT). *Neuroimage Clin* 40:103513. doi: 10.1016/j.nicl.2023.103513

Kress, B. T., Iliff, J. J., Xia, M., Wang, M., Wei, H. S., Zeppenfeld, D., et al. (2014). Impairment of paravascular clearance pathways in the aging brain. *Ann. Neurol.* 76, 845–861. doi: 10.1002/ana.24271

Lee, H. J., Lee, D. A., Shin, K. J., and Park, K. M. (2022). Glymphatic system dysfunction in obstructive sleep apnea evidenced by DTI-ALPS. *Sleep Med.* 89, 176–181. doi: 10.1016/j.sleep.2021.12.013

Lin, J., Lv, X., Niu, M., Liu, L., Chen, J., Xie, F., et al. (2017). Radiation-induced abnormal cortical thickness in patients with nasopharyngeal carcinoma after radiotherapy. *Neuroimage Clin* 14, 610–621. doi: 10.1016/j.nicl.2017.02.025

Lv, T., Zhao, B., Hu, Q., and Zhang, X. (2021). The Glymphatic system: a novel therapeutic target for stroke treatment. *Front. Aging Neurosci.* 13:689098. doi: 10.3389/fnagi.2021.689098

Lv, X. F., Zheng, X. L., Zhang, W. D., Liu, L. Z., Zhang, Y. M., Chen, M. Y., et al. (2014). Radiation-induced changes in normal-appearing gray matter in patients with nasopharyngeal carcinoma: a magnetic resonance imaging voxel-based morphometry study. *Neuroradiology* 56, 423–430. doi: 10.1007/s00234-014-1338-y

Mogensen, F. L., Delle, C., and Nedergaard, M. (2021). The glymphatic system (en) during inflammation. *Int. J. Mol. Sci.* 22, 7491. doi: 10.3390/ijms22147491

Pan, J. J., Ng, W. T., Zong, J. F., Chan, L. L., O'Sullivan, B., Lin, S. J., et al. (2016). Proposal for the 8th edition of the AJCC/UICC staging system for nasopharyngeal cancer in the era of intensity-modulated radiotherapy. *Cancer* 122, 546–558. doi: 10.1002/cncr.29795

Plog, B. A., and Nedergaard, M. (2018). The glymphatic system in central nervous system health and disease: past, present, and future. *Annu. Rev. Pathol.* 13, 379–394. doi: 10.1146/annurev-pathol-051217-111018

Qin, Y., Li, X., Qiao, Y., Zou, H., Qian, Y., Li, X., et al. (2023). DTI-ALPS: an MR biomarker for motor dysfunction in patients with subacute ischemic stroke. *Front. Neurosci.* 17:1132393. doi: 10.3389/fnins.2023.1132393

Radford, R. A., Morsch, M., Rayner, S. L., Cole, N. J., Pountney, D. L., and Chung, R. S. (2015). The established and emerging roles of astrocytes and microglia in amyotrophic lateral sclerosis and frontotemporal dementia. *Front. Cell. Neurosci.* 9:414. doi: 10.3389/fncel.2015.00414

Raju, U., Gumin, G. J., and Tofilon, P. J. (2000). Radiation-induced transcription factor activation in the rat cerebral cortex. *Int. J. Radiat. Biol.* 76, 1045–1053. doi: 10.1080/09553000050111514

Shen, T., Yue, Y. M., Ba, F., He, T. G., Tang, X. C., Hu, X. Y., et al. (2022). Diffusion along perivascular spaces as marker for impairment of glymphatic system in Parkinson's disease. *NPJ Parkinsons Dis* 8:174. doi: 10.1038/s41531-022-00437-1

Smith, S. M., Jenkinson, M., Woolrich, M. W., Beckmann, C. F., Behrens, T. E., Johansen-Berg, H., et al. (2004). Advances in functional and structural MR image analysis and implementation as FSL. *NeuroImage* 23, S208–S219. doi: 10.1016/j.neuroimage.2004.07.051

Soria, B., Martin-Montalvo, A., Aguilera, Y., Mellado-Damas, N., Lopez-Beas, J., Herrera-Herrera, I., et al. (2019). Human mesenchymal stem cells prevent neurological complications of radiotherapy. *Front. Cell. Neurosci.* 13:204. doi: 10.3389/fncel.2019.00204

Steel, G. G., Down, J. D., Peacock, J. H., and Stephens, T. C. (1986). Dose-rate effects and the repair of radiation damage. *Radiother. Oncol.* 5, 321–331. doi: 10.1016/s0167-8140(86)80181-5

Stielke, S., Keilhoff, G., Kirches, E., Mertens, P. R., Neumann, K. H., Tsokos, G. C., et al. (2012). Adhesion molecule expression precedes brain damages of lupus-prone mice and correlates with kidney pathology. *J. Neuroimmunol.* 252, 24–32. doi: 10.1016/j.jneuroim.2012.07.011

Taoka, T., Ito, R., Nakamichi, R., Nakane, T., Kawamura, M., Ishihara, S., et al. (2023). Evaluation of alterations in interstitial fluid dynamics in cases of whole-brain radiation using the diffusion-weighted image analysis along the perivascular space method. *NMR Biomed.* e5030:e5030. doi: 10.1002/nbm.5030

Taoka, T., Masutani, Y., Kawai, H., Nakane, T., Matsuoka, K., Yasuno, F., et al. (2017). Evaluation of glymphatic system activity with the diffusion MR technique: diffusion tensor image analysis along the perivascular space (DTI-ALPS) in Alzheimer's disease cases. *Jpn. J. Radiol.* 35, 172–178. doi: 10.1007/s11604-017-0617-z

Taoka, T., and Naganawa, S. (2020). Glymphatic imaging using MRI. *J. Magn. Reson. Imaging* 51, 11–24. doi: 10.1002/jmri.26892

Vecchio, L. M., Meng, Y., Xhima, K., Lipsman, N., Hamani, C., and Aubert, I. (2018). The neuroprotective effects of exercise: maintaining a healthy brain throughout aging. *Brain Plast* 4, 17–52. doi: 10.3233/BPL-180069

Verheggen, I. C. M., Van Boxtel, M. P. J., Verhey, F. R. J., Jansen, J. F. A., and Backes, W. H. (2018). Interaction between blood-brain barrier and glymphatic system in solute clearance. *Neurosci. Biobehav. Rev.* 90, 26–33. doi: 10.1016/j.neubiorev.2018.03.028

Wang, G. H., Liu, Y., Wu, X. B., Lu, Y., Liu, J., Qin, Y. R., et al. (2016). Neuroprotective effects of human umbilical cord-derived mesenchymal stromal cells combined with nimodipine against radiation-induced brain injury through inhibition of apoptosis. *Cytotherapy* 18, 53–64. doi: 10.1016/j.jcyt.2015.10.006

Wei, Y. C., Hsu, C. H., Huang, W. Y., Lin, C., Chen, C. K., Chen, Y. L., et al. (2023). Vascular risk factors and astrocytic marker for the glymphatic system activity. *Radiol. Med.* 128, 1148–1161. doi: 10.1007/s11547-023-01675-w

Wilson, C. M., Gaber, M. W., Sabek, O. M., Zawaski, J. A., and Merchant, T. E. (2009). Radiation-induced astrogliosis and blood-brain barrier damage can be abrogated using anti-TNF treatment. *Int. J. Radiat. Oncol. Biol. Phys.* 74, 934–941. doi: 10.1016/j.ijrobp.2009.02.035

Yang, L., Yang, J., Li, G., Li, Y., Wu, R., Cheng, J., et al. (2017). Pathophysiological responses in rat and mouse models of radiation-induced brain injury. *Mol. Neurobiol.* 54, 1022–1032. doi: 10.1007/s12035-015-9628-x

Yuan, H., Gaber, M. W., McColgan, T., Naimark, M. D., Kiani, M. F., and Merchant, T. E. (2003). Radiation-induced permeability and leukocyte adhesion in the rat blood-brain barrier: modulation with anti-ICAM-1 antibodies. *Brain Res.* 969, 59–69. doi: 10.1016/s0006-8993(03)02278-9

Zhang, Y. M., Chen, M. N., Yi, X. P., Li, L., Gao, J. M., Zhang, J. L., et al. (2018). Cortical surface area rather than cortical thickness potentially differentiates radiation encephalopathy at early stage in patients with nasopharyngeal carcinoma. *Front. Neurosci.* 12:599. doi: 10.3389/fnins.2018.00599

Zhang, Y. M., Gao, J. M., Zhou, H., Li, L., Liu, L. Z., Han, Z. D., et al. (2020). Pre-symptomatic local brain activity and functional connectivity alterations in nasopharyngeal carcinoma patients who developed radiation encephalopathy following radiotherapy. *Brain Imaging Behav.* 14, 1964–1978. doi: 10.1007/s11682-019-00145-0

Zhang, Y. M., Kang, Y. F., Zeng, J. J., Li, L., Gao, J. M., Liu, L. Z., et al. (2021). Surface-based falff: a potential novel biomarker for prediction of radiation encephalopathy in patients with nasopharyngeal carcinoma. *Front. Neurosci.* 15:692575. doi: 10.3389/fnins.2021.692575

Zhang, C., Sha, J., Cai, L., Xia, Y., Li, D., Zhao, H., et al. (2022). Evaluation of the glymphatic system using the DTI-ALPS index in patients with spontaneous intracerebral haemorrhage. *Oxidative Med. Cell. Longev.* 2022, 2694316–2694317. doi: 10.1155/2022/2694316

Zhang, W., Zhou, Y., Wang, J., Gong, X., Chen, Z., Zhang, X., et al. (2021). Glymphatic clearance function in patients with cerebral small vessel disease. *NeuroImage* 238:118257. doi: 10.1016/j.neuroimage.2021.118257

Zhao, L. M., Kang, Y. F., Gao, J. M., Li, L., Chen, R. T., Zeng, J. J., et al. (2021). unctional connectivity density for radiation encephalopathy prediction in nasopharyngeal carcinoma. *Front. Oncol* 11:687127. doi: 10.3389/fonc.2021.687127

frontiers | Frontiers in Neuroimaging

TYPE Original Research
PUBLISHED 25 April 2024
DOI 10.3389/fnimg.2024.1361513

Construction and evaluation of a neurofeedback system using finger tapping and near-infrared spectroscopy

Shingo Takahashi[1]*, Daishi Takahashi[1], Yuki Kuroiwa[1], Noriko Sakurai[2] and Naoki Kodama[2]

[1]Department of Healthcare Informatics, Faculty of Health and Welfare, Takasaki University of Health and Welfare, Takasaki, Japan, [2]Department of Radiological Technology, Faculty of Medical Technology, Niigata University of Health and Welfare, Niigata, Japan

OPEN ACCESS

EDITED BY
Takao Yamasaki,
Minkodo Minohara Hospital, Japan

REVIEWED BY
Junjie Wu,
Emory University, United States
Dorela Doris Shuboni-Mulligan,
Eastern Virginia Medical School, United States

*CORRESPONDENCE
Shingo Takahashi
✉ takahashi-shin@takasaki-u.ac.jp

RECEIVED 26 December 2023
ACCEPTED 09 April 2024
PUBLISHED 25 April 2024

CITATION
Takahashi S, Takahashi D, Kuroiwa Y, Sakurai N and Kodama N (2024) Construction and evaluation of a neurofeedback system using finger tapping and near-infrared spectroscopy.
Front. Neuroimaging 3:1361513.
doi: 10.3389/fnimg.2024.1361513

Introduction: Neurofeedback using near-infrared spectroscopy (NIRS) has been used in patients with stroke and other patients, but few studies have included older people or patients with cognitive impairment.

Methods: We constructed a NIRS-based neurofeedback system and used finger tapping to investigate whether neurofeedback can be implemented in older adults while finger tapping and whether brain activity improves in older adults and healthy participants. Our simple neurofeedback system was constructed using a portable wearable optical topography (WOT-HS) device. Brain activity was evaluated in 10 older and 31 healthy young individuals by measuring oxygenated hemoglobin concentration during finger tapping and neurofeedback implementation.

Results: During neurofeedback, the concentration of oxygenated hemoglobin increased in the prefrontal regions in both the young and older participants.

Discussion: The results of this study demonstrate the usefulness of neurofeedback using simple NIRS devices for older adults and its potential to mitigate cognitive decline.

KEYWORDS

near-infrared spectroscopy, neurofeedback, portable wearable optical topography device, finger tapping, prefrontal cortex

1 Introduction

Neurofeedback is a form of biofeedback that allows individuals to control their brain function by measuring neural activity and presenting this information in real-time (Ehlis et al., 2018; Sitaram et al., 2019). The method is typically used to record brain waves and provide feedback (Marzbani et al., 2016), and near-infrared spectroscopy (NIRS) devices are new tools for neurofeedback training (Ehlis et al., 2018). As confirmed in healthy people, it is possible to control hemodynamic responses in prefrontal brain regions even after several training sessions of NIRS feedback (Barth et al., 2016). Neurofeedback using a small NIRS device has also been performed (Nouchi et al., 2021) and has been shown to be useful.

Neurofeedback using NIRS is free of cumbersome restrictions on participants' movement and can improve cognitive domains in patients with stroke (Renton et al., 2017). Furthermore, the method has been shown to enhance gait and balance recovery after stroke (Mihara et al., 2021). Neurofeedback approaches based on electroencephalography (EEG) and functional magnetic resonance imaging (fMRI) have been studied in older populations (Trambaiolli et al., 2021), but there are few reports on NIRS neurofeedback in this group. Neurofeedback can potentially improve cognitive function in dementia and mild cognitive impairment (Trambaiolli et al., 2021), and neurofeedback in older people using small NIRS devices can contribute to improvements in cognitive dysfunction.

Finger-tapping performance has been shown to decline among older individuals as the brain and cognitive functions deteriorate (Suzumura et al., 2021; Sugioka et al., 2022). In addition, finger tapping is effective in improving the activities of daily living (ADL) (Liu et al., 2018), and hand training may improve dexterity and executive function and, over the long term, cognitive function (Seol et al., 2023). In general, older adults have been shown to engage a broader range of brain regions for motor control than younger adults, particularly prefrontal regions and basal ganglia networks, and motor control becomes more dependent on cognition and the prefrontal cortex (PFC) with aging (Seidler et al., 2010). These findings suggest that finger tapping may be assessed within the framework of cognitive decline in older individuals.

In this study, we constructed a simple neurofeedback system using finger tapping and NIRS and examined whether brain activity improves after training. Our objectives were as follows: (1) we tested whether neurofeedback can be performed using a portable NIRS device; (2) we tested whether older participants can perform neurofeedback training during finger tapping; and (3) we tested whether prefrontal activation occurs.

2 Materials and methods

2.1 Participants and methods

In this cross-sectional study, we constructed a simple neurofeedback system and evaluated brain activity during neurofeedback implementation using a finger-tapping task. Ten older community members (four males, six females, age: 76.6 ± 5.8, 10 right-handed) and 31 healthy young adults (13 males, 18 females, age: 20.3 ± 1.3, 30 right-handed and one left-handed) were recruited to assess brain activity using the proposed system. Patients were verbally asked if they had been diagnosed with diagnosed dementia, neurodegenerative diseases, or complications, and cases, where applicable, were considered for exclusion. Patients with orthopedic, cerebrovascular, neurologic, motor, limb or finger disorders were also considered for exclusion; however, no participants were excluded. Based on the results of previous studies, a sample size of at least 15 participants was required (Takahashi et al., 2018, 2022). This sample size could not be met for the older population.

Data from a wearable optical topography system (WOT-HS, NeU) was analyzed during neurofeedback implementation to assess brain activity during neurofeedback implementation. For neurofeedback execution and measurement, we used a three-block design with 15-s rest, 15-s tasks (neurofeedback), 15-s rest periods, and 15-s rest periods before and after the block design (Figure 1). For neurofeedback training, visual feedback based on the participant's real-time brain activity was presented on screen and finger tapping was performed with alternating hands to increase brain function (Hou et al., 2021; Nouchi et al., 2021). In the rest period, the participants were instructed to rest, with only a cross-shaped symbol appearing on the monitor during measurement.

This study was conducted in accordance with the Declaration of Helsinki. All participants were informed of the study before participation, and written informed consent was obtained. The Ethical Review Committee of Takasaki University of Health and Welfare approved the study.

2.2 NIRS-mediated neurofeedback system

We constructed a simple neurofeedback system that uses a portable WOT system and presents brain activity using a programming language (Python). In detail, we created a program to present a brain activity screen using Python from the WOT-HS measurement software and constructed a simple neurofeedback method using NIRS. This system consisted of a NIRS-based measurement device, a computer for presenting brain activity, and a monitor for visualizing feedback. A schematic of the system is shown in Figure 2. NIRS captures hemoglobin signal changes derived from local vascular responses due to neuronal activation in the brain (Hoshi and Tamura, 1993; Villringer et al., 1993), and these changes were used to provide feedback on brain activity. The WOT-HS comprises a headset, a data processing unit, and measurement software. Each participant wore a headset and sat on a chair for the experiment. The headset was worn according to the instructions in the WOT-HS manual, and the participants were instructed not to move their heads during measurement. The 34 measurement channels of the WOT-HS can measure changes in oxygenated hemoglobin, deoxygenated hemoglobin, and total hemoglobin levels in the frontal and temporal regions (Figure 3). The light sources were 730 and 850 nm, and the sampling rate was 100 ms, allowing removal of signals related to skin blood flow. A dedicated application software was used for measurement, and the waveform data and mapping images were displayed in real-time. The mapped brain activity was presented to the participants as feedback.

2.3 Finger-tapping task

Finger tapping took the form of alternating tapping with both hands, using the thumb and index finger, with one finger closed on the left and right side and the other finger open on the left and right side (Suzumura et al., 2016; Tomita et al., 2020; Sugioka et al., 2022). The participants were instructed to place their forearms on a desk before them and tap as quickly as possible in an alternating finger opening and closing motion using their index finger and thumb for

---

Abbreviations: ADL, activities of daily living; BA4, primary motor cortex; BA6, supplementary motor area; CH, channels; CI, confidence interval; DLPFC, dorsolateral prefrontal cortex; EEG, electroencephalogram; fMRI, functional magnetic resonance imaging; NIRS, near-infrared spectroscopy; PFC, prefrontal cortex; SD, standard deviation; WOT-HS, wearable optical topography system.

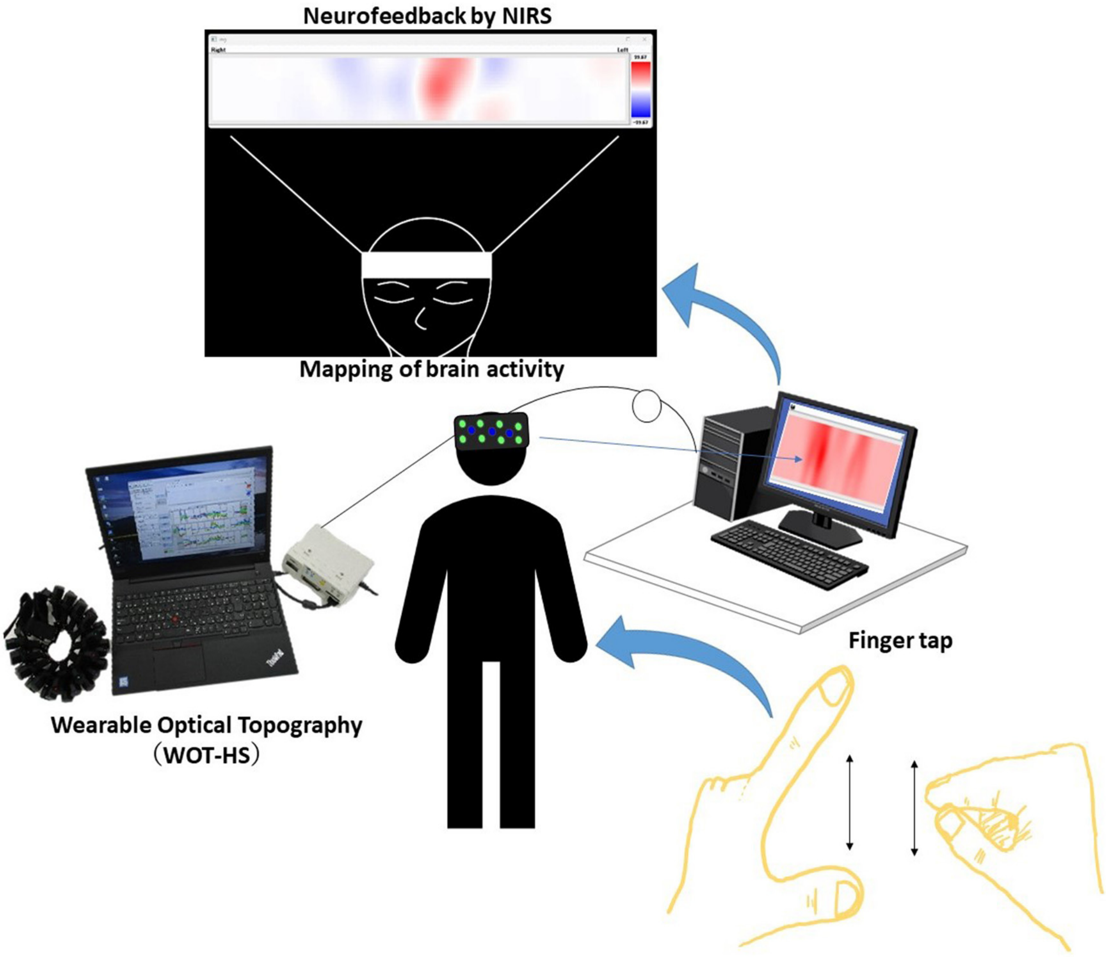

FIGURE 1
A schematic of the system. Data measured using the wearable optical topography system (WOT-HS) can be presented to the participants in real time. Changes in hemoglobin concentration (a proxy for brain activity) measured in the WOT-HS headset (34 channels) are presented on a screen. The figure at the top of the image (mapping of brain activity) is the actual screen presented to the participant. Increased and decreased hemoglobin concentrations are mapped in red and blue, respectively, while unchanged levels are shown in white.

15 s. In the open-finger configuration, they were instructed to open their fingers ∼4 cm apart to reduce inter-participant variability in movement amplitude (Tomita et al., 2020).

2.4 Data preprocessing in NIRS and data analysis

First, the NIRS signal was bandpass filtered at 0.01–0.90 Hz from the settings at the time of measurement (Klein and Kranczioch, 2019). Next, linear fitting was performed using the values at the first and last 30 s of rest to remove drift. In this correction, a least squares method was used to estimate a linear trend from the first and last rests, and the estimated value was subtracted from the data (Xu et al., 2015; von Lühmann et al., 2020). The NIRS signal was then normalized using a z-score transformation for inter-participant comparison (Megumi et al., 2023); for the z-score, the signal at each time point was divided by the mean value during the 10 s before the first task and then by the standard deviation during the 10 s before the task. Values outside ±2 times the standard deviation of the mean were excluded as outliers (Takahashi et al., 2022). To evaluate prefrontal activation, channels (CH)10–13 were analyzed as right PFC, CH16–19 as middle PFC, and CH22–25 as left PFC. The Shapiro–Wilk test was used to verify the normal distribution of the data and perform each analysis. Since the block design was such that each participant repeated each task's conditions thrice to assess the brain activity, the data between each block were added and averaged, and the two conditions of rest and task were compared. For the comparison of rest and tasks in older adults and young participants, the Wilcoxon rank-sum test was performed. We used the SPSS software (version 27.0 for Windows; IBM Corp., Armonk, NY, USA) for the statistical analyses. For multiple comparisons, the Bonferroni correction set the significance level at $< 0.0167\%$.

3 Results

Figure 4 shows the time course of changes in oxygenated hemoglobin levels in the older participants (One typical example of significant brain activation). The signal tended to increase during

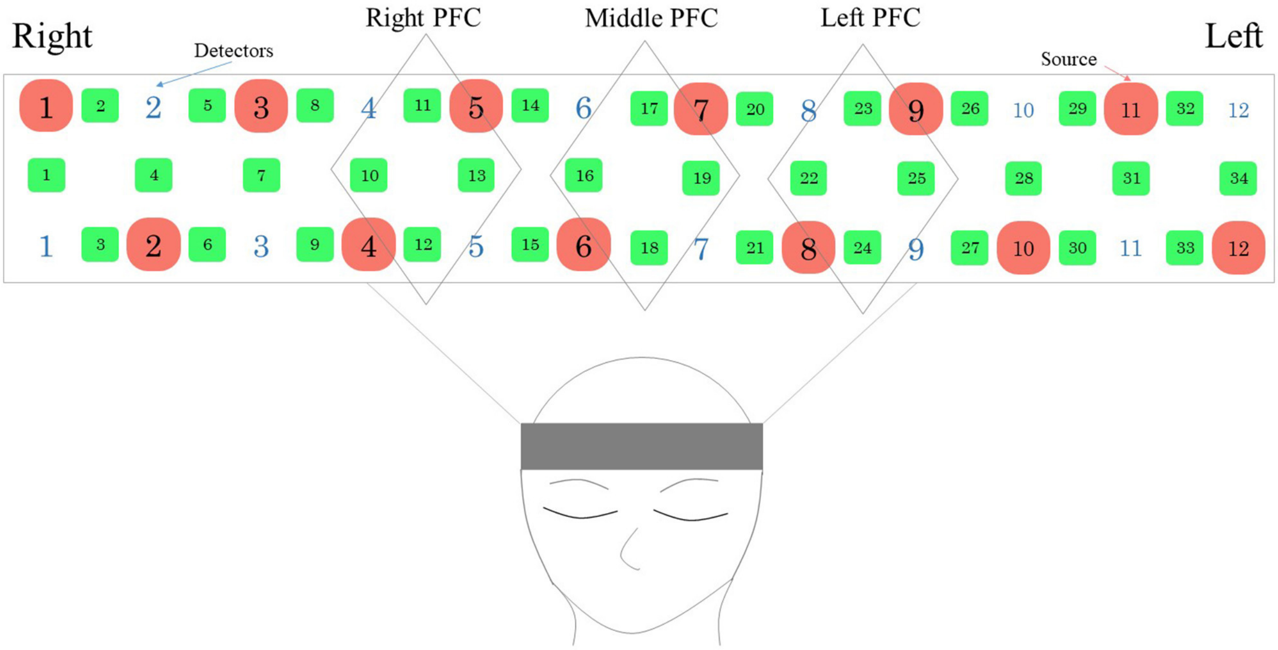

FIGURE 2
Probe placement in the WOT-HS headset. The arrangement consists of a light-emitting center and a light-receiving sensor (the sensor receives light emitted from the adjacent light-emitting center). Green numbers indicate measurement channels, red and white numbers indicate light source and detector. PFC, prefrontal cortex.

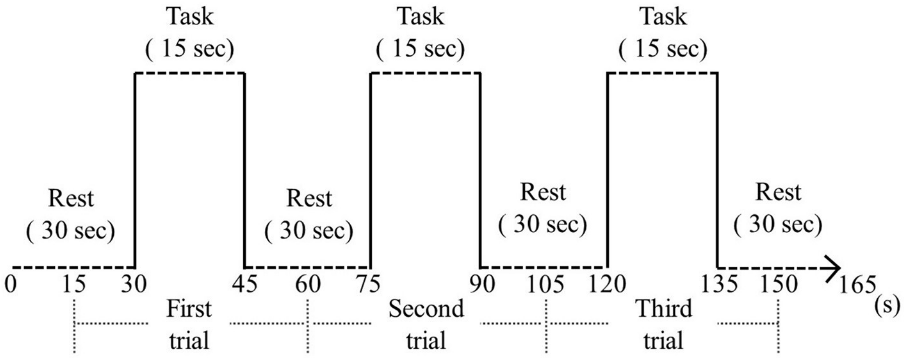

FIGURE 3
Block design. During the resting phase, a cross symbol was presented on the monitor and the participant was instructed to rest. During the task, finger tapping and neurofeedback were performed.

the implementation of the task (neurofeedback), as observed in the younger participants. At rest, after the implementation of the task, the oxygenated hemoglobin levels decreased. During the task implementation, there was an increasing trend in all left, central, and right PFC regions. Table 1 presents a comparison of the mean values in the older adults at rest before the task and during the task. The rest of the Right PFC in older adults had a mean of 0.1078 with a standard deviation of 0.2831, and the task had a mean of 1.0486 with a standard deviation of 1.1158. The z-value of the test was 2.497, and the *p*-value was 0.013, indicating a significant difference between rest and task. In Middle PFC, the rest had a mean of 0.1209 with a standard deviation of 0.1777, and the task had a mean of 0.7175 with a standard deviation of 1.7076. The test resulted in a z-value of 1.274 and a *p*-value of 0.203, indicating no significant difference between rest and task. In the Left PFC, the rest had a mean of 0.0247 and a standard deviation of 0.2904, while the task had a mean of 0.4243 and 1.3741. The test resulted in a z-value of 1.172 and a *p*-value of 0.241, indicating no significant difference between rest and task.

Figure 5 shows the time course of the changes in oxygenated hemoglobin levels in healthy young participants (one typical example of significant brain activation). Oxidized hemoglobin levels tended to increase from before the task to when neurofeedback was implemented, followed by a decrease from neurofeedback implementation to the resting state. All left, central, and right prefrontal regions showed an increasing trend during

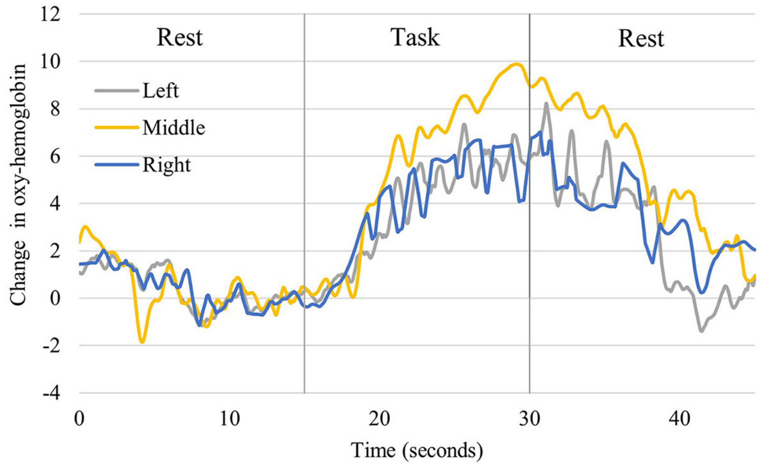

FIGURE 4
Changes in oxyhemoglobin levels recorded from right, middle, and left channels in older participants. It shows one representative person who showed significant activation. The blue line shows the values for the right, the yellow line for the central, and the gray line for the left prefrontal region.

TABLE 1 Oxyhemoglobin concentration values during each task period in older participants.

	Rest		Task (neurofeedback and finger tap)		*z*-value	*p*-value
	Average (95% CI)	SD	Average	SD		
Right PFC	0.1078 (−0.0606-0.2691)	0.2831	1.0486 (0.5102-1.7592)	1.1158	2.497	0.013*
Middle PFC	0.1209 (0.0135-0.2235)	0.1777	0.7175 (0.0665-1.8358)	1.7076	1.274	0.203
Left PFC	0.0247 (−0.1668-0.1814)	0.2904	0.4243 (−0.2648-1.2998)	1.3741	1.172	0.241

*$p < 0.0167$%. CI, confidence interval; PFC, prefrontal cortex; SD, standard deviation.

neurofeedback implementation. Table 2 compares the mean values at rest before the task and during neurofeedback. The rest of the Right PFC for young adults had a mean of 0.0004 with a standard deviation of 0.002, and the task (neurofeedback and finger tap) had a mean of 2.4799 with a standard deviation of 4.3473. In Middle PFC, Rest had a mean of 0.0033 and a standard deviation of 0.0183, while the task had a mean of 0.7957 and a standard deviation of 6.446. The test resulted in a *t*-value of −0.685 and a *p*-value of 0.498, indicating no significant difference between rest and task. In the Left PFC, the rest had a mean of −0.0023 and a standard deviation of 0.0151, while the task had a mean of 1.2267 and a standard deviation of 4.2893. The test resulted in a *t*-value of −1.595 and a *p*-value of 0.121, indicating no significant difference between rest and task. From Tables 1, 2, both older and young adults, there were no significant differences between the pre-task resting period and the neurofeedback period in the left and central prefrontal regions, while significant differences in the right prefrontal region were demonstrated.

4 Discussion

In this study, we developed a simple NIRS-based neurofeedback system and evaluated brain activity during its implementation. Neurofeedback using NIRS can either increase or decrease brain activity (Hosseini et al., 2016; Kinoshita et al., 2016; Kohl et al., 2022), and this system can respond to both types of feedback. The presentation screen can also show brain activity using mapping, waveforms, or bars. In our system, brain activity was indicated using mapping. The measurement screen can also display waveforms, allowing visualization of both maps and waveforms.

In a previous study that developed an NIRS neurofeedback system, activation in cerebral regions, including PFC, was assessed during real-time neurofeedback (Kinoshita et al., 2016). In the previous study, using a smaller device, we also found that neurofeedback altered brain activity bilaterally in dorsolateral (DL)PFC during cognitive training (Nouchi et al., 2021). In our study, we observed a significant difference between rest and task in the right PFC, as well as increasing trends in other areas. However, a degree of variation was noted. We found an increase in oxygenated hemoglobin concentration during neurofeedback, suggesting that our results are similar to those of previous studies. Furthermore, the present results suggest that neurofeedback can be effective, even with this simple system. Our results showed a significant difference only in the right PFC. This may be because the present method involved visuospatial cognitive abilities, which are related to the ability to grasp and visualize own brain activity based on brain activity mapping images. Since visuospatial processing ability is

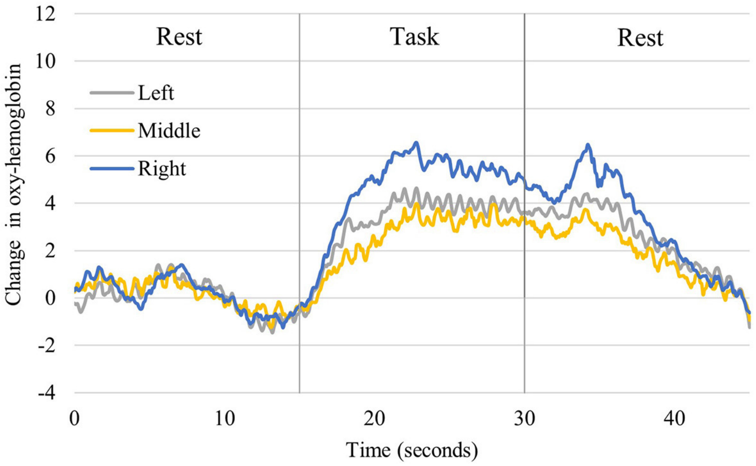

FIGURE 5
Changes in oxyhemoglobin levels recorded from right, middle, and left channels in young participants. It shows one representative person who showed significant activation. The blue line shows the values for the right, the yellow line for the central, and the gray line for the left prefrontal region.

TABLE 2 Oxyhemoglobin concentration values during each task in young.

	Rest		Task (neurofeedback and finger tap)		*z*-value	*p*-value
	Average (95% CI)	SD	Average	SD		
Right PFC	0.0004 (−0.0003-0.0012)	0.0020	1.9770 (0.775-3.1789)	3.2769	4.056	$< 0.001^*$
Middle PFC	0.0033 (−0.0034-0.01)	0.0183	0.4454 (−1.5363-2.4272)	5.4028	1.431	0.153
Left PFC	−0.0023 (−0.0078-0.0032)	0.0151	0.9188 (−0.2394-2.077)	3.1574	1.352	0.176

$^*p < 0.0167\%$. CI, confidence interval; PFC, prefrontal cortex; SD, standard deviation.

dominant in the right hemisphere (Kwon et al., 2002; Corballis, 2003; Suzuki et al., 2018), a greater activation was observed in the right PFC than in other regions, which may have resulted in a significant difference. Other than this, we could not show any other influence directly related to the significant difference in the right PFC.

Circuits involving DLPFC, PFC, and the cerebellum have been reported to control motor accuracy (Torriero et al., 2007; Abiru et al., 2016). Since finger tapping in the present study involved alternating movements, prefrontal regions were likely involved. However, the areas that control finger movement traditionally include the primary motor cortex (BA4), premotor cortex, supplementary motor area (BA6) (Sugioka et al., 2022), primary sensorimotor cortex, and the cerebellum (Turesky et al., 2018). Activation in prefrontal regions during alternating finger tapping has not been confirmed in young individuals (Takahashi et al., 2022). In our paradigm of finger tapping with neurofeedback, the concentration of oxygenated hemoglobin increased, which may also be due to the effect of this system. We believe the proposed method, which seeks to increase brain activity while performing alternating finger tapping, has a double-task element. Dual tasks that involve exercise and cognitive paradigms, such as walking, activate PFC (Holtzer et al., 2011; Kvist et al., 2023), and even in older people with mild cognitive impairment, PFC activation has been observed during dual-task walking (Doi et al., 2013). Since the method in this study may comprise a dual-task element, brain activity is expected to increase during neurofeedback.

Neurofeedback with NIRS has been shown to have strong effects, avoiding non-trivial restrictions on participants' movements, and neurofeedback therapy in patients with stroke has been shown to improve cognitive domains in these patients (Renton et al., 2017). DLPFC activation can enhance the benefits of cognitive training (Nouchi et al., 2020); in other words, it is important to increase DLPFC activity during cognitive training to enhance cognitive function (Nouchi et al., 2021). The results of this study show that neurofeedback during finger tapping enhances brain activity even in older adults. Therefore, there is potential for the prevention of dementia, and future studies are needed for more in-depth evaluations.

This study had three notable limitations. The first issue is the number of older participants. Comparisons should be made between groups of younger and older adults, as well as between older adults and cognitively impaired participants; it will be necessary to increase the number of participants and conduct additional surveys in the future. Second, this was a cross-sectional study. Previous studies on neurofeedback have evaluated function before and after intervention and reported improvements in motor function. Although other cross-sectional studies have been performed, it is desirable to conduct longitudinal measurements to evaluate improvements in brain, cognitive, and motor function. Third, we used a specific task and measurement site: we focused only on the finger-tapping task and on recording changes in prefrontal regions, but neurofeedback may be effective using other tasks and measurements in other brain regions. It is also necessary to measure task performance to further verify the effectiveness of neurofeedback.

In conclusion, a simple neurofeedback system using finger taps and NIRS was constructed to measure oxygenated hemoglobin concentration during finger taps and neurofeedback in older participants and young. In this system, the concentration of oxygenated hemoglobin during neurofeedback implementation in the two groups of participants increased. Further studies are needed to investigate the usefulness of this system in older populations.

Data availability statement

The raw data supporting the conclusions of this article will be made available by the authors, without undue reservation.

Ethics statement

The studies involving humans were approved by the Ethical Review Committee of Takasaki University of Health and Welfare. The studies were conducted in accordance with the local legislation and institutional requirements. The participants provided their written informed consent to participate in this study.

Author contributions

ST: Writing – review & editing, Writing – original draft, Methodology, Investigation, Funding acquisition, Formal analysis, Data curation, Conceptualization. DT: Writing – review & editing, Writing – original draft, Investigation, Data curation. YK: Writing – review & editing, Writing – original draft, Methodology, Investigation. NS: Writing – review & editing, Writing – original draft, Formal analysis, Conceptualization. NK: Writing – review & editing, Writing – original draft, Validation, Conceptualization.

Funding

The author(s) declare financial support was received for the research, authorship, and/or publication of this article. This work was supported in part by KAKENHI (No. 23K16496) from the Japan Society for the Promotion of Science.

Conflict of interest

The authors declare that the research was conducted in the absence of any commercial or financial relationships that could be construed as a potential conflict of interest.

Publisher's note

References

Abiru, M., Sakai, H., Sawada, Y., and Yamane, H. (2016). The effect of the challenging two handed rhythm tapping task to DLPFC activation. *Asian J. Occup. Ther.* 12, 75–83. doi: 10.11596/asiajot.12.75

Barth, B., Strehl, U., Fallgatter, A. J., and Ehlis, A. C. (2016). Near-infrared spectroscopy based neurofeedback of prefrontal cortex activity: a proof-of-concept study. *Front. Hum. Neurosci.* 10:633. doi: 10.3389/fnhum.2016.00633

Corballis, P. M. (2003). Visuospatial processing and the right-hemisphere interpreter. *Brain Cogn.* 53, 171–176. doi: 10.1016/S0278-2626(03)00103-9

Doi, T., Makizako, H., Shimada, H., Park, H., Tsutsumimoto, K., Uemura, K., et al. (2013). Brain activation during dual-task walking and executive function among older adults with mild cognitive impairment: a fNIRS study. *Aging Clin. Exp. Res.* 25, 539–544. doi: 10.1007/s40520-013-0119-5

Ehlis, A. C., Barth, B., Hudak, J., Storchak, H., Weber, L., Kimmig, A. S., et al. (2018). Near-infrared spectroscopy as a new tool for neurofeedback training: applications in psychiatry and methodological considerations. *Jpn. Psychol. Res.* 60, 225–241. doi: 10.1111/jpr.12225

Holtzer, R., Mahoney, J. R., Izzetoglu, M., Izzetoglu, K., Onaral, B., Verghese, J., et al. (2011). fNIRS study of walking and walking while talking in young and old individuals. *J Gerontol. A Biol. Sci. Med. Sci.* 66, 879–887. doi: 10.1093/gerona/glr068

Hoshi, Y., and Tamura, M. (1993). Detection of dynamic changes in cerebral oxygenation coupled to neuronal function during mental work in man. *Neurosci. Lett.* 150, 5–8. doi: 10.1016/0304-3940(93)90094-2

Hosseini, S. M. H., Pritchard-Berman, M., Sosa, N., Ceja, A., and Kesler, S. R. (2016). Task-based neurofeedback training: a novel approach toward training executive functions. *Neuroimage.* 134, 153–159. doi: 10.1016/j.neuroimage.2016.03.035

Hou, X., Xiao, X., Gong, Y., Li, Z., Chen, A., Zhu, C., et al. (2021). Functional near-infrared spectroscopy neurofeedback enhances human spatial memory. *Front. Hum. Neurosci.* 15:681193. doi: 10.3389/fnhum.2021.681193

Kinoshita, A., Takizawa, R., Yahata, N., Homae, F., Hashimoto, R., Sakakibara, E., et al. (2016). Development of a neurofeedback protocol targeting the frontal pole using near-infrared spectroscopy. *Psychiatry Clin. Neurosci.* 70, 507–516. doi: 10.1111/pcn.12427

Klein, F., and Kranczioch, C. (2019). Signal processing in fNIRS: A case for the removal of systemic activity for single trial data. *Front. Hum. Neurosci.* 13:331. doi: 10.3389/fnhum.2019.00331

Kohl, S. H., Mehler, D. M. A., Lührs, M., Thibault, R. T., Konrad, K., Sorger, B., et al. (2022). (2020). The potential of functional near-infrared spectroscopy-based neurofeedback-A systematic review and recommendations for best practice. *Front. Neurosci.* 16:907941. doi: 10.3389/fnins.2022.907941

Kvist, A., Bezuidenhout, L., Johansson, H., Albrecht, F., Ekman, U., Conradsson, D. M., et al. (2023). Using functional near-infrared spectroscopy to measure prefrontal cortex activity during dual-task walking and navigated walking: a feasibility study. *Brain Behav.* 13:e2948. doi: 10.1002/brb3.2948

Kwon, H., Reiss, A. L., and Menon, V. (2002). Neural basis of protracted developmental changes in visuo-spatial working memory. *Proc. Natl. Acad. Sci. U. S. A.* 99, 13336–13341. doi: 10.1073/pnas.162486399

Liu, B., Chen, X., Li, Y., Liu, H., Guo, S., Yu, P., et al. (2018). Effect of passive finger exercises on grip strength and the ability to perform activities of daily living for older people with dementia: A 12-week randomized controlled trial. *Clin. Interv. Aging.* 13, 2169–2177. doi: 10.2147/CIA.S174756

Marzbani, H., Marateb, H. R., and Mansourian, M. (2016). Neurofeedback: a comprehensive review on system design, methodology and clinical applications. *Basic Clin. Neurosci.* 7, 143–158. doi: 10.15412/J.BCN.03070208

Megumi, A., Shin, J., Uchida, Y., and Yasumura, A. (2023). Increased activity in the prefrontal cortex related to planning during a handwriting task. *Psychology* 5, 896–907. doi: 10.3390/psych5030059

Mihara, M., Fujimoto, H., Hattori, N., Otomune, H., Kajiyama, Y., Konaka, K., et al. (2021). Effect of neurofeedback facilitation on poststroke gait and balance recovery: A randomized controlled trial. *Neurology.* 96, e2587–e2598. doi: 10.1212/WNL.0000000000011989

Nouchi, R., Kawata, N. Y. D. S., Saito, T., Himmelmeier, R. M., Nakamura, R., Nouchi, H., et al. (2020). Dorsolateral prefrontal cortex activity during a brain training game predicts cognitive improvements after four weeks' brain training game intervention: evidence from a randomized controlled trial. *Brain Sci.* 10:560. doi: 10.3390/brainsci10080560

Nouchi, R., Nouchi, H., Dinet, J., and Kawashima, R. (2021). Cognitive training with neurofeedback using NIRS improved cognitive functions in young adults: evidence from a randomized controlled trial. *Brain Sci.* 12:5. doi: 10.3390/brainsci12010005

Renton, T., Tibbles, A., and Topolovec-Vranic, J. (2017). Neurofeedback as a form of cognitive rehabilitation therapy following stroke: a systematic review. *PLoS ONE.* 12:e0177290. doi: 10.1371/journal.pone.0177290

Seidler, R. D., Bernard, J. A., Burutolu, T. B., Fling, B. W., Gordon, M. T., Gwin, J. T., et al. (2010). Motor control and aging: Links to age-related brain structural, functional, and biochemical effects. *Neurosci. Biobehav. Rev.* 34, 721–733. doi: 10.1016/j.neubiorev.2009.10.005

Seol, J., Lim, N., Nagata, K., and Okura, T. (2023). Effects of home-based manual dexterity training on cognitive function among older adults: a randomized controlled trial. *Eur. Rev. Aging Phys. Act.* 20:9. doi: 10.1186/s11556-023-00319-2

Sitaram, R., Ros, T., Stoeckel, L., Haller, S., Scharnowski, F., Lewis-Peacock, J., et al. (2019). Author Correction: Closed-loop brain training: the science of neurofeedback. *Nat. Rev. Neurosci.* 20:314. doi: 10.1038/s41583-019-0161-1

Sugioka, J., Suzumura, S., Kuno, K., Kizuka, S., Sakurai, H., Kanada, Y., et al. (2022). Relationship between finger movement characteristics and brain voxel-based morphometry. *PLoS ONE* 17:e0269351. doi: 10.1371/journal.pone.0269351

Suzuki, K., Kita, Y., Oi, Y., Okumura, Y., Okuzumi, H., Inagaki, M., et al. (2018). Right prefrontal cortex specialization for visuospatial working memory and developmental alterations in prefrontal cortex recruitment in school-age children. *Clin. Neurophysiol.* 129, 759–765. doi: 10.1016/j.clinph.2018.01.010

Suzumura, S., Kanada, Y., Osawa, A., Sugioka, J., Maeda, N., Nagahama, T., et al. (2021). Assessment of finger motor function that reflects the severity of cognitive function. *Fujita Med. J.* 7, 122–129. doi: 10.20407/fmj.2020-013

Suzumura, S., Osawa, A., Nagahama, T., Kondo, I., Sano, Y., Kandori, A., et al. (2016). Assessment of finger motor skills in individuals with mild cognitive impairment and patients with Alzheimer's disease: relationship between finger-to-thumb tapping and cognitive function. *Jpn J. Compr. Rehabil. Sci.* 7, 19–28. doi: 10.11336/jjcrs.7.19

Takahashi, S., Kodama, N., Kawase, Y., and Takeuchi, H. (2018). Comparison between dementia patients and healthy elderly controls in oxyhemoglobin and total-hemoglobin. *IEEJ Trans. Electron. Inf. Syst.* 138, 1348–1354. doi: 10.1541/ieejeiss.138.1348

Takahashi, S., Tomita, Y., Tanaka, S., Sakurai, N., and Kodama, N. (2022). Prefrontal cerebral oxygenated hemoglobin concentration during the category fluency and finger-tapping tasks in adults with and without mild cognitive impairment: a near-infrared spectroscopy study. *Brain Sci.* 12:1636. doi: 10.3390/brainsci12121636

Tomita, Y., Tanaka, S., Takahashi, S., and Takeuchi, N. (2020). Detecting cognitive decline in community-dwelling older adults using simple cognitive and motor performance tests. *Geriatr. Gerontol. Int.* 20, 212–217. doi: 10.1111/ggi.13863

Torriero, S., Oliveri, M., Koch, G., LoLo Gerfo, E., Salerno, S., Petrosini, L., et al. (2007). Cortical networks of procedural learning: evidence from cerebellar damage. *Neuropsychologia* 45, 1208–1214. doi: 10.1016/j.neuropsychologia.2006.10.007

Trambaiolli, L. R., Cassani, R., Mehler, D. M. A., and Falk, T. H. (2021). Neurofeedback and the aging brain: a systematic review of training protocols for dementia and mild cognitive impairment. *Front. Aging Neurosci.* 13:682683. doi: 10.3389/fnagi.2021.682683

Turesky, T. K., Olulade, O. A., Luetje, M. M., and Eden, G. F. (2018). An fMRI study of finger tapping in children and adults. *Hum. Brain Mapp.* 39, 3203–3215. doi: 10.1002/hbm.24070

Villringer, A., Planck, J., Hock, C., Schleinkofer, L., and Dirnagl, U. (1993). Near infrared spectroscopy (NIRS): a new tool to study hemodynamic changes during activation of brain function in human adults. *Neurosci. Lett.* 154, 101–104. doi: 10.1016/0304-3940(93)90181-J

von Lühmann, A., Ortega-Martinez, A., Boas, D. A., and Yücel, M. A. (2020). Using the general linear model to improve performance in fNIRS single trial analysis and classification: a perspective. *Front. Hum. Neurosci.* 14:30. doi: 10.3389/fnhum.2020.00030

Xu, J., Liu, X., Zhang, J., Li, Z., Wang, X., Fang, F., et al. (2015). FC-NIRS: a functional connectivity analysis tool for near-infrared spectroscopy data. *Biomed. Res. Int.* 2015:248724. doi: 10.1155/2015/248724

frontiers | Frontiers in Neuroscience

TYPE Original Research
PUBLISHED 10 July 2024
DOI 10.3389/fnins.2024.1423014

OPEN ACCESS

EDITED BY
Zhiyong Zhao,
Zhejiang University, China

REVIEWED BY
Hao Guo,
Taiyuan University of Technology, China
Yuhu Shi,
Shanghai Maritime University, China
Li-Dan Kuang,
Changsha University of Science and Technology, China
Guoqiang Hu,
Dalian Maritime University, China

*CORRESPONDENCE
Wei-Xing Li
✉ wxli@mail.dlut.edu.cn

RECEIVED 25 April 2024
ACCEPTED 21 June 2024
PUBLISHED 10 July 2024

CITATION
Li W-X, Lin Q-H, Zhang C-Y, Han Y and Calhoun VD (2024) A new transfer entropy method for measuring directed connectivity from complex-valued fMRI data. *Front. Neurosci.* 18:1423014. doi: 10.3389/fnins.2024.1423014

A new transfer entropy method for measuring directed connectivity from complex-valued fMRI data

Wei-Xing Li[1]*, Qiu-Hua Lin[1], Chao-Ying Zhang[1], Yue Han[1] and Vince D. Calhoun[2]

[1]School of Information and Communication Engineering, Dalian University of Technology, Dalian, China, [2]Tri-Institutional Center for Translational Research in Neuroimaging and Data Science (TReNDS), Georgia State University, Georgia Institute of Technology, Emory University, Atlanta, GA, United States

Background: Inferring directional connectivity of brain regions from functional magnetic resonance imaging (fMRI) data has been shown to provide additional insights into predicting mental disorders such as schizophrenia. However, existing research has focused on the magnitude data from complex-valued fMRI data without considering the informative phase data, thus ignoring potentially important information.

Methods: We propose a new complex-valued transfer entropy (CTE) method to measure causal links among brain regions in complex-valued fMRI data. We use the transfer entropy to model a general non-linear magnitude−magnitude and phase−phase directed connectivity and utilize partial transfer entropy to measure the complementary phase and magnitude effects on magnitude−phase and phase−magnitude causality. We also define the significance of the causality based on a statistical test and the shuffling strategy of the two complex-valued signals.

Results: Simulated results verified higher accuracy of CTE than four causal analysis methods, including a simplified complex-valued approach and three real-valued approaches. Using experimental fMRI data from schizophrenia and controls, CTE yields results consistent with previous findings but with more significant group differences. The proposed method detects new directed connectivity related to the right frontal parietal regions and achieves 10.2–20.9% higher SVM classification accuracy when inferring directed connectivity using anatomical automatic labeling (AAL) regions as features.

Conclusion: The proposed CTE provides a new general method for fully detecting highly predictive directed connectivity from complex-valued fMRI data, with magnitude-only fMRI data as a specific case.

KEYWORDS

complex-valued fMRI data, transfer entropy, partial transfer entropy, directed connectivity, functional connectivity

1 Introduction

To date, a huge number of studies have investigated directed functional connectivity (FC) or functional network connectivity (FNC) using fMRI data (Demirci et al., 2009; Stevens et al., 2009; Lizier et al., 2011; Ursino et al., 2020; Crimi et al., 2021). Directed FC/FNC refers to the statistical causality between different time series from brain regions of interest (ROIs) or time courses of brain networks extracted by data-driven methods from fMRI data (Stevens et al., 2009; Ursino et al., 2020; Mahmood et al., 2022). The directed FC/FNC results have been widely used as putative biomarkers to identify/predict brain function changes linked to mental disorders such as schizophrenia (Fogelson et al., 2014; Bastos-Leite et al., 2015; Dietz et al., 2020).

Directed FC/FNC analyses can be generally classified into model-based and model-free methods. Typical model-based methods include dynamic causal modeling (DCM) (Friston et al., 2019), structural equation modeling (Bielczyk et al., 2019), and dynamic Bayesian network (Wu et al., 2014). Regarding model-free methods, the Granger causal test is frequently used to determine whether there is a linear causal relationship between ROIs and brain networks (Demirci et al., 2009; Crimi et al., 2021). Demirci et al. (2009) exploited the Granger causal test to calculate directed FNC of fMRI data and found abnormal connections from frontal areas to visual areas for patients with schizophrenia. Crimi et al. (2021) used Granger connections to classify patients with autism spectrum disorder and healthy controls.

Real-valued transfer entropy is utilized to identify the underlying non-linearly directed information between ROIs or between brain networks (Lizier et al., 2011; Ursino et al., 2020; Liu et al., 2022). Ursino et al. (2020) verified that transfer entropy is a promising method to estimate the causality of connections between regions with long time delays. Lizier et al. (2011) presented a transfer entropy method to detect causality between brain regions in cognitive tasks and showed task difficulty being related to causal strength for the motor cortex. Following this, Liu et al. (2022) proposed a scored function based on transfer entropy and conditional entropy to quantify directed FC, which accurately inferred directed connectivity networks of time series. The most commonly used method for estimating real-valued transfer entropy is the histogram-based transfer entropy (HTE), which estimates the joint probability density function via a histogram-based function. Other transfer entropy algorithms were proposed to improve the accuracy of causal inference or noise robustness, including symbolic transfer entropy (STE) (Li and Zhang, 2022), effective transfer entropy (Behrendt et al., 2019; Caserini and Pagnottoni, 2022), Renyi transfer entropy (Jizba et al., 2022; Zhang et al., 2023), and phase transfer entropy (Wang and Chen, 2020; Gu et al., 2021).

Our study is motivated by two key points. First, previous studies show non-linear FC/FNC properties in fMRI (Li et al., 2010, 2011; Motlaghian et al., 2023). The transfer entropy approach is designed to forecast non-linear causality (Schreiber, 2000), while the Granger causal test may fail as a linear model-free approach (Bastos and Schoffelen, 2016). Second, fMRI data are initially acquired as complex-valued image pairs including both magnitude and phase data (Calhoun et al., 2002; Rowe and Logan, 2004; Adali and Calhoun, 2007). A new transfer entropy approach is needed to incorporate unique and additional information from the phase data in addition to the magnitude-only fMRI data (Yu et al., 2015). The simple sum of the separate real-valued results from the magnitude and the phase data suffers from a loss of accuracy as there is also a correlation between the magnitude and the phase. As such, we propose a new complex-valued transfer entropy (CTE) to detect full causality between two complex-valued signals.

The main contributions of this study are 3-fold:

1. We propose a new CTE method to measure non-linear causal (directed) connectivity among two complex-valued signals by incorporating complementary causality between magnitude and phase using the partial transfer entropy, in addition to detecting magnitude–magnitude and phase–phase causality using transfer entropy. Simulated data verify the high accuracy of CTE compared to a simplified CTE (sCTE) without magnitude–phase causality and the three real-valued methods, including STE, HTE, and Granger causal test.
2. We evaluate the significance of the non-linear directed connectivity via a one-sample *t*-test by using a shuffling strategy of two complex-valued signals. The statistical test assists in eliminating spurious causality, ensuring the stability and accuracy of the causality measurement.
3. We analyze directed FC using experimental resting-state complex-valued fMRI data from 40 schizophrenia patients and 40 healthy controls. CTE yields results consistent with previous findings but with more significant group differences, detects new directed connectivity, and achieves higher SVM classification accuracy, compared to sCTE, STE, HTE, and Granger causal test.

2 Methods

2.1 Modeling and deviation of CTE

Figure 1 shows the framework diagram for measuring directed FC using CTE. Take two AAL regions AAL_*n*1 and AAL_*n*2 for example, each region can obtain an average complex-valued time series involving magnitude and phase. To quantify complete complex-valued causality, CTE measures magnitude–magnitude and phase–phase, and two parts of magnitude and phase causality. To guarantee the reliability of causality measurement, a causal significant test is performed. The direction of FC can be judged by the polarity of CTE. If the CTE value is positive, the direction FC points from AAL_*n*1 to AAL_*n*2; if the CTE value is negative, the direction is the opposite; if CTE equals zero, there is no directed FC between the two AAL regions.

We denote two complex-valued signals as $\mathbf{z_1} = \left\{ z_1(t) \right\} = \left[z_1(1), \ldots, z_1(T) \right]^{\mathrm{T}}$, $\mathbf{z_2} = \left\{ z_2(t) \right\} = \left[z_2(1), \ldots, z_2(T) \right]^{\mathrm{T}}$, $t = 1, \ldots, T$, and T is the data length. The two signals are represented with magnitude and phase in Eq. (1) as follows:

$$\begin{aligned} z_1 &= \boldsymbol{a} \exp\left(j\theta \right) \\ z_2 &= \boldsymbol{b} \exp\left(j\varphi \right) \end{aligned} \tag{1}$$

where $\boldsymbol{a} \in \mathbb{R}^T$ and $\boldsymbol{\theta} \in \mathbb{R}^T$ are the magnitude and phase of z_1, and $\boldsymbol{b} \in \mathbb{R}^T$ and $\boldsymbol{\varphi} \in \mathbb{R}^T$ are the magnitude and phase of z_2.

Based on the relationship between the magnitude and phase of the brain networks (Yu et al., 2015), we propose a definition of CTE

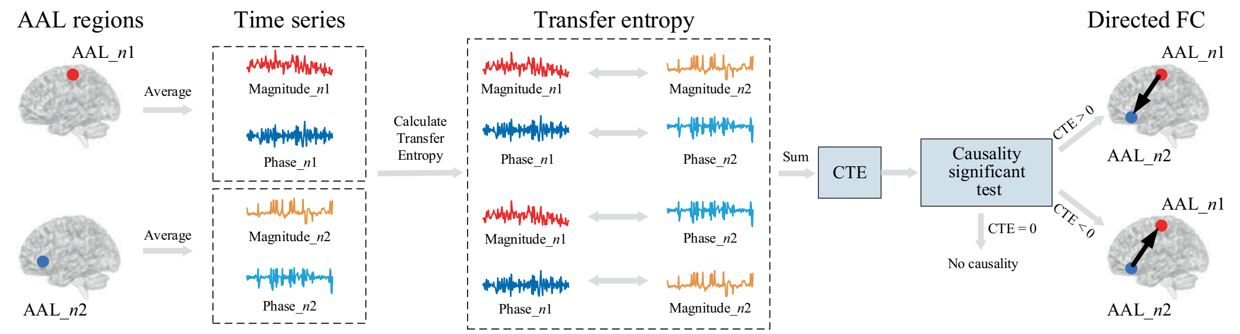

FIGURE 1
Framework diagram for directed FC measured by CTE. First, average complex-valued time series from two AAL regions are obtained. Each average time series involves magnitude and phase. To quantify complete complex-valued causality, CTE considers four parts of causality, including magnitude–magnitude, phase–phase, and two magnitude–phase causality. After the causal significant test, the directed FC between two regions is measured by CTE.

considering complete causality between two complex-valued signals. Motivated by the complex-valued mutual information introduced by Goebel et al. (2011), CTE combines the magnitude and phase to make causality inference and is represented as follows:

$$\mathcal{C}_{z1\to z2} = \mathcal{R}_{\boldsymbol{a}\to\boldsymbol{b}} + \mathcal{R}_{\theta\to\varphi} + \mathcal{R}_{\boldsymbol{a}\to\boldsymbol{b}|\theta} + \mathcal{R}_{\theta\to\varphi|\boldsymbol{a}} \tag{2}$$

where $\mathcal{R}_{\boldsymbol{a}\to\boldsymbol{b}}$ and $\mathcal{R}_{\theta\to\varphi}$ are real-valued transfer entropy from the magnitude and the phase of the two signals, respectively. $\mathcal{R}_{\boldsymbol{a}\to\boldsymbol{b}|\theta}$ and $\mathcal{R}_{\theta\to\varphi|\boldsymbol{a}}$ are partial transfer entropy (Papana et al., 2012), which extends transfer entropy to account for the presence of the third variable. We extend to quantify the complementary phase and magnitude effects on the causality $\mathcal{R}_{\boldsymbol{a}\to\boldsymbol{b}}$ and $\mathcal{R}_{\theta\to\varphi}$.

Real-valued transfer entropy $\mathcal{R}_{\boldsymbol{a}\to\boldsymbol{b}}$ and $\mathcal{R}_{\theta\to\varphi}$ in Eq. (2) can be calculated as follows (Schreiber, 2000):

$$\begin{aligned}\mathcal{R}_{\boldsymbol{a}\to\boldsymbol{b}} &= \sum p\left(\boldsymbol{b}_t,\boldsymbol{b}_{t-\tau},\boldsymbol{a}_{t-\tau}\right)\log\frac{p\left(\boldsymbol{b}_t|\boldsymbol{b}_{t-\tau},\boldsymbol{a}_{t-\tau}\right)}{p\left(\boldsymbol{b}_t|\boldsymbol{b}_{t-\tau}\right)}\\ \mathcal{R}_{\theta\to\varphi} &= \sum p\left(\varphi_t,\varphi_{t-\tau},\theta_{t-\tau}\right)\log\frac{p\left(\varphi_t|\varphi_{t-\tau},\theta_{t-\tau}\right)}{p\left(\varphi_t|\varphi_{t-\tau}\right)}\end{aligned} \tag{3}$$

where $\boldsymbol{a}\to\boldsymbol{b}$ denotes causal direction from $\boldsymbol{a}$ to $\boldsymbol{b}$, $p(\cdot)$ is a marginal probability density function, "$p(\cdot|\cdot)$" represents a condition probability density function, τ is the parameter of time delay, and $\boldsymbol{a}_{t-\tau}$ and $\boldsymbol{b}_{t-\tau}$ are delayed $\boldsymbol{a}$ and $\boldsymbol{b}$ by τ time points. By calculating the Pearson correlation coefficient between the two signals with different time delays, the time delay corresponding to the maximum correlation coefficient is selected as the value of τ.

Real-valued partial transfer entropy $\mathcal{R}_{\boldsymbol{a}\to\boldsymbol{b}|\theta}$ in Eq. (2) is determined as follows:

$$\begin{aligned}\mathcal{R}_{\boldsymbol{a}\to\boldsymbol{b}|\theta} &= -\sum p\left(\boldsymbol{b}_t|\boldsymbol{b}_{t-\tau},\theta_{t-\tau}\right)\log\left\{p\left(\boldsymbol{b}_t|\boldsymbol{b}_{t-\tau},\theta_{t-\tau}\right)\right\}\\ &+\sum p\left(\boldsymbol{b}_t|\boldsymbol{a}_{t-\tau},\boldsymbol{b}_{t-\tau},\theta_{t-\tau}\right)\log\left\{p\left(\boldsymbol{b}_t|\boldsymbol{a}_{t-\tau},\boldsymbol{b}_{t-\tau},\theta_{t-\tau}\right)\right\}\end{aligned} \tag{4}$$

In Eq. (4), it can be observed that phase θ and magnitude $\boldsymbol{a}$ are jointly used to determine the causal direction to magnitude $\boldsymbol{b}$. In other words, $\mathcal{R}_{\boldsymbol{a}\to\boldsymbol{b}|\theta}$ incorporates magnitude–phase causality between θ and $\boldsymbol{b}$ by quantifying the complementary magnitude effects of $\boldsymbol{a}$ on the causality. Similarly, $\mathcal{R}_{\theta\to\varphi|\boldsymbol{a}}$ can be calculated as follows:

$$\begin{aligned}\mathcal{R}_{\theta\to\varphi|\boldsymbol{a}} &= -\sum p\left(\varphi_t|\boldsymbol{a}_{t-\tau},\varphi_{t-\tau}\right)\log\left\{p\left(\varphi_t|\boldsymbol{a}_{t-\tau},\varphi_{t-\tau}\right)\right\}\\ &+\sum p\left(\varphi_t|\theta_{t-\tau},\varphi_{t-\tau},\boldsymbol{a}_{t-\tau}\right)\log\left\{p\left(\varphi_t|\theta_{t-\tau},\varphi_{t-\tau},\boldsymbol{a}_{t-\tau}\right)\right\}\end{aligned} \tag{5}$$

In Eqs. (2)–(5), we need to estimate condition probability density functions and joint probability density functions. We represent the condition probability density function with joint probability density functions and then estimate joint probability density functions. Taking $p\left(\boldsymbol{b}_t|\boldsymbol{b}_{t-\tau},\theta_{t-\tau}\right)$ as an example, we have the following:

$$p\left(\boldsymbol{b}_t|\boldsymbol{b}_{t-\tau},\theta_{t-\tau}\right) = \frac{p\left(\theta_{t-\tau},\boldsymbol{b}_{t-\tau},\boldsymbol{b}_t\right)}{p\left(\theta_{t-\tau},\boldsymbol{b}_{t-\tau}\right)} \tag{6}$$

where $p\left(\theta_{t-\tau},\boldsymbol{b}_{t-\tau},\boldsymbol{b}_t\right)$ and $p\left(\theta_{t-\tau},\boldsymbol{b}_{t-\tau}\right)$ are joint probability density functions. To estimate the joint probability density functions, we perform symbolic processing on each of the variables. The symbolic process helps to improve the noise robustness to traditional transfer entropy and helps capture more non-linear causality proved by the previous study (Gu et al., 2021). Taking the phase $\boldsymbol{\theta} = \left[\theta(1),\ldots,\theta(T)\right]^{\mathrm{T}}$ as an example, where superscript "T" represents the matrix transpose, the symbolic $\theta(t), 1\le t\le T$, denoted as $\theta^{*}(t)$ is computed as follows (Wessel et al., 2000):

$$\theta^{*}(t) = \begin{cases} 0: & \mu_p < \theta(t) \le (1+\beta)\mu_p\\ 1: & (1+\beta)\mu_p < \theta(t) < \infty\\ 2: & (1-\beta)\mu_p < \theta(t) \le \mu_p\\ 3: & 0 \le \theta(t) \le (1-\beta)\mu_p \end{cases}, if\ \theta(t) \ge 0 \tag{7}$$

$$\theta^{*}(t) = \begin{cases} 0: & (1+\beta)\mu_n \le \theta(t) < \mu_n\\ 1: & -\infty < \theta(t) < (1+\beta)\mu_n\\ 2: & \mu_n \le \theta(t) < (1-\beta)\mu_n\\ 3: & (1-\beta)\mu_n \le \theta(t) < 0 \end{cases}, if\ \theta(t) < 0 \tag{8}$$

where β is a control parameter and set to be 0.05 according to the previous study (Wessel et al., 2000), and μ_p and μ_n are the mean of positive and negative variables of θ, respectively. As such, we obtain the symbolic variable vector of θ as $\theta^* = \left[\theta^*(1),\ldots,\theta^*(T)\right]^{\mathrm{T}}$. For simplicity, superscript "*" is omitted. φ can be symbolized in the same way. Magnitude $\boldsymbol{a}$, $\boldsymbol{b}$ is symbolized only using Eq. (7) with non-negative values.

Then, we exploit a histogram-based method to estimate the joint probability density function by counting the number of common elements in segmented bins between vectors. Take $p\left(\boldsymbol{\theta}_{t-\tau},\boldsymbol{b}_{t-\tau}\right)$ in Eq. (6), for example, $\boldsymbol{\theta}_{t-\tau}$ is divided into k_θ equal bins with the bin index denoted as *i*, and $\boldsymbol{b}_{t-\tau}$ is divided into k_θ equal bins with the bin index as *j*. Denoting the segmented bin of $\boldsymbol{\theta}_{t-\tau}$ and $\boldsymbol{b}_{t-\tau}$ as $\Delta\theta$ and Δb, the joint probability density function $p\left(,{}_{t-\tau},\boldsymbol{b}_{t-\tau}\right)$ is estimated by counting the elements number of $\theta_{t-\tau}$ and $\boldsymbol{b}_{t-\tau}$ within the segmented bin $[\Delta\theta,\Delta b]$. The parameters of bin width $\Delta\theta$ and Δb are determined by the number of segmented bins and data length. For simplicity, the parameters $\Delta\theta$ or Δb are equal and can be selected as follows:

$$\Delta\theta = \frac{\max\left\{\left[\boldsymbol{\theta}_{t-\tau};\boldsymbol{b}_{t-\tau}\right]\right\} - \min\left\{\left[\boldsymbol{\theta}_{t-\tau};\boldsymbol{b}_{t-\tau}\right]\right\}}{T} \tag{9}$$

Thus, the joint probability density function $p\left(\boldsymbol{\theta}_{t-\tau},\boldsymbol{b}_{t-\tau}\right)$ located around the point (i,j) is represented as follows:

$$p\left(\boldsymbol{\theta}_{t-\tau},\boldsymbol{b}_{t-\tau}\right) = \frac{num(i,j)}{T-\tau} \tag{10}$$

where $num(\Delta\theta,\Delta b)$ is the number of elements between $\boldsymbol{\theta}_{t-\tau}$ and $\boldsymbol{b}_{t-\tau}$ within the segmented bin $[\Delta\theta,\Delta b]$ around (i,j).

2.2 Significance test of causality

The complex-valued transfer entropy $\mathcal{C}_{z1\to z2}$ quantifies causality from z_1 to z_2 but cannot measure the significance of the causality. As such, we define the causality significance using a statistical test together with a shuffling strategy, which has been previously used in real-valued transfer entropy studies (Bossomaier et al., 2016). The shuffling process assists in eliminating spurious causality between z_1 and z_2, ensuring the stability and accuracy of the causality measurement. Various transfer entropy differences between the original and shuffled signals are obtained by repeating the shuffling process (*R* times). Here, the number of times we perform shuffling, i.e., *R*, is set to 100. Then, one-sample *t*-test on the *R* causality differences is performed to detect the causality significance from z_1 to z_2.

If we denote the shuffled transfer entropy as $\mathcal{C}_{z1\to z2}^{\text{shuffled}}$, the transfer entropy difference $\mathcal{C}_{z1\to z2}^{*}$ is obtained in Eq. (11) as follows:

$$\mathcal{C}_{z1\to z2}^{*} = \mathcal{C}_{z1\to z2} - \mathcal{C}_{z1\to z2}^{\text{shuffled}} \tag{11}$$

Similarly, $\mathcal{C}_{z2\to z1}^{*}$ is obtained in Eq. (12) as follows:

$$\mathcal{C}_{z2\to z1}^{*} = \mathcal{C}_{z2\to z1} - \mathcal{C}_{z2\to z1}^{\text{shuffled}} \tag{12}$$

Let $\Delta\mathcal{C} = \mathcal{C}_{z1\to z2}^{*} - \mathcal{C}_{z2\to z1}^{*}$, $\Delta\boldsymbol{\mathcal{C}} = \left[\Delta\mathcal{C}^{(1)},\ldots,\Delta\mathcal{C}^{(R)}\right]^{\mathrm{T}}$ includes all the transfer entropy differences between $\mathcal{C}_{z1\to z2}^{*}$ and $\mathcal{C}_{z2\to z1}^{*}$, we perform one sample *t*-test with the false discovery rate (FDR) correction as follows (Guo and Bhaskara, 2008):

$$\Delta\mathcal{C} = \begin{cases} \Delta\bar{\mathcal{C}} & \text{p.ttest}\left(\Delta\boldsymbol{\mathcal{C}}\right) < p_{\text{th}} \\ 0, & \text{otherwise} \end{cases} \tag{13}$$

where $\Delta\bar{\mathcal{C}}$ is the mean of $\Delta\boldsymbol{\mathcal{C}}$, p_{th}=0.05. We define the causal direction by the sign of $\Delta\mathcal{C}$ as follows:

$$\text{sig\_causality} = \begin{cases} z_1 \to z_2, & \Delta\mathcal{C} > 0 \\ z_2 \to z_1, & \Delta\mathcal{C} < 0 \\ \text{no causality}, & \Delta\mathcal{C} = 0 \end{cases} \tag{14}$$

3 Experimental methods

3.1 Simulated signals

To evaluate the efficacy of CTE, we generate two sets of simulated complex-valued signals with linear and non-linear causality, respectively. Each set has three types of causal directions and is randomly generated 1,000 times and divided into 10 groups.

The baseline signals are generated using a widely used MATLAB toolbox named Granger causal connectivity analysis (GCCA) (Seth, 2010). The signals are generated with real-valued linear causality via an AR model as Seth (2010):

$$\begin{aligned} x_1(t) &= 0.95\sqrt{2}x_1(t-1) - 0.9025x_1(t-2) + w_1(t) \\ x_2(t) &= 0.5x_1(t-1) + w_2(t) \end{aligned} \tag{15}$$

where $3 \le t \le T$, T is the data length and set to be 146 to keep the same data length as in the fMRI data. $w_1(t)$ and $w_2(t)$ are random variables with zero mean and unit variance satisfying normal distribution. The linear and non-linear causality with different causality cases can be obtained by exploiting and modifying the baseline signals defined in Eq. (15).

When generating simulated signals with linear causality, the three types of simulated complex-valued signals are denoted as type L1, L2, and L3, respectively. The magnitude and phase of the two signals z_1 and z_2 from the three linear types are generated using Eqs. (16)–(18) as follows::

1. type L1:

$$\begin{aligned} a(t) &= 0.95\sqrt{2}a(t-1) - 0.9025a(t-2) + w_1(t) \\ b(t) &= 0.5a(t-1) + w_2(t) \\ \theta(t) &= 0.95a(t) - 0.9025a(t-2) + w_1(t) \\ \varphi(t) &= -0.6a(t) + w_2(t) \end{aligned} \tag{16}$$

2. type L2:

$$\begin{aligned} a(t) &= 0.95\sqrt{2}a(t-1) - 0.9025a(t-2) + w_1(t) \\ b(t) &= 0.5a(t-1) + w_2(t) \\ \theta(t) &= 0.95\theta(t) - 0.9025\theta(t-2) + w_3(t) \\ \varphi(t) &= -0.6\theta(t) + w_4(t) \end{aligned} \tag{17}$$

3. type L3:

$$\begin{aligned} a(t) &= 0.95\sqrt{2}a(t-1) - 0.9025a(t-2) + w_1(t) \\ b(t) &= 0.5a(t-1) + w_2(t) \\ \theta(t) &= r_1(t) \\ \varphi(t) &= r_2(t) \end{aligned} \tag{18}$$

where $r_1(t)$ and $r_2(t)$ are randoms without causality.

The non-linear causality can be obtained by adding quadratic and three-order terms to (Eq. 15). The magnitude and phase of the three types (N1, N2, and N3) can be generated using Eqs. (19)–(21) as follows:

1. type N1:

$$\begin{aligned} a(t) &= 0.95\sqrt{2}a(t-1) - 0.9025a(t-2) + w_1(t) \\ b(t) &= 0.5a^2(t-1) + w_2(t) \\ \theta(t) &= 0.95a(t) - 0.9025a(t-2) + w_1(t) \\ \varphi(t) &= -0.6a^3(t) + w_2(t) \end{aligned} \tag{19}$$

2. type N2:

$$\begin{aligned} a(t) &= 0.95\sqrt{2}a(t-1) - 0.9025a(t-2) + w_1(t) \\ b(t) &= 0.5a^2(t-1) + w_2(t) \\ \theta(t) &= 0.95\theta(t) - 0.9025\theta(t-2) + w_3(t) \\ \varphi(t) &= -0.6\theta^3(t) + w_4(t) \end{aligned} \tag{20}$$

3. type N3:

$$\begin{aligned} a(t) &= 0.95\sqrt{2}a(t-1) - 0.9025a(t-2) + w_1(t) \\ b(t) &= 0.5a^2(t-1) + w_2(t) \\ \theta(t) &= r_1(t) \\ \varphi(t) &= r_2(t) \end{aligned} \tag{21}$$

where $w_1(t)$, $w_2(t)$, $w_3(t)$, and $w_4(t)$ are variables with zero-valued mean, unit variance satisfying normal distribution, and without causality.

Figure 2 shows the ground truth causal directions for the three types of two simulated complex-valued signals with non-linear and linear causality. Specifically, type L1/N1 has the complete complex-valued causality including magnitude–magnitude, phase–phase, and magnitude–phase; type L2/N2 has the incomplete complex-valued causality including magnitude–magnitude and phase–phase; type L3/N3 only has magnitude–magnitude causality.

Figure 3 presents example waveforms of simulated signals z_1 and z_2 from type L1 and type N1. The ground-truth causal direction for the magnitude and phase is shown in Figure 2A. We observe the peaks of the cause signals (z_1 magnitude and z_1 phase, in red) are ahead of the effect signals (z_2 magnitude and z_2 phase, in blue) in all cases, which are consistent with the causal direction of Figure 2. To test the noise effects on CTE, we also add Gaussian noise to the simulated signals with the signal-to-noise ratio (SNR) ranging from −10 dB to 10 dB.

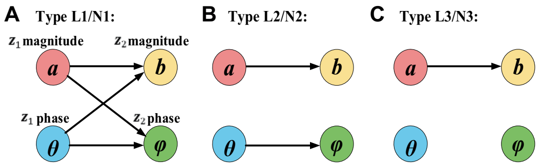

FIGURE 2
Ground truth casual direction for three types of simulated linear and non-linear signals. The arrow represents the causal direction.

3.2 Experimental fMRI data

The resting-state complex-valued fMRI data were a self-collected dataset from 80 subjects, including 40 healthy controls (HCs) and 40 patients with schizophrenia (SZs) with written subject consent overseen by the University of New Mexico Institutional Review Board. Specifically, there are 28 men and 12 women for HCs (mean age ± standard deviation: 36.25 ± 11.40) and 33 men and 7 women for SZs (mean age ± standard deviation: 40.73 ± 14.43). During the scan, all the participants were instructed to rest quietly in the scanner and keep their eyes open without sleeping and not to think of anything in particular (Lin et al., 2022). fMRI scans were acquired by a Siemens 3 T TIM Trio scanner equipped with a 12-channel head coil. The functional scan was acquired with the following parameters: TR = 2 s, TE = 29 ms, field of view = 24 cm, acquisition matrix = 64 × 64, flip angle = 75°, slice thickness = 3.5 mm, and slice gap = 1 mm. Data preprocessing was performed using the SPM software package.[1] Functional images were motion-corrected and then spatially normalized into the standard Montreal Neurological Institute space. Following spatial normalization, the data were resampled to $3 \times 3 \times 3\,\text{mm}^3$, resulting in 53 × 63 × 46 voxels. Both magnitude and phase images were spatially smoothed with an $8 \times 8 \times 8\,\text{mm}^3$ full-width half-maximum (FWHM) Gaussian kernel. Phase images were first motion corrected using the transformations computed from magnitude-only data; then, complex division of phase data by the first time point reduced the need for phase unwrapping; and spatial normalization of phase images used the warp parameters computed from magnitude-only data.

3.3 Complex-valued time series of ROI

Brodmann area (BA) and anatomical automatic labeling (AAL) atlas are two commonly used references to divide the brain into ROIs for FC analysis. Compared with BA, AAL obtains more ROIs and

---

[1] Available at: http://www.fil.ion.ucl.ac.uk/spm.

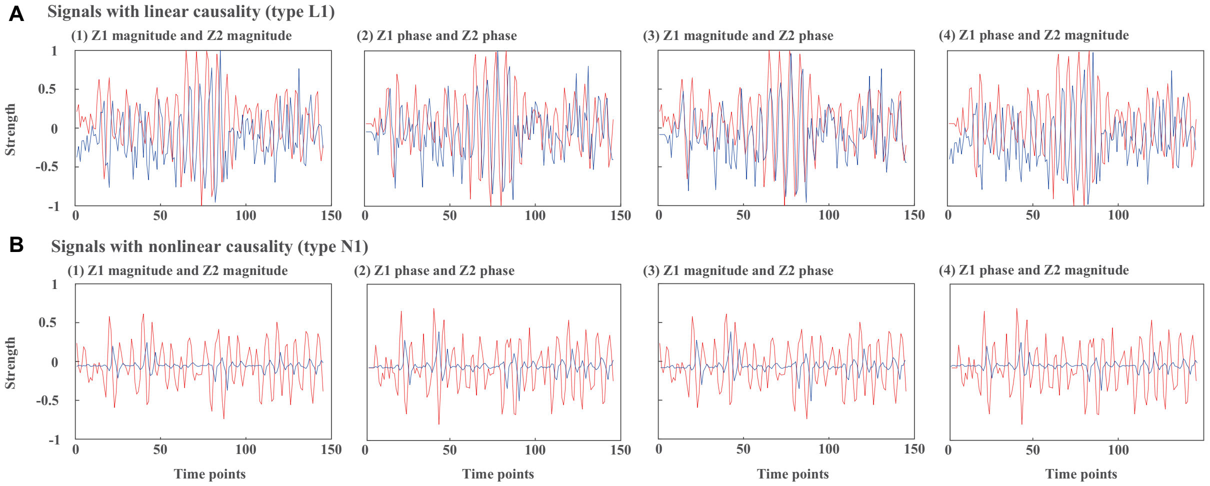

FIGURE 3

Waveforms of simulated signals z1 and z2 from **(A)** type L1 and **(B)** type N1. (1) z1 magnitude and z2 magnitude, (2) z1 phase and z2 phase, (3) z1 magnitude and z2 phase, (4) z1 phase and z2 magnitude.

involves the cerebellum regions. To achieve a more comprehensive and detailed segmentation of the brain regions, we used AAL to obtain 116 ROIs (Tzourio-Mazoyer et al., 2002) and divided the 116 ROIs into 10 brain networks proposed by Smith et al. (2009), consisting of medial visual areas (MV), occipital pole visual areas (OPV), lateral visual areas (LV), default mode network (DMN), cerebellum (CER), sensorimotor (SEM), temporal lobe (TEM), anterior DMN (ADMN), left frontal parietal area (LFP), and right frontal parietal area (RFP). By dividing the 116 ROIs into these 10 networks, it is better to reveal the regularities of connections and establish relationships between FC and FNC.

The complex-valued time series for each ROI is expressed in Eq. (22) as follows:

$$\mathbf{x}_n = \left|\bar{\mathbf{x}}_n(t)\right| \exp\left\{ j\varphi\left(\bar{\mathbf{x}}_n(t)\right)\right\} \tag{22}$$

where $\left|\bar{\mathbf{x}}_n(t)\right|\ \varphi\left(\bar{\mathbf{x}}_n(t)\right), n = 1,..,116, t = 1,..,T$ are the averaged magnitude and phase time series across all voxels within each ROI, and T denotes the total number of time points. The causality between any two ROIs can be quantified by CTE as $\Delta\mathcal{C}\left\{\mathbf{x}_{n1}, \mathbf{x}_{n2}\right\}$ using Eqs. (2), (13), and (14).

3.4 Performance measures

In order to evaluate the proposed CTE, we compare it with the three real-valued causal analysis methods STE, HTE, and Granger, and one complex-valued approach, i.e., sCTE without considering magnitude and phase causality defined in Eq. (23) as follows:

$$\tilde{\mathcal{C}}_{z1\rightarrow z2} = \mathcal{R}_{\boldsymbol{a}\rightarrow \boldsymbol{b}} + \mathcal{R}_{\theta\rightarrow\varphi} \tag{23}$$

For the real-valued causal methods, both STE and HTE calculate real-valued TE $\mathcal{R}_{\boldsymbol{a}\rightarrow \boldsymbol{b}}$ between magnitudes in Eq. (3). Specifically, STE utilized the symbolic process in Eqs. (7) and (8) before estimating joint PDF using Eqs. (9) and (10), while HTE estimates joint PDF without symbolic process.

Granger causal test is based on utilizing linear regression models to perform a statistical causality inference. Given two variables a and b, the autoregressive (AR) model of the Granger causal test is represented in Eq. (24) as follows:

$$\begin{aligned} \boldsymbol{a}_t &= \sum_{j=1}^{J} u_j \boldsymbol{a}_{t-j} + \sum_{j=1}^{J} v_j \boldsymbol{b}_{t-j} + \varepsilon_t \\ \boldsymbol{a}_t &= \sum_{j=1}^{J} c_j \boldsymbol{a}_{t-j} + \boldsymbol{\eta}_t \end{aligned} \tag{24}$$

where u_j, v_j, and c_j are the regression coefficients for the model, J is the estimated time delay between $\boldsymbol{a}$ and $\boldsymbol{b}$, and $\boldsymbol{\mu}_t$ and $\boldsymbol{\eta}_t$ are two independent series satisfying Gaussian distribution. The fitting variances of using $\boldsymbol{a}_{t-j}$, $\boldsymbol{b}_{t-j}$ to fit $\boldsymbol{a}_t$, and only using $\boldsymbol{a}_{t-j}$ are denoted as $\sigma^2\left(\boldsymbol{a}_t | , \boldsymbol{a}_{t-j} | , \boldsymbol{b}_{t-j}\right)$ and $\sigma^2\left(\boldsymbol{a}_t | \boldsymbol{a}_{t-j}\right)$, respectively. The causal direction between $\boldsymbol{a}$ and $\boldsymbol{b}$ is judged by comparing the fitting variance using Eq. (25) as follows:

$$\boldsymbol{b} \rightarrow \boldsymbol{a}, if\ \sigma^2\left(\boldsymbol{a}_t | \boldsymbol{a}_{t-j}\right) > \sigma^2\left(\boldsymbol{a}_t | , \boldsymbol{a}_{t-j} | , \boldsymbol{b}_{t-j}\right) \tag{25}$$

As such, the causal direction is evaluated by Granger causality.

For simulated signals, we calculate the accuracy of directed inference in Eq. (26), denoted as AOC, as follows:

$$\text{AOC} = N_{\text{correct}} / N_{\text{total}} \tag{26}$$

where N_{correct} is the number of correct causal direction judgments and N_{total} is the total number of causality evaluations between two signals.

For experimental fMRI data, we first calculate the average Pearson correlation coefficient between the magnitude and phase from two different ROI signals in HCs or SZs, to validate magnitude and phase dependence in Eq. (27) as follows:

$$\bar{\rho} = \frac{1}{K}\sum_{k=1}^{K}\mathrm{cor}\left(\left|\bar{\mathbf{x}}_m^{(k)}\right|, \varphi\left(\bar{\mathbf{x}}_n^{(k)}\right)\right), m, n = 1, \ldots, 116 \tag{27}$$

Second, we perform two-sample *t-tests* ($p_{\mathrm{th}} = 0.05$) on connections from HCs and SZs with the FDR correction (Guo and Bhaskara, 2008) to obtain significant intergroup differences in Eq. (28) as follows:

$$d_{n,m} = \begin{cases} t\_value & \mathrm{p.ttest2}\left(\Delta\boldsymbol{\mathcal{C}}_{n,m}^{(\mathrm{HC})}, \Delta\boldsymbol{\mathcal{C}}_{n,m}^{(\mathrm{SZ})}\right) < p_{\mathrm{th}} \\ 0, & \mathrm{otherwise} \end{cases} \tag{28}$$

where n and m represent two different ROIs or two brain networks, $\Delta\boldsymbol{\mathcal{C}}_{n,m}^{(\mathrm{HC})} = \left[\Delta\mathcal{C}_{n,m}^{(\mathrm{HC},1)}, \ldots, \Delta\mathcal{C}_{n,m}^{(\mathrm{HC},K)}\right]$ and $\Delta\boldsymbol{\mathcal{C}}_{n,m}^{(\mathrm{SZ})} = \left[\Delta\mathcal{C}_{n,m}^{(\mathrm{SZ},1)}, \ldots, \Delta\mathcal{C}_{n,m}^{(\mathrm{SZ},K)}\right]$.

Third, we compare the number of common and unique connections detected by each method. Finally, we compare the efficacy of the common and unique connections as features to classify HCs and SZs using support vector machine (SVM). The multilayer perceptron kernel is selected, and SVM is repeated 1,000 times. Given a training dataset of $K1$ subjects as $\left[\left(\boldsymbol{x}_1, y_1\right), \ldots, \left(\boldsymbol{x}_{K1}, y_{K1}\right)\right]$, where $\boldsymbol{x}_k \in \mathbb{C}^{M1}, 1 \le k \le K1$ represents the connectivity vector from the kth subject, $M1$ is the vector length, and y_k is the label denoted as either 1 or -1, indicating which class of $\boldsymbol{x}_k$ belongs to. SVM aims to find a hyperplane to maximize the distance between the dataset and the hyperplane. The hyperplane can be represented in Eq. (29) as follows:

$$f\left(\boldsymbol{x}_k\right) = \boldsymbol{\omega}^{\mathrm{T}}\phi\left(\boldsymbol{x}_k\right) + b \tag{29}$$

where $\boldsymbol{E}$ and b are parameters of the hyperplane, and $\phi\left(\boldsymbol{x}_k\right)$ is the kernel function. Multiple kernel functions can be used, e.g., the linear kernel, quadric kernel, and sigmoid kernel. By comparing the clustering performance, we select the multilayer perceptron (MLP) kernel for SVM and there are three layers including the input, hidden, and output layers. The input is the connectivity vectors $\boldsymbol{x}_k$, the non-linear activation function is $\tanh\{\cdot\}$, and the output of the MLP kernel is represented in Eq. (30) as follows (Suykens and Vandewalle, 1999):

$$\phi\left(\boldsymbol{x}_k\right) = \tanh\left\{\omega 1 \cdot \left(\boldsymbol{x}_k\right)^T \cdot \boldsymbol{x}_k + b1\right\} \tag{30}$$

where Ė1 and $b1$ are weights and biases and are initially set to be 1 and -1, respectively. As such, the SVM classifier is built based on MLP kernel and can be realized by MATLAB built-in function named "mlp_kernel."

The results are evaluated in terms of accuracy (ACC), sensitivity (SEN), and specificity (SPEC) defined in Eq. (31) as follows (Lin et al., 2022):

$$\begin{aligned} \mathrm{ACC} &= \frac{\mathrm{TP} + \mathrm{TN}}{\mathrm{TP} + \mathrm{TN} + \mathrm{FP} + \mathrm{FN}} \\ \mathrm{SEN} &= \frac{\mathrm{TP}}{\mathrm{TP} + \mathrm{FN}} \\ \mathrm{SPEC} &= \frac{\mathrm{TN}}{\mathrm{TN} + \mathrm{FP}} \end{aligned} \tag{31}$$

where TP, TN, FP, and FN denote true positive, true negative, false positive, and false negative, respectively. To mitigate overfitting and guarantee reliability, leave one out cross-validation (LOOV) is performed. Specifically, LOOV leaves out the data from one subject as test data and exploits the data from the rest of the selected subjects for training. Given that, the test data are independent of the training data in each LOOV loop. LOOV is used for cross-validation purposes, given we have limited data. As such, we repeat the validation 1,000 times.

4 Results

4.1 Simulated signals

Table 1 shows the accuracy of linear/non-linear directed inference for the three types of simulated signals without noise. Five types of directed analysis methods are compared including the proposed CTE, sCTE, and three real-valued methods: STE, HTE, and Granger. Compared with the other three transfer entropy methods (sCTE, STE, and THE), CTE obtains higher accuracy for causality inference, especially when having complete complex-valued causality (type L1/N1). Specifically, for type N1 (non-linear signals containing complete complex-valued causality), CTE achieves slightly higher accuracy than the sCTE and 18.7–85.9% higher accuracy than the three real-valued algorithms.

TABLE 1 Comparison of the mean and standard deviation of the accuracy of causality inference by five methods for simulated signals without noise.

		CTE (%)	sCTE (%)	STE (%)	HTE (%)	Granger (%)
Linear	Type L1	94.1 ± 1.5	88.4 ± 2.5	84.3 ± 4.7	52.7 ± 3.9	86.8 ± 1.7
	Type L2	89.2 ± 1.7	87.7 ± 2.8	83.5 ± 4.3	51.9 ± 4.3	89.1 ± 2.4
	Type L3	86.3 ± 3.3	85.8 ± 2.9	82.9 ± 4.1	50.3 ± 4.5	86.1 ± 2.6
Non-linear	Type N1	95.3 ± 1.3	87.5 ± 2.8	76.6 ± 3.5	66.1 ± 4.7	9.4 ± 2.9
	Type N2	91.3 ± 1.1	86.8 ± 2.6	74.2 ± 3.9	65.7 ± 4.4	8.1 ± 2.1
	Type N3	85.4 ± 3.7	83.3 ± 3.1	74.1 ± 4.1	64.3 ± 4.2	8.5 ± 2.6

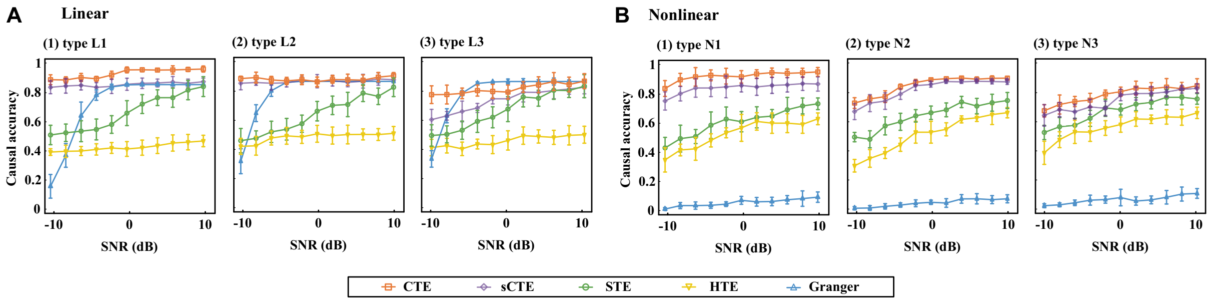

FIGURE 4
Causality accuracy for simulated signals with linear and non-linear causality under different SNRs.

Figure 4 shows the estimated causality accuracy for simulated signals with different SNRs. CTE achieves the highest accuracy and noise robustness for type L1/N1, due to the consideration of complete complex-valued causality. For type L2/N2, CTE and sCTE yield higher accuracy than three real-valued methods, including STE, HTE, and Granger, especially with low SNR (<-6 dB), due to the inclusion of phase causality. Regarding type L3/N3, CTE and the other transfer entropy algorithms have similar accuracy with high SNR (> 6 dB) as there only has magnitude causality. In this case, CTE is a general method suitable for measuring linear and non-linear causality for both complex-valued and real-valued signals. For type L3, note that Granger shows higher directed accuracy than CTE with SNR being -4 dB–4 dB. The reason is that Granger is built on the AR model for linear causality, making it optimal when only magnitude causality exists. However, Granger fails to detect non-linear causality. Therefore, considering both linear and non-linear scenarios, the proposed CTE is the optimal-directed algorithm in most cases.

4.2 Experimental fMRI data

After performing a two-sample *t*-test ($p < 0.05$, df = 78, FDR corrected) for the connections between HCs and SZs, we compare the numbers of common and unique connections detected by two different methods with significant HC-SZ differences. We select sCTE and STE as comparison methods since they have better performance for the simulated signals (refer to Figure 4).

Figure 5 shows the number of common and unique connections in terms of ten brain networks. In total, CTE obtains more common connections with sCTE than with STE (505 vs. 344), while detecting fewer unique connections with sCTE than with STE (105 vs. 266). The reason is that sCTE is closer to CTE by considering additional phase–phase causality relative to STE. Most of the common and unique connections belong to CER, which has been reported by previous studies to identify schizophrenia (Su et al., 2013; Watanabe et al., 2014). Other biomarker regions such as TEM, RFP, and visual areas (LV and MV) also show larger numbers of common and unique connections.

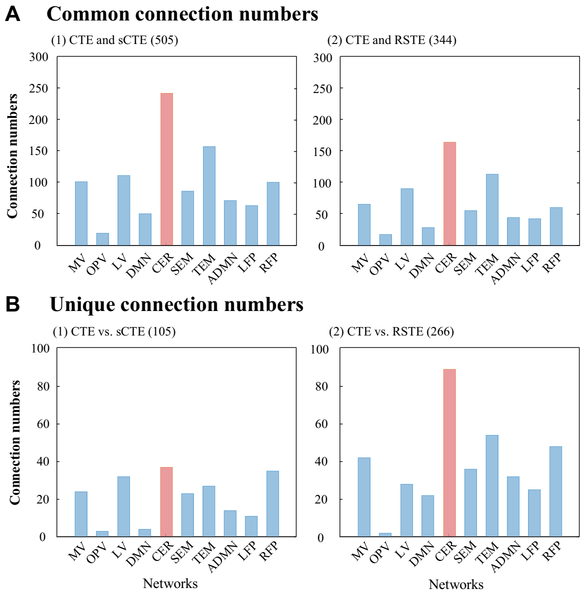

FIGURE 5
Common and unique connections between CTE and sCTE and between CTE and STE. The network with the maximum number of connections is highlighted in red.

Table 2 shows common and unique connections between CTE and sCTE/STE with the top five significant HCs-SZs differences. These connections are mainly related to the brain networks including CER, RFP, and TEM, which are consistent with the abnormal connections of schizophrenia obtained by previous studies (Su et al., 2013; Watanabe et al., 2014; Oestreich et al., 2016; Maher et al., 2019; Dietz et al., 2020; Rashidi et al., 2021). Moreover, CTE detects unique connections with highly significant HCs-SZs differences related to RFP (vs. sCTE), DMN, and TEM (vs. STE). Considering the numbers and *t*-values of the connections with significant intergroup differences in Figure 5 and Table 2, CER, TEM, and RFP may be regarded as the biomarker brain networks for identifying schizophrenia (Su et al., 2013; Nenadic et al., 2014; Watanabe et al., 2014; Oestreich et al., 2016; Zhuo et al., 2018; Rashidi et al., 2021; Sklar et al., 2021).

Figure 6 shows the SVM classification accuracy. The features are the unique or common connections obtained by CTE, sCTE, and STE. CTE exhibits the highest accuracy (92.8%) using unique connections relative to sCTE, followed by STE. As these unique connections of CTE are mainly related to RFP and CER shown in Table 2, it suggests that RFP- and CER-related connections helps to classify HCs and SZs. After verifying CTE unique connections are helpful in classification, exploiting all the significant connections

TABLE 2 Common and unique connections with the top five HCs-SZs significance.

	Top five significant connections (AAL)	Networks	*p*-values (CTE)
Common (CTE and sCTE)	(1) No.64-No.100	RFP, CER	5.50×10^{-5}
	(2) No.30-No.80	TEM	6.42×10^{-5}
	(3) No.52-No.100	MV, CER	1.76×10^{-4}
	(4) No.3-No.20	ADMN, SEM	4.59×10^{-4}
	(5) No.92-No.111	CER	4.98×10^{-4}
Common (CTE and STE)	(1) No.64-No.100	RFP, CER	5.50×10^{-5}
	(2) No.52-No.100	MV, CER	1.76×10^{-4}
	(3) No.80-No.100	TEM, CER	2.73×10^{-4}
	(4) No.67-No.92	DMN, CER	5.59×10^{-4}
	(5) No.18-No.92	TEM, CER	6.33×10^{-4}
Unique (CTE vs. sCTE)	(1) No.14-No.28	RFP, LFP	0.0147
	(2) No.56-No.86	CER, LV	0.0167
	(3) No.37-No.64	MV, RFP	0.0173
	(4) No.20-No.102	SEM, CER	0.0178
	(5) No.66-No.78	RFP, OPV	0.0178
Unique (CTE vs. STE)	(1) No.25-No.29	DMN, TEM	0.0022
	(2) No.27-No.109	DMN, CER	0.0027
	(3) No.16-No.103	RFP, CER	0.0033
	(4) No.108-No.113	CER	0.0033
	(5) No.20-No.100	SEM, CER	0.0036

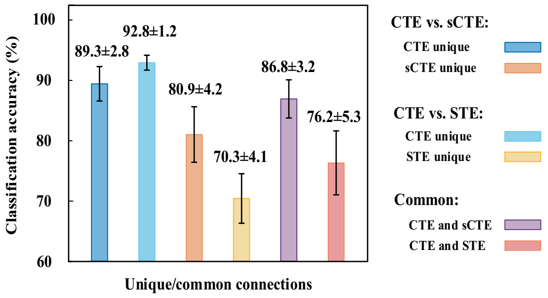

FIGURE 6
SVM classification accuracy for using unique/common connections obtained by CTE, sCTE, and STE, respectively. Unique connections of CTE achieve higher accuracy than others.

including common and unique connections for classification is evaluated in Table 3.

For all the connections with significant intergroup differences, Table 3 shows the SVM performance measures (ACC, SEN, and SPEC) from five causality algorithms. As expected, the proposed complex-valued transfer entropy methods (CTE and sCTE) achieve better performance than real-valued directed analysis methods. CTE shows the best classification performance among all the five directed analysis methods; e.g., it improves higher ACC with 10.2% (95.5% vs. 85.3%) to sCTE, 13.6% (95.5% vs. 81.9%) to STE, 18.7% (95.5% vs. 76.8%) to HTE, and 20.9% (95.5% vs. 74.6%) to Granger, respectively. The proposed CTE obtains all the highest values of the three classification measures, especially for SEN reaching to 96.3%. This suggests that CTE captures meaningful and discriminative features to identify HCs and SZ.

Several studies have employed SVM for classifying HCs and SZs, especially using FC as features. In terms of using SVM for HCs and SZs classification, we select the previous studies with similar data sizes of the dataset in the paper (40 HCs and 40 SZs) for comparison. Su et al. (2013) performed SVM to FC quantified by an extended maximal information coefficient and obtained 82.8% clustering accuracy (32 HCs and 32 SZs). By analyzing the coherence regional homogeneity value, Liu et al. (2018) demonstrated that the abnormal connections related to TEM, insula, precentral gyrus, and precuneus can be used as psychosis biomarker of schizophrenia and achieved 89.9% accuracy (31 HCs and 48 SZs). Following this, Bae et al. (2018) pointed to decreased connections in the global and local network connectivity in SZs compared with HCs, especially in DMN, left parietal region, and TEM with an accuracy of 92.1% (31 HCs and 48 SZs). Instead of using FC of magnitude data for classification, Li et al. (2024) utilized dynamic connectivity features of phase maps as features for classification and obtained 87.5% accuracy (24 HCs and 24 SZs). As mentioned above, the existing studies of real-valued connections achieved 82.8–92.1% SVM accuracy for classifying HCs and SZs. Due to making full use of both magnitude and phase fMRI data, directed FC quantified by CTE shows higher classifying accuracy (95.5%) than the previous studies with similar data sizes.

5 Discussion

To our knowledge, few studies have explored directed FC based on complex-valued fMRI data, although directed FC has been

TABLE 3 SVM classification is performed by combining unique connections and common connections.

	ACC (%)	SEN (%)	SPEC (%)
CTE	95.5 ± 2.8	96.3 ± 1.4	94.7 ± 5.1
sCTE	85.3 ± 7.2	90.5 ± 11.9	80.1 ± 9.6
STE	81.9 ± 10.1	85.0 ± 13.4	78.8 ± 12.3
HTE	76.8 ± 9.7	83.2 ± 11.2	70.4 ± 8.7
Granger	74.6 ± 8.6	77.1 ± 15.7	72.1 ± 10.9

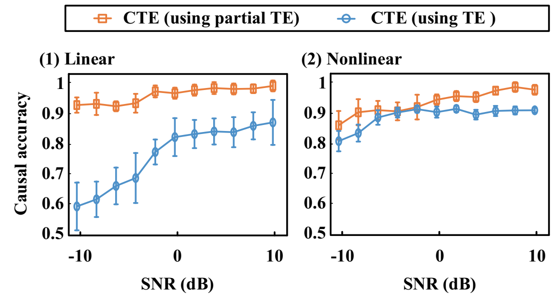

FIGURE 7
Causal inference accuracy comparison for CTE that using partial transfer entropy (shorted as partial TE) and TE, respectively. The proposed CTE using partial TE shows higher accuracy than the CTE that uses TE to directly quantify magnitude–phase causality.

increasingly studied using magnitude-only fMRI data. In this study, we propose a non-linear complex-valued directed analysis method based on transfer entropy to make full use of complex-valued fMRI data in highlighting differences between HCs and SZs. Simulated results show that our method has the highest accuracy and noisy robustness, especially for the non-linear model with complete complex-valued causality containing magnitude–magnitude, phase–phase, and magnitude–phase relationship. Experimental results show that CTE detects more unique connections with higher significant intergroup differences, thus leading to better performance in classifying HCs and SZs.

Instead of directly quantifying magnitude–phase causality, we propose to introduce partial transfer entropy to exploit the complementary phase/magnitude effects on magnitude–phase and phase–magnitude causality. This is because partial CTE can simultaneously utilize both magnitude and phase to assess causality in Eqs. (4) and (5), while transfer entropy only considers magnitude–phase or phase–magnitude dependence without the complementary phase/magnitude effects in Eqs. (32) and (33) as follows:

$$\mathcal{R}_{\boldsymbol{b}\to\boldsymbol{\theta}} = \sum p\left(\theta,\theta_{t-\tau},\boldsymbol{b}_{t-\tau}\right)\log\frac{p\left(\theta_t|\theta_{t-\tau},\boldsymbol{b}_{t-\tau}\right)}{p\left(\theta_t|\theta_{t-\tau}\right)} \qquad (32)$$

$$\mathcal{R}_{\boldsymbol{a}\to\boldsymbol{\varphi}} = \sum p\left(\varphi_t,\varphi_{t-\tau},\boldsymbol{a}_{t-\tau}\right)\log\frac{p\left(\varphi_t|\varphi_{t-\tau},\boldsymbol{a}_{t-\tau}\right)}{p\left(\varphi_t|\varphi_{t-\tau}\right)} \qquad (33)$$

As such, we use transfer entropy $\mathcal{R}_{\boldsymbol{b}\to\boldsymbol{\theta}}$ and $\mathcal{R}_{\boldsymbol{a}\to\boldsymbol{\varphi}}$ to replace partial entropy $\mathcal{R}_{\boldsymbol{a}\to\boldsymbol{b}|\boldsymbol{\theta}}$ and $\mathcal{R}_{\boldsymbol{\theta}\to\boldsymbol{\varphi}|\boldsymbol{a}}$ for comparison when calculating the proposed CTE.

Figure 7 shows directed accuracy for the simulated signals with linear and non-linear complete complex-valued causality (type L1 and N1). It presents that using partial transfer entropy (shorted as partial TE) to measure the complementary phase and magnitude effects on magnitude–phase causality shows better performance than those directly quantifying magnitude–phase causality using transfer entropy (TE), especially for quantifying the linear causality. When measuring the causality between magnitude and phase, partial TE considers more information, thus partial TE enhancing CTE noise robustness. It verifies the effectiveness of introducing partial TE in the proposed CTE definition.

To evaluate the data length effects on CTE, we change the simulated data length from 100 to 1,000 time points. CTE can keep high causality inference accuracy, especially for the signals with complete complex-valued causality (type L1 and N1). Because CTE keeps high causality inference accuracy to different data lengths, we can combine CTE and a sliding window approach for dynamic analysis. By performing causality analysis on the segmented time series, directed FC from different windows can be obtained. As such, dynamic statistical analysis can be exploited to analyze dynamics from the directed FC.

Figure 8 shows the average Pearson correlation coefficients between magnitude and phase from two different ROI signals across all the subjects in each group. The magnitude–phase correlation coefficients range from −0.2 to 0.2. This supports the magnitude–phase causality considered in the proposed method. Specifically, CER-related connections are marked with black boxes and locally magnified. There are polarity and strength differences between HCs and SZs in both magnitude–phase and phase–magnitude correlation coefficients. This suggests that the proposed complex-valued transfer entropy considering causality between magnitude–phase and phase–magnitude is essential and can capture more intergroup differences.

CER-related connections show more and higher significant intergroup differences obtained by the proposed CTE. Although the cerebellum has been reported to be associated with the motor system, a growing number of studies have found that the cerebellum is critical to processing complex functions, e.g., attention, cognition, and language (Lungu et al., 2013). Lungu et al. reviewed 234 fMRI studies published from 1997 to 2010 related to SZs and pointed out that 41.02% of the articles reported cerebellar activity related to cognitive, emotional, and executive processes in schizophrenia. In conclusion, the results of their analyses suggest that the cerebellum plays an essential functional role in schizophrenia, especially in the cognitive and executive domains. Following this, we performed searches in the abstracts of articles indexed in Scopus from 2011 to 2023 and found 218 articles that reported abnormal cerebellum-related connections in schizophrenia. These studies proved that the cerebellum is a functional hub involved in cognition, language, and emotional processing with regions, including TEM, DMN, and visual areas. For instance, Table 2 highlights Cerebelum_6_R (AAL No.100) has connections with significant HC-SZ difference, which is also consistent with previous studies. Su et al. (2013) quantified non-linear undirected connections and pointed out that cerebellum-related ROIs, especially CRBL6.R, were important in identifying schizophrenia. Zhuo et al. (2018) calculated FC density to investigate cerebellar connectivity changes of SZs and found abnormal connectivity strength of Cerebelum_6_R with visual areas (Zhuo et al., 2018).

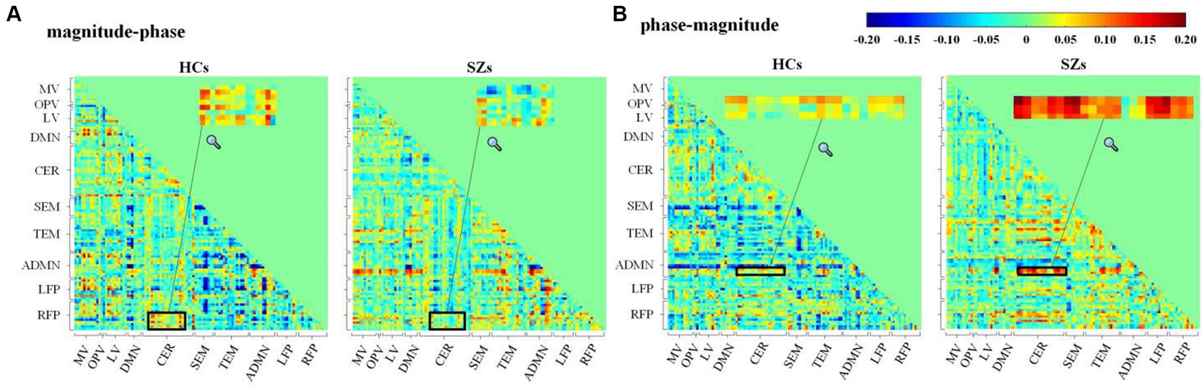

FIGURE 8
Average Pearson's correlation coefficients for **(A)** magnitude–phase and **(B)** phase–magnitude of complex-valued time series from 116 AAL ROIs across subjects in HCs or SZs.

TABLE 4 SVM classification is performed based on the directed FNC of brain networks.

	Accuracy (%)	Sensitivity (%)	Specificity (%)
CTE	88.2 ± 7.6	89.5 ± 4.8	86.9 ± 8.2
sCTE	83.1 ± 8.1	88.4 ± 6.7	77.8 ± 11.5
STE	78.3 ± 4.4	83.7 ± 7.1	72.9 ± 6.7
HTE	70.7 ± 7.8	78.0 ± 6.8	63.4 ± 5.9
Granger	71.3 ± 8.6	80.5 ± 4.9	62.1 ± 8.1

Apart from CER, CTE also detects common connections related to visual areas (MV and LV), and temporal lobe (TEM) in Table 2. These two nodes have brain functions of vision and auditory, respectively. As hallucinations are a frequent symptom of schizophrenia including visual and auditory hallucinations occupying 70% of patients with schizophrenia (Demirci et al., 2008), it is expected that MV and TEM are schizophrenia-related in terms of pathology mechanisms (Fogelson et al., 2014; Dietz et al., 2020). For unique connections detected by CTE in Table 3, abnormal connectivity mainly related to RFP is verified by previous studies. Frontal parietal regions have been shown involved in the cognitive and perceptive process (Smith et al., 2009) and are highly related to the impaired cognitive function of SZs (Roiser et al., 2013). Roiser et al. pointed out that connective abnormality related to the frontal–parietal areas may link to cognitive impairment for SZs (Roiser et al., 2013), given that the unique abnormal connectivity patterns obtained by CTE may provide additional evidence for the cognitive and perceptive impairments of schizophrenia.

In addition to FC between ROI, CTE can also measure the FNC of brain networks. We use CTE to quantify the FNC of brain networks. Table 4 shows the SVM performance of the five directed analysis methods. Similar to FC results, CTE also shows the best performance among these methods. Compared with other directed analysis methods, CTE shows better classification performance, e.g., improves higher accuracy with 5.1% (88.2% vs. 83.1%) to sCTE, 9.9% (88.2% vs. 78.3%) to STE, 17.5% (88.2% vs. 70.7%) to HTE, and 16.9% (88.2% vs. 71.3%) to HTE, respectively.

In future, our CTE approach can be extended to analyzing causal FNC of time courses extracted by blind source separation, e.g., ICA, sparse representation, and tensor decomposition. Second, dynamic-directed FC/FNC can be performed to further improve classification performance. Finally, CTE can be exploited for other mental disorders such as depressive disorder or further extended to other applications for evaluating complex-valued causality.

Data availability statement

The original contributions presented in the study are included in the article/supplementary material, further inquiries can be directed to the corresponding authors.

Ethics statement

The studies involving humans were approved by University of New Mexico Institutional Review Board. The studies were conducted in accordance with the local legislation and institutional requirements. The participants provided their written informed consent to participate in this study. Written informed consent was obtained from the individual(s) for the publication of any potentially identifiable images or data included in this article.

Author contributions

W-XL: Conceptualization, Investigation, Methodology, Software, Writing – original draft, Writing – review & editing. Q-HL: Funding acquisition, Validation, Writing – review & editing. C-YZ: Methodology, Validation, Writing – review & editing. YH: Conceptualization, Validation, Writing – review & editing. VC: Data curation, Funding acquisition, Investigation, Validation, Writing – review & editing.

Funding

The author(s) declare that financial support was received for the research, authorship, and/or publication of this article. This study was supported in part by the National Natural Science Foundation of China under Grant 61871067, in part by the NSF under Grant

2112455, in part by the NIH Grant R01MH123610, in part by the Fundamental Research Funds for the Central Universities, China, under Grant DUT20ZD220, and in part by the Supercomputing Center of Dalian University of Technology.

Conflict of interest

The authors declare that the research was conducted in the absence of any commercial or financial relationships that could be construed as a potential conflict of interest.

The reviewer L-DK declared a past co-authorship with the authors Q-HL and VC to the handling editor.

The author(s) declared that they were an editorial board member of Frontiers, at the time of submission. This had no impact on the peer review process and the final decision.

Publisher's note

References

Adali, T., and Calhoun, V. D. (2007). Complex ICA of brain imaging data. *IEEE ASSP Mag.* 24, 136–139. doi: 10.1109/SP.2007.904742

Bae, Y., Kumarasamy, K., Ali, I. M., Korfiatis, P., Akkus, Z., and Erickson, B. J. (2018). Differences between schizophrenic and normal subjects using network properties from fMRI. *J. Digit. Imaging* 31, 252–261. doi: 10.1007/s10278-017-0020-4

Bastos, A. M., and Schoffelen, J. M. (2016). A tutorial review of functional connectivity analysis methods and their interpretational pitfalls. *Front. Syst. Neurosci.* 9:175. doi: 10.3389/fnsys.2015.00175

Bastos-Leite, A. J., Ridgway, G. R., Silveira, C., Norton, A., Reis, S., and Friston, K. J. (2015). Dysconnectivity within the default mode in first-episode schizophrenia: a stochastic dynamic causal modeling study with functional magnetic resonance imaging. *Schizophr. Bull.* 41, 144–153. doi: 10.1093/schbul/sbu080

Behrendt, S., Dimpfl, T., Peter, F. J., and Zimmermann, D. J. (2019). RTransferEntropy-quantifying information flow between different time series using effective transfer entropy. *SoftwareX* 10:100265. doi: 10.1016/j.softx.2019.100265

Bielczyk, N. Z., Uithol, S., van Mourik, T., Anderson, P., Glennon, J. C., and Buitelaar, J. K. (2019). Disentangling causal webs in the brain using functional magnetic resonance imaging: a review of current approaches. *Netw. Neurosci.* 3, 237–273. doi: 10.1162/netn_a_00062

Bossomaier, T., Barnett, L., Harré, M., and Lizier, J. T. (2016). An introduction to transfer entropy: Information flow in complex systems. Berlin: Springer.

Calhoun, V. D., Adalı, T. G., Pearlson, D., van Zijl, P. C. M., and Pekar, J. J. (2002). Independent component analysis of fMRI data in the complex domain. *Magn. Reson. Med.* 48, 180–192. doi: 10.1002/mrm.10202

Caserini, N. A., and Pagnottoni, P. (2022). Effective transfer entropy to measure information flows in credit markets. *JISS* 31, 729–757. doi: 10.1007/s10260-021-00614-1

Crimi, A., Dodero, L., Sambataro, F., Murino, V., and Sona, D. (2021). Structurally constrained effective brain connectivity. *NeuroImage* 239:118288. doi: 10.1016/j.neuroimage.2021.118288

Demirci, O., Clark, V. P., Magnotta, V. A., Andreasen, N. C., Lauriello, J., Kiehl, K. A., et al. (2008). A review of challenges in the use of fMRI for disease classification/characterization and a projection pursuit application from a multi-site fMRI schizophrenia study. *Brain Imaging Behav.* 2, 207–226. doi: 10.1007/s11682-008-9028-1

Demirci, O., Stevens, M. C., Andreasen, N. C., Michael, A., Liu, J., White, T., et al. (2009). Investigation of relationships between fMRI brain networks in the spectral domain using ICA and granger causality reveals distinct differences between schizophrenia patients and healthy controls. *NeuroImage* 46, 419–431. doi: 10.1016/j.neuroimage.2009.02.014

Dietz, M. J., Zhou, Y., Veddum, L., Frith, C. D., and Bliksted, V. F. (2020). Aberrant effective connectivity is associated with positive symptoms in first-episode schizophrenia. *NeuroImage* 28:102444. doi: 10.1016/j.nicl.2020.102444

Fogelson, N., Litvak, V., Peled, A., Fernandez-del-Olmo, M., and Friston, K. (2014). The functional anatomy of schizophrenia: a dynamic causal modeling study of predictive coding. *Schizophr. Res.* 158, 204–212. doi: 10.1016/j.schres.2014.06.011

Friston, K. J., Preller, K. H., Mathys, C., Cagnan, H., Heinzle, J., Razi, A., et al. (2019). Dynamic causal modelling revisited. *NeuroImage* 199, 730–744. doi: 10.1016/j.neuroimage.2017.02.045

Goebel, B., Essiambre, R. J., Kramer, G., Winzer, P. J., and Hanik, N. (2011). Calculation of mutual information for partially coherent Gaussian channels with applications to fiber optics. *IEEE Trans. Inf. Theory* 57, 5720–5736. doi: 10.1109/TIT.2011.2162187

Gu, D., Mi, Y., and Lin, A. (2021). Application of time-delay multiscale symbolic phase compensated transfer entropy in analyzing cyclic alternating pattern (CAP) in sleep-related pathological data. *Commun. Nonlinear Sci. Numer. Simul.* 99:105835. doi: 10.1016/j.cnsns.2021.105835

Guo, W., and Bhaskara, R. M. (2008). On control of the false discovery rate under no assumption of dependency. *J. Stat. Plan Inference* 138, 3176–3188. doi: 10.1016/j.jspi.2008.01.003

Jizba, P., Lavička, H., and Tabachová, Z. (2022). Causal inference in time series in terms of Rényi transfer entropy. *Entropy* 24:855. doi: 10.3390/e24070855

Li, X., Coyle, D., Maguire, L., McGinnity, T. M., and Benali, H. (2011). A model selection method for nonlinear system identification based fMRI effective connectivity analysis. *IEEE Trans. Med. Imaging* 30, 1365–1380. doi: 10.1109/TMI.2011.2116034

Li, W.-X., Lin, Q.-H., Zhao, B.-H., Kuang, L.-D., Zhang, C.-Y., Han, Y., et al. (2024). Dynamic functional network connectivity based on spatial source phase maps of complex-valued fMRI data: application to schizophrenia. *J. Neurosci. Methods* 403:110049. doi: 10.1016/j.jneumeth.2023.110049

Li, X., Marrelec, G., Hess, R. F., and Benali, H. (2010). A nonlinear identification method to study effective connectivity in functional MRI. *Med. Image Anal.* 14, 30–38. doi: 10.1016/j.media.2009.09.005

Li, M. A., and Zhang, Y. Y. (2022). A brain functional network based on continuous wavelet transform and symbolic transfer entropy. *Acta Electron. Sin.* 50, 1600–1608. doi: 10.12263/DZXB.20210298

Lin, Q. H., Niu, Y. W., Sui, J., Zhao, W. D., Zhuo, C., and Calhoun, V. D. (2022). SSPNet: an interpretable 3D-CNN for classification of schizophrenia using phase maps of resting-state complex-valued fMRI data. *Med. Image Anal.* 79:102430. doi: 10.1016/j.media.2022.102430

Liu, Y., Guo, W., Zhang, Y., Lv, L., Hu, F., Wu, R., et al. (2018). Decreased resting-state interhemispheric functional connectivity correlated with neurocognitive deficits in drug-naive first-episode adolescent-onset schizophrenia. *Int. J. Neuropsychopharmacol.* 21, 33–41. doi: 10.1093/ijnp/pyx095

Liu, J., Ji, J., Xun, G., and Zhang, A. (2022). Inferring effective connectivity networks from fMRI time series with a temporal entropy-score. *IEEE Trans. Neural Netw. Learn. Syst.* 33, 5993–6006. doi: 10.1109/TNNLS.2021.3072149

Lizier, J. T., Heinzle, J., Horstmann, A., Haynes, J.-D., and Prokopenko, M. (2011). Multivariate information-theoretic measures reveal directed information structure and task relevant changes in fMRI connectivity. *J. Comput. Neurosci.* 30, 85–107. doi: 10.1007/s10827-010-0271-2

Lungu, O., Barakat, M., Laventure, S., Debas, K., Proulx, S., Luck, D., et al. (2013). The incidence and nature of cerebellar findings in schizophrenia: a quantitative review of fMRI literature. *Schizophr. Bull.* 39, 797–806. doi: 10.1093/schbul/sbr193

Maher, S., Ekstrom, T., Ongur, D., Levy, D. L., Norton, D. J., Nickerson, L. D., et al. (2019). Functional disconnection between the visual cortex and right fusiform face area in schizophrenia. *Schizophr. Res.* 209, 72–79. doi: 10.1016/j.schres.2019.05.016

Mahmood, U., Fu, Z., Ghosh, S., Calhoun, V., and Plis, S. (2022). Through the looking glass: deep interpretable dynamic directed connectivity in resting fMRI. *NeuroImage* 264:119737. doi: 10.1016/j.neuroimage.2022.119737

Motlaghian, S. M., Vahidi, V., Baker, B., Belger, A., Bustillo, J. R., Faghiri, A., et al. (2023). A method for estimating and characterizing explicitly nonlinear dynamic functional network connectivity in resting-state fMRI data. *J. Neurosci. Methods* 389:109794. doi: 10.1016/j.jneumeth.2023.109794

Nenadic, I., Yotter, R. A., Sauer, H., and Gaser, C. (2014). Cortical surface complexity in frontal and temporal areas varies across subgroups of schizophrenia. *Hum. Brain Mapp.* 35, 1691–1699. doi: 10.1002/hbm.22283

Oestreich, L. K. L., McCarthy Jones, S.Australian Schizophrenia Research Bank, and Whitford, T. J. (2016). Decreased integrity of the fronto-temporal fibers of the left inferior occipito-frontal fasciculus associated with auditory verbal hallucinations in schizophrenia. *Brain Imaging Behav.* 10, 445–454. doi: 10.1007/s11682-015-9421-5

Papana, A., Kugiumtzis, D., and Larsson, P. G. (2012). Detection of direct causal effects and application to epileptic electroencephalogram analysis. *Int. J. Bifurcation Chaos* 22:1250222. doi: 10.1142/S0218127412502227

Rashidi, S., Murillo-Rodriguez, J., Murillo-Rodriguez, E., Machado, S., Hao, Y., and Yadollahpour, A. (2021). Transcranial direct current stimulation for auditory verbal hallucinations: a systematic review of clinical trials. *Neural Regen. Res.* 16, 666–671. doi: 10.4103/1673-5374.295315

Roiser, J. P., Wigton, R., Kilner, J. M., Mendez, M. A., Hon, N., Friston, K. J., et al. (2013). Dysconnectivity in the frontoparietal attention network in schizophrenia. *Front. Psych.* 4:176. doi: 10.3389/fpsyt.2013.00176

Rowe, D. B., and Logan, B. R. (2004). A complex way to compute fMRI activation. *NeuroImage* 23, 1078–1092. doi: 10.1016/j.neuroimage.2004.06.042

Schreiber, T. (2000). Measuring information transfer. *Phys. Rev. Lett.* 85, 461–464. doi: 10.1103/PhysRevLett.85.461

Seth, A. K. (2010). A MATLAB toolbox for granger causal connectivity analysis. *J. Neurosci. Methods* 186, 262–273. doi: 10.1016/j.jneumeth.2009.11.020

Sklar, A. L., Coffman, B. A., and Salisbury, D. F. (2021). Fronto-parietal network function during cued visual search in the first-episode schizophrenia spectrum. *J. Psychiatr. Res.* 141, 339–345. doi: 10.1016/j.jpsychires.2021.07.014

Smith, S. M., Fox, P. T., Miller, K. L., Glahn, D. C., Fox, P. M., Clare, E., et al. (2009). Correspondence of the brain's functional architecture during activation and rest. *Proc. Natl. Acad. Sci. USA* 106, 13040–13045. doi: 10.1073/pnas.0905267106

Stevens, M. C., Pearlson, G. D., and Calhoun, V. D. (2009). Changes in the interaction of resting-state neural networks from adolescence to adulthood. *Hum. Brain Mapp.* 30, 2356–2366. doi: 10.1002/hbm.20673

Su, L., Wang, L., Shen, H., Feng, G., and Hu, D. (2013). Discriminative analysis of non-linear brain connectivity in schizophrenia: an fMRI study. *Front. Hum. Neurosci.* 7:00702. doi: 10.3389/fnhum.2013.00702

Suykens, J. A. K., and Vandewalle, J. (1999). Training multilayer perceptron classifiers based on a modified support vector method. *IEEE Trans. Neural Netw.* 10, 907–911. doi: 10.1109/72.774254

Tzourio-Mazoyer, N., Landeau, B., Papathanassiou, D., Crivello, F., Etard, O., Delcroix, N., et al. (2002). Automated anatomical labeling of activations in SPM using a macroscopic anatomical parcellation of the MNI MRI single-subject brain. *NeuroImage* 15, 273–289. doi: 10.1006/nimg.2001.0978

Ursino, M., Ricci, G., and Magosso, E. (2020). Transfer entropy as a measure of brain connectivity: a critical analysis with the help of neural mass models. *Front. Comput. Neurosci.* 14:45. doi: 10.3389/fncom.2020.00045

Wang, Y., and Chen, W. (2020). Effective brain connectivity for fNIRS data analysis based on multi-delays symbolic phase transfer entropy. *J. Neural Eng.* 17:056024. doi: 10.1088/1741-2552/abb4a4

Watanabe, T., Kessler, D., Scott, C., Angstadt, M., and Sripada, C. (2014). Disease prediction based on functional connectomes using a scalable and spatially-informed support vector machine. *NeuroImage* 96, 183–202. doi: 10.1016/j.neuroimage.2014.03.067

Wessel, N., Voss, A., Malberg, H., Ziehmann, C., Voss, H. U., Schirdewan, A., et al. (2000). Nonlinear analysis of complex phenomena in cardiological data. *Herzschrittmachertherapie Elektrophysiologie* 11, 159–173. doi: 10.1007/s003990070035

Wu, X., Wen, X., Li, J., and Yao, L. (2014). A new dynamic Bayesian network approach for determining effective connectivity from fMRI data. *Neural Comput. & Applic.* 24, 91–97. doi: 10.1007/s00521-013-1465-0

Yu, M. C., Lin, Q. H., Kuang, L. D., Gong, X. F., Cong, F., and Calhoun, V. D. (2015). ICA of full complex-valued fMRI data using phase information of spatial maps. *J. Neurosci. Methods* 249, 75–91. doi: 10.1016/j.jneumeth.2015.03.036

Zhang, J., Cao, J., Wu, T., Huang, W., Ma, T., and Zhou, X. (2023). A novel adaptive multi-scale Rényi transfer entropy based on kernel density estimation. *Chaos Solitons Fractals* 175:113972. doi: 10.1016/j.chaos.2023.113972

Zhuo, C., Wang, C., Wang, L., Guo, X., Xu, Q., Liu, Y., et al. (2018). Altered resting-state functional connectivity of the cerebellum in schizophrenia. *Brain Imaging Behav.* 12, 383–389. doi: 10.1007/s11682-017-9704-0

Frontiers in Neuroscience

Provides a holistic understanding of brain function from genes to behavior

Part of the most cited neuroscience journal series which explores the brain - from the new eras of causation and anatomical neurosciences to neuroeconomics and neuroenergetics.

Discover the latest Research Topics

See more →

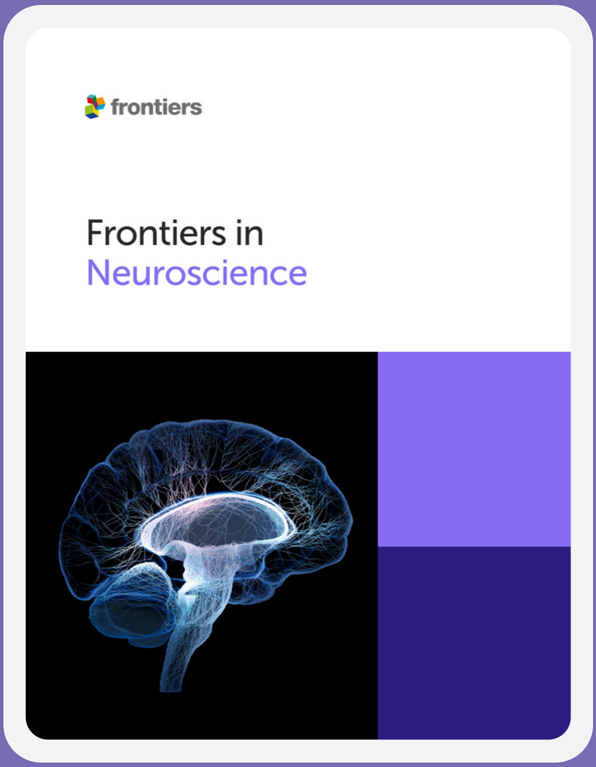
frontiers

Frontiers in
Neuroscience

Frontiers

Avenue du Tribunal-Fédéral 34
1005 Lausanne, Switzerland
frontiersin.org

Contact us

+41 (0)21 510 17 00
frontiersin.org/about/contact